

الجمهورية الجزائرية الديمقراطية الشعبية
République Algérienne Démocratique et Populaire
Ministère de L'Enseignement Supérieur et de la Recherche Scientifique



UNIVERSITÉ FERHAT ABBAS - SETIF-1

FACULTÉ DE TECHNOLOGIE

THÈSE

Présentée au Département de génie des procédés

Pour l'obtention du diplôme de

DOCTORAT

Domaine : Sciences et Technologie

Filière : Génie des procédés

Option : Génie Chimique

Par

TOUAHRIA Youcef Islam

THÈME

Étude expérimentale et théorique des propriétés biologiques et inhibitrices de corrosion d'une nouvelle série de dérivés hydrazone.

Soutenu le 09/10/2024 devant le Jury:

ZOUAOUI Ahmed	Professeur	Univ. Ferhat Abbas Sétif-1	Président
CHAFAI Nadjib	M.C.A	Univ. Ferhat Abbas Sétif-1	Directeur de thèse
HARKAT Hassina	Professeur	Univ. Mostefa Ben Boulaid Batna-2	Examinatrice
KERKOUR Rachida	M.C.A	Univ. Abdelhafid Boussouf-Mila	Examinatrice
HELLAL Abdelkader	Professeur	Univ. Ferhat Abbas Sétif-1	Examineur
BENQUERBA Yacine	Professeur	Univ. Ferhat Abbas Sétif-1	Membre invité

الجمهورية الجزائرية الديمقراطية الشعبية
Democratic and Popular Republic Of Algeria
Ministry of Higher Education and Scientific Research



FERHAT ABBAS UNIVERSITY ABBAS - SETIF-1

FACULTY OF TECHNOLOGY

THESIS

Presented at Department of Process Engineering

For obtaining the degree of:

DOCTORATE

Domaine : Sciences and Technologie

Field:Process Engineering

Special filed:Chemical Engineering

Presented by

TOUAHRIA Youcef Islam

TOPIC

Experimental and theoretical study of the biological and corrosion-inhibiting properties of a new series of hydrazone derivatives.

Presented publicly on 10/09/2024 to the jury committee of:

ZOUAOUI Ahmed	Professor	Univ. Ferhat Abbas Sétif-1	President
CHAFAI Nadjib	M.C.A	Univ. Ferhat Abbas Sétif-1	Supervisor
HARKAT Hassina	Professor	Univ.Mostefa Ben Boulaid. BATNA-2	External Examiner
KERKOUR Rachida	M.C.A	Univ. Abdelhafid Boussouf-Mila	External Examiner
HELLAL Abdelkader	Professor	Univ. Ferhat Abbas Sétif-1	Examiner
BENGUERBA Yacine	Professor	Univ. Ferhat Abbas Sétif-1	Invited member

Acknowledgement

I would like to convey my deepest thanks to **Allah**, the Most Gracious and most Merciful, for providing me with guidance and support during the preparation of my thesis. I acknowledge the divine wisdom that has enlightened my path in the pursuit of knowledge with humility.

I would like to express my gratitude to my supervisor, **Dr. CHAFAI Nadjib** from the bottom of my heart for all of their help and support during the completion of this thesis. The result of this endeavor has been greatly influenced by their knowledge, support, and commitment. It is a great blessing that served as my mentor. In addition to freely sharing his knowledge and insights, he also offered constructive feedback that greatly aided in the development of this thesis.

I am extremely thankful for **Pr ZOUAOUI Ahmed's** readiness to accept the presidency and for his priceless input during the evaluation procedure.

I sincerely thank them for the invaluable time, knowledge, and careful assessment that the distinguished jury members, **Pr. HARKAT Hassina, Dr. KERKOUR Rachida**, and **Pr. HELLAL Abdelkader**, provided. This thesis is much better because of each member's own viewpoint and observations.

I am deeply grateful to the esteemed staff of the University of Ferhat Abbas Setif 1 Laboratory of Electrochemistry of molecular materials and complexes of Components (LEMMC) for their invaluable assistance in seeing this thesis through to completion.

Dr. MOUMNI Wahiba for her constant assistance, direction, and attitude of cooperation have tremendously improved the caliber of this thesis and have been crucial in helping to overcome numerous obstacles that have come up while working on it. Also, I have to thank **Dr. MEHRI Mona** for her support and guidance, without forgetting the Lab engineers **Mrs. souad**, **Mrs. fouzia** and **Mr. Abdallah**.

I would particularly like to express my heartfelt thanks to **Professor Benguerba Yacine** for his outstanding advice, constant encouragement, and priceless mentoring during the whole thesis. I really thank him for his exceptional assistance, knowledge, and commitment. His contribution has had an ongoing impact on this thesis, and I sincerely appreciate the significant role he has performed.

I extend my heartfelt gratitude to **Dr. Boublija Abir** for her invaluable contributions and unwavering support throughout this research. Her exceptional expertise and relentless dedication have been instrumental in the successful completion of this study. This acknowledgment seeks to recognize and appreciate **Dr. Boublija Abir's** significant role in this project. Her profound insights and meticulous efforts have greatly enhanced the quality and depth of the findings presented in this thesis. The improved conclusions and overall excellence of the work are a testament to the positive impact of her contributions.

I would like to express my sincere gratitude to **Dr. Amel Boudechicha** for her remarkable support and valuable contributions to my doctoral research. Her expert guidance in the experimental part, especially in the biological assays and the investigation of the bioactivity of hydrazone derivatives, has been essential to the success of this work.

To the late **Dr. Abed Lina** May Allah grant her soul eternal peace and reward her for the knowledge and kindness she shared with those around her.

My sincere gratitude is extended to **Professor Ehab Alshamaila** of Jordan for his assistance and direction during this research. His deep expertise and perceptive criticism have been extremely helpful in determining the focus and caliber of this work.

The administrative team of the department which was led by **Dr. CHEBIRA Fakhri** and now under leading of **Dr. BOUKAZOULA Taib** has shown incredible commitment to ensure this project moves forward without difficulties. They have been an inspiration because of their promptness, effectiveness, and dedication to developing a culture of academic success

I would like to express my sincere gratitude to the administrative team of the Faculty of Technology, especially **Ibtissam, Lynda, Meriam** and **Sonia**, for their support and assistance throughout my doctoral defense. Their professionalism has been invaluable in ensuring the smooth progress of my work. Thank you for your help and continuous encouragement.

I am also deeply thankful to all the **doctors** and **professors** who have been part of my educational experience.

I am grateful to my **family**, **My parents Ammar** and **Zahra**, **My brothers Mohamed**, **Ahmed**, **My sister Nada** and **My wife Dounia** for their tremendous encouragement. Also I am grateful to my colleagues and the academic community as a whole for their important contributions to my intellectual and personal growth. I sincerely appreciate your help, inspiration, and role in both my professional and personal development.

TOUAHRIA Youcef Islam

Dedication

To my most beloved father, Ammar

To my dear mother Zahra the heart and spirit of the family

To my dear wife Dounia

To my Brothers Mohamed and Ahmed

To my dear Sister Nada

To my Uncles Hakim and Mohamed

To my colleague Abir

**To my friends : Djamai ,Tarek , Abdrahman, Badis , ALwalidane
bouden and alioui, Amine.**

**To my jordanian friends: Qosai ,Yazan,Tarek,Rakan and Ahmed.
Colleagues and All my family.**

To khalti HOURIA and her husband Ami KHLIFA

To everyone who helped me.

List of Figures

Figure I. 1: Chemical structure methylamine, dimethylamine, and trimethylamine.....	6
Figure I. 2: General equation for amide.....	7
Figure I. 3: Chemical structure of imine compounds.....	8
Figure I. 4: Diazonium salt's structure.....	8
Figure I. 5: Carbazide chemical structure: A) diphenylcarbazide and B) Carbohydrazide.....	9
Figure I. 6: Some examples of well-known nitrogen-containing heterocyclic compounds.....	9
Figure I. 7: The synthesis methodologies for hydrazone linkages (a) condensation between hydrazine and ketone/aldehyde (b) the Japp-Klingemann reaction and (c) substitution of aryl halide with non-substituted hydrazones.....	13
Figure I. 8: hydrazone formation mechanism.....	14
Figure I. 9: Active centers of hydrazones.....	15
Figure I. 10: The metallic corrosion reaction steps in an aqueous media.....	17
Figure I.11: Chemical structure of (E)-1-(3-nitrobenzylidene)-2-(p-tolyl)hydrazine (E-NBPTH).....	21
Figure I. 12: Chemical structures (HYD-3) and (HYD-4).....	21
Figure I. 13: Chemical structures of N'((2chlorobenzo[h]quinolin3yl)methylene) benzohydrazide.....	22
Figure I.14: Commonly prescribed marketed drugs bearing hydrazone nucleus.....	23
Figure I. 15: Chemical structure of A)1-(naphthalen-1-ylmethylene)-2-phenylhydrazine B)1,2-bis(naphthalen-1-ylmethylene)hydrazine.....	24
Figure I. 16: Chemical structure of aromatic hydrazones synthesized by Adjissi et al. [54].	

Figure I. 17: Chemical structure of antifungal hydrazones.....	26
Figure I. 18: General structure of synthesized thiadiazolyl hydrazones [59].....	27
Figure II. 1: Schematic synthesis under reflux.	34
Figure II. 2: Thin layer chromatography (TLC).....	35
Figure II.3: Photograph of the melting point apparatus.....	36.
Figure II.4: Spectrophotometry apparatus.....	37
Figure II. 5: FTIR spectrometers apparatus.....	38
FigureII.6 : Example of Nyquist Plot.....	42
Figure III. 1: Reaction scheme of the studied hydrazones NBHZ and HBHZ.....	56
Figure III. 2: Reaction scheme of the studied hydrazones HHZB and MHZN.....	58
Figure III. 3: UV-Vis spectrums of obtained hydrazones A) NBHZ, B) HBHZ, C) HHZB, and D) MHZN.....	65.
Figure III. 4: UV-Vis spectrums of obtained hydrazones: A) NBHZ, B) HBHZ, C) HHZB, and D) MHZN.....	68
Figure III. 5: A) ^1H and B) ^{13}C NMR spectrums of NBHZ.....	70.
Figure III. 6: A) ^1H and B) ^{13}C NMR spectrums of HBHZ.....	72
Figure III. 7: A) ^1H and B) ^{13}C NMR spectrums of HHZB.....	75
Figure III. 8. A) ^1H and B) ^{13}C NMR spectrums of MHZN.....	78
Figure IV. 1: Optimized geometries of target aromatic hydrazone compounds: A) NBHZ, and B) HBHZ C) MHZN, and D) HHZB.....	81
Figure IV. 2: The experimental and calculated UV-Vis spectra of target aromatic hydrazone compounds: NBHZ (A , C) , HBHZ (B , D), MHZN (E , F) and HHZB (G , H).....	83
Figure IV. 3. The experimental, calculated FT-IR spectra and Correlation diagram between experimental and calculated wavenumbers of the target aromatic hydrazone compounds: NBHZ (A-C) and HBHZ (D-F).....	85

Figure IV. 4: The experimental, calculated FT-IR spectra and Correlation diagram between experimental and calculated wavenumbers of the target aromatic hydrazone compounds: MHZN (A-C) and HHZB (D-F).....	89.
Figure IV. 6: Atomic orbital compositions of the frontier molecular orbital for A) HHZB and B) MHZN.....	93.
Figure IV. 7: DOS spectrum of the aromatic hydrazone compounds: A) NBHZ, B) HBHZ, C) MHZN, and D) HHZB.....	94
Figure IV. 8: Total electron density mapped with molecular electrostatic potential surface of the aromatic hydrazones: A) NBHZ, B) HBHZ, C) HHZB, and D) MHZN.....	95
Figure IV. 9: The plot of Mulliken atomic charge distribution in geometry of the aromatic hydrazones: A) NBHZ, B) HBHZ, C) MHZN, and D) HHZB.....	97.
Figure IV. 11: Localized orbital locator maps of the aromatic hydrazone compounds.....	102
Figure IV. 12: Average localized ionization energy maps of the aromatic hydrazone compounds: A) NBHZ, B) HBHZ, C) MHZN, and D) HHZB.....	103.
Figure IV. 13: The RDG scatter plots (left) and NCI plots (right) isosurface ($s = 0.5$ a.u.) of the aromatic hydrazones: A) NBHZ, B) HBHZ, C) MHZN, D) HHZB, and E) color map and chemical explanation.....	105
Figure V.1: Nyquist plots for XC48 carbon steel in 1M HCl solution in absence and in presence of various concentrations of MHZN at 25 °C.....	106
Figure V.2: Potentiodynamic polarization curves obtained for the XC48 carbon steel electrode in 1M HCl solution in presence of various concentrations of MHZN at 25°C.....	108
Figure V.3: Langmuir adsorption isotherm of XC48 carbon steel in 1M HCL solution in presence of MHZN inhibitor.....	109
Figure V.4: 2D (on the Left) and 3D (on the Right) AFM images of carbon steel surface; (a) Polished carbon steel, (b) Carbon steel in 1 M HCl, (c) Carbon steel in 1 M HCl 7.5×10^{-5} M o inhibitor.....	111
Figure V.5: Illustration of the protection mechanism of MHZN on XC 48 surface.....	112
Figure V.6: Equilibrium configurations of the adsorbed inhibitor molecule on Fe (100) surface in (a) Side view and (b) Top view.....	114

Figure V.7: Optimized COSMO-RS 3D structures and charge surface regions of the investigated compound binary interactions with Fe cluster.....116

Figure V.8: Optimized COSMO-RS 3D structures and charge surface regions of the investigated compound binary interactions with Fe cluster.....117

Figure V.9 : Molecular graphical representation using QTAIM for the adsorption of MHZN inhibitor system onto the composite surface XC48.....118

Figure VI.1 Reduction of the DPPH• radical by A-H, where (AH) is a compound capable of yielding an H to the DPPH radical.....122

Figure VI. 2. IC₅₀ of NBHZ, HBHZ, and BHT; Linear regression between intern concentration and the inhibition percentage.....124.

Figure VI.3: IC₅₀ of MHZN, HHZB, and BHT; Linear regression between intern concentration and the inhibition percentage.....125

Figure VI.4. A) Crystal Structure of NADPH-Oxidase, B) Best docked pose visualization of HBHZ with NADPH-Oxidase, C) The best docked pose visualization of NBHZ with NADPH-Oxidase, D) The best docked pose visualization of MHZN with NADPH-Oxidase, E) The best docked pose visualization of HHZB with NADPH-Oxidase, and F) The best docked pose visualization of BHT with NADPH-Oxidase.....130

Figure VI. 5: 3D and 2D Binding-interaction diagrams of HBHZ (A and B), NBHZ (C and D), HHZB (E and F), MHZN (G and H) and BHT (I and J) with NADPH-Oxidase.....133

Figure VI. 6: Crystal structure of selected proteins (a) 1Q8I, (b) 1QD9, (c) 3L9S, and (d) 5IIP135

Figure VI. 7:. Best docked pose visualization of MHZN and HHZB with 1QD9, 5IIP, 1Q81 and 3L9S.....137

Figure VI. 8: 3D and 2D Binding-interaction diagrams of MHZN and HHZB with 1QD9, 5IIP, 1Q81 and 3L9.....138

List of Tables

Table III. 1: Chemical and physical properties of the synthesized hydrazones.....	60
Table III. 2: Solubility test of NBHZ.....	62.
Table III. 3: Solubility test of HBHZ.....	62
Table III. 4: Solubility test of HHZB.....	63
Table III. 5: Solubility test of MHZN.....	63
Table IV.1. Experimental and theoretical selected wavenumber values of the target aromatic hydrazone compounds.....	86
Table IV.2: Experimental and theoretical selected wavenumber values of the target aromatic hydrazone compounds MHZN and HHZB.....	89
TableIV.3: Quantum Chemical Parameters of the aromatic hydrazone compounds	93
Table IV.4: Natural population analysis of NBHZ and HBHZ.....	97
Table IV 5: Natural population analysis of MHZN, and HHZB.....	99
Table V.1. Impedance parameters and inhibition efficiency values for carbon steel XC48 in 1.0 M HCl solution containing different concentrations of MHZN at 298 K.....	107
Table V.2: Polarization parameters and the inhibition efficiency of carbon steel corrosion in 1.0 M HCl medium without and with different concentrations of MHZN at 298 K.....	108
Table V.3: Standard thermodynamic parameters of the adsorption of MHZN and HHZB in	
Table V.4.: The roughness obtained from AFM of carbon steel surfaces in 1 M HCl solution without and with inhibitor at 298 K.....	110
Table V.5: Comparison of the inhibition efficiency of MHZN with that of some hydrazone derivatives previously published.....	113

Table V.6: Interaction and binding energies between the inhibitor molecules and Fe (110) surface.....115

Table VI.1. Bond dissociation enthalpy (BDE), Ionization potential (IP), Proton dissociation enthalpy (PDE), proton affinity (PA) and Electron transfer enthalpy (ETE) of NBHZ, HBHZ MHZN and HHZB calculated in Kcal/mol at B3LYP/6-311 G (d, p) level in gas phase....127

Table VI. 2: Molecular docking results and interactions of the investigated ligands with NADPH-Oxidase.....131

Table VI.3: MIC values ($\mu\text{g/mL}$) of hydrazone derivatives against gram-negative and gram-positive bacterial strains.....134

Table VI.4: Molecular docking results and interactions of the investigated ligands.139

List of Abbreviations

A	Electronic affinity
ALIE	Average localized ionization energy
Abs	Absorbance of the substance
ATCC	American type culture collection
AC	Alternating Current
AFM	Atomic Force Microscopy
B3LYP	Becke Three Parameters Lee-Yang-Parr .
BHT	Butyl hydroxy toluene
BDE	Bond Dissociation Energy
C	Concentration
CE	counter electrode
C_{dl}	Capacitance double layer
DMSO	Dimethyl sulfoxide
DPPH	2,2-diphenyl-1-picrylhydrazyl
DMF	Dimethylformamide
DFT	Density functional theory
DOS	Density of States
ELF	Electron localization function
EIS	Electrochemical Impedance Spectroscopy
EtOH	Ethanol
ETE	Electron Transfer Entropy .
FRAP	Ferric Reducing Antioxidant Power
HAT	Hydrogen atom transfer .
HBHZ	4-[(2E)-2-(2-hydroxybenzylidene) hydrazinyl] benzoic acid
HHZB	{(2E)-2-[(2-hydroxynaphthalen-1-yl) methylidene] hydrazinyl} benzoic
HBA	hydrogen bond acceptor
HOMO	Highest Occupied Molecular Orbital
HBA	Hydrogen BondsAcceptor
HBD	Hydrogen Bond Donate
IR	Infra red
IP	Ionization Potential
IC	Inhibition concentration
IE	Inhibition efficacy
LOL	Localized orbital locator
LUMO	Lowest Unoccupied Molecular Orbital
MEP	Molecular electrostatic potential
MDS	Molecular dynamic simulations
MP	Melting point
MW	Molecular Weight
MHB	Mueller Hinton broth
MIC	Minimum inhibitory concentration .
MHZN	1 {(E)-[2-(4methylphenyl)hydrazinylidene]methyl}naphthalen-2-ol

List of Abbreviations

MeOH	Methanol
NBHZ	4-[(2E)-2-(2-nitrobenzylidene) hydrazinyl] benzoic acid .
NMR	Nuclear magnetic resonance
NCI	Non-covalent interaction
OD	Optical Density
OCP	Open Circuit Potential
PED	Potential Energy Distribution
PDE	Proton Dissociation Energy
PDB	Protein Data Bank
PA	Proton Affinity .
TD-DFT	Time Dependent -Density functional theory
TLC	Thin layer chromatography
TAC	Total Antioxidant Capacity)
TTC	triphenyltetrazolium chloride
THF	Tetrahydrofuran
TEAC	Trolox equivalent antioxidant capacity
QTAIM	Quantum theory of atoms in molecules
RDG	Reduced density gradient
R_f	Retention factor
ROS	Reactive Oxygen Species
R_s	Resistance Solution
UV	Ultra violet
SCE	Saturated Calomel Electrode
SET-PT	Single electron transfer-proton transfer
SPLET	Sequential proton loss electron transfer
VMD	Visual Molecular Dynamics

Table of contents

Dedication	I
Acknowledgement	II
List of Figures	IV
List of Tables	VIII
List of Abbreviations	X
General Introduction	1

Chapter I

I.1. Nitrogen element N.....	5
II.2. Nitrogen in organic chemistry.....	5
II.2.1. Amines.....	6
II.2.2. Amides.....	6
II.2.3. Nitrile.....	7
II.2.4. Imines.....	7
II.2.5. Diazonium salts.....	8
II.2.6. Carbazide.....	8
II.2.7. Heterocyclic compounds.....	9
II.2.8. Hydrazine.....	9
II.8.1. Hydrazine synthesis.....	10
II.8.2. Hydrazine and amine reactivity.....	10
II.8.3. Hydrazine derivatives.....	11
II.2.9. Hydrazone.....	11
II.2.9.1 History.....	12
II.2.9.2. Reaction formation and mechanism.....	13
II.2.9.3. Hydrzones properties.....	15
II.2.9.3.1. Chemical properties.....	15
II.2.9.3.2. Physical properties.....	15
III. Corrosion.....	16
III.1. Electrochemical corrosion.....	16
III.2 Effect of various parameters on corrosion.....	17
III.3. Forms of corrosion.....	18
A) Uniform corrosion (Generalized).....	18
B) Localized corrosion.....	19
III.4. Corrosion protection.....	19

III.4.1 Corrosion inhibitors.....	20
A) Anodic Inhibitors:.....	20
C) Mixed Inhibitors:.....	20
III.4.1.2. Chemical Composition:.....	21
A) Organic Inhibitors:.....	21
B) Inorganic Inhibitors:.....	21
IV. Hydrazone Applications.....	21
VI.2. In biological activity.....	23
IV.2.2. Antibacterial and antifungal activities.....	26
IV.2.3 Anticancer.....	27
IV.2.3 Anti-tuberculosis TB agents.....	27
IV.3. Coordination chemistry.....	28
References.....	29

Chapter II

II.1. Synthesis under reflux.....	34
II.2. Chemicals.....	35
II.3. Thin Layer Chromatography.....	35
II.4. Melting point.....	36
II.5. UV-vis spectroscopy.....	36
II.7. NMR spectroscopy.....	39
II.8. Biological activity.....	40
II.8.1 Antioxidant in vitro assay.....	40
II.8.1 Antibacterial in vitro assay.....	41
II.9. Electrochemical tests.....	42
II.9.1. EIS electrochemical impedance spectroscopy.....	42
II.9.2. Tafel analysis.....	43
II.10. Atomic Force Microscopy (AFM).....	44
II.11. Computational chemistry.....	45
II.11.1. Density functional theory (DFT) study.....	45
II.11.1.1 Highest energy molecular orbital HOMO and lowest energy molecular orbital LUMO.....	45
II.11.1.2. Electronegativity.....	46

II.11.1.3. Ionization energy.....	46
II.11.1.4. Electron affinity.....	46
II.11.1.5. Nucleophilicity and electrophilicity.....	47
II.11.1.6. Hardness and softness.....	47
II.11.1.7. Chemical potential.....	47
II.11.1.7. Molecular electrostatic potential (MEP).....	48
II.11.1.8. Density of states (DOS) analysis.....	48
II.11.1.9. Reduced density gradient (RDG) analysis.....	49
II.11.1.10. Electron Localization Function (ELF) and Localized Orbital Locator (LOL) analyses.....	49
II.11.1.11. Average localized ionization energy (ALIE).....	50
II.12. Molecular Dynamic Simulations (MDS).....	51
II.13. Molecular docking.....	51
II.13. PED analysis.....	52
References.....	52

Chapter III

III.1. Organic synthesis procedure of the hydrazones.....	55
III.1.1. 4-[(2E)-2-(2-nitrobenzylidene)hydrazinyl] benzoic acid (NBHZ).....	55
III.2.2. 4-[(2E)-2-(2-hydroxybenzylidene) hydrazinyl] benzoic acid (HBHZ).....	56
III.3.3. {(2E)-2-[(2-hydroxynaphthalen-1-yl)methylidene]hydrazinyl} benzoic HHZB.....	57
III.3.4. 1{(E)-[2-(4methylphenyl)hydrazinylidene]methyl}naphthalen-2-ol (MHZN).....	58
III.2. Physical and chemical properties of the obtained hydrazones.....	60
III.3. Spectroscopy analyses.....	64
III.3.1 UV- Vis Spectroscopy.....	64
III.3.2 FT-IR Spectroscopy.....	66
III.3.2.1. NBHZ and HBHZ FT-IR spectrums.....	66
III.3.2.2. MHZN and HHZB FT-IR spectrums.....	68
III.3.3. NMR analysis.....	69
III.3.3.1 ¹ H NMR spectra NBHZ.....	69
III.3.3.2. ¹³ C NMR spectra NBHZ.....	70
III.3.3.3. ¹ H NMR spectra HBHZ.....	71
III.3.3.4. ¹³ C NMR spectra HBHZ.....	74
III.3.3.5. ¹ H NMR spectra HHZB.....	74
III.3.3.6. ¹³ C NMR spectra HHZB.....	78
III.3.3.7. ¹ H NMR spectra MHZN.....	78

III.3.3.8. ¹³ C NMR spectra MHZN.....	78
III.4. Conclusion.....	79

Chapter IV

IV.1. DFT study.....	80
IV.1.1. Molecular geometry and structure optimization.....	80
IV.1.2. UV-Vis calculated spectrums.....	81
IV.1.3 FT-IR calculated spectrums.....	84
IV.1.4 Frontier molecular orbitals (FMOs) and reactivity indices.....	91
IV.2 Density of states (DOS) analysis.....	94
IV.3 Molecular surface electrostatic potential (MEP).....	95
IV.4 Mulliken population analysis.....	96
IV.5. Topology analysis of electronic structure.....	100
IV.5.1. Localized Orbital Locator (LOL) and Electron Localization Function (ELF).....	100
IV.5.2. Average localized ionization energy (ALIE).....	103
IV.5.3. Reduced density gradient (RDG) analysis.....	103
References.....	102

Chapter V

V.1. Electrochemical measurements.....	105
V.1.1. EIS measurements.....	106
V.1.2. Polarization curves.....	107
V.1.3. Adsorption isotherm.....	108
V.2. Atomic Force Microscopy.....	110
V.3. Protection mechanism and comparison with other hydrazones.....	111
V.4. Molecular dynamic simulations (MDS).....	113
V.5. COSMO-RS implementation.....	115
V.6 Non-covalent interaction (NCI) analysis.....	116
V.7. Quantum theory of atoms in molecules (QTAIM) analysis.....	117
References.....	118

Chapter VI

VI.1. Antioxidant activity.....	121
VI.2 Antioxidant mechanism exploitation.....	126
VI.2 .1 HAT mechanism.....	127
VI.2 .2. Single electron transfer followed by proton transfer (SET-PT).....	127

VI.2 .3. Sequential proton loss electron transfer (SPL-ET) mechanism.....	128
IV.3. Molecular Dockings studies.....	128
IV.4.Antibacterial activity evaluation.....	134
VI.4.1 Molecular docking.....	136
References.....	141
General conclusion.....	145

General introduction

General introduction

The natural process of corrosion is the breakdown of materials, often metals, caused by chemical reactions with their surroundings. It is a widespread problem that can impact many different sectors of the economy, infrastructure, and common items. Metals react with oxygen and moisture to generate metal oxides or other compounds in the most prevalent type of corrosion. The type of material, its exposure to corrosive chemicals, and the environment all have an impact on corrosion. Pollutants in the air, acids, and salts can all quicken the corrosion process. High humidity, coastal places, and industrial settings are frequently associated with heightened corrosion concerns [1–3].

The application of inhibitors, protective coatings, and corrosion-resistant materials are examples of preventive methods against corrosion. Stainless steel and other corrosion-resistant alloys are made to withstand challenging conditions. Coatings serve as barriers to shield the metal from corrosive substances, such as paints and galvanization. In addition, compounds known as inhibitors can be added or used to slow down the corrosion process. From an economic standpoint, corrosion is a serious problem that affects many sectors of the economy, infrastructure, and general economic performance. Corrosion has significant direct and indirect costs that include both material and immaterial expenses [4,5].

The study of carbon-containing molecules, which are the building blocks of life, is the main emphasis of the field of organic chemistry. The structural and functional variety of organic molecules is largely attributed to nitrogenous chemicals, which are important in organic chemistry. Nitro compounds, amides, amines and hydrazones are nitrogen-containing compounds that are also necessary components of many industrial products, agrochemicals, and medications. Nitrogen is a basic component in the complex web of organic chemistry because of its adaptability in establishing bonds and taking part in reactions [6,7].

Hydrazones are a significant family of nitrogenous chemicals in organic chemistry. Hydrazine reacts with carbonyl molecules, like aldehydes or ketones, to create these chemicals. Interesting chemical and biological characteristics are frequently displayed by the resultant hydrazones [8]. Because hydrazones can go through a variety of changes, such as reduction, oxidation, and cyclization processes, they are used in organic synthesis. As intermediates in the production of several bioactive molecules, they find use in the development of agrochemicals,

medicines and corrosion protection. Hydrazones' unique structural characteristics and reactivity add to the complex terrain of nitrogen-containing molecules in organic chemistry. On the other hand, owing to their capacity to create a barrier on metal surfaces, these substances have been investigated for their potential as corrosion inhibitors in a variety of sectors [9–11].

Antioxidants are compounds that prevent or postpone the oxidation of other molecules. Hydrazones, with their distinct chemical structure, have been investigated for their potential as antioxidants [12]. Hydrazines react with aldehydes or ketones to form hydrazones, which have strong antibacterial properties. They act by changing the permeability of cell membranes, preventing the synthesis of proteins, or suppressing the formation of cell walls. A Minimum Inhibitory Concentration (MIC) test can be used against gram-positive *B. subtilis* and *S. aureus*, gram-negative *S. enterica* and *E. coli*, and gram-positive *B. subtilis* to determine their efficacy. Furthermore, molecular docking studies can improve drug design by predicting and analyzing the interaction between hydrazones and bacterial targets.

In this context; the synthesis and characterization of four distinct hydrazone derivatives are thoroughly investigated in this thesis. The compounds are intended for use in corrosion inhibition and antioxidant activity. They have unique structural properties and have been carefully designed. Furthermore, the research includes a comprehensive analysis using Density Functional Theory (DFT) computations to elucidate the molecular details of these substances. This thesis is organized into six chapters, each one focuses on a significant finding from this extensive study.

This thesis' first chapter offers a thorough analysis of the body of research on hydrazones and the variety of uses for which they are used. This chapter seeks to contextualize the role of hydrazones in corrosion inhibition and biological activity by reviewing prior studies. This chapter's insights offer a strong basis for comprehending the synthesis and characteristics of hydrazones.

On the other hand, the materials and techniques used during the experiment are described in considerable detail in the second chapter. This chapter provides guidance for the experimental procedures carried out in later stages of the investigation, from the choice of reagents to the particular synthesis processes. Interpreting the outcomes in subsequent chapters requires a thorough understanding of the procedures used.

In addition, the synthesis and characterization of the four hydrazones are covered in detail in the third chapter, which builds on the literature review and materials/methods chapters. Using a variety of spectroscopic and analytical techniques, The fourth chapter addresses the quantum chemical calculation of the obtained hydrazones the five chapter elucidate the corrosion inhibition efficiency of the studied compounds Finally, the last chapter showing experimental tests . In order to gain a better knowledge of the hydrazones' reactivity and possible uses in formulations for antibacterial and antioxidants. Moreover, Molecular docking studies provide important insights into the biological potential of hydrazones by elucidating the interaction between the compounds and certain targets.

References

- [1] P. Hammonds, An Introduction to Corrosion and its Prevention, *Compr. Chem. Kinet.* 28 (1989) 233–279. [https://doi.org/10.1016/S0069-8040\(08\)70400-X](https://doi.org/10.1016/S0069-8040(08)70400-X).
- [2] B. El Ibrahim, J.V. Nardeli, L. Guo, An Overview of Corrosion, *ACS Symp. Ser.* 1403 (2021) 1–19. <https://doi.org/10.1021/bk-2021-1403.ch001>.
- [3] R.G. Buchheit, H. Guan, S. Mahajanam, F. Wong, Active corrosion protection and corrosion sensing in chromate-free organic coatings, *Prog. Org. Coatings.* 47 (2003) 174–182. <https://doi.org/10.1016/j.porgcoat.2003.08.003>.
- [4] M. Finšgar, J. Jackson, Application of corrosion inhibitors for steels in acidic media for the oil and gas industry: A review, *Corros. Sci.* 86 (2014) 17–41. <https://doi.org/10.1016/j.corsci.2014.04.044>.
- [5] R. Payal, Green Corrosion Inhibitors for Coatings, (2021) 147–174. <https://doi.org/10.21741/9781644901496-7>.
- [6] N. Compounds, Nitrogen Compounds, *Enol. Chem.* (2012) 183–193. <https://doi.org/10.1016/b978-0-12-388438-1.00012-1>.
- [7] P. Heyse, I. De Vilder, M. Vanneste, Smart durable and self-healing textile coatings, Elsevier Ltd, 2016. <https://doi.org/10.1016/B978-0-08-100263-6.00004-6>.
- [8] G. Verma, A. Marella, M. Shaquiquzzaman, M. Akhtar, M.R. Ali, M.M. Alam, A review exploring biological activities of hydrazones, *J. Pharm. Bioallied Sci.* 6 (2014) 69–80. <https://doi.org/10.4103/0975-7406.129170>.
- [9] S. Rollas, Ş. Güniz Küçükgülzel, Biological activities of hydrazone derivatives, *Molecules.* 12 (2007) 1910–1939.
- [10] F.-F. Tian, F.-L. Jiang, X.-L. Han, C. Xiang, Y.-S. Ge, J.-H. Li, Y. Zhang, R. Li, X.-L. Ding, Y. Liu, Synthesis of a novel hydrazone derivative and biophysical studies of its interactions with bovine serum albumin by spectroscopic, electrochemical, and molecular docking methods, *J. Phys. Chem. B.* 114 (2010) 14842–14853.
- [11] M. Singh, N. Raghav, Biological activities of hydrazones: A review, *Int. J. Pharm. Pharm. Sci.* 3 (2011) 26–32.
- [12] I.O. Alisi, A. Uzairu, S.E. Abechi, In silico design of hydrazone antioxidants and analysis of their free radical-scavenging mechanism by thermodynamic studies, *Beni-Suef Univ. J. Basic Appl. Sci.* 8 (2019) 1–11.

Chapter I: Bibliography reseach

This chapter delves into the study of hydrazones, an important class of nitrogenous compounds that have been extensively researched in the literature due to their wide range of uses and characteristics. Hydrazones' stability and adaptability have made them essential to organic chemistry throughout history. We go over their chemical properties and investigate their wide range of applications, including materials science, pharmaceuticals, and organic synthesis as well as their use as intermediates. We also talk about how they could be used as biological agents, like antimicrobials and anticancer agents, and to inhibit corrosion. This chapter gives a thorough introduction to hydrazones, emphasizing their chemical makeup, historical background, and range of uses.

I.1. Nitrogen element N

Nitrogen is the most prevalent element in the atmosphere, which is also the only free element in nature. The only significant nitrogen ores are massive concentrations of KNO_3 and NaNO_3 in the deserts of Chile and Russia. In comparison, the Earth's crust is comparatively lacking in nitrogen [1].

Nitrogen may participate in a maximum of four electron-pair bonding using sp^3 hybrid orbitals because it has four valence orbitals (one 2s and three 2p). Because of repulsive interactions between lone pairs of electrons on nearby atoms, nitrogen does not form long chains, in contrast to carbon. The reduced internuclear distances that the smaller nuclei encounter makes these interactions crucial. Chains of no more than three N atoms can form stable compounds containing N-N bonds, such as the azide ion (N_3). By using pi overlap could form bonds with itself $\text{N}\equiv\text{N}$ (942 KJ/mol) this multiple bonds is highly strong and can make N_2 is the more stable form of nitrogen on the other hand N-N (167 KJ/mol) and $\text{N}=\text{N}$ (418 KJ/mol) are less stable than $\text{N}\equiv\text{N}$ making the compounds which containing them thermodynamically unstable [2].

N_2 interacts with H_2 to produce ammonia NH_3 and O_2 to give NO and NO_2 , and carbon to produce cyanogen ($\text{N}\equiv\text{C}-\text{C}\equiv\text{N}$). Combined with hydrogen, nitrogen can produce two other essential binary molecules. Hydrogen azide, also known as hydrazoic acid (HN_3), is an explosive, colorless chemical. Another potentially explosive substance is hydrazine (N_2H_4), which is employed in boiler corrosion prevention and as a rocket fuel [3].

II.2. Nitrogen in organic chemistry

Nitrogen-containing compounds, also known as nitrogenous compounds or nitrogen compounds, are organic molecules that contain nitrogen atoms in their chemical structures including amines, amino acids, amino alcohols, amides and lactams, nitro compounds, imines, nitriles, diazonium salts, hydrazides, carbazides, oximes, and heterocyclic compounds such as imidazole, triazole, and tetrazole [4–6]. These compounds span a wide range of classes and have diverse

properties and applications across various fields of science, industry, and everyday life. Here are some common categories of nitrogen-containing compounds:

II.2.1. Amines

One or more nitrogen atoms are bound to carbon atoms to form amines, which are chemical molecules. They can be divided into three groups: tertiary (three alkyl or aryl groups), secondary (two alkyl or aryl groups), and primary (one alkyl or aryl group connected to the nitrogen). Amines are crucial in synthetic organic chemistry and serve crucial roles in biological processes like neurotransmission [7].

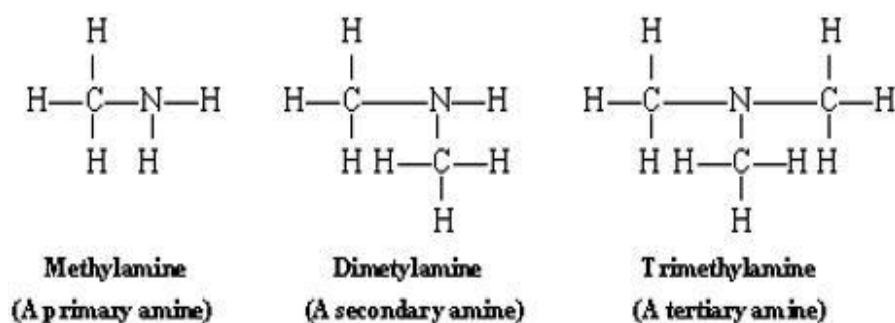


Figure I. 1: Chemical structure methylamine, dimethylamine, and trimethylamine.

The number of hydrogens substituted is denoted by the labels primary (one), secondary (two), and tertiary (three). While tertiary amines have no hydrogens on the electronegative nitrogen atom, primary and secondary amines can form hydrogen bonds with one another.

II.2.2. Amides

Amides are compounds in which a nitrogen atom is bonded to a carbonyl carbon (C=O) and one or more carbon atoms. They are commonly found in proteins and peptides, as well as in synthetic polymers like nylon.

A nitrogen atom linked to a carbonyl carbon atom is the distinguishing characteristic of an amine. A condensation reaction produces amides, much like it does with esters. Amidates are produced when an amine and a carboxylic acid condense, as in contrast to esters, which are produced when an alcohol and a carboxylic acid condense [8].

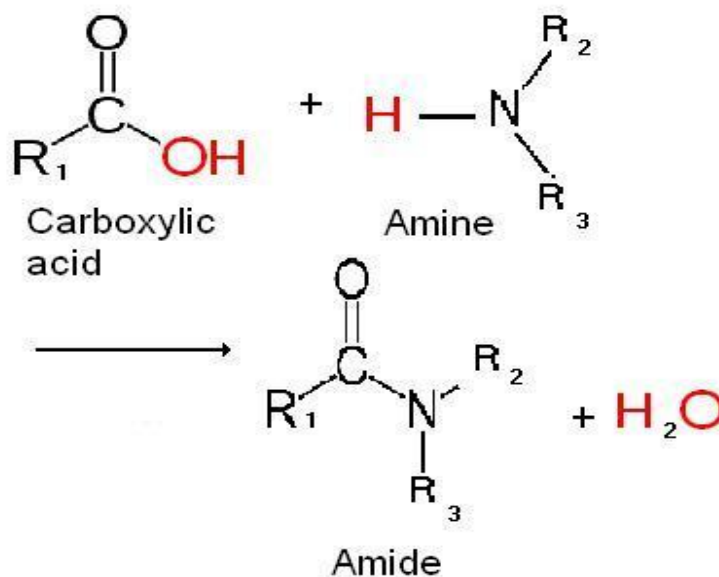


Figure I. 2: General equation for amide.

II.2.3. Nitrile

Cyanocompounds, often known as nitriles, are organic substances with a -CN functional group. Cyanocarbons are organic compounds that contain a nitrile group. Nitriles are naturally occurring polar chemicals that can be found in both plant and animal sources. From both terrestrial and aquatic sources, more than 120 nitriles have been isolated. Brussel sprouts, cauliflower, and cabbage are just a few examples of plants that contain nitriles [9].

Nitrile compounds can participate in a variety of processes in the field of organic chemistry, such as reduction, addition, oxidation, hydrolysis, and elimination. Two notable instances of these reactions are the Pinner and Blaise reactions, which highlight nitriles as participants that are electrophilic. The Thorpe reaction, which is known to cause intramolecular condensation of nitriles by nucleophilic addition, serves as an example [10].

II.2.4. Imines

A class of organic substances known as imines is important to both organic chemistry and biochemistry. They are created when a primary amine reacts with a carbonyl substance, usually a ketone or an aldehyde.

In this process, a water molecule is lost, and an imine linkage a double bond made of nitrogen and carbon is formed. Imines are flexible transitions in a range of chemical processes. One of their important roles is in the biosynthesis of amino acids and their incorporation into proteins. They are also found in many natural products, including alkaloids and antibiotics [11,12].

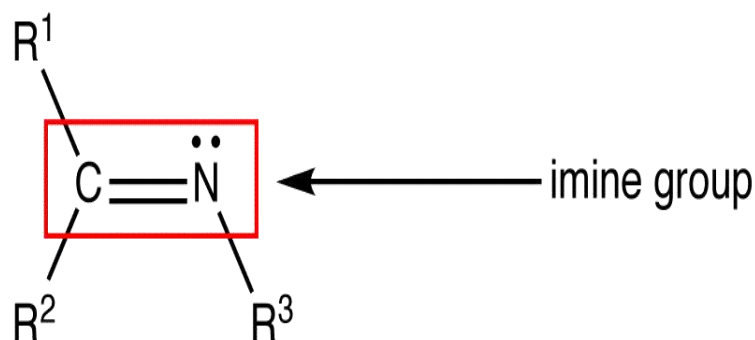


Figure I. 3: Chemical structure of imine compounds.

Imines are used as precursors in synthetic organic chemistry to create a variety of molecules that contain nitrogen. They can be reduced to create primary amines, which are crucial components used in the production of agrochemicals, medicines, and other complex compounds. Furthermore, imines are useful in the construction of intricate molecular structures because they can react with a wide range of electrophiles and nucleophiles to produce a variety of products.

II.2.5. Diazonium salts

The diazonium salts (**di** refers to ‘two’, **azo** is indicative of ‘nitrogen’ and **ium** implies that it is **cationic** in nature), or diazonium compounds, are the class of organic compounds with the general formula $R-N_2^+X^-$ where X is an organic or inorganic anion (for example, Cl^- , Br^- , BF_4^- , etc.) and R is an alkyl or aryl group [13].

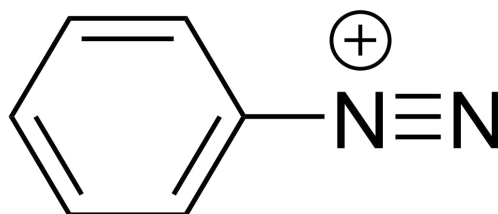


Figure I. 4: Diazonium salt’s structure.

The typical process for creating diazonium salts involves reacting an amine typically an aromatic aniline with a nitrite source. These can then carry out a number of further reactions in which the diazonium group is substituted, either by a nucleophile (forming a triazene, for example) or by a radical mechanism (forming a Sandmeyer reaction), or both [14].

II.2.6. Carbazide

A functional group in chemistry known as a carbazide has the general formula $RNH-NH(C=O)NH-NHR$. They may result from the condensation of hydrazine and carbonic acid. The most basic carbazide is carbohydrazide (Figure I.5 (B)), while diphenylcarbazine (Figure I.5 (A)) which is employed as an analytical reagent, is another popular carbazine [15].

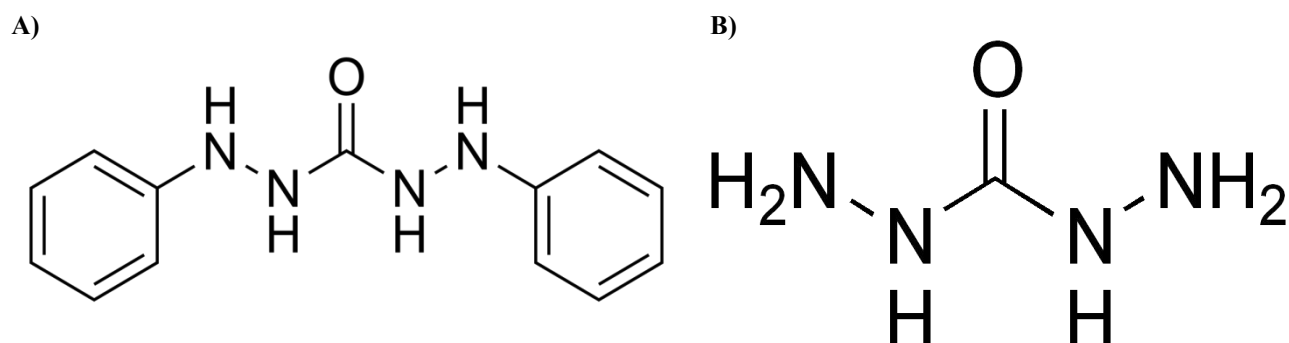


Figure I. 5: Carbazide chemical structure: A) diphenylcarbazide and B) Carbohydrazide.

II.2.7. Heterocyclic compounds

Heterocyclic compounds that contain nitrogen have at least one nitrogen atom in their ring structure. Heterocyclic compounds are organic compounds with one or more non-carbon components (usually nitrogen, oxygen, sulfur, etc.) atoms in the ring. These substances have numerous uses in pharmaceuticals, agrochemicals, materials science, and are essential in the study of organic chemistry [16].

The presence of one or more nitrogen atoms in the ring structures of these compounds results in a variety of chemical and biological characteristics. Natural goods and artificial molecules with a variety of uses and purposes are typical places to find them [17].

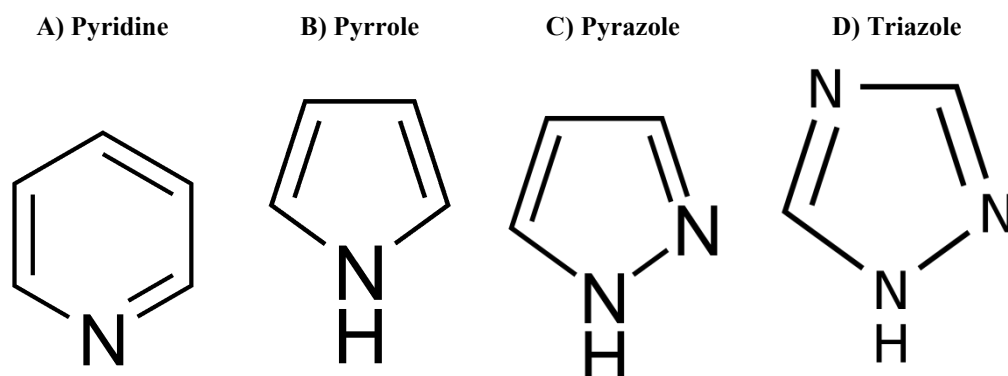


Figure I. 6: Some examples of well-known nitrogen-containing heterocyclic compounds.

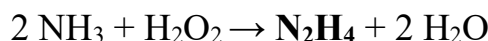
II.2.8. Hydrazine

The hydrazines are a family of chemical compounds derived from hydrazine ($\text{H}_2\text{N}-\text{NH}_2$) by replacing one or more atoms of H with hydrocarbon-containing radicals, such as 2,4-dinitrophenylhydrazine. they are called also diazane or diamine with chemical formula (N_2H_4) is a simple hydrazine form it was synthesized for a first time by the german chimist Thiodor Curtinus back in 1889 is a powerful reducing agent and nucleophile that exhibits diverse reactivity due to the presence of nitrogen-nitrogen (N-N) bonds and lone pairs of electrons on the nitrogen atoms. Its versatile chemistry makes it useful in various applications [18].

II.8.1. Hydrazine synthesis

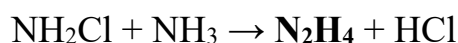
It can be obtained through several synthetic pathways: oxidation of ammonia, oxidation of urea, chlorine-based oxidation.

- **Ammonia oxidation peroxide process** in this reaction hydrazine is obtained from ammonia and hydrogen peroxide. Using a ketone as catalyst [19].



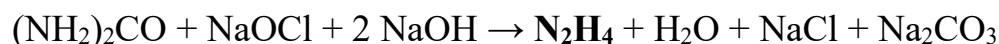
- **Chlorine based oxidation Oling Rashing process**

Without using a ketone catalyst, sodium hypochlorite (the main component of many bleaches) and ammonia can be used to make hydrazine. This technique depends on the formation of the N-N single bond via the interaction of monochloramine with ammonia as well as a byproduct, hydrogen chloride [20].



- **Oxidation of urea**

Urea can be oxidized in place of ammonia in a procedure similar to the Raschig process. The oxidant is once more sodium hypochlorite [21]. The net response is displayed below:



II.8.2. Hydrazine and amine reactivity

Despite the nitrogen present in both hydrazine and amines, their differing reactivity is caused by differences in their molecular makeup and structures. Given that hydrazine has two nitrogen atoms with lone pairs and an N-N link, it has a greater capacity to give electrons than most amines, making it a stronger reducing agent. Hydrazine is hence especially effective at reducing species such as metal ions and metal oxides. Amphetamines have lowering properties as well, but usually not to the same extent as hydrazine. On the other hand, hydrazine is widely used as a hydrogen source in catalytic hydrogenation reactions because of its ability to donate hydrogen atoms (Hydrogenation Potential). Amines can also be used for hydrogenation, however because hydrazine has two hydrogen atoms per molecule making it work better [22].

In order to achieve diazotization Nitrous acid (HNO_2) and hydrazine can react to form diazonium salts, which can lead to diazotization processes. This reaction cannot be seen with amines. Diazo compounds are produced via a unique reaction termed diazotization of hydrazine and are employed in a wide range of chemical reactions. In retreat. Azine derivatives can be created by the

reaction of amines and hydrazine with carbonyl compounds. But hydrazine can generate more complicated azines and hydrazones than amine since it has two nitrogen atoms and an N-N link.

In conclusion, while lone pairs and nitrogen atoms are shared by hydrazine and amines, these compounds differ greatly in terms of their ability to reduce, their nucleophilicity, and their participation in certain processes. Because of its unique characteristics, such as its two hydrogen atoms per molecule and its N-N bond, hydrazine is more reactive than amines.

II.8.3. Hydrazine derivatives

Derived from the adaptable hydrazine molecule (N_2H_4), hydrazine derivatives are a broad class of chemicals that have become essential in many commercial applications. The hydrazine structure is carefully changed and substituted to create these derivatives, which provide a variety of molecules with distinct characteristics. These substances are useful in medicine, agriculture, and materials research. They come in a variety of forms, from the simple hydrazine hydrate to more complex ones like methylhydrazine and phenylhydrazine. Their importance goes beyond their reactivity, which makes them indispensable ingredients in rocket propellant composition and useful instruments in organic synthesis. Moving on from hydrazine derivatives, we get to hydrazones, which are a particular class of chemicals that are created when hydrazines condense with substances that contain carbonyls.

II.2.9. Hydrazone

Hydrazones are a class of organic compounds that have a rich history in the field of chemistry, dating back to their initial discovery and subsequent development in the late 19th century. Here we will delve into the historical evolution of hydrazones within the realm of organic synthesis.

II.2.9.1 History

The origins of hydrazones can be traced to the pioneering work of Emil Fischer in the late 19th century. Fischer, a German chemist and Nobel laureate, conducted extensive research on the reactions of carbonyl compounds and their derivatives. His investigations into the reaction between hydrazine and aldehydes or ketones led to the identification of a new class of compounds, which he termed "hydrazones." Fischer's seminal work on hydrazones not only expanded the understanding of chemical reactivity but also laid the groundwork for subsequent investigations into their synthesis and applications. Fischer's meticulous experimental work, bolstered by his keen insights into chemical structure, revealed the formation of a distinctive class of compounds characterized by the presence of a carbon-nitrogen double bond ($C=N$) bridging the hydrazine moiety with the carbonyl compound. This striking feature prompted Fischer to christen these compounds as "hydrazones," signifying their derivation from hydrazine [23].

Following Fischer's foundational research, hydrazones gained prominence as versatile intermediates in various synthetic pathways. Early 20th-century chemists, including Arthur Michael and Adolf von Baeyer, contributed to the exploration of hydrazone reactions and mechanisms. Michael's work on the synthesis of β -diketones through the reaction of hydrazones with ketones, known as the Michael reaction, highlighted the importance of hydrazones in the formation of complex organic molecules.

The mid-20th century witnessed further advancements in hydrazone chemistry, with researchers focusing on their diverse applications. Notably, the hydrazone functional group found utility in the realm of medicinal chemistry. Hydrazone derivatives demonstrated potential as pharmaceutical agents, with notable examples including hydralazine, a vasodilator used to treat hypertension, and isoniazid, an anti-tuberculosis drug. These applications underscored the significance of hydrazones in drug design and development [24].

In 20th and 21st century, advancements in synthetic methodologies and spectroscopic techniques facilitated a deeper understanding of hydrazone chemistry. Transition metal-catalyzed reactions, including hydrazone cross-coupling reactions, emerged as powerful tools for constructing complex molecular architectures. Additionally, hydrazones found applications in areas such as coordination chemistry, supramolecular chemistry, and material science [25,26].

The historical progression of hydrazones from their discovery by Emil Fischer to their modern applications highlights the enduring importance of these compounds in the landscape of organic chemistry. From fundamental research on their synthesis and reactivity to their pivotal roles in drug discovery and materials science, hydrazones continue to captivate the attention of chemists seeking to unlock new synthetic strategies and innovative applications

II.2.9.2. Reaction formation and mechanism

Three synthetic processes can produce hydrazones: condensation between hydrazines and ketones or aldehydes (route A), Japp-Klingemann reaction (pathway B), coupling between aryl diazonium salts and beta-keto esters or acids (pathway C), and coupling reaction between aryl halides and non-substituted hydrazones (pathway C). These procedures produce crystalline hydrazones, which make their purification easier (Figure I.7) [27,28].

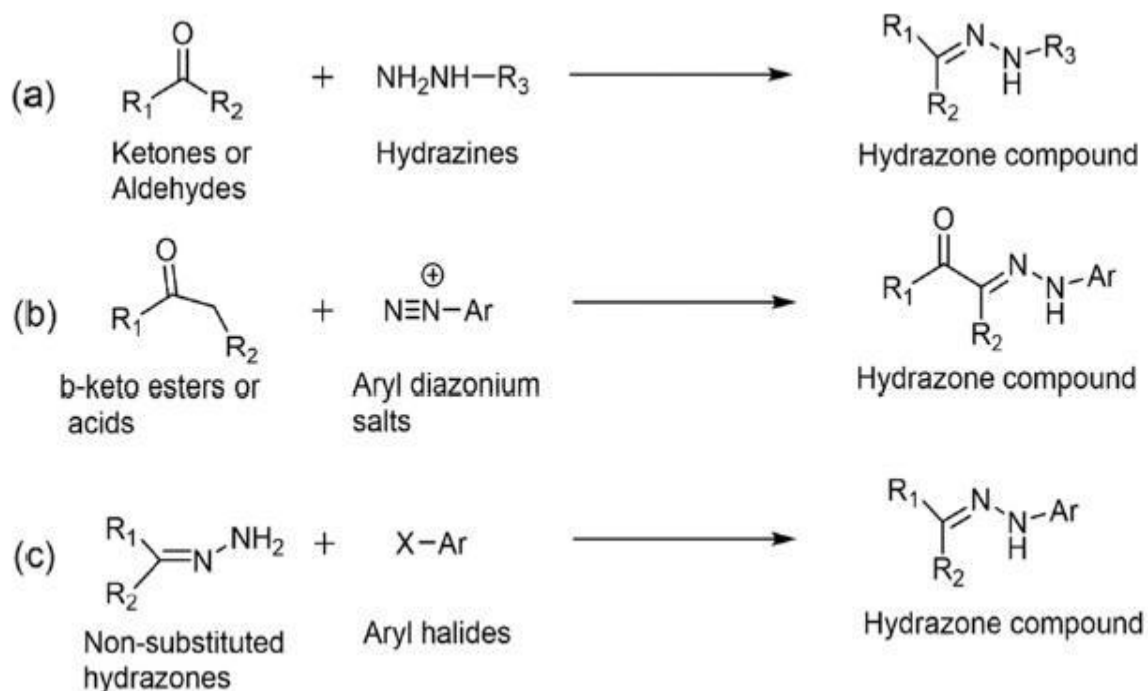


Figure I. 7: The synthesis methodologies for hydrazone linkages (a) condensation between hydrazine and ketone/aldehyde (b) the Japp-Klingemann reaction and (c) substitution of aryl halide with non-substituted hydrazones.

The mechanism of hydrazone formation involves the condensation reaction between a hydrazine derivative and a carbonyl compound (aldehyde or ketone). The reaction proceeds through several steps:

➤ **Nucleophilic Addition:**

The hydrazine derivative ($\text{R}-\text{NH}-\text{NH}_2$) acts as a nucleophile, attacking the carbonyl carbon of the aldehyde or ketone ($\text{R}'-\text{C}=\text{O}$). The lone pair of electrons on the nitrogen atom of the hydrazine attacks the electrophilic carbon of the carbonyl group. This leads to the formation of a tetrahedral intermediate.

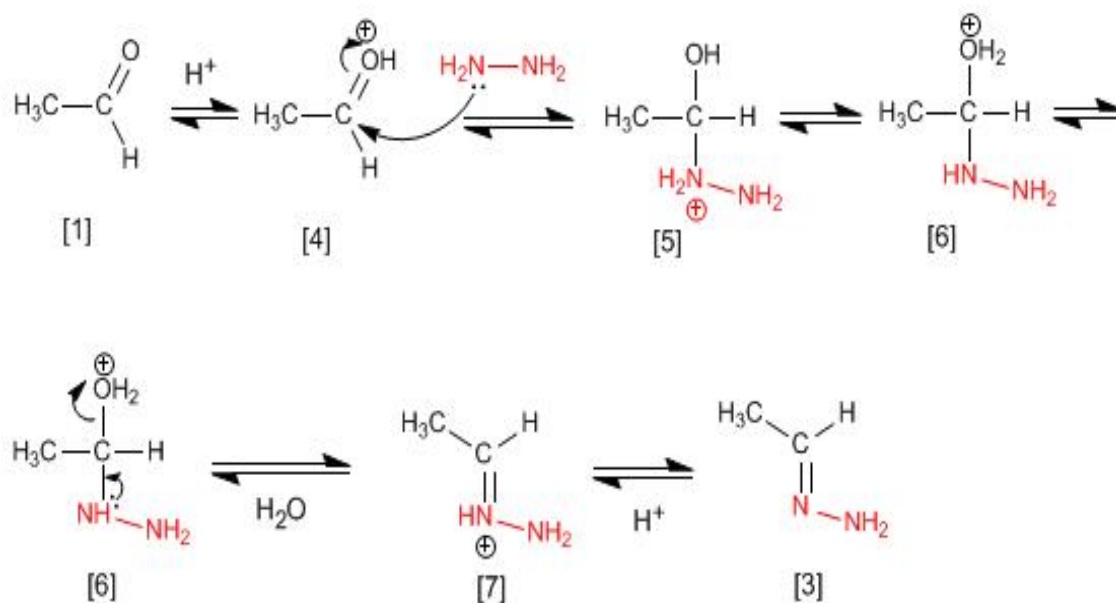


Figure I. 8: hydrazone formation mechanism

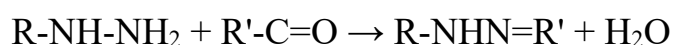
➤ **Proton Transfer and Water Elimination:**

In this step, a proton transfer occurs from the hydrazine nitrogen to the oxygen of the carbonyl group. This proton transfer is followed by the elimination of a water molecule, resulting in the formation of a C=N double bond between the nitrogen of the hydrazine derivative and the carbon of the carbonyl compound. The resulting compound is the hydrazone (R-NHN=R').

➤ **Tautomeric Equilibrium:**

Depending on the nature of substituents and reaction conditions, hydrazones can exist in two tautomeric forms: keto and enol. The enol tautomer possesses a hydrogen atom on the carbon adjacent to the C=N bond, which can undergo tautomeric shifts between the keto and enol forms.

The overall reaction can be represented as follows:



Worthy to mention that the versatility of the hydrazone functional group arises from its ability to participate in various chemical reactions, including further transformations, metal coordination, and biological interactions. This makes hydrazones valuable intermediates in organic synthesis and materials chemistry.

II.8.3.1.3 Reactivity of hydrazones

Two connected nitrogen atoms of different types are found in hydrazones, along with a carbon-nitrogen double bond that is conjugated with the terminal nitrogen atom's lone electron pair.

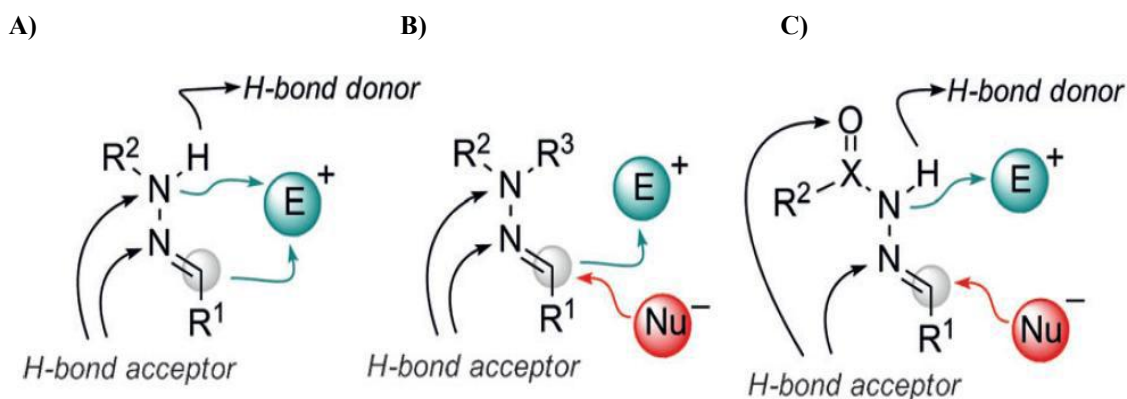


Figure I. 9: Active centers of hydrazones.

The key contributors to the hydrazones' chemical and physical characteristics are these regions. Although the amino-type nitrogen in the hydrazone group is more reactive, both nitrogen atoms are nucleophilic. Both electrophilic and nucleophilic properties can be seen in the carbon atom of the hydrazone group [29]. The active centers of N-monosubstituted hydrazones (A), N,N-dialkylhydrazones (B), and N-acylhydrazones (C) as depicted in Figure I.9.

II.2.9.3. Hydrazones properties

II.2.9.3.1. Chemical properties

Since hydrazones include nitrogen atoms with lone pairs, they have special chemical characteristics that make them weak bases. Hydrazones can react with protons to generate hydrazone salts. Furthermore, these compounds are susceptible to reduction processes, in which they can be reduced to the corresponding hydrazine or substituted hydrazine compounds by use of certain agents. Moreover, the hydrazone functional group's nitrogen atoms exhibit nucleophilic activity, which permits them to interact with electrophilic reagents in processes. This range of reactions demonstrates the hydrazones' varied chemical reactivity [30].

II.2.9.3.2. Physical properties

Molecular structure, size, and functional groups all affect the melting and boiling temperatures of hydrazones; as a result, solid hydrazones with medium-high melting points are the norm. Because of differences in polarity and hydrogen bonding interactions, hydrazones are soluble in a wide range of solvents. Hydrazones are prone to hydrolysis and other chemical reactions that destroy the C=N bond, even though they can be stable in some situations. Furthermore, hydrazones may display E/Z isomerism (geometric isomerism) if the substituents surrounding the C=N double bond differ [30].

The structural changes of hydrazone are what give it a greater efficacy than hydrazine. The molecular structure of hydrazone, which results from the condensation of a hydrazine compound

with a carbonyl group, is expanded and more adaptable. This enlarged structure enables the development of numerous chemical interactions and binding possibilities improving biological functions and increasing efficacy across a range of applications.

Because of its structural modifications, hydrazone is more effective than hydrazine. The condensation of a hydrazine compound with a carbonyl group produces hydrazone, which has an enlarged and more flexible molecular structure. The formation of many chemical interactions and binding opportunities is made possible by this expanded structure, which enhances biological activities and boosts effectiveness in a variety of applications.

III. Corrosion

ISO8044 defines corrosion as the result of a metallic material's physicochemical interaction with its surrounding atmosphere. This interaction modifies the metal's properties and has the potential to significantly damage the metal's function, the environment it is in, or the technical system it is a part of [31]. Notably, a variety of methods can cause a metal to corrode, including chemical, electrochemical (or aqueous) corrosion, The process of biochemical corrosion Dehydrated corrosion occurs when there is gaseous corrosion.

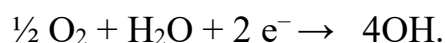
III.1. Electrochemical corrosion

Aqueous corrosion, another name for electrochemical corrosion, is the process by which metals corrode as a result of reactions with their surroundings, especially when water and electrolytes are present. Metal structures deteriorate as a result of electrochemical processes in this kind of corrosion [32]. Typically, the following steps are involved in the corrosion process:

A) Anode Reaction: Metal atoms lose electrons at the anode and become metal ions in solution. We call this process oxidation. When metals corrode in aquatic conditions, the general anodic process is commonly depicted as follows:



B) Cathode Reaction: Reduction processes take place at the cathode. In aqueous corrosion, oxygen reduction is typically a frequent cathodic reaction:



In this step, airborne oxygen is converted to hydroxide ions.

An electrochemical process can go through several phases, as Figure I.9 shows. A redox reaction goes through the following stages:

1. Material moves between the solution and the electrode surface by convection, diffusion, and migration during mass transfer.

2. Within the electric double layer, charge transfer takes place at the metal surface.
3. Chemical reactions, which include dehydration, complexations, and proton exchanges, can occur either before or after electron transfer.
4. Surface processes like adsorption and desorption influence the electrochemical process's general dynamics.

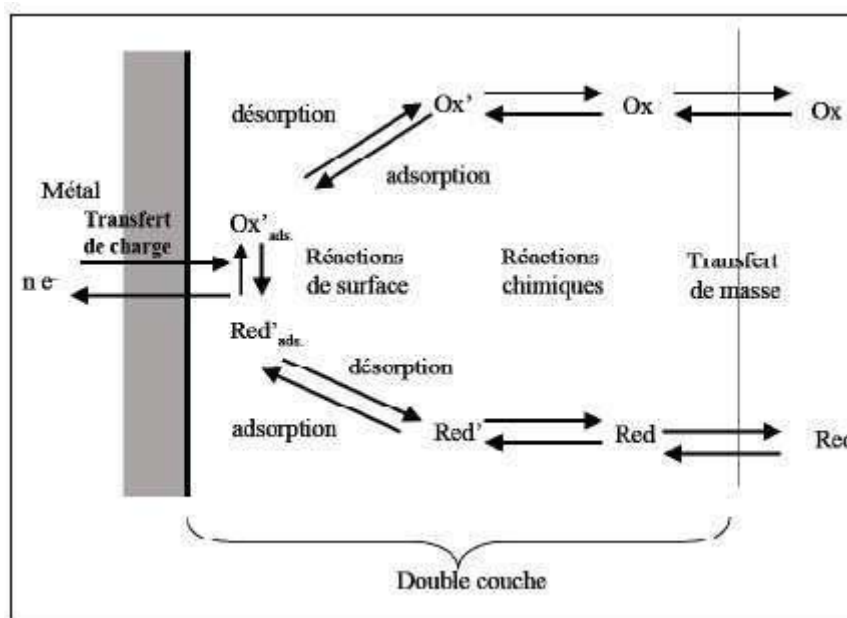


Figure I. 10: The metallic corrosion reaction steps in an aqueous media.

III.2 Effect of various parameters on corrosion

One of the most important factors affecting how metals deteriorate in various situations is temperature and its effect on corrosion. Because they provide more energy, elevated temperatures frequently speed up corrosion reactions by raising reaction rates. Because of the increased kinetic energy, ions in solution are more mobile, which facilitates mass transfer and makes it simpler for corrosive species to reach the metal surface [33].

The pH of the surrounding environment has a big impact on how metals behave when they corrode. Low pH environments that are acidic make metals far more prone to corrosion. The solution's acidity facilitates the disintegration of passive oxide layers on the metal surface, making it more susceptible to rapid corrosion. Although corrosion rates are often lower in neutral pH situations, the particular properties of the metal and its surroundings are still very important in determining the degree of corrosion [34–36].

The hydrodynamic regime, which controls the properties of fluid flow, has a complex impact on corrosion processes. Mass transport is accelerated in dynamic fluid environments, which speeds up the transfer of corrosive species to the metal surface and causes corrosion to accelerate. Sufficient

fluid flow encourages a more even dispersion of corrosive substances, reducing the possibility of the localized corrosion that is seen in stagnant environments [37].

Metal corrosion is greatly influenced by oxygen, which affects the process in a number of ways. Iron rusting is an example of an oxidation reaction, in which metals combine with oxygen to generate metal oxides. Corrosion products are created when oxygen reacts with metal ions. These compounds can accelerate corrosion or have a protective effect [38,39].

Implementing corrosion control and prevention techniques, such as the use of protective coatings, corrosion inhibitors, and controlled atmospheres to regulate the influence of oxygen on metal corrosion in various situations, requires an understanding of these varied impacts.

III.3. Forms of corrosion

A) Uniform corrosion (Generalized)

A type of corrosion known as uniform corrosion is defined by a metal's uniform and even dissolution over its whole exposed surface. This type of corrosion causes a steady decrease of material thickness, which compromises the metal's structural integrity. In contrast to localized corrosion, which affects particular regions, uniform corrosion appears as a complete assault, leaving the surface susceptible to degradation on the entire surface [40].

Temperature, the corrosive environment, and the characteristics of the metal all have an impact on uniform corrosion rates, which are frequently predictable. A rusted or dull surface, for example, is a perceptible change in the metal's appearance that indicates uniform corrosion. It is possible for this process to produce corrosion products such as metal hydroxides or oxides.

Using corrosion inhibitors, protective coatings, or corrosion-resistant materials are some ways to stop or lessen uniform corrosion. Finding and fixing uniform corrosion problems requires routine inspection and maintenance procedures. This kind of corrosion, which affects steel, aluminum, and copper-based structures and components, is prevalent in many industrial applications.

B) Localized corrosion

A unique kind of corrosion known as "localized corrosion" causes focused damage as opposed to homogeneous deterioration by focusing on particular regions of a metal surface. Pitting, crevice, and galvanic corrosion are common instances of localized corrosion; these types of corrosion are condition-specific [41].

Pitting corrosion causes tiny holes or pits to form on the metal surface; this causes concentrated damage in certain regions, which presents problems. Conversely, crack corrosion happens in small areas or fissures where there is limited availability of oxygen or strong ions, which

leads to localized degradation. Localized corrosion at the anodic site results from the electrochemical reaction between dissimilar metals in contact, which is known as galvanic corrosion.

Using corrosion-resistant materials, protecting coatings, and design changes to remove crevices are all necessary to prevent and mitigate localized corrosion. For efficient mitigation and early detection, routine inspection is essential. This type of corrosion can happen in a variety of industrial contexts, such as chemical processing facilities, maritime locations, and infrastructure exposed to harsh weather. It is crucial to comprehend the particular kinds and conditions that lead to localized corrosion in order to put techniques in place that guarantee the durability and integrity of metal components in a variety of applications.

III.4. Corrosion protection

The durability and integrity of structures and components depend heavily on the protection of materials from corrosion. There are several tactics used to stop or lessen corrosion:

Paints and varnishes, for example, function as barriers that keep the metal surface isolated from corrosive environments, therefore decreasing the risk of corrosion. Corrosion inhibitors can be applied directly to the metal or delivered into the surrounding environment to reduce electrochemical processes. They are particularly useful in corrosive environments [42–44].

To prevent corrosion, cathodic protection entails converting the metal surface into a cathode. Common techniques include impressed current systems and sacrificial anodes. Sacrificial protection is offered by galvanizing, or coating steel or iron with zinc, which corrodes instead of the underlying metal. On the other side Corrosion resistance is increased in metals by alloying them with such elements. Stainless steel is one material that has a passive oxide coating of chromium in it. Modifications to the design, such as rearranging structures to remove areas prone to corrosion, are efficient preventive strategies [45].

Exposure to corrosive elements is minimized by environmental control, which includes temperature and humidity regulation. Early corrosion identification is aided by regular examination and maintenance, such as coating restoration and section replacement. To reduce susceptibility, it is essential to select materials that are resistant to corrosion, such as aluminum or stainless steel.

III.4.1 Corrosion inhibitors

An inhibitor is defined as a chemical that is added to the corrosion system at a concentration that is suitable for its efficacy. It reduces the rate at which the metal corrodes without appreciably altering the amount of corrosive chemicals present in the hostile environment [46,47]. Numerous chemicals have an inhibiting effect and are classified based on a number of factors:

III.4.1.1 Mechanism of Action

A) Anodic Inhibitors:

These inhibitors function by slowing down the anodic reaction, or oxidation, rate that occurs during corrosion. On the metal surface, they create a barrier that prevents the loss of metal ions.

B) Cathodic Inhibitors:

During the corrosion process, cathodic inhibitors lower the rate of reduction (cathodic reaction). Usually, they create a shield to stop oxygen or other cathodic reactants from being reduced on the metal's cathodic sites.

C) Mixed Inhibitors:

By inhibiting both oxidation and reduction processes, mixed inhibitors provide a protective layer that protects against both anodic and cathodic reactions.

III.4.1.2. Chemical Composition:

A) Organic Inhibitors:

The organic chemicals which make up organic inhibitors provide a shielding layer on the surface of the metal. Amines, amides, and organic salts are typical examples.

B) Inorganic Inhibitors:

Generally, inorganic chemicals make up inorganic inhibitors. Phosphates, chromates, and silicates are a few examples of substances that create protective coatings on the surface of metals.

IV. Hydrazone Applications

Given to a distinctive combination of chemical and physical properties hydrazones are versatile substances with uses in numerous fields of chemistry, including organic synthesis, materials science, and pharmaceutical chemistry.

IV.1 Corrosion inhibitors

Interestingly, hydrazones compounds have been investigated and evaluated for their potential as inhibitors of corrosion. These synthesized hydrazones have proven to be effective corrosion inhibitors, proving their value in corrosion prevention. Because the hydrazone group forms a protective layer on the metal surface, it is probably contributing to the inhibitory action. Researchers may have used weight loss analysis, surface characterization techniques, and electrochemical tests to determine the corrosion inhibition efficiency in these experiments. The results might shed light on which metals or alloys hydrazones are most effective at preventing corrosion. The field of metal coatings, surface treatments, and the creation of corrosion-resistant materials are a few examples of industries where the potential of hydrazones as corrosion inhibitors could lead to useful applications.

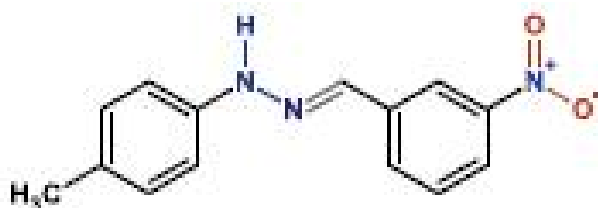


Figure I. 11: Chemical structure of (E)-1-(3-nitrobenzylidene)-2-(p-tolyl)hydrazine (E-NBPTH).

The synthesis, characterization, and corrosion inhibition behavior of an aromatic hydrazone derivative, namely (E)-1-(3-nitrobenzylidene)-2-(p-tolyl)hydrazine (E-NBPTH), are investigated in the work by Chafai et al. [47]. The chemical was created by condensing an aromatic aldehyde and an aromatic hydrazine in refluxing methanol. Several spectroscopic techniques, such as carbon-13 nuclear magnetic resonance (^{13}C NMR), infrared (IR), proton nuclear magnetic resonance (^1H NMR), and UV-visible (UV-vis) spectroscopy, were used to identify and study the molecular structure of E-NBPTH. The paper highlights the compound's efficacy as a mixed-type inhibitor in sulfuric acid by providing a thorough examination of its synthesis, characterization, and corrosion inhibition properties of (E)-1-(3-nitrobenzylidene)-2-(p-tolyl)hydrazine. Combining theoretical and experimental methods improves our knowledge of the molecular behavior of the molecule and provides important new information for possible real-world applications in corrosion prevention.

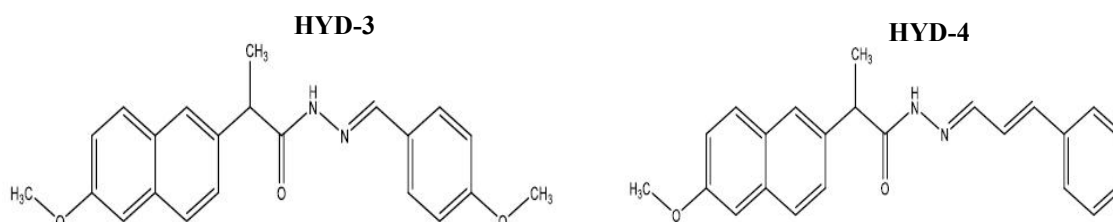


Figure I. 12: Chemical structures (HYD-3) and (HYD-4).

The objective of the study published by Abdelkarim Chaouik et al. [48] was to assess the corrosion inhibition capabilities of two newly synthesized hydrazone derivatives, (E)-N'-(4-methoxybenzylidene)-2-(6-methoxynaphthalen-2-yl)propanehydrazide (HYD-3) and N'-cyclohexylidene-2-(6-methoxynaphthalen-2-yl)propanehydrazide (HYD-4) (Figure I.12), for mild steel in acidic HCl solution. The investigation utilized electrochemical techniques and SEM-EDS analysis for surface characterization. Both inhibitors demonstrated exceptional protection efficiency, with HYD-3 exhibiting the best inhibition effect at 90% (at 5×10^{-3} M). Potentiodynamic polarization

results indicated that both inhibitors acted as mixed-type inhibitors, and their adsorption isotherms aligned with the Langmuir model. Impedance spectroscopy tests revealed that the inhibitors positively influenced mild steel corrosion by increasing polarization resistance with higher inhibitor concentrations. SEM-EDS analysis suggested the formation of protective films by the studied compounds on the mild steel surface.

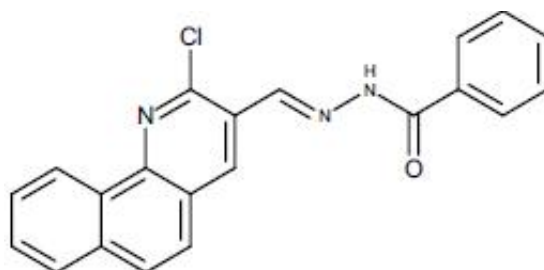


Figure I. 13: Chemical structures of N'((2-chlorobenzo[h]quinolin-3-yl)methylene)benzohydrazide.

Three newly created chemical compounds derived from benzo[h]quinoline hydrazone derivatives were to be synthesized and their corrosion inhibition characteristics evaluated in the study published by Sayed et al. [49]. FTIR, ¹H-NMR, ¹³C-NMR, and mass spectroscopy were used to characterize the structures of the compounds. To assess the compounds' ability to suppress corrosion in 1 M HCl for carbon steel (CS), various electrochemical techniques were utilized, such as Potentiodynamic Polarization, Electrochemical Frequency Modulation and Electrochemical Impedance Spectroscopy (EIS). According to the electrochemical measurements, compound VII showed a noteworthy level of corrosion inhibition efficacy. Analysis using SEM and EDX provided additional proof that a passive layer had formed on the CS surface. These results highlight the possibility of using derivatives of benzoquinoline hydrazone as efficient organic corrosion inhibitors for carbon steel in harsh conditions.

VI.2. In biological activity

Hydrazones and their derivatives are employed in the design and synthesis of therapeutic molecules in medicinal chemistry. They have the capacity to function as bioactive substances, such as antioxidant, anti-inflammatory, antiviral, antibacterial, and anticancer substances. Their responsiveness enables the creation of focused drug delivery systems.

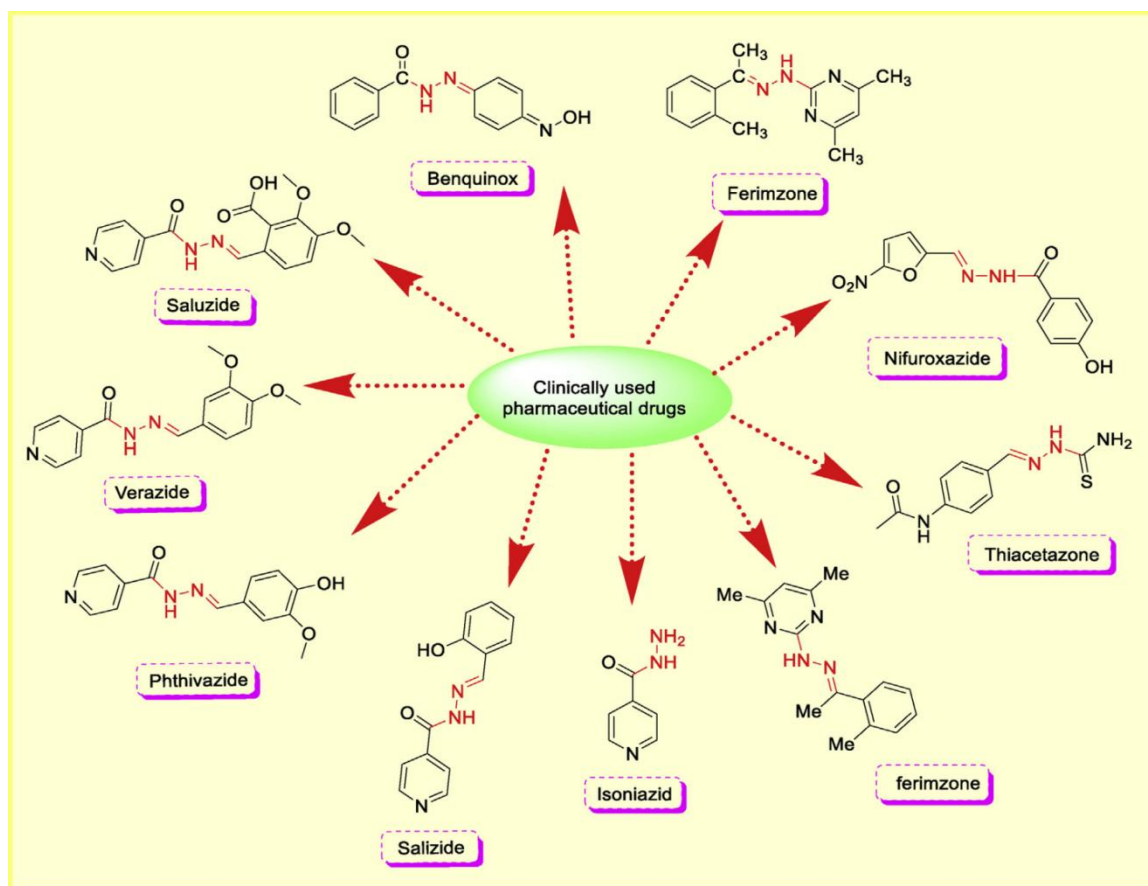


Figure I. 14: Commonly prescribed marketed drugs bearing hydrazone nucleus.

IV.2.1 Antioxidant activity

The term "antioxidant activity" indicates a substance's capacity to offset or mitigate the damaging effects of free radicals within the body. Free radicals are extremely reactive chemicals that can harm DNA, proteins, and cells, which can result in a number of illnesses and the aging process. Antioxidants reduce oxidative stress by neutralizing free radicals, assisting in the body's defense against this damage. Antioxidants are commonly obtained from vitamins (like C and E), minerals (such zinc and selenium), and a variety of phytochemicals that are present in fruits, vegetables, and other plant-based diets [50].

Antioxidant test review entails a thorough analysis of techniques intended to measure a substance's antioxidant capacity. A range of assays are utilized to evaluate a compound's capacity to mitigate oxidative stress by gauging its influence on reactive oxygen species or free radicals. The Trolox Equivalent Antioxidant Capacity (TEAC) assay, the Oxygen Radical Absorbance Capacity (ORAC) assay, the Ferric Reducing Ability of Plasma (FRAP) and DPPH assay are common tests. By providing quantitative measurements of antioxidant activity, these assays enable researchers to evaluate the relative efficacy of various substances or mixtures. Evaluation criteria can include things like repeatability, accuracy, and sensitivity [51].

Antioxidants work through many mechanisms to mitigate the harmful effects of free radicals, which are very reactive chemicals capable of causing injury to cells and tissues. These mechanisms include chelating metal ions involved in the generation of free radicals, donating electrons to stabilize free radicals (e.g., vitamins C and E), scavenging reactive oxygen species (ROS), inhibiting enzyme activity contributing to oxidative processes, and regenerating other antioxidants (e.g., vitamin C regenerates vitamin E).

Important mechanisms in chemical reactions include HAT (Hydrogen Atom Transfer), SPT (Single Electron Transfer), ET (Electron Transfer), and SET-PT (Sequential Electron Transfer-Proton Transfer), which are especially relevant in the context of oxidation-reduction processes. Understanding these mechanisms is crucial in the study of redox reactions, oxidation-reduction chemistry, and various biological processes. These mechanisms play essential roles in reactions that are relevant to fields such as organic chemistry, biochemistry, and material science. Researchers often leverage these mechanisms to design and optimize chemical reactions for specific applications, including the development of antioxidants or the study of electron transfer in biological systems [52].

As it was reported in many published studies hydrazones have exhibited antioxidant potential cannot be underestimated which assist in neutralizing harmful free radicals and protect cells from oxidative stress-related damage. In this context we exhibit in this part some hydrazone derivatives which showed an antioxidant activity.

A study was published by Jasril et al. [53] two hydrazone derivatives were synthesized using 1-naphthaldehyde and hydrazine (either phenylhydrazine or hydrazine hydrate) under microwave irradiation. The antioxidant activity and toxicity of these compounds were assessed using the DPPH assay and BSLT method, respectively. The structures of the synthesized compounds were confirmed through various spectroscopic techniques, including UV, FTIR, HRMS, and $^1\text{H-NMR}$. The results indicate that the hydrazone derived from phenylhydrazine exhibited strong antioxidant activity with an IC_{50} value of $28.90 \mu\text{g/mL}$, while the hydrazone derived from hydrazine hydrate showed inactive antioxidant properties ($\text{IC}_{50} > 1000 \mu\text{g/mL}$) according to the DPPH assay.

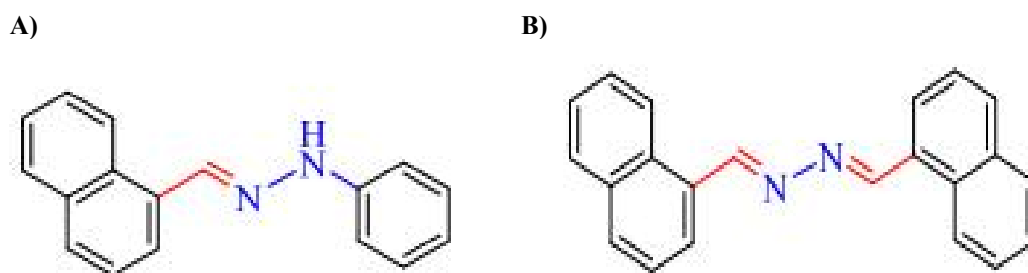


Figure I. 15: Chemical structure of A) 1-(naphthalen-1-ylmethylene)-2-phenylhydrazine B) 1,2-bis(naphthalen-1-ylmethylene)hydrazine.

Using a variety of heterocyclic aldehydes, Adjissi et al. [54] produced derivatives of aromatic hydrazone and thoroughly investigated their antioxidant properties. The resulting compounds demonstrated strong radical scavenging capabilities, establishing them as potent antioxidants. By doing a theoretical investigation in addition to their experiments, the researchers were able to gain a deeper knowledge of the antioxidant behavior of these hydrazone derivatives.

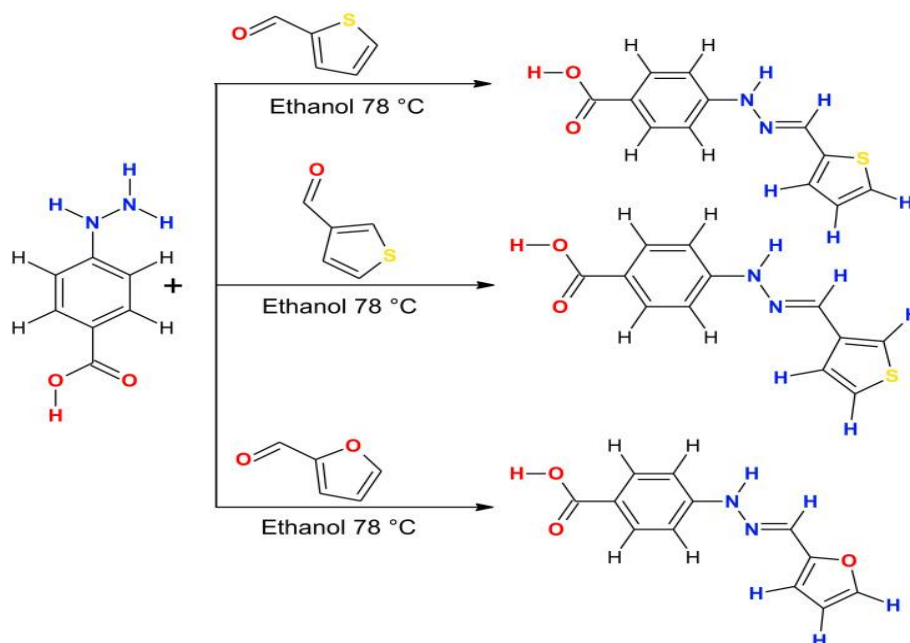


Figure I. 16: Chemical structure of aromatic hydrazones synthesized by Adjissi et al. [54].

IV.2.2. Antibacterial and antifungal activities

Hydrazones have been studied as possible antifungal and antibacterial treatments because of their capacity to impede growth by targeting essential enzymes and processes in germs. Some novel quinoxalinone hydrazone derivatives were described and studied by Evranos et al. [55]. Gram-positive *S. aureus* ATCC-29213, and Gram-negative *E. coli* ATCC-25922 bacterial strains were used to test their in-vitro antibacterial activity. Using ofloxacin as the reference medication, it was discovered that compounds showed rather moderate action toward both types of bacterial strains. According to Cordeiro et al. [56] various hydrazone analogues generated from isoniazid were investigated for their in-vitro antifungal activity against *Coccidioides posadasii*. However, compound 25 had the strongest antifungal activity against the *Coccidioides posadasii* strain, with a MIC value of 100–400 mg/ml, among the synthesized compounds. As a result, (Figure I.17 (A)), *N'*-[(*E*)-1-(4-methylphenyl) ethylidene]pyridine-4-carbohydrazide (Figure I.17 (B)), and *N'*-[(*E*)-1-(phenyl)ethylidene]pyridine-4-carbohydrazide (Figure I.17 (C)) may be employed in the future to treat fungus infections, according to the results of the current identification.

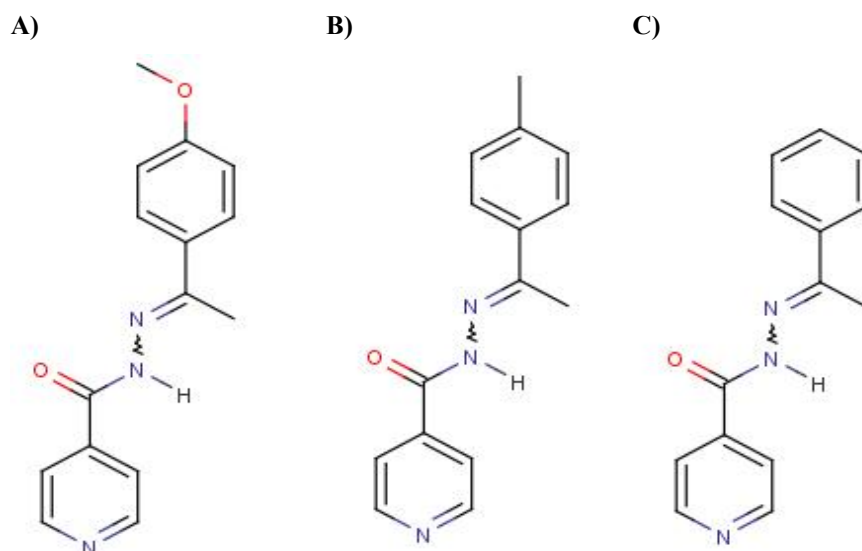


Figure I. 17: Chemical structure of antifungal hydrazones.

IV.2.3 Anticancer

Certain hydrazones have demonstrated promising anticancer characteristics by preventing cancer cells from proliferating, triggering apoptosis (programmed cell death), and interfering with vital biological functions. Dandawate et al. [57] synthesized a series of novel plumbagin hydrazonates by addition of hydrazone part in its structure the obtained compounds showed tangible enhancement in anticancer activity of plumbagin. Additionally, Zhao et al. [58] have succeeded in synthesizing benzoisindolin hydrazones from diphyllin. These derivatives displayed potent cytotoxic activity against three human cancer cell lines.

IV.2.3 Anti-tuberculosis TB agents

The growing threat of drug-resistant strains of *Mycobacterium TB* makes the discovery of novel anti-tuberculosis hydrazone chemicals imperative. The precise processes and effectiveness of hydrazone derivatives against tuberculosis, however, may differ based on the compound's structure and formulation. It is crucial to remember that research in this area is still ongoing.

To determine the safety, bioavailability, and therapeutic potential of these substances for the treatment of tuberculosis, additional research is usually carried out, including *in vitro* and *in vivo* evaluations. Dogan et al. [59] developed a special group of thiadiazolyl hydrazones Figure I.17 which were then tested for their potency against tuberculosis *in vitro*. With minimum inhibitory concentrations (MIC) varying between 0.78 and 6.25 mg/ml, the majority of these drugs demonstrated excellent antitubercular activity.

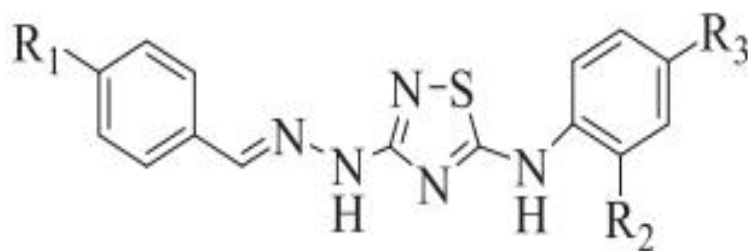


Figure I. 18: General structure of synthesized thiadiazolyl hydrazones [59].

IV.3. Coordination chemistry

In coordination complexes involving metal ions, hydrazones can act as ligands. Numerous applications for these compounds exist in the fields of materials research, sensing, and catalysis, it has been reported in paper was published by ahmed alsherifi a synthesis of new hydrazone derivatives 1-(phenyl-hydrazono)-propan-2-one (PHP), 1-(p-tolylyhydrazono)-propan-2-one (THP), 1-[(4-chloro-hydrazono)]-propan-2-one (CHP) forwarded to be applied as nickel and copper ligands complexes [60].

References

- [1] E. John, *An A-Z Guide to The Elements*, Oxford University Press, USA, 2001.
- [2] P.C. Samartzis, A.M. Wodtke, All-nitrogen chemistry: how far are we from N60?, *Int. Rev. Phys. Chem.* 25 (2006) 527–552.
- [3] K.H.T. Leghari, S. J., N.A. Wahocho, G.M. Laghari, A.H. Laghari, G.M. Bhabhan, and A.A. Lashari., Role of nitrogen for plant growth and development: A review. *Advances in Environmental Biology*.10(9):209-219., *Adv. Environ. Biol.* 10 (2016) 209–218.
- [4] R.M. Abu Shmeis, *Water Chemistry and Microbiology*, 1st ed., Elsevier B.V., 2018. <https://doi.org/10.1016/bs.coac.2018.02.001>.
- [5] R. Irie, *5.5 Oxidation: C-N Bond Formation by Oxidation: C-H Bond Activation*, Elsevier Ltd., 2012. <https://doi.org/10.1016/B978-0-08-095167-6.00507-3>.
- [6] A.R. Shaikh, M. Farooqui, R.H. Satpute, S. Abed, Overview on Nitrogen containing compounds and their assessment based on ‘International Regulatory Standards,’ *J. Drug Deliv. Ther.* 8 (2018) 424–428. <https://doi.org/10.22270/jddt.v8i6-s.2156>.
- [7] D.N. Aljamali, Review In Chemistry of Amines, *Int. Technol. Innov. Res. J.* 1 (2015) 1–9.
- [8] O.D. Sparkman, Z.E. Penton, F.G. Kitson, O.D. Sparkman, Z.E. Penton, F.G. Kitson, Chapter 10 – Amides, *Gas Chromatogr. Mass Spectrom.* (2011) 243–248. <https://doi.org/10.1016/B978-0-12-373628-4.00010-1>.
- [9] H.S. Toogood, D. Mansell, J.M. Gardiner, N.S. Scrutton, 7.11 Reduction: Enantioselective Bioreduction of C-C Double Bonds, Elsevier Ltd., 2012. <https://doi.org/10.1016/B978-0-08-095167-6.00713-8>.
- [10] H.D. Shin, X. Guo, R.R. Chen, *Biocatalysis for Chiral Synthesis*, *Bioprocess. Value-Added Prod. from Renew. Resour. New Technol. Appl.* (2006) 351–371. <https://doi.org/10.1016/B978-044452114-9/50014-1>.
- [11] L. Boucherit, M. Al-Noaimi, D. Daoud, T. Douadi, N. Chafai, S. Chafaa, Synthesis, characterization and the inhibition activity of 3-(4-cyanophenylazo)-2,4-pentanedione (L) on the corrosion of carbon steel, synergistic effect with other halide ions in 0.5 M H₂SO₄, *J. Mol. Struct.* 1177 (2019) 371–380. <https://doi.org/10.1016/j.molstruc.2018.09.079>.
- [12] S.C. Cosgrove, A. Brzezniak, S.P. France, J.I. Ramsden, J. Mangas-Sanchez, S.L. Montgomery, R.S. Heath, N.J. Turner, *Imine Reductases, Reductive Aminases, and Amine Oxidases for the Synthesis of Chiral Amines: Discovery, Characterization, and Synthetic Applications*, 1st ed., Elsevier Inc., 2018. <https://doi.org/10.1016/bs.mie.2018.04.022>.
- [13] I. V. Ledenyova, V. V. Didenko, K.S. Shikhaliev, *Chemistry of pyrazole-3(5)-diazonium salts*

- (Review), *Chem. Heterocycl. Compd.* 50 (2014) 1214–1243. <https://doi.org/10.1007/s10593-014-1585-1>.
- [14] D.L. Browne, J.L. Howard, C. Schotten, *Continuous Flow Processing as a Tool for Medicinal Chemical Synthesis*, Third Edition, Elsevier, 2017. <https://doi.org/10.1016/B978-0-12-409547-2.12288-7>.
- [15] S. Sattari Alamdar, A Review on Synthesis of Carbohydrazone Derivatives, *Asian J. Green Chem.* 7 (2023) 91–109. <https://doi.org/10.22034/ajgc.2023.383255.1370>.
- [16] T. Qadir, A. Amin, P.K. Sharma, I. Jeelani, H. Abe, A Review on Medicinally Important Heterocyclic Compounds, 2022. <https://doi.org/10.2174/18741045-v16-e2202280>.
- [17] E. Kabir, M. Uzzaman, A review on biological and medicinal impact of heterocyclic compounds, *Results Chem.* 4 (2022) 100606. <https://doi.org/10.1016/j.rechem.2022.100606>.
- [18] T. Vahedpour, M. Hamzeh-Mivehroud, S. Hemmati, S. Dastmalchi, Synthesis of 2-Pyrazolines from Hydrazines: Mechanisms Explained, *ChemistrySelect.* 6 (2021) 6483–6506. <https://doi.org/10.1002/slct.202101467>.
- [19] H. Hayashi, *Hydrazine Synthesis by a Catalytic Oxidation Process*, 1990. <https://doi.org/10.1080/01614949009351352>.
- [20] M. Elkhatib, C. Duriche, L. Peyrot, R. Metz, H. Delalu, Synthesis of 1-amino-2-methylindoline by raschig process: Kinetics of the oxidation of 1-amino-2-methylindoline by chloramine, *Int. J. Chem. Kinet.* 34 (2002) 515–523. <https://doi.org/10.1002/kin.10078>.
- [21] J.E. Troyan, Properties, Production, and Uses of Hydrazine, *Ind. Eng. Chem.* 45 (1953) 2608–2612. <https://doi.org/10.1021/ie50528a020>.
- [22] L. He, B. Liang, Y. Huang, T. Zhang, Design strategies of highly selective nickel catalysts for H₂ production via hydrous hydrazine decomposition: A review, *Natl. Sci. Rev.* 5 (2018) 356–364. <https://doi.org/10.1093/nsr/nwx123>.
- [23] C. Bernades, M. Carravetta, S.J. Coles, E.R.H. Van Eck, H. Meekes, M.E.M. Da Piedade, M.B. Pitak, M. Podmore, T.A.H. De Ruiter, L.C. Sögütöglü, R.R.E. Steendam, T. Threlfall, The Curious Case of Acetaldehyde Phenylhydrazone: Resolution of a 120 Year Old Puzzle where Forms with Vastly Different Melting Points Have the Same Structure, *Cryst. Growth Des.* 19 (2019) 907–917. <https://doi.org/10.1021/acs.cgd.8b01459>.
- [24] B. Mathew, J. Suresh, M. J Ahsan, G. E Mathew, D. Usman, P. NS Subramanyan, K. F Safna, S. Maddela, Hydrazones as a privileged structural linker in antitubercular agents: A review, *Infect. Disord. Targets (Formerly Curr. Drug Targets-Infectious Disord.)* 15 (2015) 76–88.
- [25] L.A. Tatum, X. Su, I. Aprahamian, Simple hydrazone building blocks for complicated functional materials, *Acc. Chem. Res.* 47 (2014) 2141–2149.

- <https://doi.org/10.1021/ar500111f>.
- [26] M. Khalid, A. Ali, S. Abid, M.N. Tahir, M.U. Khan, M. Ashfaq, M. Imran, A. Ahmad, Facile Ultrasound-Based Synthesis, SC-XRD, DFT Exploration of the Substituted Acyl-Hydrazones: An Experimental and Theoretical Slant towards Supramolecular Chemistry, *ChemistrySelect*. 5 (2020) 14844–14856. <https://doi.org/10.1002/slct.202003589>.
- [27] D.K. Kölmel, E.T. Kool, Oximes and Hydrazones in Bioconjugation: Mechanism and Catalysis, *Chem. Rev.* 117 (2017) 10358–10376. <https://doi.org/10.1021/acs.chemrev.7b00090>.
- [28] X. Su, I. Arahamian, Hydrazone-based switches, metallo-assemblies and sensors, *Chem. Soc. Rev.* 43 (2014) 1963–1981. <https://doi.org/10.1039/c3cs60385g>.
- [29] R. Brehme, D. Enders, R. Fernandez, J.M. Lassaletta, Aldehyde N,N-dialkylhydrazones as neutral acyl anion equivalents: Umpolung of the imine reactivity, *European J. Org. Chem.* (2007) 5629–5660. <https://doi.org/10.1002/ejoc.200700746>.
- [30] C. Lu, B. Htan, C. Ma, R.Z. Liao, Q. Gan, Acylhydrazone Switches: E/Z Stability Reversed by Introduction of Hydrogen Bonds, *European J. Org. Chem.* 2018 (2018) 7046–7050. <https://doi.org/10.1002/ejoc.201801466>.
- [31] R. Javaherdashti, How corrosion affects industry and life, *Anti-Corrosion Methods Mater.* 47 (2000) 30–34. <https://doi.org/10.1108/00035590010310003>.
- [32] R.A. Buchanan, E.E. Stansbury, Electrochemical corrosion, in: *Handb. Environ. Degrad. Mater.*, Elsevier, 2005: pp. 81–103.
- [33] R. Songbo, G. Ying, K. Chao, G. Song, X. Shanhua, Y. Liqiong, Effects of the corrosion pitting parameters on the mechanical properties of corroded steel, *Constr. Build. Mater.* 272 (2021) 121941. <https://doi.org/10.1016/j.conbuildmat.2020.121941>.
- [34] G. Bayramoğlu, T. Alemdaroğlu, S. Kedici, A.A. Aksüt, The effect of pH on the corrosion of dental metal alloys, *J. Oral Rehabil.* 27 (2000) 563–575. <https://doi.org/10.1046/j.1365-2842.2000.00549.x>.
- [35] M. Pour-Ghaz, O. Burkan Isgor, P. Ghods, The effect of temperature on the corrosion of steel in concrete. Part 2: Model verification and parametric study, *Corros. Sci.* 51 (2009) 426–433. <https://doi.org/10.1016/j.corsci.2008.10.036>.
- [36] Y. Prawoto, M. Ikeda, S.K. Manville, A. Nishikawa, Design and failure modes of automotive suspension springs, *Eng. Fail. Anal.* 15 (2008) 1155–1174. <https://doi.org/10.1016/j.engfailanal.2007.11.003>.
- [37] X. Liu, C. Gong, L. Zhang, H. Jin, C. Wang, Numerical study of the hydrodynamic parameters influencing internal corrosion in pipelines for different elbow flow configurations,

- Eng. Appl. Comput. Fluid Mech. 14 (2020) 122–135.
<https://doi.org/10.1080/19942060.2019.1678524>.
- [38] H.-R. Jung, U.-J. Kim, G.-T. Seo, H.-D. Lee, C.-S. Lee, Effect of Dissolved Oxygen (DO) on Internal Corrosion of Water Pipes, *Environ. Eng. Res.* 14 (2009) 195–199.
<https://doi.org/10.4491/eer.2009.14.3.195>.
- [39] H. Jung, K.J. Kwon, E. Lee, D.G. Kim, G.Y. Kim, Effect of dissolved oxygen on corrosion properties of reinforcing steel, *Corros. Eng. Sci. Technol.* 46 (2011) 195–198.
<https://doi.org/10.1179/1743278210Y.0000000008>.
- [40] Y. Zhao, A.R. Karimi, H.S. Wong, B. Hu, N.R. Buenfeld, W. Jin, Comparison of uniform and non-uniform corrosion induced damage in reinforced concrete based on a Gaussian description of the corrosion layer, *Corros. Sci.* 53 (2011) 2803–2814.
<https://doi.org/10.1016/j.corsci.2011.05.017>.
- [41] G.S. Frankel, N. Sridhar, Understanding localized corrosion, *Mater. Today.* 11 (2008) 38–44.
[https://doi.org/10.1016/S1369-7021\(08\)70206-2](https://doi.org/10.1016/S1369-7021(08)70206-2).
- [42] G. Grundmeier, W. Schmidt, M. Stratmann, Corrosion protection by organic coatings: Electrochemical mechanism and novel methods of investigation, *Electrochim. Acta.* 45 (2000) 2515–2533. [https://doi.org/10.1016/S0013-4686\(00\)00348-0](https://doi.org/10.1016/S0013-4686(00)00348-0).
- [43] H.A. Mohamed, Preparation and application of new ecofriendly inhibitor in varnishes for protection of corrosion of steel, *Corros. Eng. Sci. Technol.* 45 (2010) 262–267.
<https://doi.org/10.1179/174327809X397839>.
- [44] J.E.O. Mayne, Corrosion Prevention by Paints, *Trans. IMF.* 29 (1952) 146–163.
<https://doi.org/10.1080/00202967.1952.11869596>.
- [45] P. Pedferri, Cathodic protection and cathodic prevention, *Constr. Build. Mater.* 10 (1996) 391–402. [https://doi.org/10.1016/0950-0618\(95\)00017-8](https://doi.org/10.1016/0950-0618(95)00017-8).
- [46] P.B. Raja, M. Ismail, S. Ghoreishiamiri, J. Mirza, M.C. Ismail, S. Kakooei, A.A. Rahim, Reviews on Corrosion Inhibitors: A Short View, *Chem. Eng. Commun.* 203 (2016) 1145–1156. <https://doi.org/10.1080/00986445.2016.1172485>.
- [47] N. Chafai, S. Chafaa, K. Benbouguerra, A. Hellal, M. Mehri, Synthesis, spectral analysis, anti-corrosive activity and theoretical study of an aromatic hydrazone derivative, *J. Mol. Struct.* 1181 (2019) 83–92. <https://doi.org/10.1016/j.molstruc.2018.12.073>.
- [48] A. Chaouiki, M. Chafiq, M.R. Al-Hadeethi, H. Lgaz, R. Salghi, S.K. Abdelraheem, I.H. Ali, S.A.M. Ebraheem, I.M. Chung, S.K. Mohamed, Exploring the corrosion inhibition effect of two hydrazone derivatives for mild steel corrosion in 1.0 M HCl solution via electrochemical and surface characterization studies, *Int. J. Electrochem. Sci.* 15 (2020) 9354–9377.

- <https://doi.org/10.20964/2020.09.95>.
- [49] A.G. Sayed, A.M. Ashmawy, W.E. Elgammal, S.M. Hassan, M.A. Deyab, Synthesis, description, and application of novel corrosion inhibitors for CS AISI1095 in 1.0 M HCl based on benzoquinoline derivatives, *Sci. Rep.* 13 (2023) 1–23. <https://doi.org/10.1038/s41598-023-39714-1>.
- [50] M.N. Alam, N.J. Bristi, M. Rafiquzzaman, Review on in vivo and in vitro methods evaluation of antioxidant activity, *Saudi Pharm. J.* 21 (2013) 143–152. <https://doi.org/10.1016/j.jsps.2012.05.002>.
- [51] C. Dokki, Methods for Determining the Antioxidant Activity: A Review, *Alexandria J. Food Sci. Technol.* 11 (2014) 31–42. <https://doi.org/10.12816/0025348>.
- [52] R.R. Kotha, F.S. Tareq, E. Yildiz, D.L. Luthria, Oxidative Stress and Antioxidants—A Critical Review on In Vitro Antioxidant Assays, *Antioxidants.* 11 (2022). <https://doi.org/10.3390/antiox11122388>.
- [53] Jasril, E. Juwiyatri, S.N. Fauza, N. Afriana, Synthesis, in vitro antioxidant activity, and toxicity evaluation of hydrazone derivatives naphthalene-1-ylmethylene hydrazine, *J. Phys. Conf. Ser.* 2049 (2021) 1–7. <https://doi.org/10.1088/1742-6596/2049/1/012050>.
- [54] L. Adjissi, N. Chafai, K. Benbouguerra, I. Kirouani, A. Hellal, H. Layaida, M. Elkolli, C. Bensouici, S. Chafaa, Synthesis, characterization, DFT, antioxidant, antibacterial, pharmacokinetics and inhibition of SARS-CoV-2 main protease of some heterocyclic hydrazones, *J. Mol. Struct.* 1270 (2022) 134005. <https://doi.org/10.1016/j.molstruc.2022.134005>.
- [55] B. Evranos Aksöz, S.S. Gürpınar, M. Eryılmaz, Antimicrobial activities of some pyrazoline and hydrazone derivatives, *Turkish J. Pharm. Sci.* 17 (2020) 500–505. <https://doi.org/10.4274/tjps.galenos.2019.42650>.
- [56] R. De Aguiar Cordeiro, F.J. De Farias Marques, R. De Aguiar Cordeiro, M.R. Da Silva, A.D.M. Malaquias, C.V.S. De Melo, J. Mafezoli, M.D.C.F. De Oliveira, R.S.N. Brilhante, M.F.G. Rocha, T. De Jesus Pinheiro Gomes Bandeira, J.J.C. Sidrima, Synthesis and antifungal activity in vitro of isoniazid Derivatives against *histoplasma capsulatum* var. *Capsulatum*, *Antimicrob. Agents Chemother.* 58 (2014) 2504–2511. <https://doi.org/10.1128/AAC.01654-13>.
- [57] P. Dandawate, E. Khan, S. Padhye, H. Gaba, S. Sinha, J. Deshpande, K. Venkateswara Swamy, M. Khetmalas, A. Ahmad, F.H. Sarkar, Synthesis, characterization, molecular docking and cytotoxic activity of novel plumbagin hydrazones against breast cancer cells, *Bioorganic Med. Chem. Lett.* 22 (2012) 3104–3108.

<https://doi.org/10.1016/j.bmcl.2012.03.060>.

- [58] Y. Zhao, J. Hui, D. Wang, L. Zhu, J.H. Fang, X.D. Zhao, Synthesis, cytotoxicity and proapoptosis of novel benzoisindolin hydrazones as anticancer agents, *Chem. Pharm. Bull.* 58 (2010) 1324–1327. <https://doi.org/10.1248/cpb.58.1324>.
- [59] H. Doğan, Ş.D. Doğan, M.G. Gündüz, V.S. Krishna, C. Lherbet, D. Sriram, O. Şahin, E. Sarıpınar, Discovery of hydrazone containing thiadiazoles as Mycobacterium tuberculosis growth and enoyl acyl carrier protein reductase (InhA) inhibitors, *Eur. J. Med. Chem.* 188 (2020). <https://doi.org/10.1016/j.ejmech.2020.112035>.
- [60] L.D. Popov, A.N. Morozov, I.N. Shcherbakov, Y.P. Tupolova, V. V Lukov, V.A. Kogan, Metal complexes with polyfunctional ligands based of bis(hydrazones) of dicarbonyl compounds, *Russ. Chem. Rev.* 78 (2009) 643–658. <https://doi.org/10.1070/rc2009v078n07abeh003890>.

Chapter II :

Materials and

Methods

The purpose of this chapter is to provide an in-depth analysis of the wide range of materials used and the related techniques used to accomplish the desired results. In order to achieve the desired outcomes, we want to thoroughly investigate all of the many components, materials, and approaches that have been carefully selected and put into practice.

II.1. Synthesis under reflux

Reflux synthesis is a widely used laboratory technique in organic chemistry for carrying out chemical reactions that require a high temperature and exclusion of light, moisture or air. This method involves heating a reaction mixture in a round-bottom flask fitted with a condenser which allows volatile reactants or solvents to evaporate and then condense back into reaction mixture. This process is usually performed with condenser figure II.1 which is a water-cooling system to insure the condensation.

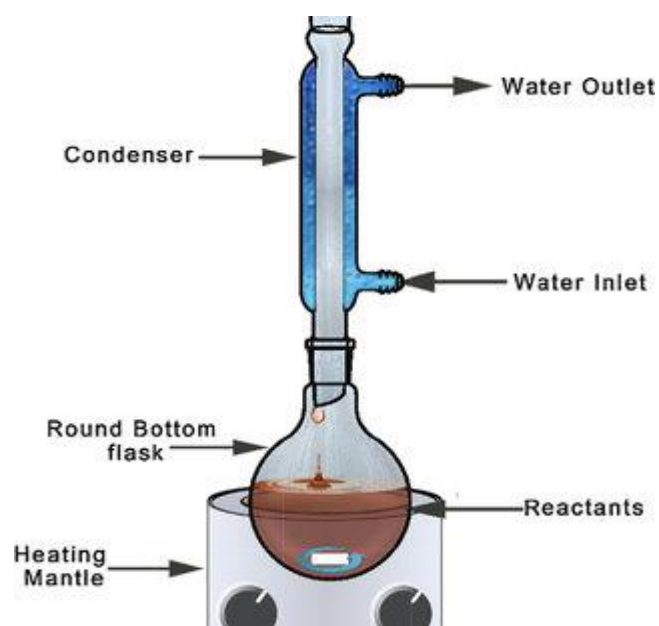


Figure II. 1: Schematic synthesis under reflux.

The main purpose of Synthesis under reflux is to maintain a homogeneous temperature in reactional media especially those imply a solvent use or volatile byproducts this can be obtained by using hot plate. In addition, stirrer can insure the mechanical stirring. In our study we basically depended on the synthesis under reflux in order to produce a novel organic hydrazones derivative based on condensation of aromatic hydrazine with aromatic aldehydes.

II.2. Chemicals

All the reagents used for the synthesis of hydrazones were purchased from sigma aldrich 4-Hydrazinobenzoic acid , 4Methylphenylhydrazine, 2-Nitrobenzaldehyde 2-Hydroxynaphtaldehyde, Salicylaldehyde, Methanol, Ethanol, Dimethylsulfoxide DMSO, Acetone Acetonitrile, Tetrahydrofuran THF, Dimethylformamide DMF, Dichloromethane, Acetate ethyle, Chloroform, Ether petroleum, Ether diethyl, DPPH and Hydrochloric acid HCl .

II.3. Thin Layer Chromatography

To separate and evaluate mixtures of substances, chemists utilize the chromatographic technique known as thin layer chromatography (TLC). It is a straightforward and affordable technique that is frequently used for qualitative analysis of the substances in a combination [1].

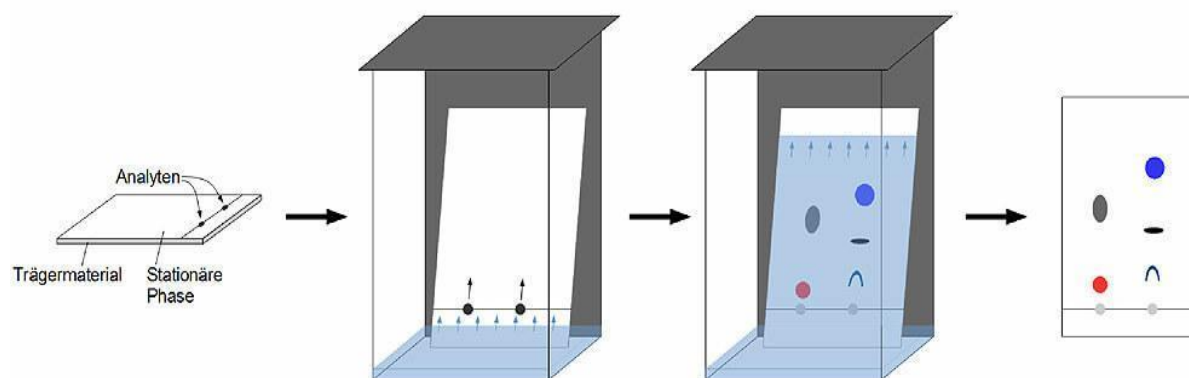


Figure II. 2: Thin layer chromatography (TLC).

The stationary phase in TLC is an extremely thin, flat, and inert layer that is often comprised of alumina or silica gel. A thin, uniform surface is produced by coating this layer onto a glass or plastic plate, and by using a capillary tube or a micropipette, a little amount of the mixture to be separated is spotted or put close to the bottom of the TLC plate. To create a clean separation, it is crucial to use a small, focused spot of application.

Depending on their affinity for the stationary phase and mobile phase, the mixture's constituent parts move up the TLC plate at various speeds. Polar compounds tend to drift away from the baseline more slowly than less polar molecules.

In TLC, the relative migration distance (R_f) is an essential variable. It is computed by dividing the compound's distance from the beginning point (where the sample was applied) by the solvent front's distance. Under specific conditions, each compound has a distinct R_f value, making it useful for compound identification.

II.4. Melting point

Melting point information is helpful in many other domains, including chemistry. It can be used to assess a sample's grade, confirm a compound's identity and purity, and monitor the evolution of chemical reactions. The pharmaceutical industry, in particular, regularly uses melting point analysis to verify the purity of therapeutic components [2].



Figure II.3: Photograph of the melting point apparatus.

An instrument called a melting point apparatus is commonly used to determine melting points. A melting point capillary or a capillary tube with a little amount of the substance within is then introduced into the apparatus. The temperature is gradually raised, and the melting point is marked as the point at which the first drop of liquid is seen. In our study we used BUCHI melting point B-540 apparatus Figure II.3 to determine the MP of each obtained product.

II.5. UV-vis spectroscopy

UV-Vis spectroscopy, also referred to as ultraviolet-visible spectroscopy, is a well-liked analytical technique for analyzing the absorption and transmission of light by molecules, frequently in the ultraviolet (UV) and visible (Vis) portions of the electromagnetic spectrum. This technique is highly useful for studying the electrical transitions of molecules since it can provide valuable information about the concentration and chemical makeup of the molecules [3].

The principle of UV-Vis spectroscopy is the concept that molecules can absorb light in the UV and visible spectrum when their electrons move from lower energy states (called the ground state) to higher energy states (called the excited state). The energy of the photon that is absorbed corresponds to the energy difference between both states, and this energy is

often in the UV or visible range. The components of a standard UV-Vis spectrophotometer include a light source (often a UV lamp or tungsten lamp), a monochromator to choose a particular wavelength of light, a sample holder, and a detector (commonly a photodiode array or a photomultiplier tube). The device measures the light's intensity before and after the sample is exposed to it, and the absorbance is calculated using the difference in intensities [4].



Figure II.4: Spectrophotometer apparatus. .

A UV-Vis spectrum shows the wavelength dependence of absorption. The spectrum's peaks represent the wavelengths of light that the sample absorbs. The location and magnitude of these peaks provide information about the properties and concentration of the species that is absorbing the light. In this context, Beer-Lambert Law relates the absorbance of light to the concentration of a solution. It states that absorbance A_{abs} is directly proportional to the concentration C , path length l and molar absorptivity ϵ . This law is fundamental in determining concentrations using UV-Vis spectroscopy.

$$A_{\text{abs}} = \epsilon \cdot C \cdot l \quad \text{Eq. (1)}$$

In UV-Vis spectroscopy, electronic transitions refer to the transfer of electrons between different energy levels within a molecule. The most prevalent kinds are $n \rightarrow \pi^*$ transitions, in which non-bonding electrons (n) are excited to a π^* orbital, and $\pi \rightarrow \pi^*$ transitions, in which electrons in a π -bond move to an anti-bonding π^* orbital. $\sigma \rightarrow \sigma^*$ transitions, which need higher energy and are frequently seen in the UV region, happen in saturated compounds when electrons in a σ bond are promoted to an anti-bonding σ^* orbital. These transitions reveal information about the conjugation and functional groups that make up a molecule's electronic structure.

II.6 FT-IR spectroscopy.

Fourier Transform infra-red A potent analytical method for examining how matter and electromagnetic radiation interact in the infrared part of the electromagnetic spectrum is infrared spectroscopy. This method is frequently used in the domains of chemistry, materials science, and other sciences to analyze substances both qualitatively and quantitatively using their vibrational and rotational modes [5].

The foundation of FTIR spectroscopy is the idea that molecules absorb infrared light at precise frequencies that correspond to the vibrational modes of the atoms that make them up. Some of the infrared light that enters a sample is absorbed at these distinctive frequencies while the remaining light is transmitted. An FTIR spectrometer may provide an infrared spectrum that contains details on the chemical structure and structural composition of the sample by measuring the intensity of transmitted or absorbed light as a function of wavelength.

An FTIR spectrum is composed of wavenumber peaks (wavelength reciprocals) that are related to the vibrational frequencies of the chemical bonds in the sample. These peaks are interpreted by analysts to denote chemical structures and functional groups. Quantitative data regarding the makeup of the sample can also be obtained from the peak intensities. FTIR spectrometers are made up of a Source of infrared light which is Usually, an infrared source with a broad spectrum, like a tungsten filament or a globular source.



Figure II. 5: FTIR spectrometers apparatus.

II.7. NMR spectroscopy

The broad applicability and non-destructive character of NMR spectroscopy across numerous scientific domains have revolutionized our comprehension of molecular structures and processes.

(NMR) is a powerful analytical technique that is primarily used in physics, chemistry, and biology to study the properties of atomic nuclei. It provides a wealth of knowledge regarding the composition, behavior, and chemical environment of molecules, making it an invaluable resource in many scientific fields [6].

The magnetic characteristics of atomic nuclei are used in NMR. Some atomic nuclei, such as hydrogen (protons) or carbon-13, absorb energy and resonate at particular frequencies when placed in a high magnetic field and exposed to radio frequency radiation. These resonances are found by the NMR spectrometer, and the information gathered from them can be utilized to ascertain the sample's chemical and structural composition. Chemical shifts, or peaks at particular frequencies, can be seen in NMR spectra. The chemical shift is influenced by the nucleus's local chemical environment, which reveals details about the nearby atoms' chemical relationships.

Our synthesized hydrazones have been characterized using NMR. The H NMR and C NMR spectra were collected in DMSO-*d* 6 solvent using a Bruker Advance 300 NMR spectrometer running at 400 MHz.

II.8. Biological activity.

II.8.1 Antioxidant in vitro assay

Assays for antioxidant activity evaluate a material's ability to scavenge harmful free radicals or reactive oxygen species (ROS) in order to shield biological systems from oxidative stress. Antioxidants are essential for preserving general health because they help shield cells and tissues from damage caused by oxidative stress, which is connected to several diseases, including as cancer, cardiovascular disease, and aging. The anti-oxidant potential of a specific item can be assessed using a variety of techniques, including DPPH (2,2-diphenyl-1-picrylhydrazyl), FRAP (ferric reducing antioxidant power), TEAC (Trolox equivalent antioxidant capacity), and TAC (total antioxidant capacity) [7]. The DPPH radical is neutralized by antioxidants through electron or hydrogen donation. The antioxidant transfers an electron or hydrogen atom to the DPPH radical, converting it into a stable, non-radical DPPH-H molecule. This reaction results in a color change from violet to yellow, allowing the antioxidant capacity of a compound to be measured in vitro.

We have chosen in our lab the DPPH method for some reasons which are simple, quick and affordable. The DPPH assay is a commonly used technique to assess the antioxidant activity of diverse substances, including natural extracts, artificial antioxidants,

and meals. The DPPH radical can be neutralized by antioxidants by donating electrons, which causes a change in color that can be measured spectrophotometrically.

The half-maximal inhibitory concentration (IC_{50}) values, which represent the concentration of the sample necessary to scavenge 50% of the DPPH radicals, are commonly used to express the antioxidant activity. A lower IC_{50} value suggests a more potent antioxidant.

On the other hand the reaction between the antioxidant and free radicals can be occurred by three well known mechanisms which are hydrogen transfer (HAT), SET-PT (Single Electron Transfer-Proton Transfer) mechanism and Sequential Proton Loss Electron Transfer (SPLET) [8,9]. The one-step HAT technique facilitates the identification of a compound's reactive sites; it has been established that one useful metric for examining the structure-activity connections of hydrazone antioxidants is the dissociation enthalpy of the -OH group. A lower BDE value means that the corresponding OH bond is more easily broken and less stable indicating a stronger antioxidant capability, Thus, the BDE value is calculated using Eq. (1):

$$BDE = H(ArO\cdot) + H(H^+) - H(ArOH) \quad \text{Eq. (2)}$$

Regarding SET-PT mechanism there are two primary steps: The first step is the transfer of one electron, which results in the radical ($ArOH^+$) being produced, and the ionization potential (IP) is the dependent parameter which is a measure of the energy required to remove an electron from a system of molecules. The breakdown of the O-H bond is the next step in this mechanism and it is explained by the proton dissociation enthalpy (PDE) parameter Eqs. (2) and (3) are used to determine the IP and PDE, respectively. Antioxidants with lower IP have a higher propensity to directly transfer electrons to produce radical anions.

$$IP = H(ArOH^+) + H(e^-) - H(ArOH) \quad \text{Eq. (3)}$$

$$PDE = H(ArO\cdot) + H(H^+) - H(ArOH^+) \quad \text{Eq. (4)}$$

In the mechanism sequential proton loss electron transfer (SPLET) the antioxidant action is divided into two parts, firstly an anion (ArO^-) is generated when a proton is released by ArOH. The proton affinity (PA) value, which is determined by Eq. (4):

$$PA = H(ArO^-) + H(H^+) - H(ArOH) \quad \text{Eq. (5)}$$

Secondly ArO^- releases an electron, which the free radical takes and is then trapped by the proton, causing ArO to change into a stable radical. In this chemical reaction, the

thermodynamic parameter is the electron transfer enthalpy (ETE), which can be computed using Eq. (5):

$$\text{ETE} = H(\text{ArO}^\cdot) + H(e^-) - H(\text{ArO}^-) \quad \text{Eq. (6)}$$

II.8.1 Antibacterial in vitro assay

A collection of potentially pathogenic species is represented by the chosen microorganisms, which are also useful assay bacteria for evaluating antibacterial efficacy. We used four ATCC (American type culture collection) strains. The gram-positive ones were *Staphylococcus aureus* ATCC 25923 and *Bacillus subtilis* ATCC 6633P. The gram negatives were, *Escherichia coli* ATCC 25922 and *Salmonella enterica* ATCC 13076.

II.8.1.1 Preparation of the inoculum

The following describes how the inoculum was made: Initially, a pure and young culture (18 hours old) was used to create a bacterial suspension with an opacity of 0.5 McFarland (or 10^8 CFU/ml). By adding extra culture, the opacity level which corresponds to an optical density that ranges between 0.08 and 0.1 at 620 nm can be changed to modify the optical density (OD) as necessary.

II.8.1.2 Finding the minimum inhibitory concentration (MIC):

According to Eloff et al. [42] the MIC is the lowest antibacterial agent concentration at which no bacterial growth is seen after 24 hours. To determine the MIC, the 96-well plate microdilution method was employed. Three duplicates of each test were run in Mueller-Hinton broth (MHB).

Using a 96-well culture plate, serial dilutions within the selected concentration range were made. The organic compounds were initially dissolved in 1 mg/ml (stock concentration) of aqueous dimethyl sulfoxide DMSO (1%) solution. Two serial dilutions (V/V) of the original test concentration were performed. 50 μ l of bacterial suspension and 50 μ l of molecules diluted in MHB were added to each well for inoculation, and the wells were then incubated for 24 hours at 37°C. Using only the naked eye, observation was done at the conclusion of this incubation phase. To measure bacterial growth, 40 μ L of 2,3,5-triphenyltetrazolium chloride (TTC, 2 mg/mL) was introduced along with a dye indicator. Another two hours were spent in the dark incubating the plate. The minimum inhibitory concentration (MIC) of a chemical was defined as the lowest concentration at which color changes could not be observed.

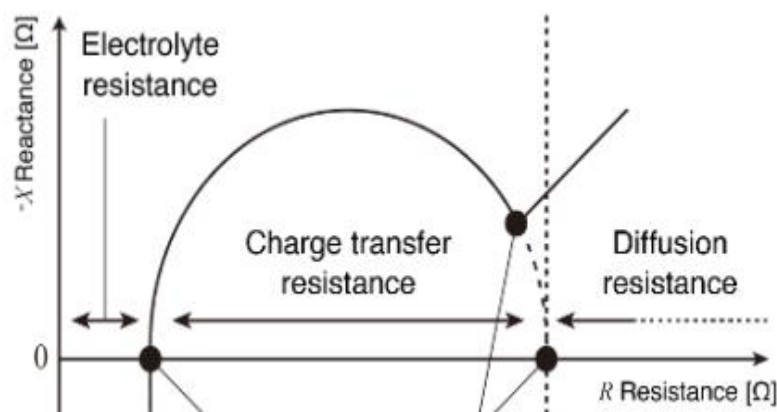
II.9. Electrochemical tests

Electrochemical experiments such as tafel analysis, electrochemical impedance measurement and weight loss are used to study the behavior of chemical reactions involving electron transport at the interface between an electrode and an electrolyte solution [10]. These experiments are widely used in many fields, such as chemistry, materials science, electrochemistry, and biology, to investigate the electrochemical characteristics of substances and reaction kinetics.

II.9.1. EIS electrochemical impedance spectroscopy

EIS provides a useful explanation of the kinetics and processes of electrochemical reactions as well as the impedance, or resistance, to electrical current flow in a system as a function of frequency [11,12].

An electrochemical system is exposed to an alternating current pulse with a predetermined frequency and amplitude in order to operate according to the EIS principle. The AC signal's waveform can be sinusoidal. The complex impedance (Z), which combines components for reactance (X) and resistance (R), is a standard way to measure how the system responds to this AC signal. The resistance to flow of an AC current system is measured using impedance. For every frequency, the impedance response is measured and documented. This results in the creation of an impedance spectrum or impedance vs. frequency diagram.



FigureII.6 : Example of Nyquist Plot

For investigations on corrosion on the other side, EIS can help determine corrosion rates, processes, and the effectiveness of corrosion inhibitors. EIS can provide information on processes pertaining to mass transport (diffusion), charge transfer reactions, and interface capacitance.

II.9.2. Tafel analysis

Tafel is an electrochemical technique used to study the kinetics of electrochemical reactions, especially those involving corrosion. It is named Julius Tafel in honor of the German chemist who made significant advances in electrochemistry in the late 19th and early 20th centuries. The Tafel test is widely used to determine variables like as corrosion rates, corrosion potentials, and the rate of electrochemical reactions [13].



Figure II. 7: Potentiostat device .

The Tafel test typically involves a three-electrode electrochemical cell. The three electrodes are the working electrode (the material under investigation), a reference electrode (often a saturated calomel electrode or a silver/silver chloride electrode), and a counter electrode.

II.10. Atomic Force Microscopy (AFM)

It is a high-resolution imaging and measurement method that is applied in a number of scientific and engineering disciplines to investigate the surface features, topography, and mechanical characteristics of materials at the nanoscale. AFM scans a sharp tip (probe or cantilever) over the sample while measuring the forces that interact with the surface to produce a three-dimensional profile of the surface [14].

The contact forces between the tip and the sample surface are the basis for how AFM works. Van der Waals, electrostatic, and capillary forces are some of these forces.

AFM (atomic force microscopy) provides detailed insights into the mechanical properties, including roughness, texture, and stiffness of a surface in addition to high-resolution imaging. AFM is able to quantify surface roughness at the nanoscale, providing fine details about the texture of the material by measuring the forces of interaction between the tip and the surface. Furthermore, by exerting force on the surface, AFM evaluates the

material's elasticity and stiffness (Young's modulus), which makes it an effective tool for researching mechanical characteristics like adhesion, hardness, and viscoelastic behavior. AFM is very useful for studies in material science, nanotechnology, and biology because of these features.

II.11. Computational chemistry

II.11.1. Density functional theory (DFT) study

Density functional theory (DFT) is a powerful computational method used in quantum chemistry and condensed matter physics to predict and understand the electronic structure and behavior of molecules, solids, and materials. It is a widely used method because it strikes a balance between accuracy and computational economy. The idea of electron density, a crucial aspect of a quantum mechanical system, is the basis of DFT. DFT searches for the ground-state electron density that minimizes the system's overall energy, in contrast to wavefunction-based methods like Hartree-Fock theory, which directly solve the many-body Schrödinger equation [15,16].

DFT is a valuable tool in the study of chemical reactivity. Chemical reactivity is the term used to describe chemical reactions between molecules that produce new substances. DFT is a helpful tool for understanding these processes at the quantum level [17].

HOMO and LUMO are important words in the context of quantum chemistry and molecular orbital theory. They represent the Highest Occupied Molecular Orbital (HOMO) and the Lowest Unoccupied Molecular Orbital (LUMO), respectively. The electrical properties and structure of molecules are described by the following expressions:

II.11.1.1 Highest energy molecular orbital HOMO and lowest energy molecular orbital LUMO

The HOMO is the highest energy molecular orbital found in molecules that contain electrons. It represents the orbital containing the energetic electrons. The electrons in the HOMO are the easiest to access in order to participate in chemical reactions. This is because, in comparison to electrons in lower energy orbitals, they are held by the nucleus with greater energy and less tensile force. A nucleophilic reaction is one in which the HOMO transfers electrons to other molecular orbitals during a chemical reaction [18].

The LUMO is the lowest energy molecular orbital in an electron-depleted molecule. It shows the orbital to which more electrons could travel if they were accepted by the molecule. It is commonly associated with electrophilic reactions due to its electron-accepting capacity throughout atomic orbitals. Charge transfer and chemical reactions can be facilitated by

interactions between the LUMO and HOMO of two molecules that involve the transfer of electrons.

$$\Delta E_{gap} = E_{LUMO} - E_{HOMO} \quad \text{Eq. (7)}$$

The HOMO-LUMO gap, or energy differential between the HOMO and LUMO, is a crucial element in influencing a molecule's reactivity. Higher reactivity is usually indicated by smaller HOMO-LUMO gaps.

Understanding the HOMO and LUMO states of a molecule is essential to quantum mechanics and computational chemistry. Scientists utilize these concepts to predict and explain chemical reactivity as well as to build and enhance molecules for specific uses, such as medicine development or materials research. The distribution of electron density inside these orbitals and the HOMO-LUMO gap are useful tools for understanding how molecules interact with one another during chemical reactions.

II.11.1.2. Electronegativity

The ability of an element to draw electrons into a chemical bond is measured by its electronegativity.

$$\chi = -\mu \quad \text{Eq. (8)}$$

The polarity of the bond can be determined by the difference in electronegativity between the atoms in a molecule, and this can also affect the direction of electron flow in processes [19].

II.11.1.3. Ionization energy

The energy necessary to eject an electron from an atom or an ion is known as ionization energy. Less reactivity is typically associated with higher ionization energy because it is more challenging to remove electrons from these species [20].

$$I = -E_{HOMO} \quad \text{Eq. (9)}$$

II.11.1.4. Electron affinity

Electron affinity is the term for the energy change that occurs when an atom or ion accepts an electron. It provides information on how well an atom can take on new electrons. Higher electron affinities are frequently correlated with greater reactivity as electron acceptors [21].

$$A = -E_{LUMO} \quad \text{Eq. (10)}$$

II.11.1.5. Nucleophilicity and electrophilicity

Nucleophilicity is the ability of a substance to donate electrons to another molecule, usually in a nucleophilic substitution process. The high electron density that sets nucleophiles apart usually occurs in their HOMO. Electrophilicity is the inclination of a molecule or species to accept electrons, usually in electrophilic addition or substitution processes. The presence of electron-deficient centers, which are a feature of electrophiles, is indicated by the presence of a significant positive charge in the LUMO [22].

$$\omega = \frac{\mu^2}{2\eta} \quad \text{Eq. (11)}$$

II.11.1.6. Hardness and softness

These characteristics relate to the response of the species. Because they have low electron affinities and large ionization energies, hard species are less likely to start chemical reactions. Because they have lower ionization energies and higher electron affinities, soft species are more prone to react [23]. A system's ability to withstand variations in electron density is referred to as its hardness. A "hard" system is one that resists change as much as possible, indicating that it will usually hold onto its current configuration regardless of outside influences.

$$\eta = \frac{E_{LUMO} - E_{HOMO}}{2} \quad \text{Eq. (12)}$$

Conversely, softness describes how easily a system adapts to variations in electron density. An electron distribution in a "soft" system can be changed more readily and it responds to outside disturbances more readily.

$$\sigma = \frac{1}{\eta} \quad \text{Eq. (13)}$$

II.11.1.7. Chemical potential

Chemical potential is a temperature- and concentration-dependent measure of a substance's propensity to react. A high chemical potential implies greater reactivity [24].

$$\mu = \frac{-(I + A)}{2} \quad \text{Eq. (14)}$$

These descriptors are essential resources for understanding and predicting chemical interactions because they provide a quantitative framework for assessing the reactivity of molecules and species. Scientists use these phrases to explore reaction mechanisms, synthesize novel chemicals, and enhance chemical processes.

II.11.1.7. Molecular electrostatic potential (MEP)

A notion in theoretical chemistry known as molecular electrostatic potential (MEP) sheds light on how electrostatic charge is distributed within molecules. Electrostatic potential maps (MEP) are a useful tool for visualizing regions of high (negative potential) and low (positive potential) electron density [25]. These regions are commonly represented by the colors red and blue, respectively.

Quantum chemical techniques, frequently based on density functional theory or Hartree-Fock, are used to calculate MEP while accounting for the molecule electron density distribution. Recognizing red areas as electron-rich regions that appeal to electrophiles and blue areas as electron-poor regions that appeal to nucleophiles is necessary for MEP interpretation. MEP is helpful in understanding and forecasting chemical selectivity and reactivity. Reactants are more likely to interact in regions of opposite electrostatic potential, which helps in the interpretation of nucleophilic or electrophilic assaults. MEP is also used in drug design molecular docking studies, providing information on molecular binding interactions. Moreover, solvation effects can be taken into account in MEP calculations, offering a more thorough comprehension of molecular interactions in various settings. Molecular electrostatic potentials, in general, are an effective tool in theoretical and computational chemistry that can be used for the creation of drugs, catalysts, and a basic knowledge of chemical interactions.

In our present work, for molecular analysis and calculations, Becke's three parameter hybrid exchange functional with Lee-Yang-Parr correlation functional (B3LYP) was used in conjunction with DFT. The Gaussian 09 program was used to perform quantum chemical calculations, and the following parameters were calculated: ionization potential, electron affinities, electronegativity, chemical potential, global hardness, global softness, and electrophilicity index.

II.11.1.8. Density of states (DOS) analysis

Comprehending the electrical characteristics of materials requires a fundamental grasp of density of states (DOS) analysis, which is a fundamental concept in condensed matter physics and materials research. In order to design semiconductor devices, conduct superconductivity research, and create new materials for electronic and photonic applications, it is critical to have an understanding of how electrons are distributed in a material's energy levels [26].

In essence, DOS analysis aids in characterizing the energy levels and associated probabilities that electrons have access to within a material. A DOS curve, which illustrates the density of electron states as a function of energy, is commonly used to represent these energy states. A useful tool for comprehending the electrical structure of materials and forecasting their behavior under various circumstances is the DOS curve.

Finding a material's electronic characteristics, such as its electrical conductivity, optical absorption, and thermal behavior, is one of the main goals of DOS analysis. The bandgap, which is the energy range where no electron states are accessible, can be found by closely scrutinizing the DOS curve. In general, insulators have huge bandgaps, whereas semiconductors and conductors have minimal or no band gaps

II.11.1.9. Reduced density gradient (RDG) analysis

To understand the nature of chemical bonding inside molecules, computational chemists employ the Reduced Density Gradient (RDG) analytical method. It is frequently used in the study of quantum chemistry to comprehend the distribution of electrons in molecules as well as the types, strengths, and properties of covalent bonds, non-covalent interactions, such as hydrogen bonds and van der Waals interactions, and other bonding characteristics [27].

RDG analysis is based on a molecule's electron density, which is a key aspect of quantum chemistry. The probability distribution of electrons within a molecule is represented by the electron density, which is often estimated using quantum mechanical techniques like DFT. Maps with different colors are frequently used to display RDG analysis results. Different colors on these maps stand for various kinds of interactions. Regions denoting covalent connections, for instance, might be depicted in one color, while regions denoting non-covalent interactions, might be depicted in a different color.

II.11.1.10. Electron Localization Function (ELF) and Localized Orbital Locator (LOL) analyses

In computational chemistry, the electron distribution and localization in molecules are analyzed using the Localized Orbital Locator (LOL) and Electron Localization Function (ELF) principles and computations. These techniques shed light on the makeup of chemical bonds and the distribution of electron pairs inside molecules [28].

ELF is a mathematical function that quantifies how much an electron is localized within a molecule in a specific area of space. ELF's main objective is to locate and describe areas with significant electron localization. Understanding the nature of chemical bonding in

molecules with intricate electrical structures is made easier by this. High electron localization, reminiscent of traditional chemical bonding, is indicated by ELF values near 1. These areas are linked to lone pairs or strong covalent bonds. Conversely, ELF values near 0.5 indicate non-bonding or delocalized electron pairs. ELF is frequently utilized in molecular structure analysis because it offers a thorough comprehension of bonding patterns and the extent of electron localization or delocalization. A common visual representation of ELF data is an ELF map, in which various hues denote varying levels of electron localization. Usually, lower ELF regions are depicted in one hue and high ELF regions in another [29].

LOL is a technique developed to examine how much molecular orbitals are confined to particular areas of a molecule. LOL's main goal is to detect and measure the degree of orbital localization, which provides information about the makeup of chemical bonds and electron distribution.

II.11.1.11. Average localized ionization energy (ALIE)

The average energy needed to extract an electron from a certain area of a molecule is known as the average localized ionization energy. The energy required to remove an electron, or ionization energy, varies depending on the structure of a molecule. By determining the mean ionization energy for distinct areas inside a molecule, the average localized ionization energy can be used to understand the trends in electron removal across the molecular structure [30].

Quantum chemistry techniques like density functional theory and Hartree-Fock are used to calculate the average localized ionization energy while taking the molecule's electronic structure into account. This idea is useful for understanding and forecasting chemical reactivity since it may be used to pinpoint areas that are more likely to lose electrons. It is essential to conversations regarding reaction mechanisms, electron transfer processes, and a molecule's general behavior during chemical reactions. To sum up, the average localized ionization energy can be a valuable instrument in comprehending the subtle trends of electron removal in a molecule, which can provide insights into its behavior and reactivity in different chemical environments.

II.12. Molecular Dynamic Simulations (MDS)

A molecular system is represented by MDS as a group of interacting atoms or molecules. Potential energy functions, which can contain terms for bond stretching, angle bending, and non-bonded interactions (including van der Waals forces and electrostatic interactions), are commonly used to characterize the forces between these particles [31].

The positions and velocities of the particles in the system are predicted at each time step by numerically integrating Newton's equations of motion over short time increments. To imitate the behavior of the system over an extended length of time, this process is repeated. On the other hand In order to maintain the appropriate conditions throughout the simulation, MDS frequently includes temperature and pressure management algorithms, enabling the study of systems under certain thermodynamic ensembles.

Many scientific fields, including chemistry, biology, and materials research, have extensive uses for MDS. Phase transitions, chemical processes, protein folding, and the mechanical characteristics of materials are among the phenomena it is used to investigate.

II.13. Molecular docking

Molecular docking is a computer method that predicts the preferred orientation, binding affinity, and binding mode of two interacting molecules. It is applied in the fields of computational chemistry and molecular biology. It is especially useful for researching the relationship between a small ligand molecule and a bigger macromolecule, like a protein or nucleic acid. Predicting the most suitable spatial configuration for two molecules in order to create a stable complex is the purpose of molecular docking. Predicting how a medication molecule will connect to its target protein or comprehending how a ligand and receptor interact are examples of common applications [32].

In molecular docking, the ligand and the receptor are the two primary parts. Usually, the receptor is a bigger biomolecule like a protein or nucleic acid, while the ligand is a smaller molecule like a medication or substrate. Additionally, A score function is used in molecular docking to assess and prioritize various ligand binding orientations inside the receptor binding region. The scoring function assists in determining the most likely binding mode and predicts the binding affinity.

For the molecular docking analysis in this work, the iGEMDOCK application version 2.1 was utilized, and the Protein Data Bank (www.rcsb.org) was consulted to obtain the crystal structure of PDB ID:2CDU Based on the DFT calculation of the optimized structures of obtained hydrazones at the B3LYP functional and 6-311G (d,p) standard basis sets, a grid box of $30 \text{ \AA} \times 30 \text{ \AA} \times 30 \text{ \AA}$ was chosen to be located at the receptor's active site with the coordinates. The proteins were stripped of their water molecules, and H atoms were added. The ligand was then docked and adjusted. Furthermore, all complexes' interactions are visualized and examined using Accelry's Discovery Studio Visualizer.

II.13. PED analysis

A technique for examining the contributions of different vibrational modes to the total potential energy changes during a vibrational transition, like an infrared absorption event, is called potential energy distribution analysis, or PED analysis. The important vibrational modes involved in a certain infrared absorption are revealed by PED. It aids in comprehending a molecule's vibrational dynamics, particularly how various modes affect the total potential energy changes during a particular transition. PED analysis facilitates the identification of the primary vibrations accountable for the spectral patterns that have been noticed by measuring the contributions of various vibrational modes. In order to understand the molecular structure and behavior and to interpret experimental results, this can be very important. Applications of PED analysis can be found in many branches of chemistry, including the investigation of molecular structure, the study of reaction processes, and the comprehension of intermolecular interactions. It is especially helpful for determining how modifications to molecular environments affect particular vibrational modes [33]. In our work, the VEDA 4 program was used to estimate PED for each vibration mode in order to help the investigation of infra-red vibrations.

References

- [1] M. Santiago, S. Strobel, *Thin layer chromatography*, 1st ed., Elsevier Inc., 2013. <https://doi.org/10.1016/B978-0-12-420067-8.00024-6>.
- [2] I. V. Tetko, Y. Sushko, S. Novotarskyi, L. Patiny, I. Kondratov, A.E. Petrenko, L. Charochkina, A.M. Asiri, How accurately can we predict the melting points of drug-like compounds?, *J. Chem. Inf. Model.* 54 (2014) 3320–3329. <https://doi.org/10.1021/ci5005288>.
- [3] Fun Man Fung, *UV Vis spectroscopy - YouTube*, Natl. Univ. Singapore. (2004) 337–338. <https://doi.org/10.1007/b94239>.
- [4] G. Verma, M. Mishra, *Development and Optimization Of UV-Vis Spectroscopy - A Review*, *World J. Pharm. Res.* 7 (2018) 1170–1180. <https://doi.org/10.20959/wjpr201811-12333>.
- [5] C. Berthomieu, R. Hienerwadel, *Fourier transform infrared (FTIR) spectroscopy*, *Photosynth. Res.* 101 (2009) 157–170. <https://doi.org/10.1007/s11120-009-9439-x>.
- [6] K.C. Wong, *Review of NMR Spectroscopy: Basic Principles, Concepts and Applications in Chemistry*, *J. Chem. Educ.* 91 (2014) 1103–1104. <https://doi.org/10.1021/ed500324w>.

- [7] I.G. Munteanu, C. Apetrei, Analytical methods used in determining antioxidant activity: A review, *Int. J. Mol. Sci.* 22 (2021) 3380. <https://doi.org/10.3390/ijms22073380>.
- [8] M. Biela, J. Rimarčík, E. Senajová, A. Kleinová, E. Klein, Antioxidant action of deprotonated flavonoids: Thermodynamics of sequential proton-loss electron-transfer, *Phytochemistry*. 180 (2020). <https://doi.org/10.1016/j.phytochem.2020.112528>.
- [9] M. Najafi, K.H. Mood, M. Zahedi, E. Klein, DFT/B3LYP study of the substituent effect on the reaction enthalpies of the individual steps of single electron transfer-proton transfer and sequential proton loss electron transfer mechanisms of chroman derivatives antioxidant action, *Comput. Theor. Chem.* 969 (2011) 1–12. <https://doi.org/10.1016/j.comptc.2011.05.006>.
- [10] J.N. Murray, Electrochemical test methods for evaluating organic coatings on metals: An update. Part I. Introduction and generalities regarding electrochemical testing of organic coatings, *Prog. Org. Coatings*. 30 (1997) 225–233. [https://doi.org/10.1016/S0300-9440\(96\)00677-7](https://doi.org/10.1016/S0300-9440(96)00677-7).
- [11] Y. Zou, J. Wang, Y.Y. Zheng, Electrochemical techniques for determining corrosion rate of rusted steel in seawater, *Corros. Sci.* 53 (2011) 208–216. <https://doi.org/10.1016/j.corsci.2010.09.011>.
- [12] H.S. Magar, R.Y.A. Hassan, A. Mulchandani, Electrochemical impedance spectroscopy (Eis): Principles, construction, and biosensing applications, *Sensors*. 21 (2021). <https://doi.org/10.3390/s21196578>.
- [13] S.K. Roy, *Corrosion Rates From Polarization Resistance Measurements.*, (1981).
- [14] A. Trache, G.A. Meininger, Atomic force microscopy (AFM), *Curr. Protoc. Microbiol.* (2008) 1–17. <https://doi.org/10.1002/9780471729259.mc02c02s8>.
- [15] K.S. Thanthiriwatte, E.G. Hohenstein, L.A. Burns, C.D. Sherrill, Assessment of the performance of DFT and DFT-D methods for describing distance dependence of hydrogen-bonded interactions, *J. Chem. Theory Comput.* 7 (2011) 88–96.
- [16] L. Türker, T. Atalar, S. Gümüş, Y. Çamur, A DFT study on nitrotriazines, *J. Hazard. Mater.* 167 (2009) 440–448. <https://doi.org/10.1016/j.jhazmat.2008.12.134>.
- [17] I. V. Solovyev, Combining DFT and many-body methods to understand correlated materials, *J. Phys. Condens. Matter.* 20 (2008). <https://doi.org/10.1088/0953-8984/20/29/293201>.
- [18] P.I. Djurovich, E.I. Mayo, S.R. Forrest, M.E. Thompson, Measurement of the lowest unoccupied molecular orbital energies of molecular organic semiconductors, *Org.*

- Electron. 10 (2009) 515–520. <https://doi.org/10.1016/j.orgel.2008.12.011>.
- [19] R.P. Iczkowski, J.L. Margrave, Electronegativity, *J. Am. Chem. Soc.* 83 (1961) 3547–3551. <https://doi.org/10.1021/ja01478a001>.
- [20] G. Reiser, K. Müller-Dethlefs, Rotationally resolved zero kinetic energy photoelectron spectroscopy of nitric oxide, *J. Phys. Chem.* 96 (1992) 9–12. <https://doi.org/10.1021/j100180a004>.
- [21] D.W. Niles, G. Margaritondo, Heterojunctions: Definite breakdown of the electron affinity rule, *Phys. Rev. B.* 34 (1986) 2923.
- [22] P. Pérez, L.R. Domingo, A. Aizman, R. Contreras, The electrophilicity index in organic chemistry in: *Theoretical Aspects of Chemical Reactivity, Theor. Asp. Chem. React.* 19 (2007) 139–201.
- [23] J.L. Gázquez, Hardness and softness in density functional theory, *Chem. Hardness.* 80 (2006) 27–43. <https://doi.org/10.1007/bfb0036798>.
- [24] A. Toro-Labbé, Characterization of chemical reactions from the profiles of energy, chemical potential, and hardness, *J. Phys. Chem. A.* 103 (1999) 4398–4403. <https://doi.org/10.1021/jp984187g>.
- [25] D.S. Kosov, P.L.A. Popelier, Atomic partitioning of molecular electrostatic potentials, *J. Phys. Chem. A.* 104 (2000) 7339–7345. <https://doi.org/10.1021/jp0003407>.
- [26] S.K. O’Leary, An analytical density of states and joint density of states analysis of amorphous semiconductors, *J. Appl. Phys.* 96 (2004) 3680–3686. <https://doi.org/10.1063/1.1778478>.
- [27] S. Khan, H. Sajid, K. Ayub, T. Mahmood, Adsorption behaviour of chronic blistering agents on graphdiyne; excellent correlation among SAPT, reduced density gradient (RDG) and QTAIM analyses, *J. Mol. Liq.* 316 (2020) 113860. <https://doi.org/10.1016/j.molliq.2020.113860>.
- [28] K. Rajalakshmi, M. Vetrivel, NBO and Topology (MESP, ELF, LOL) Analysis of 2-Hydroxypropanamide, *Int. J. Adv. Sci. Res. Eng. Trends.* 5 (2020) 50–58.
- [29] D. Shilpa, K. Sadasivam, M. Thirumoorthy, Topology analysis of six phytochemicals through ELF and LOL basins – A DFT study, *Indian J. Chem.* 62 (2023) 1171–1177. <https://doi.org/10.56042/ijc.v62i11.2900>.
- [30] P. Politzer, J.S. Murray, F.A. Bulat, Average local ionization energy: A review, *J. Mol. Model.* 16 (2010) 1731–1742. <https://doi.org/10.1007/s00894-010-0709-5>.
- [31] C. Chen, J. Wan, W. Li, Y. Song, Water contact angles on quartz surfaces under supercritical CO₂ sequestration conditions: Experimental and molecular dynamics

- simulation studies, *Int. J. Greenh. Gas Control.* 42 (2015) 655–665. <https://doi.org/10.1016/j.ijggc.2015.09.019>.
- [32] S. Agarwal, R. Mehrotra, Mini Review_ An overview of Molecular Docking, *JSM Chem.* 4 (2016) 1024–1028. https://www.researchgate.net/profile/Shweta-Agarwal-7/publication/303897563_Mini_Review_An_overview_of_Molecular_Docking/links/575b9fb108aed884620da00a/Mini-Review-An-overview-of-Molecular-Docking.pdf.
- [33] V. Darugar, M. Vakili, S.F. Tayyari, F.S. Kamounah, Validation of potential energy distribution by VEDA in vibrational assignment some of β -diketones; comparison of theoretical predictions and experimental vibration shifts upon deuteration, *J. Mol. Graph. Model.* 107 (2021) 107976. <https://doi.org/10.1016/j.jmgm.2021.107976>.

Chapter III : Synthesis and characterization

In this chapter, we present the synthesis of four hydrazone derivatives. The two hydrazines, 4-methylphenylhydrazine and phenylhydrazine, are the starting ingredients for the synthesis. Moreover, different aldehydes and benzoic acid are used to create the desired hydrazones. The synthesis process is based on a previously published method that has been recorded in the body of current literature. Benzoic acid and other aldehydes react with hydrazines in a reaction that elucidates the synthesis process. It is through this chemical mechanism that derivatives of hydrazone are formed. The variety of the created hydrazones is enhanced by the selection of aldehydes, which enables the synthesis of unique molecules with a range of chemical characteristics. After synthesis, spectroscopic methods are used to characterize the resulting hydrazone derivatives. These analytical techniques, like spectroscopy, attempt to clarify and validate the synthetic substances' chemical structure. Spectroscopic examination offers significant insight of the hydrazone derivatives' molecular structure, bond forms, and general structural characteristics. Understanding the hydrazones' chemical characteristics and confirming the viability of the production route depend heavily on spectroscopic characterization.

III.1. Organic synthesis procedure of the hydrazones

III.1.1. 4-[(2E)-2-(2-nitrobenzylidene)hydrazinyl] benzoic acid (NBHZ)

NBHZ was synthesized by condensation of equimolar amounts of 4-phenylhydrazinylbenzoic acid (1 mmol, 0.152 mg) and 2 nitrobenzaldehyde (1 mmol, 0.151 mg) under ethanol reflux at 75 °C for 6 h (Figure III. 1). Filtered, then rinsed with ethanol and allowed to dry in the air after the brown precipitate had formed. On Merck silica gel plates, the reaction was tracked using thin layer chromatography (TLC) and the stain could be observed with UV light. Afterwards, the obtained product was characterized via characterization techniques.

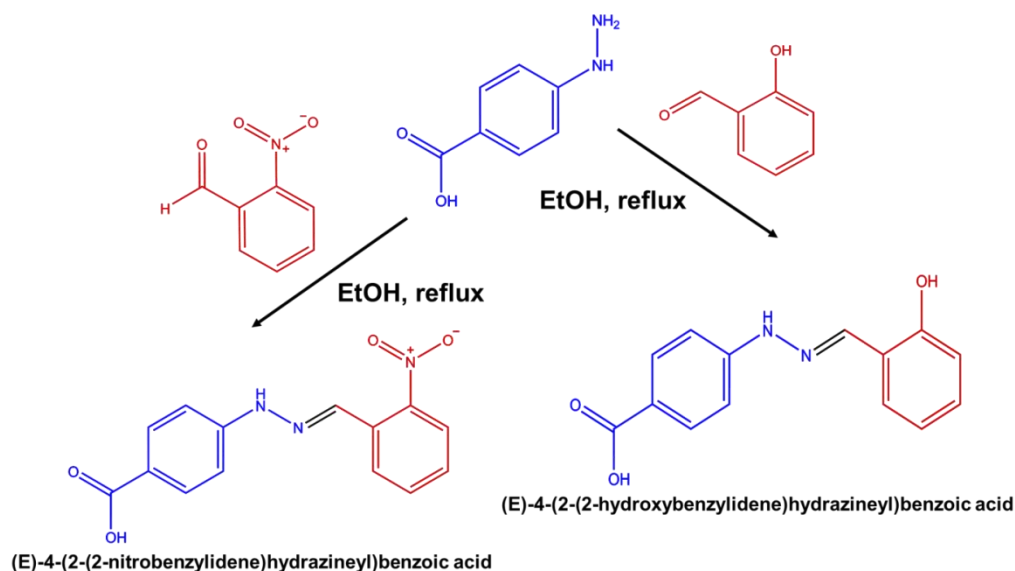


Figure III. 1: Reaction scheme of the studied hydrazones NBHZ and HBHZ.

Yield: 70%, **Melting point** 267.1 °C, **Color:** brown ; **MW**=285.25 g/mol , **UV-Vis(ethanol):** λ_{max} (nm): 205 (π - π^*), 276.47 (π - π^*), 299 (n - π^*), 388 nm (n - π^*); **IR (solid state) ν_x (cm^{-1}):** $\nu_{\text{O-H}}$ (3613) , $\nu_{\text{N-H}}$ (3301), $\nu_{\text{C-HArom}}$ (3079), $\nu_{\text{C-HAliph}}$ (2981), $\nu_{\text{C=O}}$ (1684), $\nu_{\text{C=N}}$ (1604), $\nu_{\text{N-N}}$ (1159); **$^1\text{H NMR}$ (400 MHz, DMSO- d_6), δ (ppm):** 7,15 (d, 2H, $J=12$ Hz), 7,55 (t, 1H, $J=8$ Hz), 7,75 (t, 1H, $J=8$ Hz), 7,86 (d, 2H, $J=12$ Hz), 8,01 (d, 1H, $J=8$ Hz), 8,19 (d, 1H, $J=8$ Hz), 8,35 (s, 1H), 11,27 (s, 1H, -NH) 12,38 (s, 1H, OH); ; **$^{13}\text{C NMR}$ (75 MHz, DMSO- d_6), δ (ppm):**112.19 (C3,C5), 121.9 (C1) ;125.06 (C1'), 127.8 (C3'), 129.3 (C5'), 129.8 (C6'), 131.6 (C2, C6),133.7 (C4'), 133.9 (C=N), 147.64 (C2'), 148.4 (C4), 167.6 (COOH)..

III.2.2. 4-[(2E)-2-(2-hydroxybenzylidene) hydrazinyl] benzoic acid (HBHZ)

Likewise, HBHZ was generated using the ex-precEDURE mixing equimolar amounts of 4-phehydrazinylbenzoic acid (1 mmol, 0.152 mg) and 2 hydroxybenzaldehyde (1 mmol, 0.122 mg) under ethanol reflux at 75 °C (Figure III.1) after three hours a yellow precipitate had formed. Thin layer chromatography (TLC) to follow the reaction On Merck silica gel plates. Afterwards, the obtained product was characterized via physicochemical techniques.

Yield: 58%, **Melting point** 280°C, **Color:** yellowish, **MW**=256g/mol ; **UV-Vis(ethanol):** λ_{max} (nm): 205 (π - π^*), 234 (π - π^*), 354 nm (n - π^*); **IR (solid state) ν_x (cm^{-1}):** $\nu_{\text{O-H}}$ (3609) , $\nu_{\text{N-H}}$ (3262), $\nu_{\text{C-HArom}}$ (3057), $\nu_{\text{C-HAliph}}$ (2991), $\nu_{\text{C=O}}$ (1668), $\nu_{\text{C=N}}$ (1593), $\nu_{\text{N-N}}$ (1146); **$^1\text{H NMR}$ (400 MHz, DMSO- d_6),**

$\delta(\text{ppm})$: 6,86-6,92 (m, 2H), 7,05 (dl, 2H, $J=8$ Hz), 7,21 (td, 1H, $J=4$; 8 Hz), 7,66 (dd, 1H, $J=2$; 8Hz), 7,86 (d, 2H, $J=12$ Hz), 8,27 (s, 1H), 10.30 (s, 1H, OH), 10.85 (s, 1H, NH), 12.32 (s, 1H, COOH);

; ^{13}C NMR (75 MHz, DMSO- d_6), $\delta(\text{ppm})$: 111.41 (C3, C5), 116.46 (C3'), 119.82 (C1), 120.82 (C5'), 121,0 (C6'); 127.31 (C1'), 130.28 (C4'), 131.79 (C2, C6), 138.85 (C=N), 148.2 (C4), 156.2 (C2'), 167.3 (COOH).

III.3.3. {(2E)-2-[(2-hydroxynaphthalen-1-yl)methylidene]hydrazinyl}benzoic HHZB

HHZB is a hydrazone with molecular formula $\text{C}_{18}\text{H}_{14}\text{N}_2\text{O}_3$ was synthesized by condensation equimolar amounts of '4-phhydrazinylbenzoic acid' (1 mmol, 0.152 mg) and '2 hydroxy-1-naphthaldehyde' (1 mmol, 0.172 mg) After being heated under Methanol reflux at a temperature of 64°C for 12 hours, the resulting reaction was intense. Once cooled, the solid yellow precipitate was formed and filtered, as shown in Figure III.2. The resulting product was thoroughly washed with MeOH and dried. The final product, 4-[(2E)-2-[(2-hydroxynaphthalen-1-yl)methylidene]hydrazinyl]benzoic acid HHZB was obtained with a yield of 71%. The progress of the reaction was monitored using TLC analysis. Following the reaction, the resulting product underwent characterization using various techniques. The hydrazone compound that was obtained demonstrated solubility in a wide range of organic solvents, including ethanol, THF, DMF, DMSO and acetone.

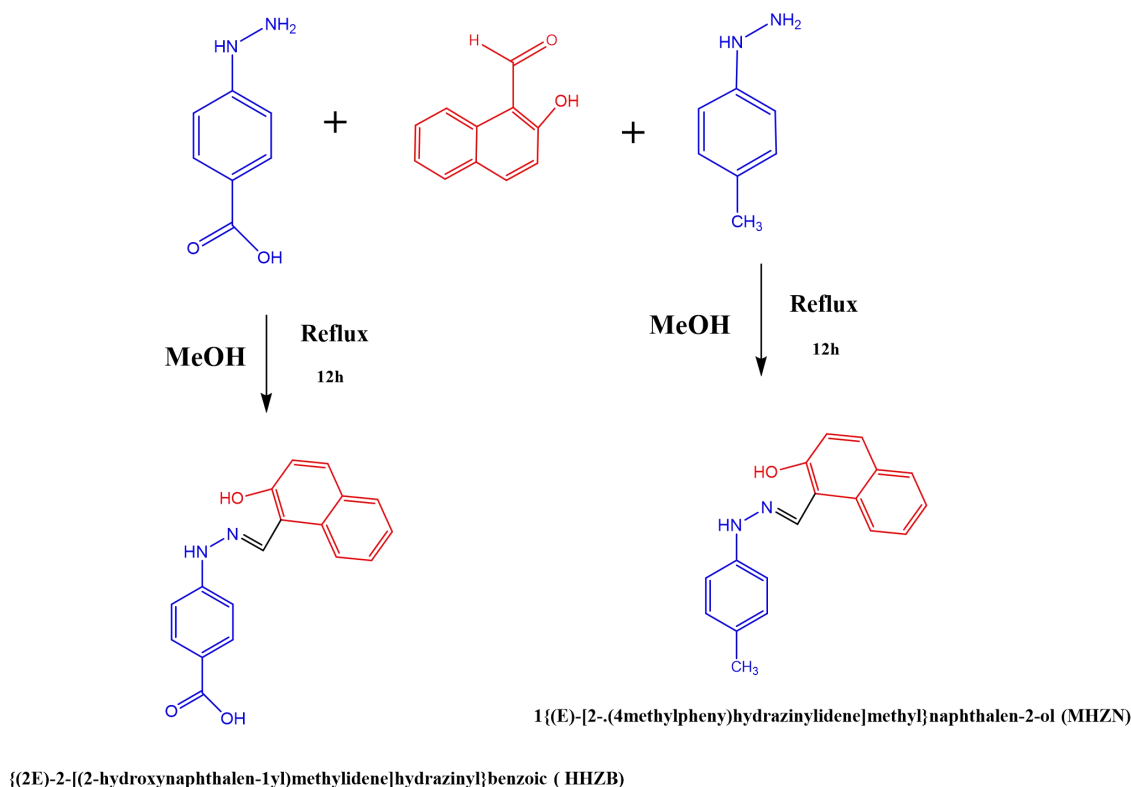


Figure III. 2: Reaction scheme of the studied hydrazones HHZB and MHZN.

HHZB. Yield: 71%, **Melting point** 275°C, **Color:** yellow mustard; **UV-Vis(Ethanol):** λ_{max} (nm): 205 π - π^* 250 π - π^* 324 (n- π^*) 337 (n- π^*) 385 nm n- π^* 402 nm n- π^* **IR (solid state) ν_x (cm^{-1}):** $\nu_{\text{O-H}}$ 3666, $\nu_{\text{N-H}}$ 3272, $\nu_{\text{C-H arom}}$ 2977, $\nu_{\text{C=O}}$ 1675, $\nu_{\text{C=N}}$ 1604, $\nu_{\text{N-N}}$ 1159, $\nu_{\text{C-O}}$ 1056 **$^1\text{H NMR}$ (300 MHz, CDCl_3 Chloroform), δ (ppm),** 7.06 (d, 2H, $J=8\text{Hz}$), 7.24 (d, 1H, $J=8\text{Hz}$), 7.39 (td, 1H, $J=2$; 8Hz), 7.60 (td, 2H, $J=4$; 8Hz), 7.86-7.92 (m, 4H), 8.54 (dl, 1H, $J=8\text{Hz}$), 8.99 (s, 1H, CH=N), 10.97 (s, 1H, COOH), 11.53 (s, 1H, NH), 12.33 (s, 1H, OH) **$^{13}\text{C NMR}$ (300 MHz, CDCl_3 Chloroform), δ (ppm):** 110.7(C1'), 111.3(C2,C6), 118.8(C8'), 121.1(C3'), 122.5(C6'), 123.9(C7'), 127.9(C4'), 128.6(C4a), 129.3(C5'), 131.5(C3,C5), 131.6(C8a), 131.9(C4), 139.8(C1), 148.4 (C=N), 156.4(C2') 167.7 (COOH).

III.3.4. 1{(E)-[2-(4methylphenyl)hydrazinylidene]methyl}naphthalen-2-ol (MHZN)

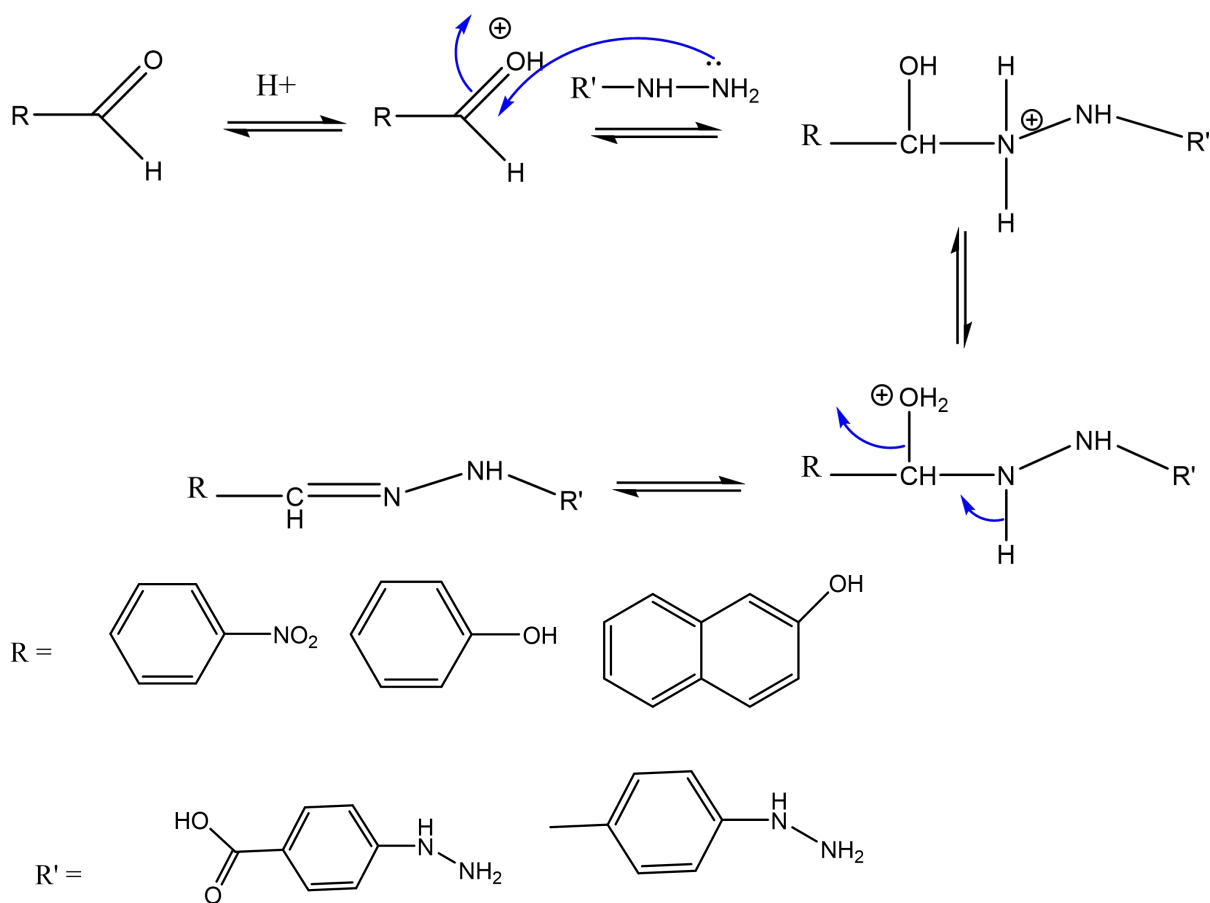
The studied hydrazone derivative, namely 1{(E)-[2-(4methylphenyl)hydrazinylidene]methyl}naphthalen-2-ol (MHZN) with molecular formula $\text{C}_{18}\text{H}_{16}\text{N}_2\text{O}$ was synthesized by condensation equimolar amounts of '4p-tolyhydrazine' (1 mmol, 0.158 mg) and '2 hydroxy-1-

naphtaldehyde (1 mmol, 0.172 mg).the reaction was heated under Methanol reflux at 65 °C for 12 h. Figure III.2 .After cooling, The formed yellow precipitate(solid) was filtered, washed with methanol and finally exposed to the air to dry in order to obtain 74% of MHZN. The reaction was monitored using thin layer chromatography (TLC) on Merck silica gel plates and the spots were visualized by UV light. Afterwards, the obtained product was characterized via characterization techniques the obtained hydrazone is soluble in most organic solvent such as ethanol, THF, DMF, DMSO and acetone.

MHZN.Yield: 74%, Melting point 190°C , Color: yellow ; UV-Vis(ethanol) λ_{\max} (nm): 205 π - π^* 254 π - π^* 336 (n- π^*) 383 nm (n- π^*); **IR (solid state) ν_x (cm⁻¹):** $\nu_{\text{O-H}}$ 3671 , $\nu_{\text{N-H}}$ 3318 , $\nu_{\text{C-HArom}}$ 2981 , $\nu_{\text{C-HAliph}}$ 2898, $\nu_{\text{C=N}}$ 1608 , $\nu_{\text{N-N}}$ 1145, **¹H NMR (300 MHz,CDCl₃Chloroform), δ (ppm):** 2.34 (s,3H, CH₃), 6.97(dl,2H, $J=6$ HZ), 7.15(dl,2H, $J=9$ HZ),. 7.27(dl,1H, $J=3$; 9 HZ), 7.38(td,1H, $J=3$; 6 HZ), 7.49-7.52(m, 2H), 7.75(d,2H, $J=9$ HZ), 7.81(d,1H, $J=9$ HZ), 8.0(d,1H, $J=9$ HZ), 8.71 (s, 1H , -NH), 12.15 (s, 1H, -OH) **¹³C NMR (300 MHz,CDCl₃Chloroform), δ (ppm)**20,6(CH₃), 109,1(C1), 112.1(C2',C6'), 118,9(C8), 119,9(C3), 123,3(C6), 127 (C7), 128,4 (C4), 129,1 (C5), 130,1 (C3', C5'), 130,4 (C4a), 131,0 (C4'), 131,4 (C8a), 137,4 (C1'), 141.4 (C=N), 156,8 (C2).

III.4. Proposed reaction mechanism

According to the suggested reaction mechanism for hydrazones, an intermediate hydrazone compound is formed when a hydrazine and a carbonyl group are added nucleophilically. A tetrahedral intermediate is formed as a result of the nitrogen atom in hydrazine's nucleophilic attack on an aldehyde or ketone's carbonyl carbon at the beginning of the reaction. The hydrazone structure is characterized by the formation of a C=N double bond, which results from the intermediate's proton transfer and water elimination. Usually, an acid catalyzes the reaction, which increases the carbonyl group's electrophilicity and speeds up the reaction process.



III.2. Physical and chemical properties of the obtained hydrazones

The experiment produced hydrazones with unique chemical and physical characteristics Table III.1. These compounds' physical properties, which varied in terms of solubility (Tables III.2, 3, 4 and 5) and color offered important clues about their general properties. Important details regarding the stability and purity of the hydrazones were provided by the observed melting points.

Table III. 1: Chemical and physical properties of the synthesized hydrazones.

Hydrazone	formula	Molecular Weight	Melting point	R_f (dichloromethane+ethyl acetate)	Color	Yield (%)	Structure

NBHZ	C₁₄H₁₁N₃O₄	285.25 g/mol	267.1 °C	0.7	brown	70.00	
HBHZ	C₁₄H₁₂N₂O₃	256.25g/mol	280°C	0.60	yellowish	58.00	
HHZB	C₁₈H₁₄N₂O₃	306.31 g/mol	275 °C	0.52	Yellow mustard	71.00	
MHZN	C₁₈H₁₆N₂O	276.33g/mol	190°C	0.92	Yellowish	74.00	

It can be observed that depending on which particular aldehydes are used in their production, these hydrazones display a variety of structural and functional properties. The hydrazones' yield highlights the effectiveness of the reaction conditions and the accuracy with which the chemical transformations were controlled. The four synthesized hydrazones' melting points were determined, and the results demonstrated significant differences from the corresponding starting materials, highlighting the transformational effect of the hydrazone synthesis process. Interestingly, one of these hydrazones had a melting point that was noticeably lower than the initial materials. The presence of a methyl group during synthesis may be the cause of this interesting variation, which modifies the compound's overall

molecular structure and physical characteristics. The compound's packing arrangement or intermolecular forces may have changed as a result of the additional methyl group's impact on molecular geometry, as shown by the compound's decreased melting point. This result raises additional questions about the subtle effects of hydrazone derivatives. On the other hand, The retention factor R_f was obtained by deviding hydrazone's distance traveled over the solvent's distance traveled the obtained results indicating HHZB is the most polar one among the four hydrazoes with retention factor $R_f=0.52$

Table III. 2: Solubility test of NBHZ.

Solubility Degree	unsolube	Slightly soluble	Soluble	unsolube	Slightly soluble	Soluble
Solvent	Cold			Warm		
Ethanol			+			+
Methanol			+			+
DMSO			+			+
DMF			+			+
Acetone			+			+
Acetonitrile		+				+
THF			+			+
Dichloromethane		+				+
Acetate ethyle		+				+
Water	+			+		
Chloroform		+			+	
Ether petrolum		+			+	
Ether diethylic		+			+	

Table III. 3: Solubility test of HBHZ.

Solubility Degree	unsolube	Slightly soluble	Soluble	unsolube	Slightly soluble	Soluble
Solvent	Cold			Warm		
Ethanol			+			+
Methanol			+			+
DMSO			+			+
DMF			+			+
Acetone			+			+
Acetonitrile		+				+
THF			+			+
Dichloromethane		+				+

Acetate ethyle		+				+
Water	+			+		
Chloroform		+			+	
Ether petrolum		+			+	
Ether diethylic		+			+	

Table III. 4: Solubility test of HHZB.

Solubility Degree	unsolube	Slightly soluble	Soluble	unsolube	Slightly soluble	Soluble
Solvent	Cold			Warm		
Ethanol			+			+
Methanol			+			+
DMSO			+			+
DMF			+			+
Acetone			+			+
Acetonitrile		+				+
THF			+			+
Dichloromethane		+				+
Acetate ethyle		+				+
Water	+			+		
Chloroform		+			+	
Ether petrolum		+			+	
Ether diethylic		+			+	

Table III. 5: Solubility test of MHZN.

Solubility Degree	unsolube	Slightly soluble	Soluble	unsolube	Slightly soluble	Soluble
Solvent	Cold			Warm		
Ethanol			+			+
Methanol			+			+
DMSO			+			+
DMF			+			+
Acetone			+			+
Acetonitrile			+			+
THF			+			+
Dichloromethane			+			+

Acetate ethyle			+			+
Water			+			+
Chloroform			+			
Ether petrolum		+			+	
Ether diethylic		+			+	

Different solvents were used to properly evaluate the solubility of each hydrazone, and the results were quite interesting. These hydrazones showed a remarkable level of solubility in almost all solvents that were tested, indicating their adaptability and possible use in a variety of chemical situations. One noteworthy exception did, however, show that they were only insoluble in water. The particular chemical characteristics of hydrazones may be responsible for their distinctive behavior in aqueous environments. This highlights the significance of comprehending hydrazone solubility characteristics for efficient use in various applications.

III.3. Spectroscopy analyses

The hydrazones that were synthesized underwent thorough spectroscopic examinations, such as UV-Vis, NMR, and FTIR, in order to shed light on their molecular structure and offer comprehensive understanding of their chemical structure. The electronic transitions within the compounds were investigated using UV-Vis spectroscopy, which provided insights into the conjugation and aromaticity of the hydrazones. By examining the vibrational modes of chemical bonds, FTIR spectroscopy was essential in the identification of functional groups. The FTIR spectra included peaks that corresponded to distinctive functional groups, which provided additional evidence of the effective synthesis of hydrazones. The NMR spectra, particularly the carbon 13 and proton NMR spectra, provided important information about the atom-by-atom arrangements inside the molecules, confirming the formation of hydrazones. Collectively, these spectroscopic approaches gave a thorough understanding of the molecular structure of the derived hydrazones, permitting precise characterization and opening the way for possible applications in diverse scientific and industrial contexts.

III.3.1 UV- Vis Spectroscopy

The experimental UV-Vis spectrums of both hydrazones were obtained in ethanol solvent at room temperature (Figure III.3). It is noticeable that in experimental spectrum NBHZ the appearance of five bands in ultraviolet range whereas three characteristic bands in the theoretical one. The experimental spectrum exhibits a band at 205 and 225 nm which are referred to π - π^* transitions usually

appear in unsaturated compounds resulting of C=C aromatic ring group which caused by the electron transition from π bonding orbitals to π^* anti-bonding orbitals. In return, the $n-\pi^*$ electronic transitions are caused by the existence of heteroatoms O and N that are in the molecular structure of NBHZ. Therefore, the band situated in 275 nm in experimental is related to the $n-\pi^*$ electronic transition which may be produced by the C=N in which electrons transfer from n nonbonding to π anti-bonding orbitals. Also, for the bands that appear at 346.37,386 nm is attributed to $n-\pi^*$ which may be induced by C=O carbonyl group.

The HBHZ experimental spectrum depicts three characteristic bands between 200-400nm range 205 ,233, 351.7 nm related to presence also $\pi-\pi^*$ $n-\pi^*$ electronic transitions resulting of C=C aromatic ring group and existence of heteroatoms O and N that are in the molecular (OH, C=N and C=O) structure of HBHZ.

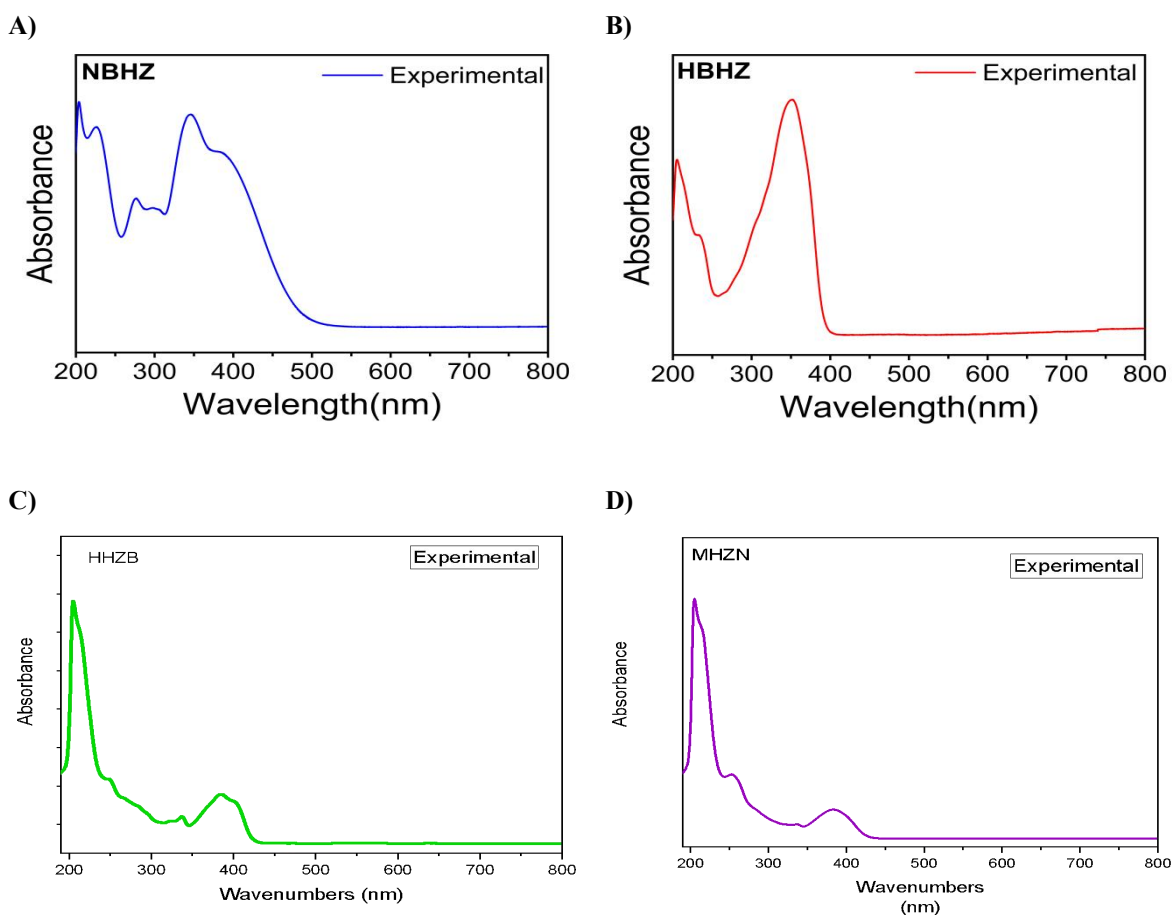


Figure III. 3: UV-Vis spectrums of obtained hydrazones A) NBHZ, B) HBHZ, C) HHZB, and D) MHZN.

The experimental UV-Vis spectrum exhibits a band with almost the same values at 205 nm , 254 nm for HHZB and 205 nm , 250 nm for MHZN which are referred to π - π^* transitions usually appear in unsaturated compound resulting of C=C aromatic ring group which caused by the electron transition from π bonding orbitals to π^* antibonding orbitals. In return the n - π^* electronic transitions are caused by the existence of heteroatoms O, N that are in the molecular structure of both hydrazones Therefore, The bands situated in 336 nm for HHZB and 337 nm for MHZN are related to n - π^* electronic transition which may be induced by OH of aldehyde part in which electrons transfer from n nonbonding to π antibonding orbitals. On the other hand the appeared band in MHZN spectrum located at 324 nm is related to OH of carboxylic group, also for the band that appears in both spectrum at 383 nm is attributed to n - π^* which may be produced by C=N group. Whereas the neighboring band 402 nm is may assigned to carbonyl group n - π^* electronic transition.

III.3.2 FT-IR Spectroscopy

The FTIR spectrum underwent extensive examination, which produced a detailed and nuanced study that produced a number of perceptive interpretations. Careful analysis has allowed us to match certain peaks and troughs in the spectrum with particular vibrational modes of the chemical bonds in the produced hydrazones. The identification and confirmation of important functional groups contained in the molecules has been made possible by this rigorous examination.

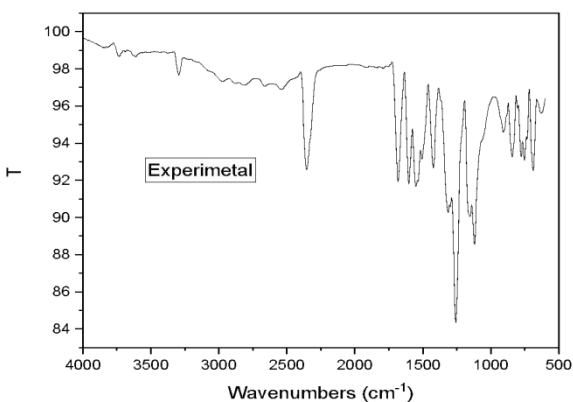
III.3.2.1. NBHZ and HBHZ FT-IR spectrums

- The peak positions in the NBHZ and HBHZ spectrums, 3613 cm^{-1} and 3628 cm^{-1} , respectively, are ascribed to stretching vibrations of the OH. It is widely known that N-H vibrations can readily manifest as abrupt peaks in one band amine secondary between 3100 and 3500 cm^{-1} at higher wavenumbers in the infrared spectrum. Consequently, the peak observed at 3301 cm^{-1} is attributed to the stretching vibration of the N-H secondary amine group of NBHZ; the peak for HBHZ was observed at 3262 cm^{-1} in the spectrum.,
- Stretching vibrations of C=N of hydrazones are typically detected in the 1500 cm^{-1} to 1700 cm^{-1} range. Thus, it can be seen that C=N vibration stretching is responsible for the distinctive peaks at 1604 cm^{-1} for NBHZ and 1593 cm^{-1} for HBNH.
- Hydrazones' stretching vibrations of C=N are usually observed in the 1500 – 1700 cm^{-1} range. Therefore, it is evident that the characteristic peaks at 1604 cm^{-1} for NBHZ and 1593 cm^{-1} for

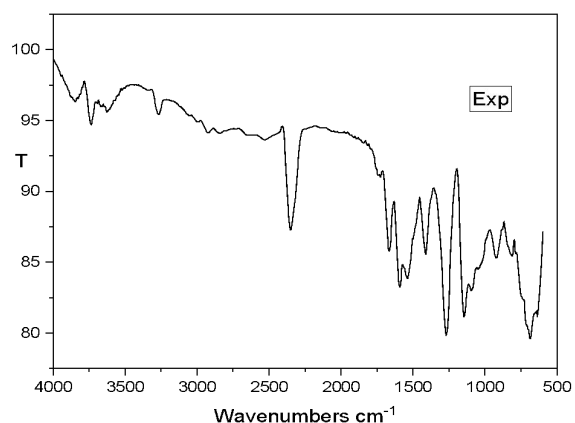
HBNH are caused by C=N vibration stretching. The N–N stretching vibration of the azomethine group for both hydrazones are appeared at 1159 cm^{-1} for NBHZ and 1143 cm^{-1} for HBHZ.

- The nitro group is easy to identify since its distinctive group frequencies may be identified mostly independently of the remainder of the molecule. The NO_2 group has stretching vibrations that are asymmetric (range: $1570\text{--}1485\text{ cm}^{-1}$) and symmetric (range: $1370\text{--}1320\text{ cm}^{-1}$). As a result, the peak at 1506 cm^{-1} is caused by the NO_2 group's asymmetric stretching vibrations. The NO_2 group's symmetric stretching vibration is at 1315 cm^{-1} .
- The C=C stretching vibrations usually ranging from 1625 to 1430 cm^{-1} . In this present study, the C=C stretching vibrations are found at 1546 cm^{-1} and 1423 cm^{-1} in both synthesized hydrazones FT-IR spectrums. The aromatic ring's C-C stretching vibration modes are usually found in the $1380\text{--}1280\text{ cm}^{-1}$ range. Therefore, the C-C stretching vibration may be responsible for the peak that appears at 1295 cm^{-1} for NBHZ and 1268 cm^{-1} for HBHZ. Additionally, the region between 2850 and 3100 cm^{-1} which corresponds to the C-H stretching vibrations, is attributed to either aromatic or aliphatic stretching vibration modes. The analysis of the recorded FT-IR spectrum revealed that the aromatic C-H asymmetric and symmetric stretching vibrations for NBHZ emerge as peaks at 3174 and 3079 cm^{-1} , while the hydrazone for HBHZ was discovered at 3057 cm^{-1} .

A)



B)



C)

D)

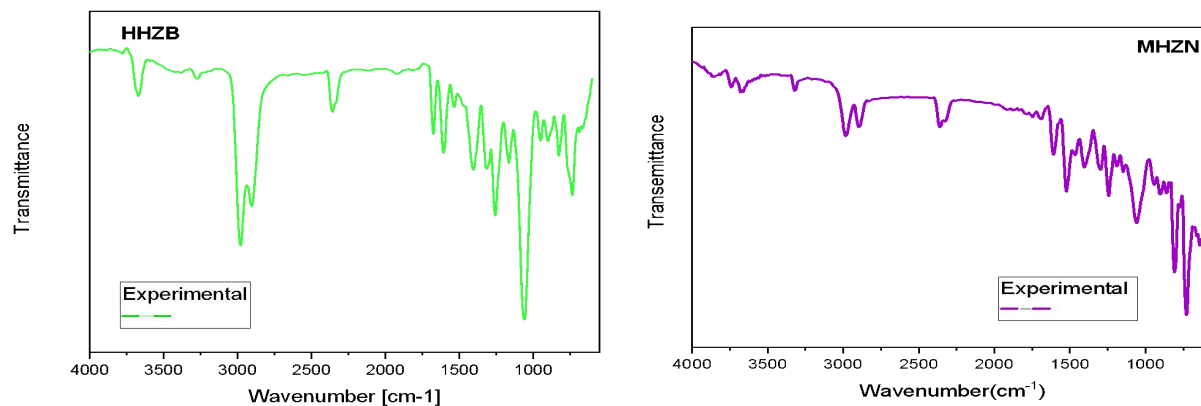


Figure III. 4: UV-Vis spectrums of obtained hydrazones: A) NBHZ, B) HBHZ, C) HHZB, and D) MHZN.

III.3.2.2. MHZN and HHZB FT-IR spectrums

After a thorough analysis of both hydrazones' FT IR spectra, the following findings were drawn: The peaks that appeared at 3207 cm^{-1} in the MHZN and 3675 cm^{-1} in the HHZB spectrums are caused by O-H stretching vibrations. It is well known that at higher wavenumbers in the infrared spectrum, N-H vibrations can easily appear as sharp peaks in one band amine secondary between 3100 and 3500 cm^{-1} . The peak observed at 3312 cm^{-1} can thus be attributed to the N-H secondary amine group stretching vibration of MHZN; HHZB was observed at 3376 cm^{-1} in the spectra. Hydrazones' stretching vibrations of C=N are usually observed in the 1500 – 1700 cm^{-1} range. Therefore, it is clear that C=N vibration stretching is responsible for the characteristic peaks at 1604 cm^{-1} for MHZN and 1593 cm^{-1} for HHZB. Moreover, the aliphatic stretching vibration is clearly observable at 2984 cm^{-1} for MHZN and 2981 cm^{-1} for HHZB. For every one of them. In addition, for both hydrazones, the azomethine group's N–N stretching vibration can be seen at 1184 cm^{-1} for MHZN and 1159 cm^{-1} for HHZB.

The C=C stretching vibrations have a typical range of 1625 – 1430 cm^{-1} . In these hydrazones, the C=C stretching vibrations are found at 1509 cm^{-1} for HHZB and 1519 cm^{-1} for MHZN. The C-C stretching vibration modes of the aromatic ring usually take place in the 1380 – 1280 cm^{-1} range. As a result, the C-C stretching vibration can be responsible for the peak that developed at 1291 cm^{-1} for MHZN and 1255 cm^{-1} for HBHZ.

Moreover, they designate the range between 2850 and 3100 cm^{-1} which corresponds to the C-H stretching vibrations, as either aromatic or aliphatic stretching vibration modes. The FT-IR spectrum analysis demonstrated that the HBHZ hydrazone peak was located at 3010 cm^{-1} , whereas the aromatic

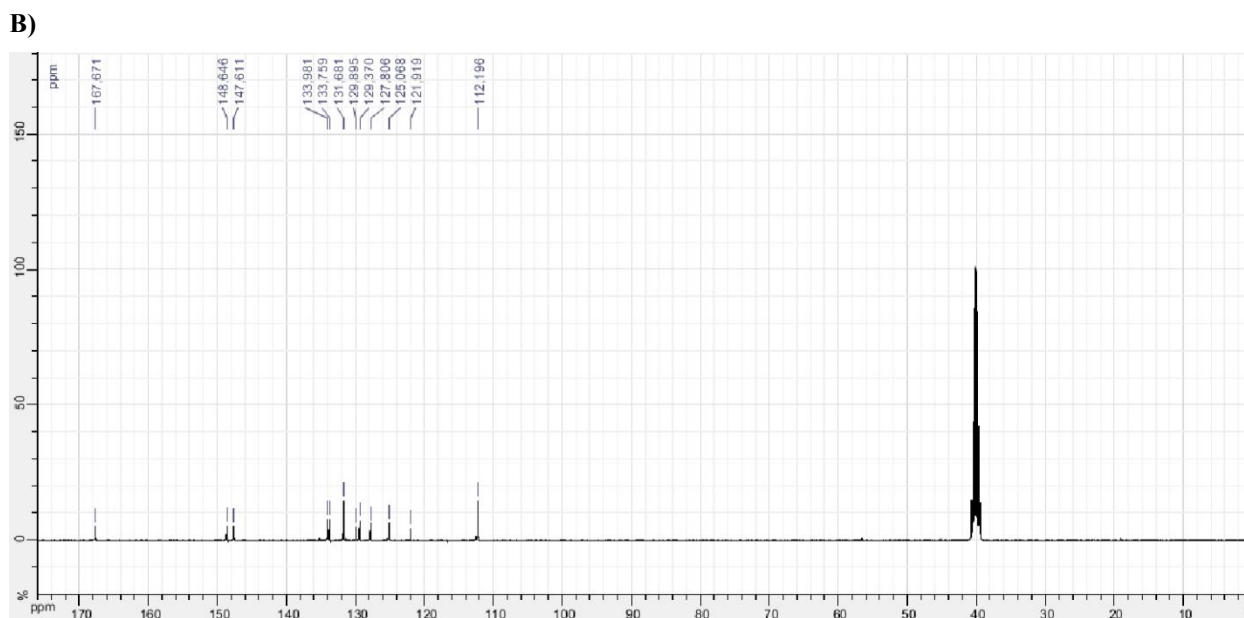


Figure III. 5: A) ^1H and B) ^{13}C NMR spectrums of NBHZ.

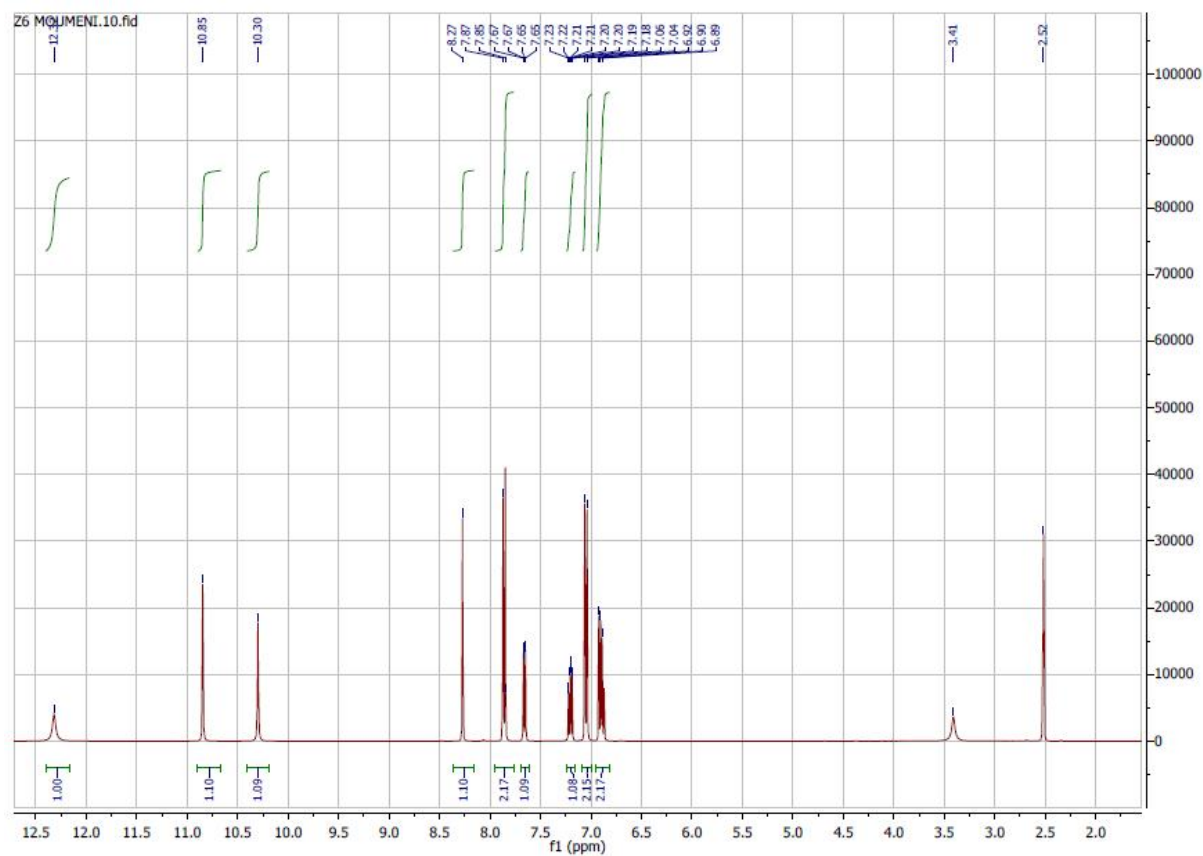
III.3.3.2. ^{13}C NMR spectra NBHZ

In Figure III.5 (B), the ^{13}C NMR chemical shift was displayed. The following distinctive signals have been revealed by analyzing the ^{13}C NMR experimental spectrum that was obtained: The carbon of the azomethine group of hydrazone $\text{C}=\text{N}$ was detected as a singlet signal at 147.64 ppm, and the carbon of the aromatic ring connected to the azomethine group (CAr-N-N) is linked to the peak that emerged in the downfield region at 148.46 ppm. Furthermore, in the downfield region all other aromatic ring carbons are observed to collectively resonate from 112.189 to 133.981 ppm. However, the carbonyl group of the carboxylic acid group ($\text{C}=\text{O}$)-OH is found in the downfield region at 167.6 ppm and is responsible for the sharp singlet signal.

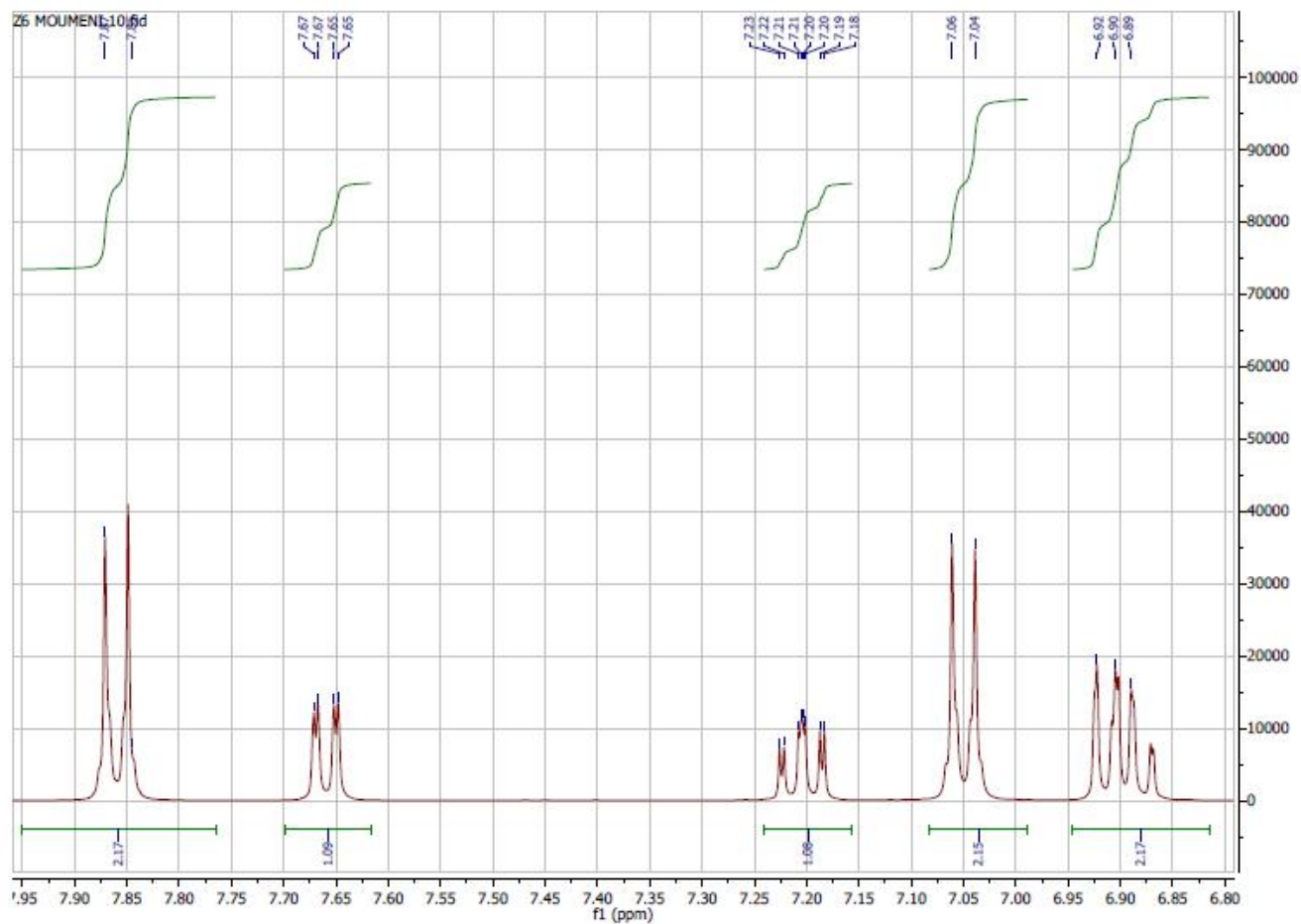
III.3.3.3. ^1H NMR spectra HBHZ

Analyzing the ^1H NMR HBHZ spectrum Figure III.6 (B) allowed for the identification of the signals that explain the amount of protons within the hydrazone structure: all signals between 6.82 and 7.87 ppm are caused by protons in aromatic rings, while a single peak emerges at 2.51 ppm and is caused by DMSO solvent. The matching peak of the aliphatic group of the hydrazone moiety CALiph is present concurrently at 8.27 ppm. Furthermore, at 10.30 ppm, the proton of the amine group with the azomethine group is still present. Furthermore, the proton of the hydroxyl group OH in the aldehyde

portion corresponds to the signal that occurred in the downfield region at 10.85 ppm as a singlet, whereas the carboxylic acid group's proton of OH is situated at 12.32 ppm.



A)



B)

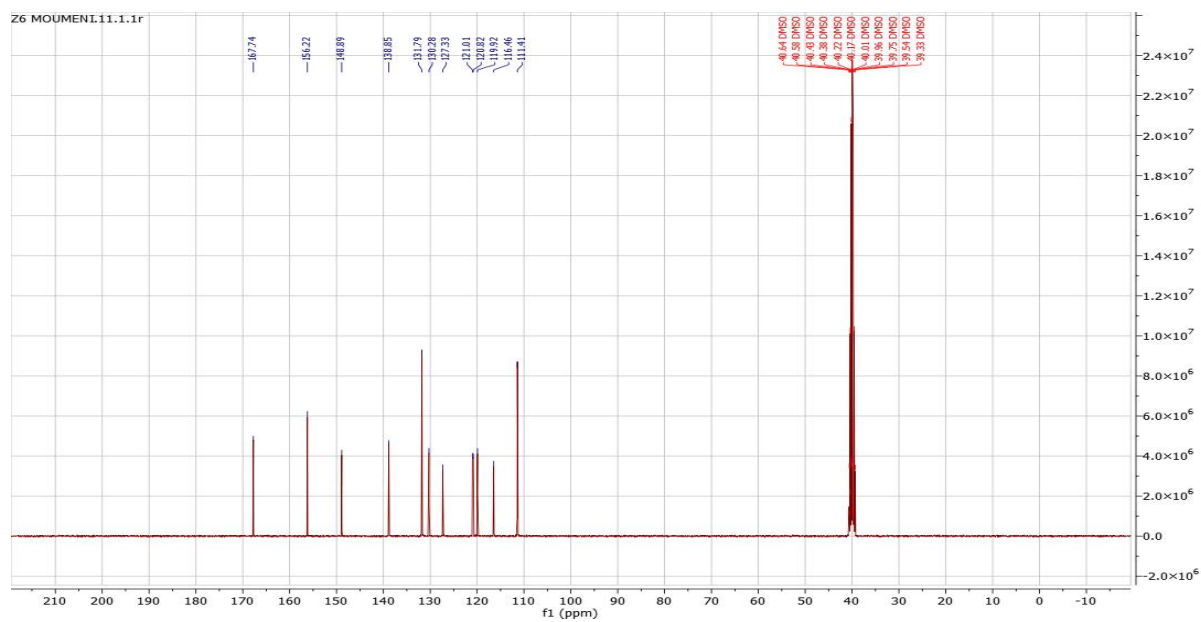


Figure III. 6: A) ¹H and B) ¹³C NMR spectrums of HBHZ.

III.3.3.4. ^{13}C NMR spectra HBHZ

Similarly, following a thorough analysis of ^{13}C NMR HBHZ Figure III.6 (B), the following unique signals were discovered: The carbonyl group of the carboxylic acid group ($\text{C}=\text{O}$)-OH is referenced by a sharp singlet signal at 169.3 ppm in the downfield region. The carbon atom associated with the hydroxyl group of naphthalene ($\text{C}-\text{OH}$) was determined to be at 157.2 ppm as a sharp singlet signal. Additionally, the carbon atom within the azomethine group of hydrazone $\text{C}=\text{N}$ was identified at 143.3 ppm appearing as a singlet signal, while the appeared peak at 148.2 ppm is attributed to the carbon of the aromatic ring connected with azomethine group ($\text{C}_{\text{Ar}}-\text{N}-\text{N}$). Furthermore, it is observed that the collective resonance of all other aromatic ring carbons ranges from 111.41 to 131.79 ppm.

III.3.3.5. ^1H NMR spectra HHZB

Aromatic proton resonances observed within the range 7.04 and 8.53 ppm, accounting for a total 10 protons. Furthermore, a singlet resonance at 8.99 ppm is attributed to the proton of ($\text{N}-\underline{\text{C}}\text{H}$). The ($\text{N}-\underline{\text{H}}$) group within the hydrazone moiety resonates at the at 10.92 ppm. On the other hand, in the in the high chemical shifts values a distinct sharp singlet at 12.33 ppm is due to a proton of the hydroxyl group ($-\text{OH}$) while another singlet at 10.97 ppm is indicative of the carboxylic acid group proton ($\text{CO}-\underline{\text{O}}\text{H}$)

A)

B)

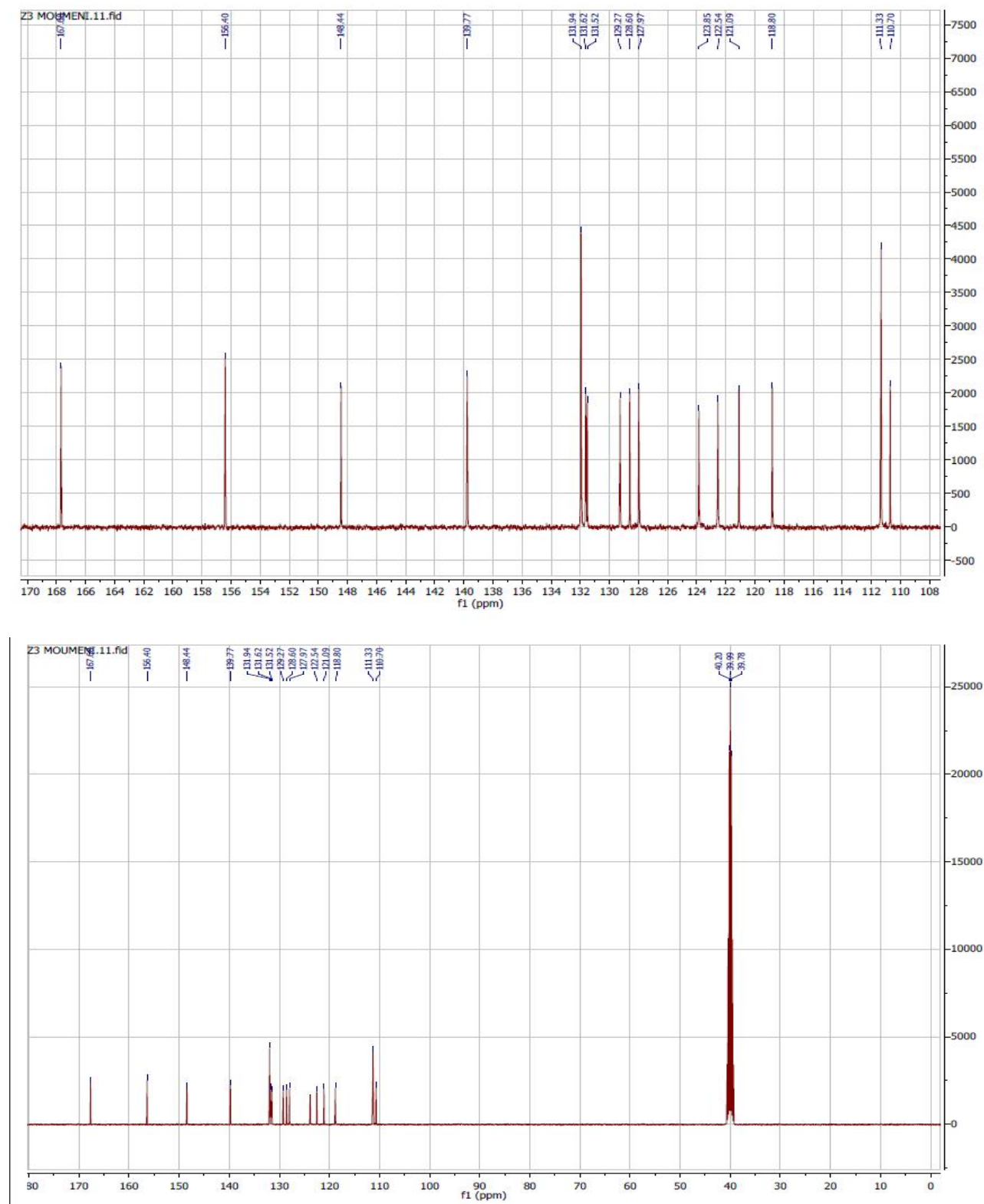


Figure III. 7: A) ^1H and B) ^{13}C NMR spectrums of HHZB.

III.3.3.6. ^{13}C NMR spectra HHZB

At 139.77 ppm, the carbon in the azomethine group ($\text{C}=\text{N}$) resonates as a singlet signal. On the other hand, a peak at 148.44 ppm can be found in the downfield region for the carbon of the aromatic ring that is attached to the azomethine group ($\text{C}_{\text{Ar}}\text{-N-N}$). Furthermore, the downfield region's aromatic ring carbons resonate collectively between 110.7 and 131.94 ppm. In the meantime, the carbon bound to the hydroxyl group (C-OH) is indicated by a sharp singlet signal at 156.4 ppm in the downfield area, and the carbon assigned to the carboxylic acid (COOH) is shown by a signal at 167.68 ppm.

III.3.3.7. ^1H NMR spectra MHZN

A clear peak at 2.34 ppm can be seen in the ^1H NMR spectra of MHZN, which is due to the three protons of the methyl group (C-H_3). The NH group of the hydrazone moiety may be responsible for an additional signal at 8.71 ppm. Aromatic proton signals are clearly visible between 6.95 and 7.98 ppm, indicating 10 protons. Additionally, in the downfield area of the spectrum, a sharp singlet at 12.15 ppm corresponds to a proton of the hydroxyl group ($-\text{OH}$). In addition, a singlet at 8.01 ppm is associated with the (N-CH) moiety's CH group proton.

III.3.3.8. ^{13}C NMR spectra MHZN

Analyzing the experimental spectrum the ^{13}C NMR revealed a peak found at 20.64 ppm is associated with the methyl group's carbon (C-H_3). The azomethine group carbon of hydrazone ($\text{C}=\text{N}$) resonates as a singlet signal at 141.24 ppm. On the other hand, the carbon of the aromatic ring connected to the azomethine group ($\text{C}_{\text{Ar}}\text{-N-N}$) is responsible for the peak located in the downfield region at 137.41 ppm. Furthermore, the downfield region's additional aromatic ring carbons all resonate collectively between 109.06 and 131.37 ppm. In addition, the downfield region's sharp singlet signal at 156.7 ppm is associated with the carbon bonded to the hydroxyl group (C-OH).

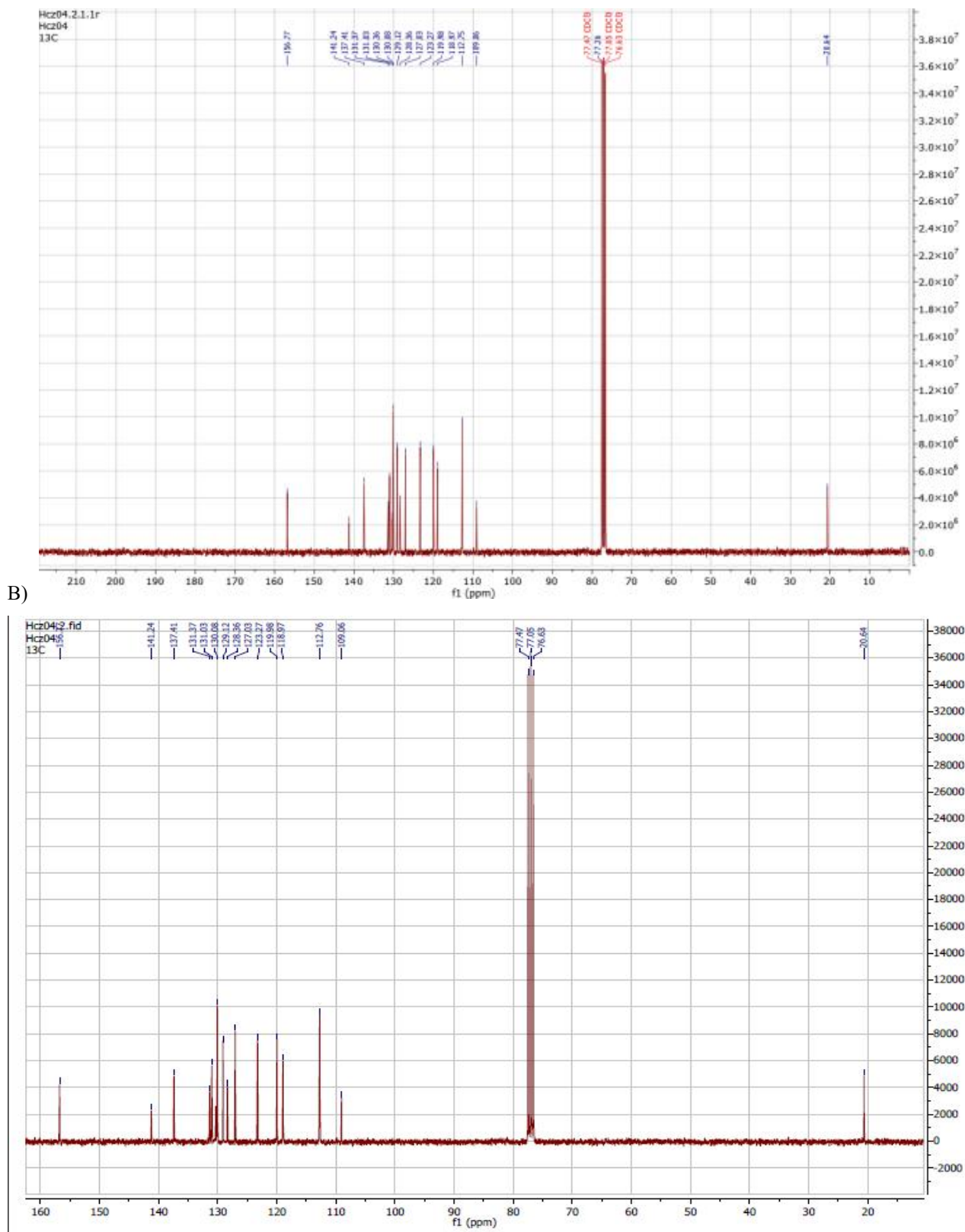


Figure III. 8. A) ^1H and B) ^{13}C NMR spectrums of MHZN.

III.4. Conclusion

Four hydrazone derivatives were successfully synthesized, and their structures were examined using spectral methods. Due to their distinct functional groups, these hydrazones have a range of properties which influence their biological and electrochemical applications. In particular, we assessed their capacity to control corrosion as well as their biological activities, which include antibacterial and antioxidant. The outcomes of these investigations support the thorough evaluation of the produced compounds and facilitate future studies and possible uses of the hydrazone derivatives in a range of scientific domains.

Chapter VI
Evaluation of the
biological activities of
the synthesized
hydrazones

Chapter IV Structural and electronic study using Quantum Chemical Calculations

In this chapter, we explore four hydrazone chemical structures computationally and optimize their geometries using sophisticated simulation methods. We evaluate important indices that provide information about the electronic characteristics and reactivity of these molecules using quantum chemical calculations. We also conduct a thorough topological analysis using tools like the Reduced Density Gradient (RDG), Electron Localization Function (ELF), Molecular Electrostatic Potential (MEP), and Localized Orbital Locator (LOL). The charge distribution, bonding properties, and non-covalent interactions inside the hydrazone structures are all thoroughly understood thanks to these analyses.

IV.1. DFT study

IV.1.1. Molecular geometry and structure optimization

The aromatic hydrazones compound's molecular geometry was meticulously optimized using DFT-B3LYP/6-311G (d, p) level of theory, as depicted in Figure IV. 1 The optimization process yielded the highest structural parameters for the four hydrazones NBHZ, HBHZ, MHZN and HHZB revealing significant bond distances and angles that govern their three-dimensional 3D arrangements. For NBHZ, the key optimized bond distances were observed in (N19-C18), (O8-C7-C4), and (C15-C17-C13-C12) with bond distances of 1.48, 125.242, and 178.576, respectively. Conversely, in HBHZ, noteworthy bond distances were identified in (C17-C14), (C17-C14-C13), and (N10-N9-C7-C3) with bond distances of 1.49, 123.99, and 179.968, respectively. Also, for MHZN the optimized bonds distances were found in (C16, C21) 1.477, (O22, C21, C16) 125.234 and (C16, C21, O28, H37)179.993. On the other side for HHZB were found to be in (C16, C21)1.509, (C1, C12, N13) 122.432, (H34, C20, C18, H34) 179.826.

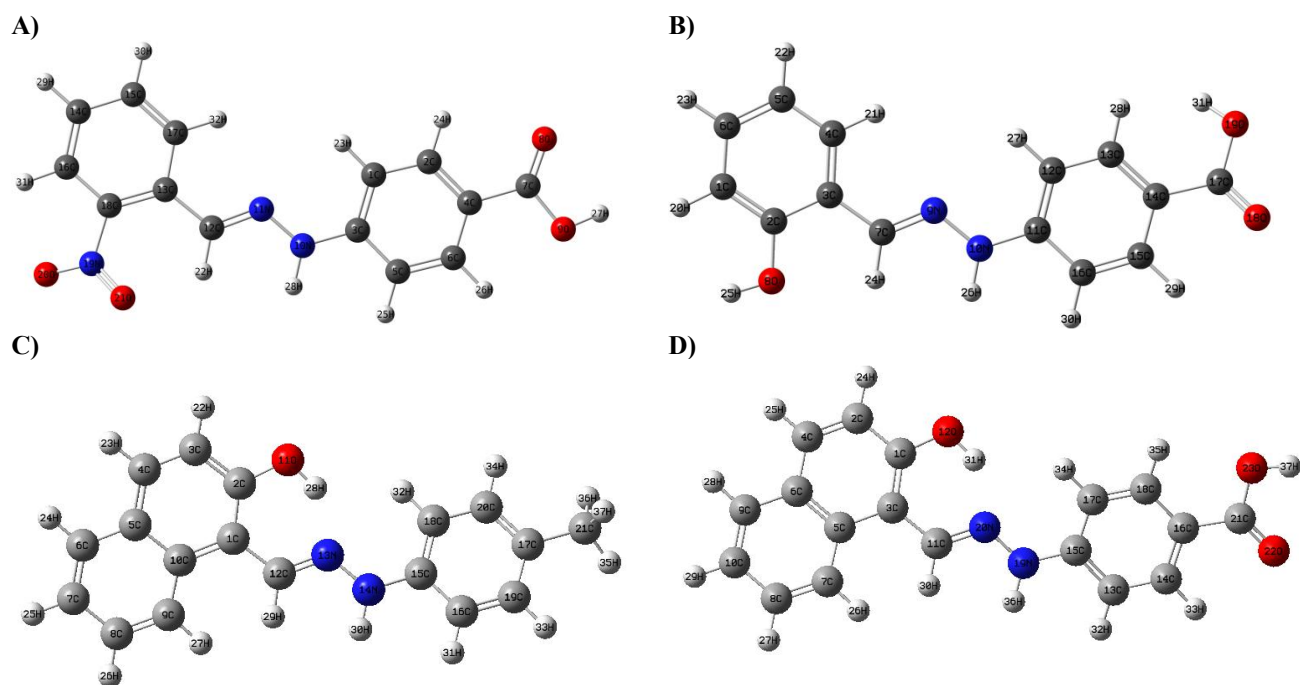


Figure IV. 1: Optimized geometries of target aromatic hydrazone compounds: A) NBHZ, and B) HBHZ C) MHZN, and D) HHZB.

Comprehensive information on additional bond angles, bond lengths, and dihedral angles for NBHZ, HBHZ, MHZN and HHZB can be found in Tables S. 1, 2, 3 and 4 respectively. The structural optimization was carried out for the gas phase under C1 symmetry, ensuring accurate representation and stability of the molecule, which is essential for understanding their reactivity and potential applications. Notably, the maximum dipole moment values were found to be 0.8089, 0.8726, 2.5185 and 3.7422 debye, respectively, highlighting the compounds' polarity [1].

IV.1.2. UV-Vis calculated spectrums

The experimental UV-Vis spectrums of both hydrazones were obtained in ethanol solvent at room temperature Figure IV.2. Their corresponding theoretical UV spectrums were calculated at TD-DFT method at B3LYP/6-311(d,p) level in ethanol solvent [2].

Chapter IV Structural and electronic study using Quantum Chemical Calculations

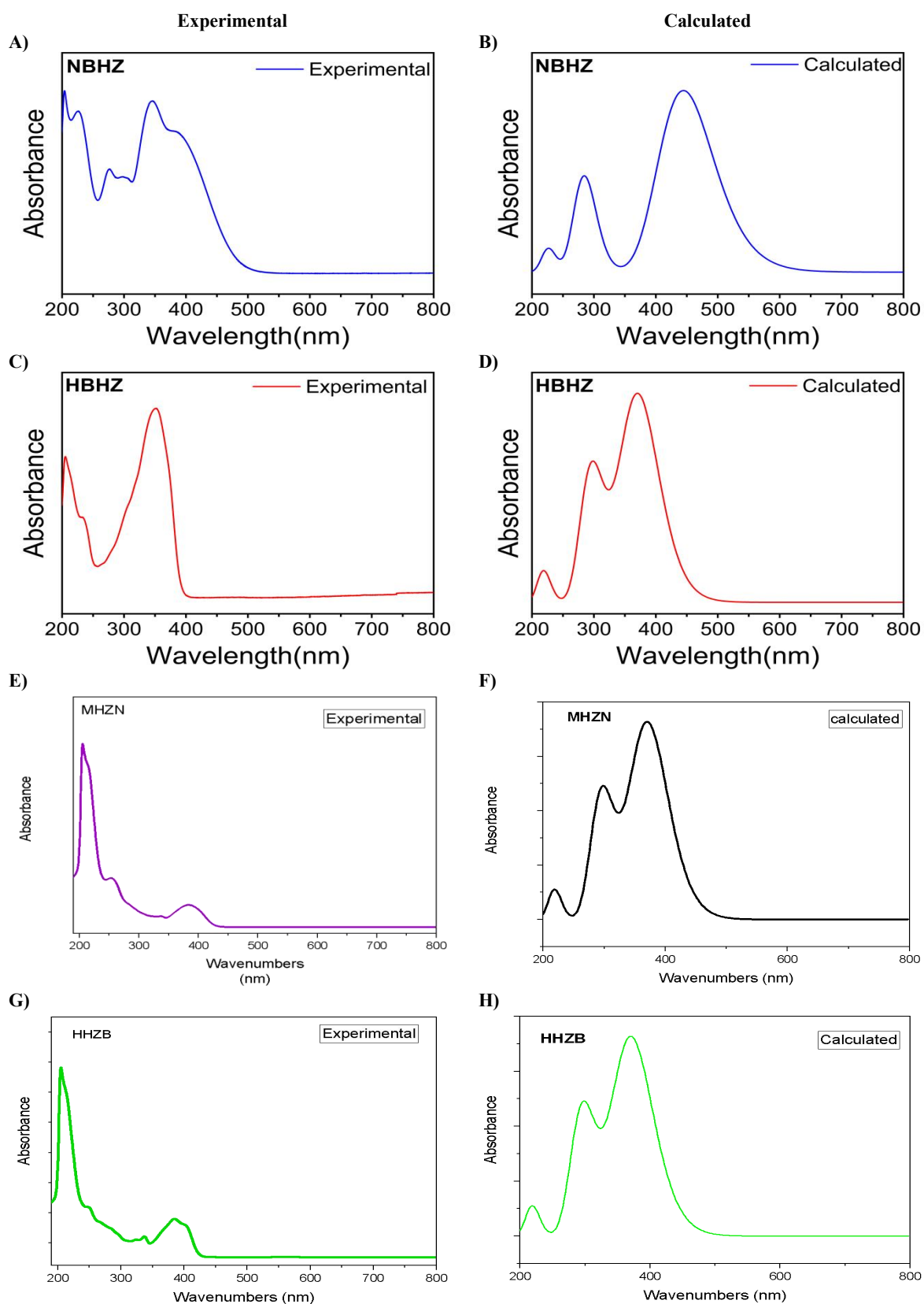


Figure IV. 2: The experimental and calculated UV-Vis spectra of target aromatic hydrazone compounds: NBHZ (A , C) , HBHZ (B , D), MHZN (E , F) and HHZB (G , H).

It is noticeable that in the experimental spectrum NBHZ the appearance of five bands in ultraviolet range whereas three characteristic bands in the theoretical one. The experimental spectrum exhibits a band at 205, 225 nm and 205 nm in theoretical one which are referred to $\pi-\pi^*$ transitions usually appear in unsaturated compounds resulting of C=C aromatic ring group which caused by the electron transition from π bonding orbitals to π^* anti-bonding orbitals. In return, the $n-\pi^*$ electronic transitions are caused by the existence of heteroatoms O and N that are in the molecular structure of NBHZ. Therefore, the band situated in 275 nm in experimental and 264.4 nm in calculated is related to the $n-\pi^*$ electronic transition which may be produced by the C=N in which electrons transfer from n nonbonding to π antibonding orbitals. Also, for the bands that appear at 346.37,386 nm in experimental spectrum and the given one by calculation 425.31 nm are attributed to $n-\pi^*$ which may be induced by C=O carbonyl group. The HBHZ experimental spectrum depicts three characteristic bands between 200-400 nm range 205, 233, 351.7 nm and three bands in theoretical ones 220, 296 and 370 nm, referred to presence also $\pi-\pi^*$ $n-\pi^*$ electronic transitions resulting of C=C aromatic ring group and existence of heteroatoms O and N that are in the molecular (OH, C=N and C=O) structure of HBHZ. In addition we could notice that the hydrazones have no absorbance in the visible range [3].

Likewise after examination the MHZN and HHZB spectrums whether experimental and theoretical we could observe the following characteristic peaks: For MHZN (exp: 206, 255, cal:220,302) resulting of the presence $\pi-\pi^*$ electronic transitions indicate the existence C=C aromatic ring group and (exp:384 nm, cal:370 nm) induced of $n-\pi^*$ electronic transitions that may refer to C=N which appeared in UV range 200-400 nm and for HHZB (Exp: 205, 250,336, 384.6 nm Cal:221,304,375 nm) both spectrums exhibit almost the same appeared bands just one difference can be seen at the wavenumber 336 nm may be due to carboxylic acid effect which distinguish the HHZB from MHZN that causes the $n-\pi^*$ transitions.

All results of the theoretical evaluations are compared with experimental measurements it can be seen that are in good agreement.

IV.1.3 FT-IR calculated spectrums

The experimental and theoretical FT-IR spectra of NBHZ and HBHZ are shown in Figures IV.3 and IV.4. The characteristic vibrations are arranged and listed in Tables IV.5 and IV.6 for comparative purpose. The calculated vibrational frequencies have been scaled with the factor of 0.9614 [4]. Also, to explore the vibrational assignments of hydrazones, we have conducted the PED analysis of the investigated compound. In this context, the observed vibrational frequencies and PED assignments are tabulated in Tables IV.1 and IV.2 [5].

After analyzing the previously mentioned spectra and consulting Table IV.1, the subsequent deductions have been made: O-H stretching vibrations are identified as the peaks seen at 3613 cm^{-1} in the NBHZ spectrum and 3628 cm^{-1} in the HBHZ spectrum. It is important to note that the computed values and PED calculations exhibit a considerable degree of consistency. It is a well-known fact that N-H vibrations in the infrared spectrum usually appear as strong peaks between 3100 and 3500 cm^{-1} at higher wavenumbers. As a result, the N-H secondary amine group stretching vibration in NBHZ is responsible for the observed peak at 3301 cm^{-1} ; in the HBHZ spectrum, this peak is observed at 3262 cm^{-1} . Additionally, the PED contribution supports this assignment, which is more supported by the PED contribution of 100%. In hydrazones, the stretching vibrations linked to C=N often appear in the 1500 – 1700 cm^{-1} range. Notably, the stretching vibration of C=N is responsible for the notable peaks seen at 1604 cm^{-1} for NBHZ and 1593 cm^{-1} for HBNH. The PED contribution highlights the support for this mode even more, reaching about 70% for NBHZ and 59% for HBNH.

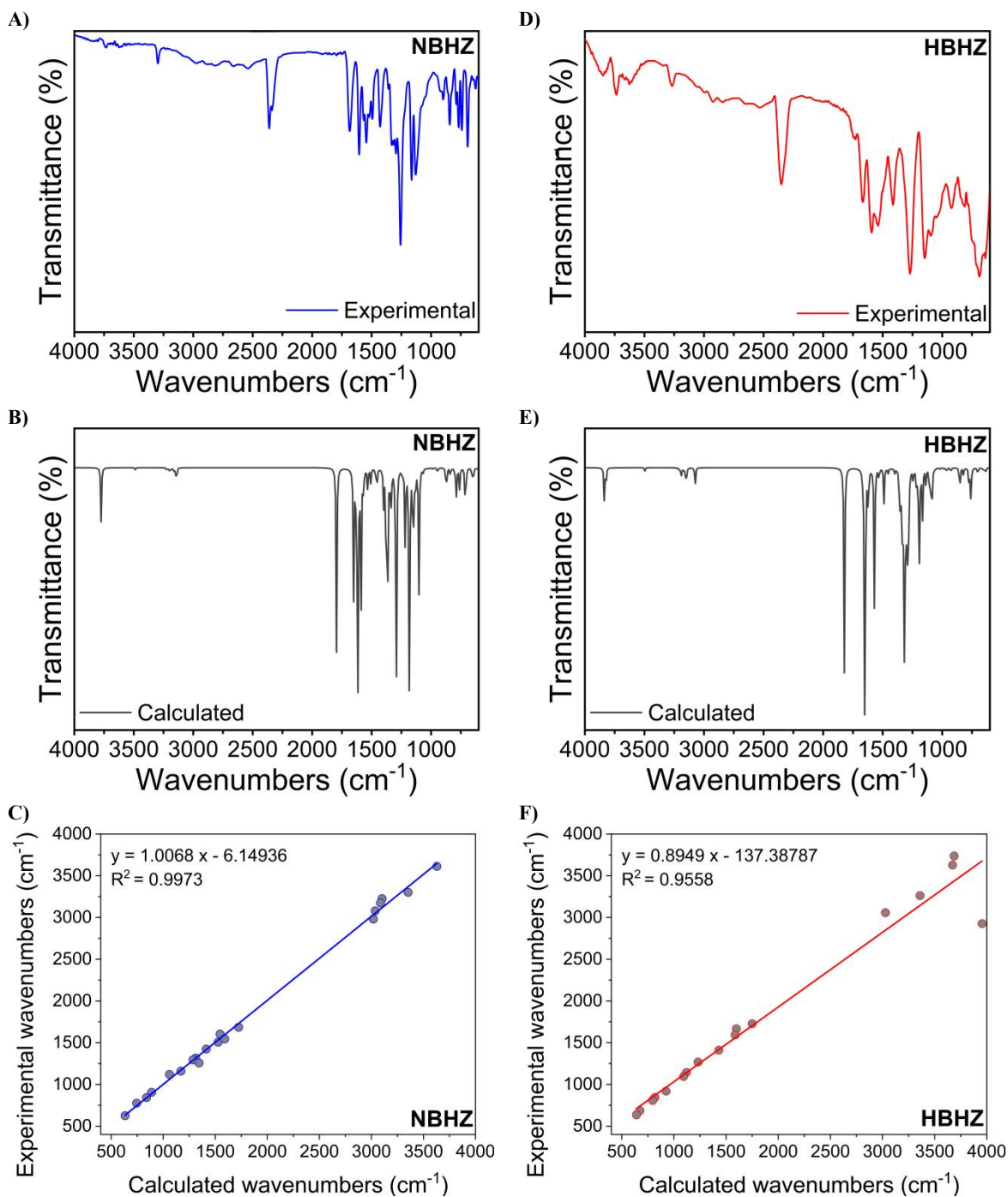


Figure IV. 3. The experimental, calculated FT-IR spectra and Correlation diagram between experimental and calculated wavenumbers of the target aromatic hydrazone compounds: NBHZ (A-C) and HBHZ (D-F).

Chapter IV Structural and electronic study using Quantum Chemical Calculations

Table IV. 1. Experimental and theoretical selected wavenumber values of the target aromatic hydrazone compounds.

NBHZ				HBHZ			
Assignment PED	Vibrational frequency (cm ⁻¹)			Vibrational frequency (cm ⁻¹)			
	Experimental	Theoretical		Assignment PED	Experimental	Theoretical	
		Unscaled	Scaled			Unscaled	Scaled
v O-H (100)	3613	3774	3629	v O-H (100)	3737	3836	3687
vN-H (100)	3301	3488	3352	v O-H (100)	3628	3820	3672
v C-H _{Ar} (97)	3174	3211	3087	vN-H (100)	3262	3495	3360
v C-H _{Ar} (97)	3079	3159	3037	v C-H _{Ar} (97)	3057	3150	3028
vCH _{Aliph} (99)	2981	3141	3019	vCH _{Aliph} (92)	2927	3074	3955
vC=O (83)	1684	1795	1725	v C=O (85)	1727	1821	1750
vC=N (70)	1604	1608	1546	vC=N (70)	1667	1664	1599
vasNO ₂ (55)	1506	1589	1527	v C=C (40)	1593	1650	1587
vs NO ₂ (58)	1315	1365	1312	v C-C (57)	1268	1281	1232
v C-C (20)	1295	1338	1286	β _t H-C=C(41)	1423	1488	1431
v N-C (11) β HCN (34)	1257 (β HCN)	1399	1344	v N-N (41)	1143	1166	1120
v C=C (54)	1546	1655	1591	β _H -CC (48)	1095	1137	1093
v C-O (59)	1120	1103	1060	δ H-C=N-N (63)	919	963	925
vC=C 37 H-C=C 41	1423(v C=C)	1470	1413	ρ _{out} H-C- C=C(41)	844	852	818
v N-N (27) ;β _H - CC (41)	1159 (v N-N)	1191	1170	ρ _{out} H-C- C=C(88)	808	828	796
δ H-C=N-N (86)	906 (δ H-C=N- N)	945	889	ρ _{ou} C-C=C-C (59)	686	702	674
ρ _{out} H-C-C=C(24) ρ _{out} C-C=C-C (29)	775(ρ _{out} H-C- C=C)	759	745	β _C -C=C (66)	636	667	641
αNO ₂ (10) β _C - C=C (50)	842 (α O-N-O)	874	840				

Notes: δ: twisting, ω: wagging, v: stretching, v_s:symetric stretching α: scissoring, ρ: torsion, β: in plan bending and . ρ_{out} bending out of plan.

. . Furthermore, for NBHZ and HBHZ, the aliphatic stretching vibration is clearly visible at 2981 cm⁻¹ and 2927 cm⁻¹, respectively. The PED contribution, which accounts for around 97% in the case of NBHZ and 92% in the case of HBHZ, highlights the strong support for this modality. Moreover, the peak found at 906 cm⁻¹ in NBHZ and 919 cm⁻¹ in HBHZ most likely represents the out-of-plane bending twisting mode. Notably, the PED contribution significantly strengthens this interpretation, reaching 86% for NBHZ and 63% for HBHZ. Furthermore, the azomethine group's N–N stretching vibration can be clearly seen in both hydrazones, with NBHZ exhibiting it at 1159 cm⁻¹ and HBHZ at 1143 cm⁻¹. Identifying the NO₂ group is relatively straightforward due to its distinct group frequencies, which can be recognized independently of the rest of the molecule. The stretching vibrations of the NO₂ group encompass both asymmetric

Chapter IV Structural and electronic study using Quantum Chemical Calculations

(1570–1485 cm^{-1}) and symmetric (1370–1320 cm^{-1}) modes. In this context, the peak observed at 1506 cm^{-1} is attributed to the asymmetric stretching vibrations of the NO_2 group, aligning closely with the calculated value of 1527 cm^{-1} obtained experimentally. Furthermore, the PED contribution to this mode is significant, accounting for nearly 55%.

The NO_2 group's symmetric stretching vibration is located at 1315 cm^{-1} , which is quite near to the theoretical peak at 1312 cm^{-1} . In addition, this mode has a significant PED contribution of 58%. Most notably, Tables IV.1 and IV.2 describes the identified ring stretching, which includes both in-plane and out-of-plane bending vibrations.

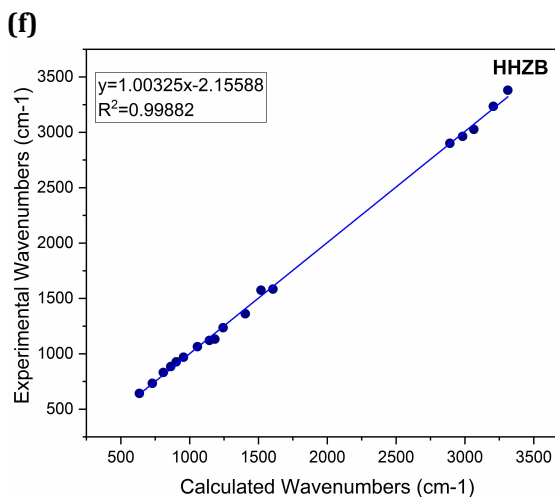
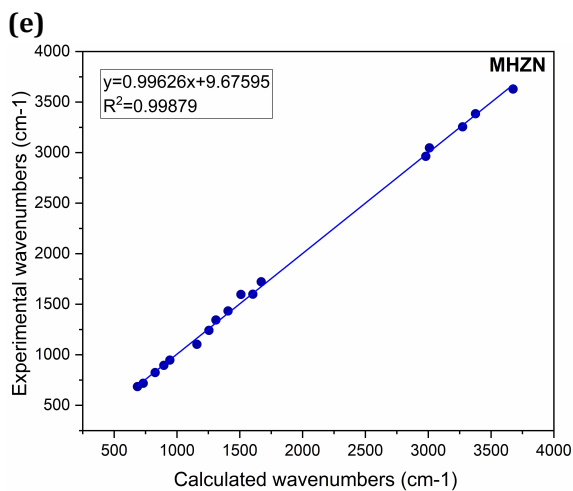
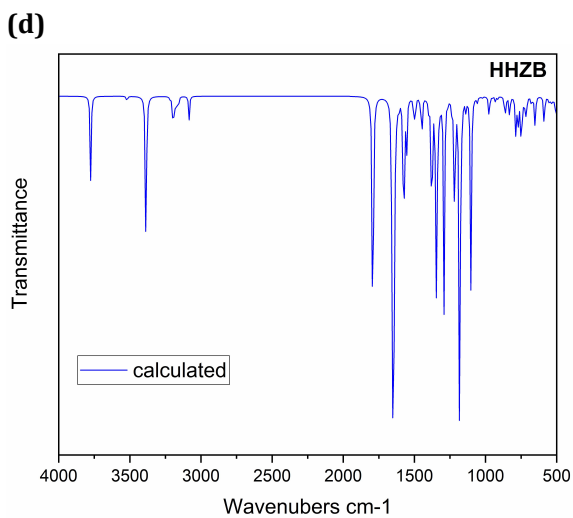
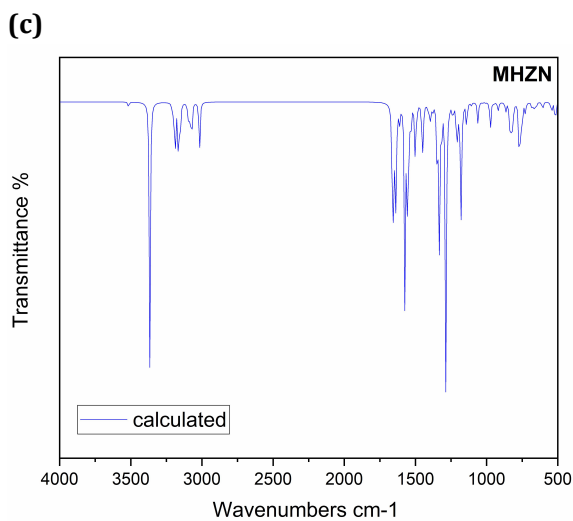
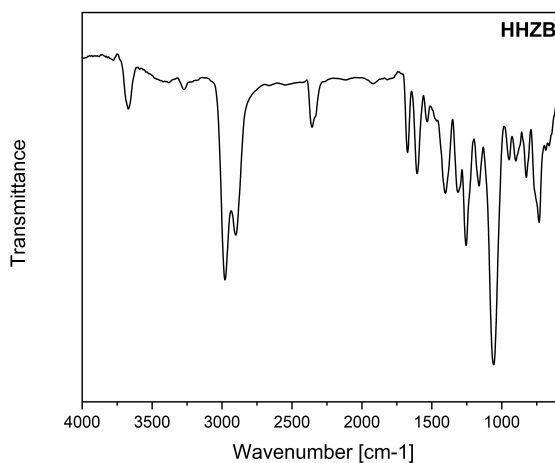
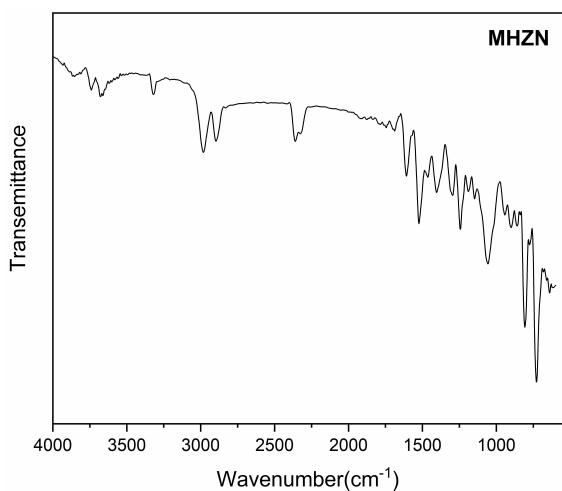
Typically, the stretching vibrations linked to $\text{C}=\text{C}$ lie between 1625 and 1430 cm^{-1} . The FT-IR spectra of the synthesized hydrazones in our current study show $\text{C}=\text{C}$ stretching vibrations at 1546 cm^{-1} and 1423 cm^{-1} . Furthermore, the aromatic ring's $\text{C}-\text{C}$ stretching vibration modes are often anticipated to lie between 1380 and 1280 cm^{-1} . For NBHZ and HBHZ, the observed peaks at 1295 cm^{-1} and 1268 cm^{-1} , respectively, are therefore most likely caused by the $\text{C}-\text{C}$ stretching vibration. On the other hand, the computed value and PED exhibit a good agreement Tables IV.1 and IV.2. Furthermore, they assign either aromatic or aliphatic stretching vibration modes to the range between 2850 and 3100 cm^{-1} , which corresponds to the $\text{C}-\text{H}$ stretching vibrations. The analysis of the recorded FT-IR spectrum revealed that the aromatic $\text{C}-\text{H}$ asymmetric and symmetric stretching vibrations for NBHZ emerge as peaks at 3174 and 3079 cm^{-1} , while the hydrazone for HBHZ was identified at 3057 cm^{-1} .

Furthermore, the calculated vibrations values obtained by DFT-B3LYP/6-311 G(d,p) method show favorable concurrence with experimental ones as depicted in Figure IV.4 (B and E). Moreover, the PED corresponding to these pure modes are presented and compiled in Table IV.2.

(a)

(b)

Chapter IV Structural and electronic study using Quantum Chemical Calculations



Chapter IV Structural and electronic study using Quantum Chemical Calculations

Figure IV. 4: The experimental, calculated FT-IR spectra and Correlation diagram between experimental and calculated wavenumbers of the target aromatic hydrazone compounds: MHZN (A-C) and HHZB (D-F).

Table IV.2: Experimental and theoretical selected wavenumber values of the target aromatic hydrazone compounds MHZN and HHZB.

Assignment PED	MHZN			HHZB			
	Vibrational frequency (cm ⁻¹)			Vibrational frequency (cm ⁻¹)			
	Experimental	Theoretical		Assignment PED	Experimental	Theoretical	
		Unscaled	Scaled			Unscaled	Scaled
v O-H (99)	3207	3366	3235	v O-H (100)	3675	3775	3629
vN-H (100)	3312	3516	3380	v O-H (99)	3376	3520	3384
v C-H _{Ar} (97)	3065	3147	3027	vN-H (100)	3274	3286	3255
v C-H _{Aliph} (99)	2984	3083	2963	v C-H _{Ar} (84)	3010	3170	3047
vCH _{Aliph} (97)	2891	3017	2901	vCH _{Aliph} (99)	2981	3083	2963
vC=N (54)	1606	1648	1584	v C=O (82)	1671	1792	1722
v C=C (52)	1519	1638	1575	vC=N (19)	1604	1664	1599
β H-C-H (95) 4-SUBalip	1405	1417	1362	v C=C (44)	1509	1661	1597
v C-C (40) β HNN (14)	1291 (v C-C)	1286	1236	v C-C (57)	1255	1291	1241
v N-N (38)	1184	1179	1133	β _H H-O-C(19)	1407	1491	1433
H-C=C (56)	1144	1167	1121	v C=C (48)	1310	1399	1344
vC-C 37 H-C=C 41	1057(H-C=C)	1107	1064	v C-C (34)	1255	1291	1241
β H-C-H (19) βH-C-C (58)	956 (βH-C-C)	1008	969	v N-N (42)	1159	1147	1103
δ _{out} bending H-C=C-H (68)	903	966	928	δ _{out} bending H-C-C-H (72)	944	985	947
ρ _{out} bending(H-C=N-N) (88)aliph	863	921	885	ρ _{out} bending H-C=N-N (88)	896	931	895
ρ _{out} bendingH-C-C=C(64)	809	866	832	ω H-C-C=C(65)	827	858	824
ρ _{out} H-O-C=C(64)	729	763	733	ρ _{out} H-O-C=C(74)	732	747	718
ρ _{out} C-C=C-C (75)	635	668	642	ρ _{out} C-C=C-C (75)	686	713	685

Note: δ: twisting, ω: wagging, v: stretching, v_s: symmetric stretching α: scissoring, ρ: torsion, β: in plan bending and . ρ_{out} bending out of plan.

The following conclusions have been resulted after an accurate examination of both hydrazones FT-IR spectrums: O-H stretching vibrations are responsible for the peaks that showed up at 3207 cm⁻¹ in the MHZN and 3675 cm⁻¹ in the HHZB spectrums. However, it is important to note that there is a good agreement between the estimated values and PED estimations. It is widely known that N-H vibrations can readily manifest as abrupt peaks in one band amine secondary between 3100 and 3500 cm⁻¹ at higher wavenumbers in the infrared spectrum. The N-H secondary amine group stretching vibration of MHZN is therefore responsible for the peak that occurred at 3312 cm⁻¹; HHZB appeared at 3376 cm⁻¹ in the spectrum. Moreover, the PED contribution of 100% supports this mode more.

Stretching vibrations of C=N of hydrazones are typically detected in the 1500 cm^{-1} to 1700 cm^{-1} range. As a result, it is evident that the distinctive peaks at 1604 cm^{-1} for MHZN and 1593 cm^{-1} for HHZB are caused by C=N vibration stretching. This mode is further reinforced by the PED contribution, which is around 54% and 19%, respectively.

Furthermore, for both MHZN and HHZB, the aliphatic stretching vibration is clearly visible at 2984 cm^{-1} and 2981 cm^{-1} , respectively. For each of them, the PED contribution of about 99% lends greater weight to this mode. Additionally, the PED contribution of 88% for both MHZN and HHZB further supports the possibility that the out of plan bending twisting mode is the peak seen at 863 and 896 cm^{-1} respectively. The N-N stretching vibration of the azomethine group for both hydrazones appears at 1184 cm^{-1} for MHZN and 1159 cm^{-1} for HHZB. The standard range of the C=C stretching vibrations is 1625–1430 cm^{-1} . The C=C stretching vibrations in these hydrazones are detected at 1519 cm^{-1} for MHZN and 1509 cm^{-1} for HHZB. The FT-IR spectrums show a PED contribution of approximately 52% and 44%, respectively. The aromatic ring's C-C stretching vibration modes typically occur in the 1380–1280 cm^{-1} range. Therefore, it is possible to attribute the peak that formed at 1291 cm^{-1} for MHZN and 1255 cm^{-1} for HBHZ to the C-C stretching vibration. The computed value and PED, however, show a strong agreement Table IV.2. Furthermore, they assign either aromatic or aliphatic stretching vibration modes to the range between 2850 and 3100 cm^{-1} , which corresponds to the C-H stretching vibrations. The analysis of the recorded FT-IR spectrum revealed that the aromatic C-H asymmetric and symmetric stretching vibrations for MHZN give rise to C-H stretching vibration peaks at 3065 cm^{-1} , whereas the HBHZ hydrazone peak was at 3010 cm^{-1} with a good PED contribution. As shown in figure IV.4 (B and E), the estimated vibration values obtained by the DFT-B3LYP/6-311 G(d,p) approach exhibit favorable concordance with experimental ones. Additionally, Table IV.2 presents and sums up the PED for these pure modes.

IV.1.4 Frontier molecular orbitals (FMOs) and reactivity indices

Using Frontier Molecular Orbital (FMO) analysis, compounds' electronic characteristics, optical potential, and reactivity can all be efficiently evaluated [6]. The aromatic hydrazone compounds' HOMO and LUMO orbitals are shown in figure IV.5. These orbitals are essential chemical quantum descriptors that are used to explain the chemical reactivity of molecules. The HOMO is associated with the molecule's ability to donate electrons, whereas the LUMO serves

Chapter IV Structural and electronic study using Quantum Chemical Calculations

as an electron acceptor, signifying the molecule's ability to receive electrons. An essential measure that indicates the stability and reactivity of the molecule is the energy gap (ΔE_{gap}) between the HOMO and LUMO. A lower ΔE_{gap} value indicates that the molecule is more easily excited, which increases its chemical reactivity and may cause it to become less stable. On the other hand, very high ΔE_{gap} values suggest increased stability. Predicting the behavior of the compound in chemical reactions and interactions requires an understanding of this energy gap. Compared to HBHZ and MHZN, NBHZ and HHZB have a smaller ΔE_{gap} , which implies that they are more reactive to stimulation and have a larger molecular content. Therefore, compared to the comparatively stable HBHZ and MHZN, NBHZ and HHZB may be more dynamic and reactive molecules. The atomic orbital compositions of the border molecular orbitals for the hydrazone compounds under investigation are shown in Figures IV.5 and IV.6. Positive phases are shown by the color orange, and negative phases by the color purple.

Analyzing the figures allows for easy observation of the positioning and location of both molecular orbitals in the molecule structures. For instance, in NBHZ, the HOMO density concentrates on the aromatic ring containing the carboxylic group, with a notable presence around carbon atom C7 of the carboxylic group whereas in HHZB concentrates between aromatic rings of hydroxynaphtalidene group around the carbon C6. Meanwhile, the LUMO density localizes on the NO₂ nitro group and extends towards carbon atom C18 of the aromatic ring, which also includes the same nitro group and for HHZB the LUMO density localizes on C5 of hydroxynaphtalidene group. These spatial distributions of HOMO and LUMO orbitals provide valuable insights into potential electron-donating and electron-accepting interactions and reactivity in NBHZ and HHZB.

Similar to how the HOMO density in MHZN localizes on the C5 and C10, in HBHZ it localizes on the carboxylic group towards the carbon atom C17. Conversely, the aromatic ring that contains the hydroxybenzylidene group—more precisely, the carbon atom C7 of the hydroxybenzylidene moiety is where the LUMO density is primarily found. This implies that the LUMO orbital has a high electron density in this area, suggesting that it could be involved in interactions that donate electrons and be chemically reactive.

Furthermore, the electron-donating and electron-accepting characteristics of hydrazone molecules are largely determined by the HOMO and LUMO energy levels, also referred to as

Chapter IV Structural and electronic study using Quantum Chemical Calculations

E_{HOMO} and E_{LUMO} , respectively. As was previously mentioned, the HOMO and LUMO orbitals play a crucial role in the computation of critical chemical reactivity parameters, which form a strong correlation between the stability and chemical reactivity of the molecule. All of the DFT global reactivity descriptors are shown in Table IV.7, where the compounds' capacity to donate or receive electrons, respectively, determines their chemical reactivity. The values of χ and η are important in this regard. Greater η values imply better resistance to electron transfer processes, whereas higher χ values indicate a stronger desire to attract electrons [7].

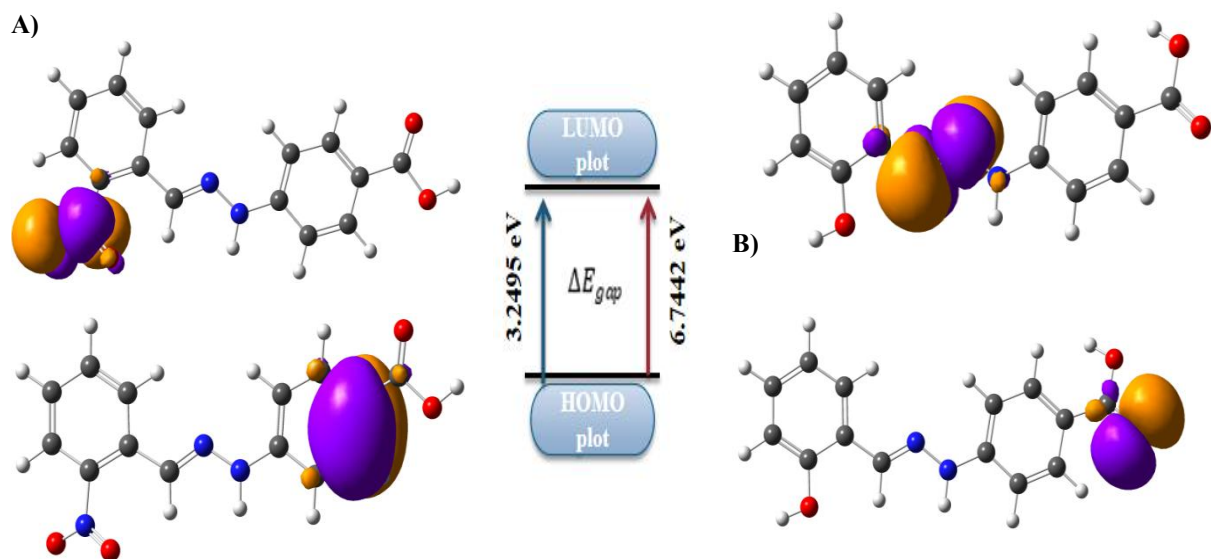


Figure IV. 5: Atomic orbital compositions of the frontier molecular orbital for A) NBHZ and B) HBHZ.

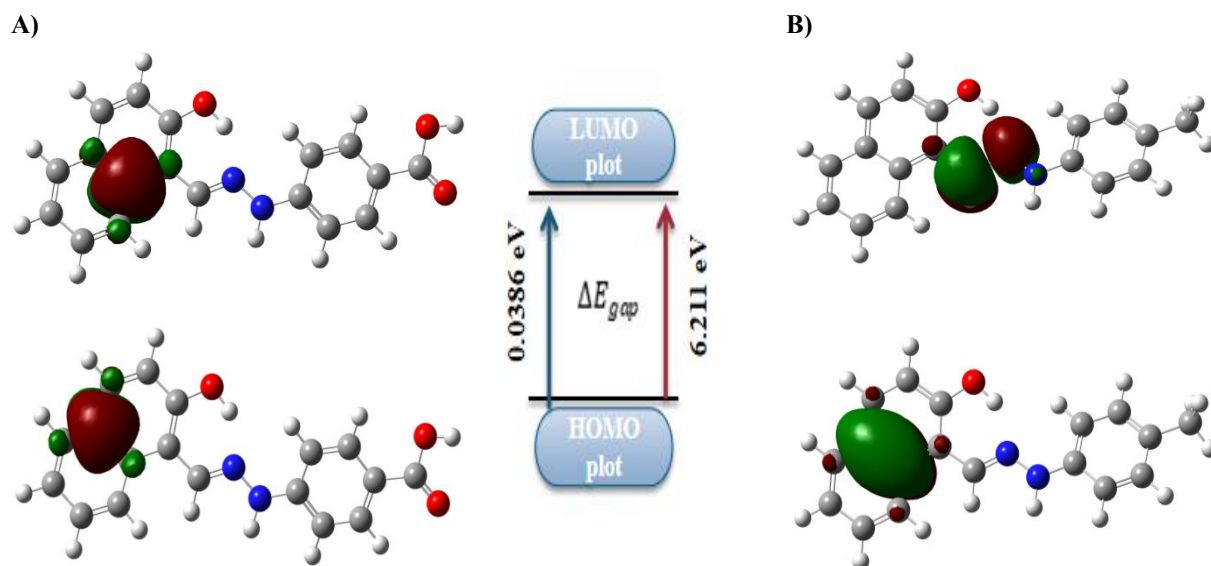


Figure IV. 6: Atomic orbital compositions of the frontier molecular orbital for A) HHZB and B) MHZN.

On the other hand, the parameter σ quantifies the molecular polarizability, providing valuable insights into the ease of charge transfer processes. By gaining an in-depth understanding of these reactivity descriptors, comprehensive insights into the electronic structure and behavior of hydrazone compounds can be obtained. Thus, the exploration of these global reactivity descriptors enhances our grasp of the compounds' chemical properties, paving the way for the rational design of novel materials with precise and optimized functionalities [8].

Table IV. 3: Quantum Chemical Parameters of the aromatic hydrazone compounds calculated at DFT - B3LYP/6311G d p level of theory.

Quantum Chemical Parameters	NBHZ	HBHZ	MHZN	HHZB
Total Energy (E_T , a.u)	-1005.42	-876.10	-880.48	-1029.79
E_{HOMO} (eV)	-7.0496	-6.7162	-6.4145	-2.9154
E_{LUMO} (eV)	-3.8101	0.0281	-0.2035	-2.9540
Energy gap (E_g , eV)	3.2395	6.7442	6.2110	0.0386
Ionization potential (I, eV)	7.0496	6.7162	+6.4145	+2.9154
Electron Affinity (A, eV)	3.8101	-0.0281	+0.2035	+2.9540
Hardness (η , eV)	1.6197	3.3721	3.1055	-0.0193
Softness (σ , eV)	0.3087	0.1483	0.33220	51.8134
Chemical potential (μ , eV)	-5.4298	-3.3441	-3.309	-2.9347
Electronegativity (χ , eV)	5.4298	3.3441	3.309	2.9347
Global Electrophilicity (ω , eV)	4.5506	0.8291	1.7629	-223.12

IV.2 Density of states (DOS) analysis

With the help of the reliable Multiwfn software package, we performed Density of States (DOS) analysis to look into the molecular orbital group contributions. The DOS curves, shown in Figure IV.7, provides crucial details regarding the electronic structure of the molecules by assigning distinct colors to various energy levels. In the DOS plot, the HOMO is represented by the orange hue, and the LUMO by the purple color. Comprehending the stability and chemical reactivity of the compounds requires an understanding of their HOMO and LUMO [9,10].

A)

B)

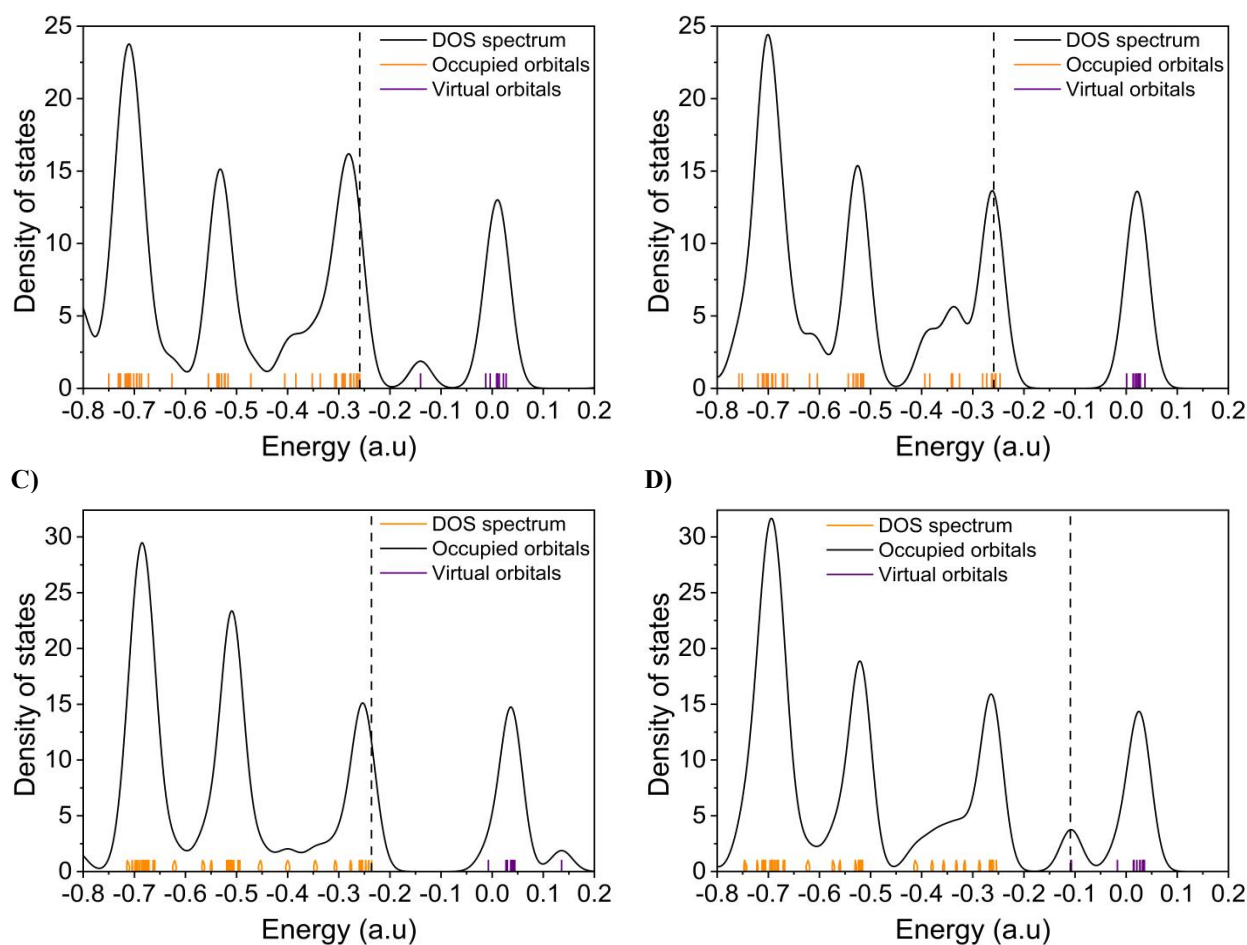


Figure IV. 7:DOS spectrum of the aromatic hydrazone compounds: A) NBHZ, B) HBHZ, C) MHZN, and D) HHZB.

Density of States (DOS) refers to the distribution of electronic states at different energy levels within a molecule. For hydrazones, the DOS plot provides insight into how the molecular orbitals are populated with electrons and the relative energy levels of these states. We observe a high peak at the -0.7 energy level in the DOS of hydrazones, it indicates that a significant number of electronic states (molecular orbitals) are concentrated at or around that specific energy.

IV.3 Molecular surface electrostatic potential (MEP)

Using DFT calculations at the optimum geometry, the produced hydrazone compounds' molecular electrostatic potential (MEP) surface maps were produced, as shown in Figure VI.8. Understanding the electronic density is essential to comprehending molecular reactivity, and the MEP surface map is a trustworthy resource for important details regarding the distribution of charges in three-dimensional space (3D). The MEP map provides a clear visual representation of

the charge distribution surrounding the molecule, helping us to identify possible molecular reactions and comprehend the structure of chemical interactions.

When looking at the MEP maps, one can see that the red areas show negative zones, which are places rich in electrons and correspond to all hydrazones' electrophilic reactivity. Interestingly, oxygen atoms predominate in the more electronegative regions, indicating that these atoms are in charge of electrophilic processes. In order to understand the structure of chemical interactions and detect potential molecular reactions, the MEP map presents a clear visual representation of the charge distribution surrounding the molecule. The molecular electrostatic potential (MEP) maps indicate that the red regions correspond to areas of negative potential, which are electron-rich and associated with the electrophilic reactivity of all hydrazone derivatives. Notably, the most electronegative zones are predominantly located around oxygen atoms, implying that these atoms play a key role in facilitating electrophilic interactions[11–13].

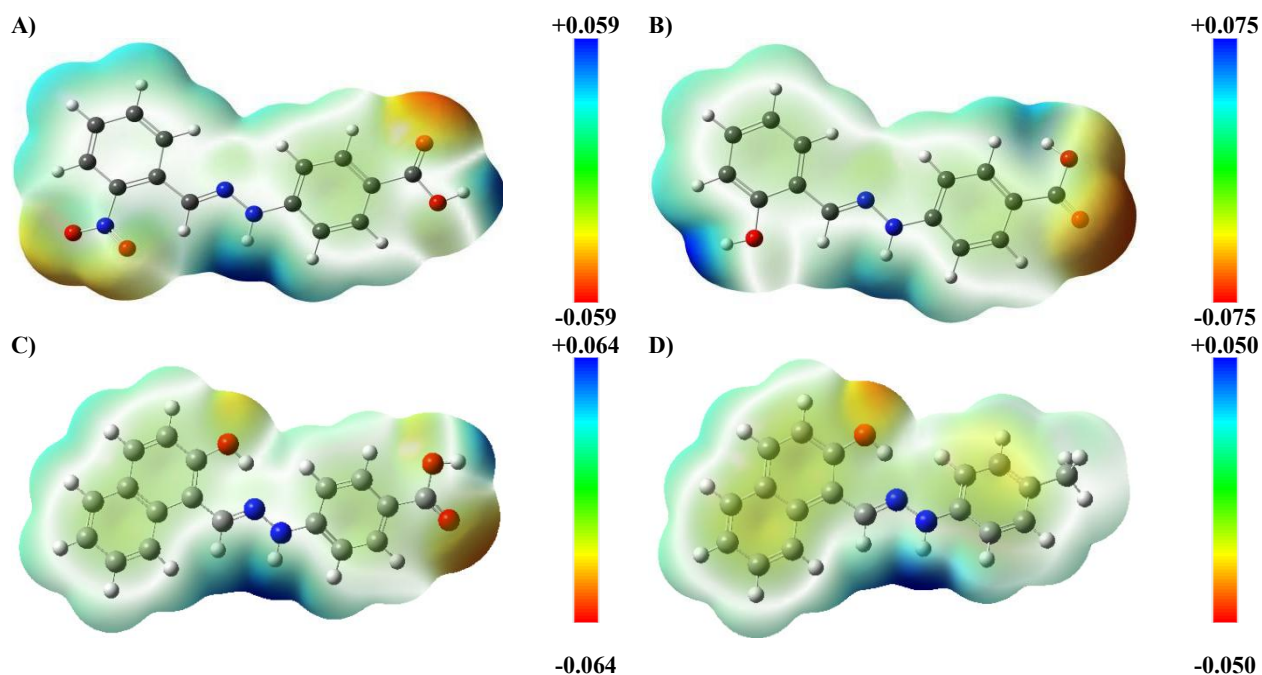


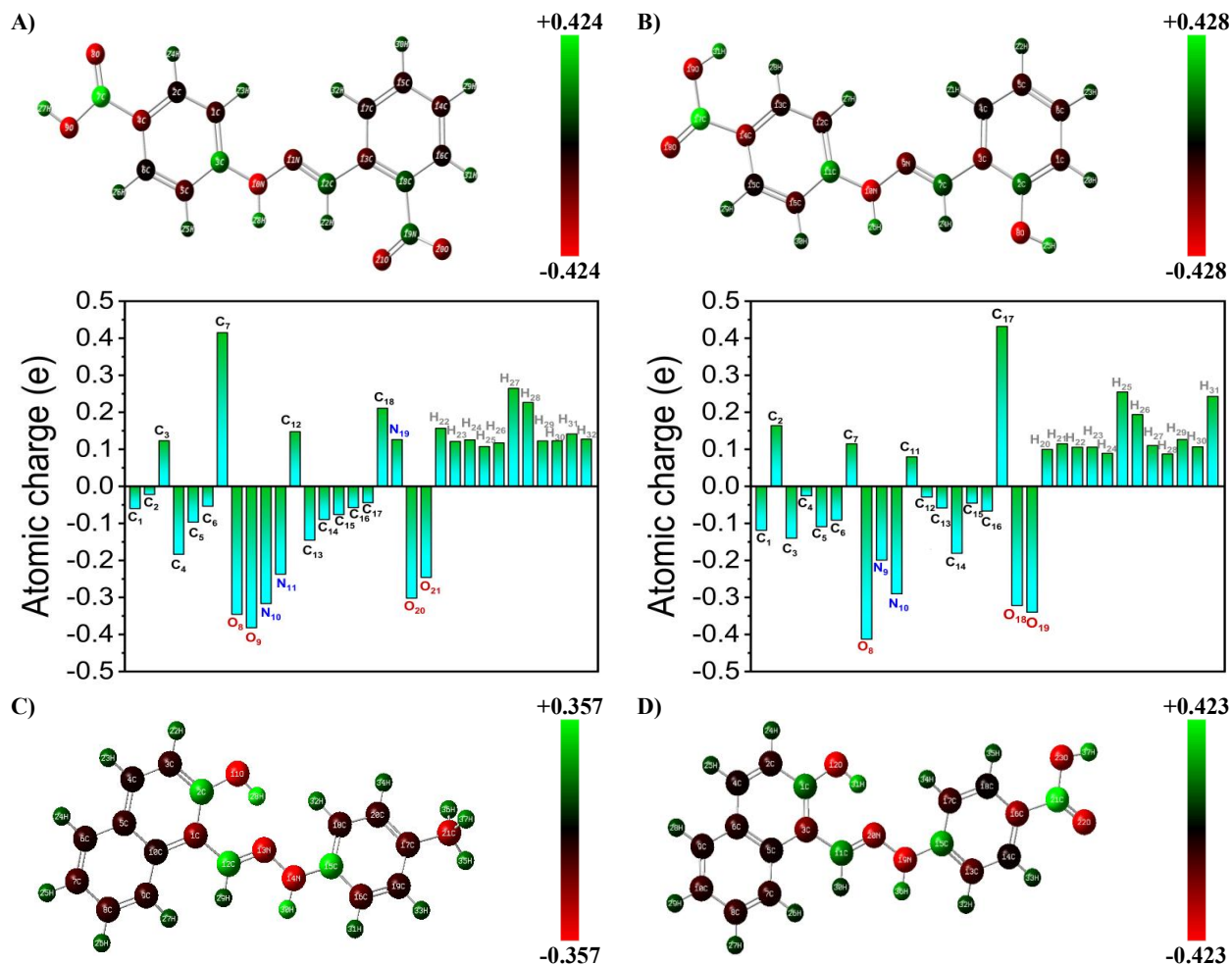
Figure IV. 8:Total electron density mapped with molecular electrostatic potential surface of the aromatic hydrazones: A) NBHZ, B) HBHZ, C) HHZB, and D) MHZN.

IV.4 Mulliken population analysis

Mulliken charge is a well-known quantity that provides insight into how atomic displacements impact the electronic structure and is intimately linked to molecular vibrational

Chapter IV Structural and electronic study using Quantum Chemical Calculations

properties. This makes it crucial for characterizing the bonds that make up a molecule's core, which in turn influences its electronic structure and structurally distorted characteristics like dipole moment, polarizability, and hyperpolarizability [14]. A comprehensive inquiry was conducted to clarify the charge transfer in our material. The natural population analysis results are shown in Tables IV.4 and IV.5, and the Mulliken population analysis results are shown in Figure VI.9 which shows the net atomic charges for the hydrazone compounds.



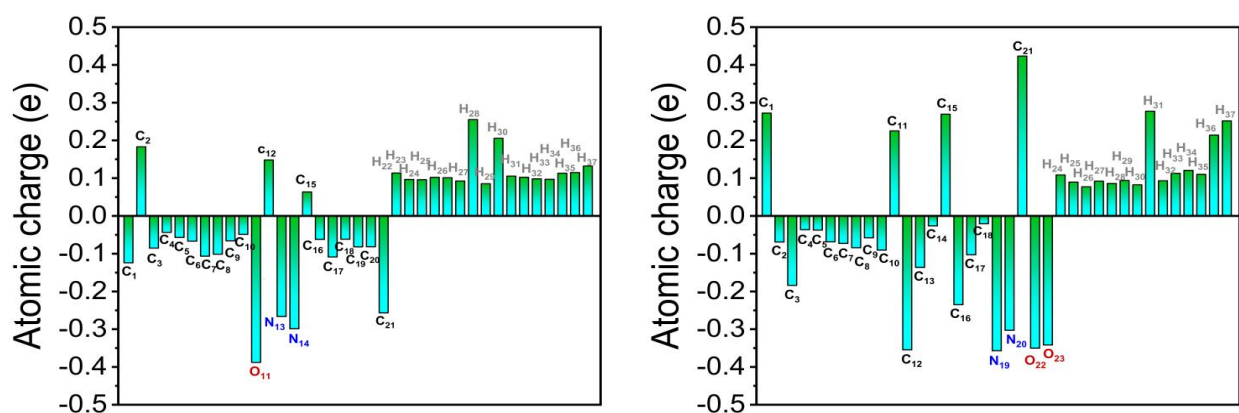


Figure IV. 9: The plot of Mulliken atomic charge distribution in geometry of the aromatic hydrazones: A) NBHZ, B) HBHZ, C) MHZN, and D) HHZB.

The carbon, oxygen, and nitrogen atoms in both compounds exhibit negative charges, indicating regions with high electron density. Interestingly, the carbon atoms in hydrazone molecules display both positive and negative charges, highlighting their dual reactivity. Additionally, all molecules contain positively charged hydrogen atoms, while the electronegative oxygen atoms consistently carry negative charges.

Table IV. 4: Natural population analysis of NBHZ and HBHZ.

NBHZ						HBHZ					
Atom	Natural Charge	Natural population				Atom	Natural Charge	Natural population			
		Core	Valence	Rydberg	Total			Core	Valence	Rydberg	Total
C1	-0.25115	1.99889	4.23757	0.01469	6.25115	C1	-0.28351	1.99893	4.26922	0.01536	6.28351
C2	-0.11457	1.99893	4.10043	0.01521	6.11457	C2	0.34389	1.99862	3.6358	0.02168	5.65611
C3	0.19399	1.99887	3.78666	0.02048	5.80601	C3	-0.11409	1.99886	4.09784	0.01738	6.11409
C4	-0.18428	1.99884	4.16746	0.01799	6.18428	C4	-0.15744	1.99893	4.14392	0.01459	6.15744
C5	-0.22082	1.99901	4.20718	0.01463	6.22082	C5	-0.20633	1.99906	4.1918	0.01547	6.20633
C6	-0.15648	1.99903	4.14231	0.01513	6.15648	C6	-0.17778	1.99907	4.16331	0.0154	6.17778
C7	0.82038	1.99931	3.13382	0.0465	5.17962	C7	0.05648	1.9992	3.9151	0.02923	5.94352
O8	-0.60373	1.99978	6.59609	0.00785	8.60373	O8	-0.70732	1.99976	6.69965	0.0079	8.70732
O9	-0.72164	1.99975	6.71397	0.00791	8.72164	N9	-0.27218	1.9993	5.25175	0.02112	7.27218
N10	-0.44603	1.99932	5.42751	0.01921	7.44603	N10	-0.44404	1.99933	5.42474	0.01997	7.44404
N11	-0.29417	1.99932	5.27321	0.02164	7.29417	C11	0.18959	1.99887	3.79025	0.02129	5.81041
C12	0.09266	1.99911	3.87446	0.03376	5.90734	C12	-0.20209	1.99888	4.18684	0.01637	6.20209
C13	-0.04273	1.99882	4.02588	0.01803	6.04273	C13	-0.15691	1.99892	4.14343	0.01455	6.15691
C14	-0.1824	1.99906	4.16821	0.01513	6.1824	C14	-0.16406	1.99883	4.14745	0.01778	6.16406
C15	-0.15552	1.99906	4.14178	0.01469	6.15552	C15	-0.14868	1.99901	4.13309	0.01657	6.14868
C16	-0.16753	1.999	4.15167	0.01686	6.16753	C16	-0.21022	1.999	4.19547	0.01575	6.21022
C17	-0.1713	1.99901	4.15597	0.01632	6.1713	C17	0.81479	1.99927	3.14082	0.04511	5.18521

Chapter IV Structural and electronic study using Quantum Chemical Calculations

C18	0.07447	1.99859	3.90462	0.02232	5.92553	O18	-0.56455	1.99979	6.55678	0.00798	8.56455
N19	0.47351	1.99932	4.48052	0.04665	6.52649	O19	-0.69522	1.99976	6.68684	0.00862	8.69522
O20	-0.41924	1.99989	6.41057	0.00879	8.41924	H20	0.20088	0	0.79579	0.00333	0.79912
O21	-0.34498	1.99974	6.32947	0.01577	8.34498	H21	0.22249	0	0.77408	0.00343	0.77751
H22	0.22037	0	0.77396	0.00567	0.77963	H22	0.2009	0	0.79722	0.00188	0.7991
H23	0.22342	0	0.77303	0.00355	0.77658	H23	0.1999	0	0.79821	0.00189	0.8001
H24	0.22501	0	0.77173	0.00326	0.77499	H24	0.16805	0	0.82562	0.00633	0.83195
H25	0.20336	0	0.79374	0.00291	0.79664	H25	0.46743	0	0.52755	0.00502	0.53257
H26	0.21739	0	0.77999	0.00262	0.78261	H26	0.33632	0	0.6566	0.00708	0.66368
H27	0.48259	0	0.51138	0.00602	0.51741	H27	0.21867	0	0.77801	0.00332	0.78133
H28	0.36753	0	0.62653	0.00594	0.63247	H28	0.18937	0	0.80685	0.00378	0.81063
H29	0.21052	0	0.78775	0.00173	0.78948	H 29	0.22502	0	0.77199	0.00299	0.77498
H30	0.20818	0	0.79001	0.00181	0.79182	H30	0.20708	0	0.79002	0.0029	0.79292
H31	0.23325	0	0.76386	0.00289	0.76675	H31	0.46353	0	0.53106	0.00541	0.53647
H32	0.22993	0	0.76647	0.0036	0.77007						

For example, the oxygen atoms in the NO₂ and OH groups have negative charges in NBHZ, with the largest negative value being found in the OH group's O9. Notably, the carbon atoms C3, C7, C12, and C18 are positively charged, while the remaining carbon atoms in the chemical system are negatively charged. The nitro group's N19 atom has the largest positive charge, while the azomethine group's N atom has a negative charge. Moreover, hydrogen atoms have positive charges ranging from 0.192 to 0.479. Positive and negative charges on the O, N, and H atoms, respectively, may account for the formation of intermolecular interactions with other molecules through the sharing of paired electrons with acceptor molecules [15].

On the other hand, a number of basic concepts in quantum chemistry and molecular orbital theory support in explaining how atoms and molecules are structured electronically. These include Rydberg, Charge, Core, and Valence, each of which has a unique function in comprehending the characteristics of molecules. The net electric charge that arises from an imbalance between protons and electrons in a molecule or atom is referred to as charge. Protons and electrons make up an equal number in a neutral atom or molecule, but ions can have either a positive (cation) or negative (anion) charge depending on electron gain or loss. The electrons that are most closely bound to the nucleus are called core electrons. Their energy levels are the lowest, and they are usually not involved in chemical reactions or bonding. For example, the two 1s electrons in an atom of carbon are core electrons. These electrons do not take part in bonding, but they do protect the nucleus and have an impact on the effective nuclear charge that the outer

Chapter IV Structural and electronic study using Quantum Chemical Calculations

electrons sense. The valence electrons, on the other hand, are the outermost electrons and are found in the highest energy orbitals. An atom's chemical behavior, including its capacity to form bonds with other atoms, is determined by these electrons. High-energy orbitals connected to excited states of atoms or molecules are known as Rydberg states. These electrons are frequently involved in ionization and are only weakly bound to the nucleus.

Table IV. 5: Natural population analysis of MHZN, and HHZB.

MHZN						HHZB					
Atom	Natural	Natural population				Atom	Charge	Natural population			
	Charge	Core	Valence	Rydberg	Total			Core	Valence	Rydberg	Total
C1	-0.11071	1.9987	4.09478	0.01724	6.11071	C1	0.39311	1.99878	3.58406	0.02405	5.60689
C2	0.35457	1.99866	3.62392	0.02285	5.64543	C2	-0.23913	1.99902	4.22395	0.01616	6.23913
C3	-0.25552	1.99894	4.24153	0.01505	6.25552	C3	-0.17382	1.99888	4.15961	0.01533	6.17382
C4	-0.15753	1.9989	4.1448	0.01383	6.15753	C4	-0.14372	1.99904	4.12982	0.01486	6.14372
C5	-0.06654	1.99889	4.05136	0.01628	6.06654	C5	-0.01556	1.99892	4.00212	0.01451	6.01556
C6	-0.16888	1.99904	4.15427	0.01556	6.16888	C6	-0.07611	1.99892	4.06223	0.01495	6.07611
C7	-0.20121	1.99908	4.18679	0.01534	6.20121	C7	-0.20127	1.99903	4.18782	0.01442	6.20127
C8	-0.17877	1.99907	4.16488	0.01481	6.17877	C8	-0.18172	1.9991	4.16704	0.01559	6.18172
C9	-0.19065	1.99904	4.1776	0.01402	6.19065	C9	-0.16378	1.99904	4.1493	0.01545	6.16378
C10	-0.02995	1.99878	4.01539	0.01577	6.02995	C10	-0.21163	1.99909	4.1967	0.01584	6.21163
O11	-0.69927	1.99976	6.69124	0.00827	8.69927	C11	0.07232	1.99919	3.90254	0.02595	5.92768
C12	0.06865	1.99919	3.90479	0.02737	5.93135	O12	-0.67187	1.99973	6.66321	0.00892	8.67187
N13	-0.30792	1.99929	5.2864	0.02222	7.30792	C13	-0.24994	1.99903	4.23651	0.0144	6.24994
N14	-0.43209	1.99933	5.41276	0.01999	7.43209	C14	-0.12925	1.99905	4.11431	0.01589	6.12925
C15	0.14814	1.99884	3.83169	0.02133	5.85186	C15	0.19272	1.99896	3.7879	0.02042	5.80728
C16	-0.19401	1.999	4.17922	0.01579	6.19401	C16	-0.20773	1.99888	4.19064	0.0182	6.20773
C17	-0.00633	1.99899	3.9928	0.01454	6.00633	C17	-0.25244	1.99903	4.23901	0.0144	6.25244
C18	-0.21887	1.9989	4.20588	0.01409	6.21887	C18	-0.13127	1.99906	4.11731	0.0149	6.13127
C19	-0.19129	1.99902	4.17717	0.0151	6.19129	N19	-0.3637	1.99923	5.34636	0.0181	7.3637
C20	-0.20375	1.99888	4.18989	0.01498	6.20375	N20	-0.33106	1.99926	5.30841	0.02339	7.33106
C21	-0.57746	1.9992	4.5692	0.00905	6.57746	C21	0.8103	1.99927	3.14113	0.0493	5.1897
H22	0.21745	0	0.77946	0.00309	0.78255	O22	-0.61525	1.99976	6.60692	0.00857	8.61525
H23	0.20307	0	0.7942	0.00273	0.79693	O23	-0.69628	1.99975	6.68785	0.00868	8.69628
H24	0.20092	0	0.7963	0.00278	0.79908	H24	0.2192	0	0.7777	0.0031	0.7808
H25	0.19726	0	0.80084	0.00189	0.80274	H25	0.204	0	0.79317	0.00283	0.796
H26	0.19704	0	0.80044	0.00252	0.80296	H26	0.19095	0	0.80616	0.00289	0.80905
H27	0.19195	0	0.80513	0.00292	0.80805	H27	0.20133	0	0.79619	0.00248	0.79867
H28	0.49302	0	0.50095	0.00603	0.50698	H28	0.20094	0	0.79616	0.0029	0.79906
H29	0.15721	0	0.83714	0.00564	0.84279	H29	0.20384	0	0.7937	0.00246	0.79616
H30	0.34299	0	0.65067	0.00634	0.65701	H30	0.16187	0	0.83321	0.00492	0.83813
H31	0.20672	0	0.79018	0.00311	0.79328	H31	0.49623	0	0.49688	0.00689	0.50377
H32	0.2051	0	0.79083	0.00407	0.7949	H32	0.2011	0	0.79593	0.00297	0.7989
H33	0.20057	0	0.79664	0.00279	0.79943	H33	0.22549	0	0.77116	0.00335	0.77451
H34	0.19977	0	0.79712	0.00311	0.80023	H34	0.21762	0	0.77939	0.003	0.78238
H35	0.19913	0	0.79896	0.00191	0.80087	H35	0.22186	0	0.7755	0.00265	0.77814
H36	0.20069	0	0.79736	0.00195	0.79931	H36	0.36408	0	0.62901	0.00691	0.63592
H37	0.20646	0	0.79146	0.00208	0.79354	H37	0.47856	0	0.51446	0.00698	0.52144

IV.5. Topology analysis of electronic structure

IV.5.1. Localized Orbital Locator (LOL) and Electron Localization Function (ELF)

To provide insights into the electron density distribution and bonding properties of the title molecule, topology research has been carried out with the aid of the robust Multiwfn software tool. For the purpose of locating lone pairs, bond pairs, and determining the degree of bonding inside a molecule [16], the LOL and ELF calculations are useful resources. The LOL and ELF investigations' two-dimensional color shade maps add to our understanding of the system's electron charge distribution in a complete way.

Figures IV.10 and IV.11 displays the ELF and LOL color shade maps for NBHZ, HBHZ, MHZN, and HHZB. The ELF scale has a range of 0.0 to 1.0. The maximum limit, denoted by white (1.0), represents localized electron zones that can be either bonding or non-bonding. Yellow to green hues (0.5) indicate intermediate ELF values, whereas blue patches indicate lower ELF values related to non-bonding electrons. The title molecules are notable for having a delocalized electron cloud, which is shown by the presence of a blue zone around the carbon and oxygen atoms. This property might enhance the chemicals' antioxidant activity.

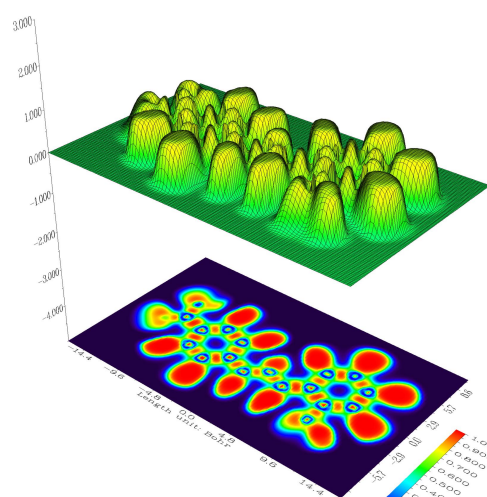
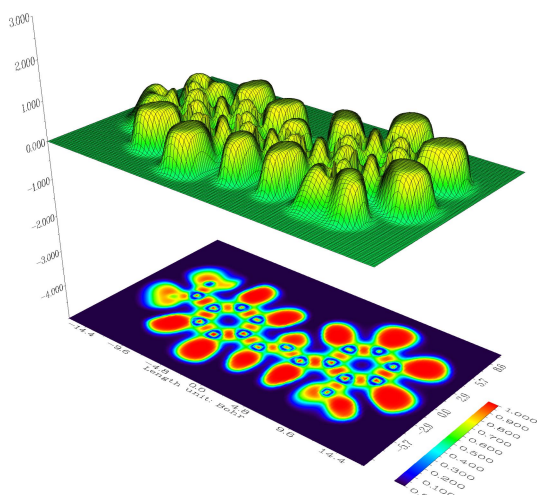
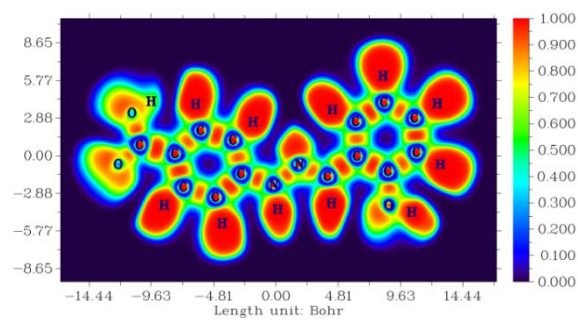
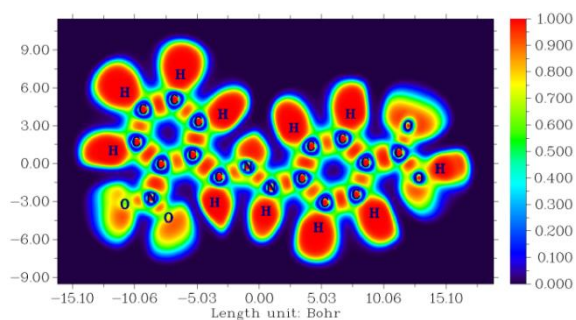
Additionally, the LOL analysis was very helpful in examining the synthetic aromatic hydrazone molecules [17]. The LOL study has yielded significant new knowledge regarding the biological interactions between the atoms in the molecule. In Bohr units, LOL values for all chemicals vary from -15.10 to -14.44. These values correspond to color ranges from blue to red, between 0.000 and 0.800. The blue tint on the LOL maps indicates strongly delocalized n-orbitals at the oxygen, nitrogen, carbon, and other surrounding areas of the molecule. Conversely, the red color highlights tightly localized n-orbitals at hydrogen atoms.

The combination of LOL and ELF inquiries yields a thorough comprehension of electron location and bonding characteristics in the generated hydrazones. This information is crucial for understanding the properties and reactivity of these hydrazone compounds and could be used to create novel materials with specialized uses, especially when considering the antioxidant activity of the materials.

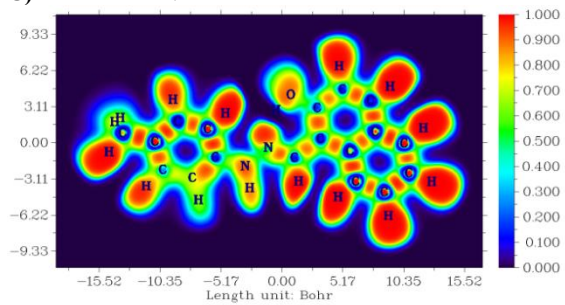
A) NBHZ

B) HBHZ

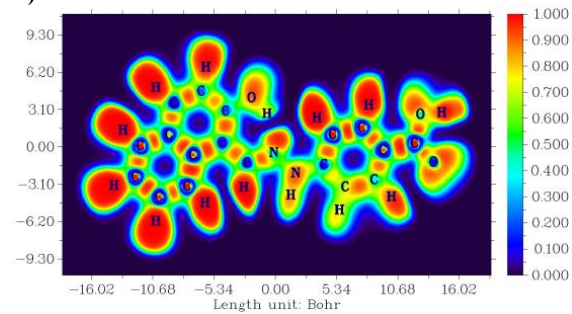
Chapter IV Structural and electronic study using Quantum Chemical Calculations



C) MHZN



D) HHZB



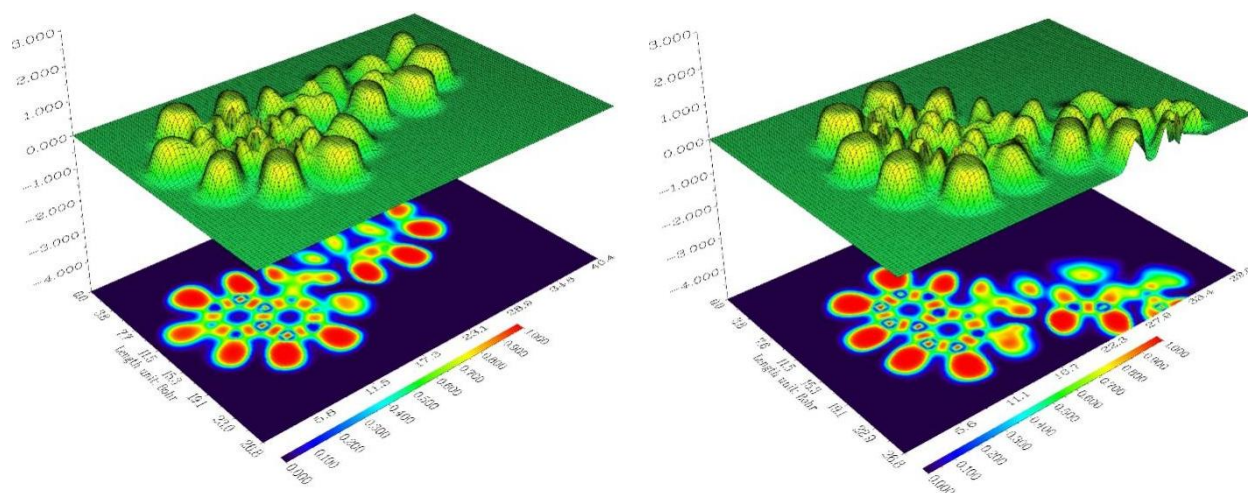


Figure IV. 10: Electron localized function maps of the aromatic hydrazone compounds

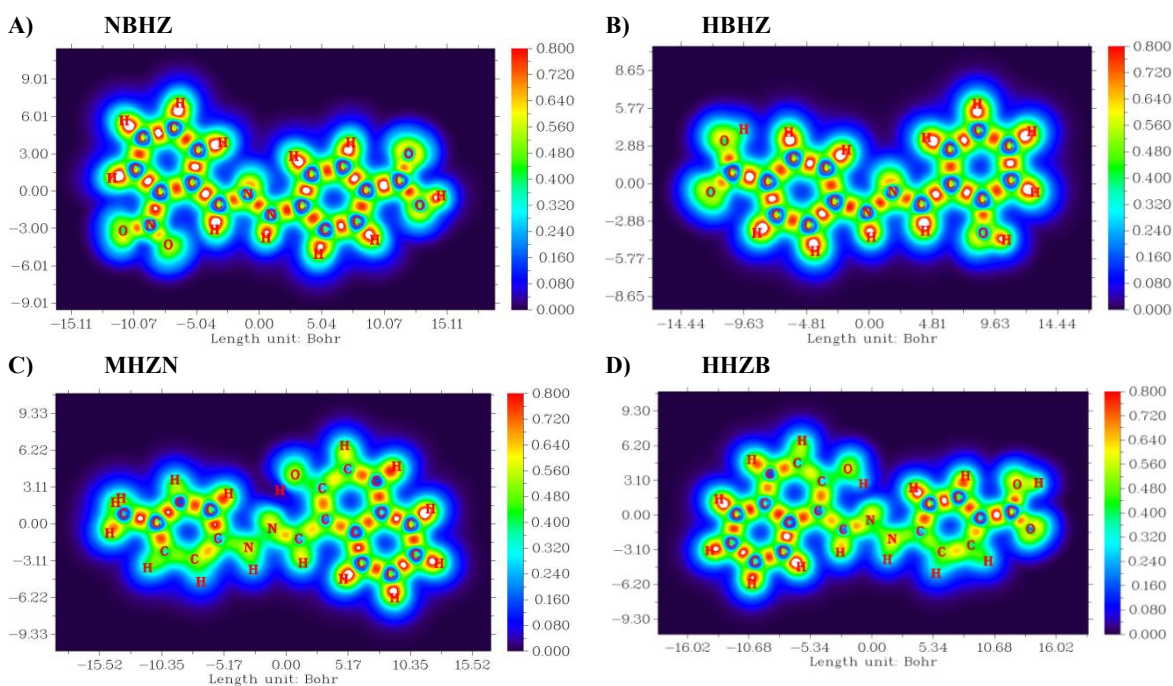


Figure IV. 11: Localized orbital locator maps of the aromatic hydrazone compounds

IV.5.2. Average localized ionization energy (ALIE)

Understanding Average Localized Ionization Energy (ALIE) is necessary to comprehend the electron removal process in a particular chemical system. For instance, electrophilic or radical reaction sites often have lower ALIE values, indicating the presence of strongly bound electrons and good sites for electron removal.

Figure VI.12 shows the maps that show each molecule's average localized ionization energy. The greenish-blue regions indicate that there are delocalized electrons at the carbon, nitrogen, and oxygen atoms. These electrons are responsible for different resonance structures and the exceptional stability of the compounds known as aromatic hydrazone. Even though the molecule under study lacks stable sigma bonds at carbon atoms exposed to proton absorption, blue areas represent them. On the other hand, red regions show a lot of bonds even when the molecule under investigation lacks these links [18,19].

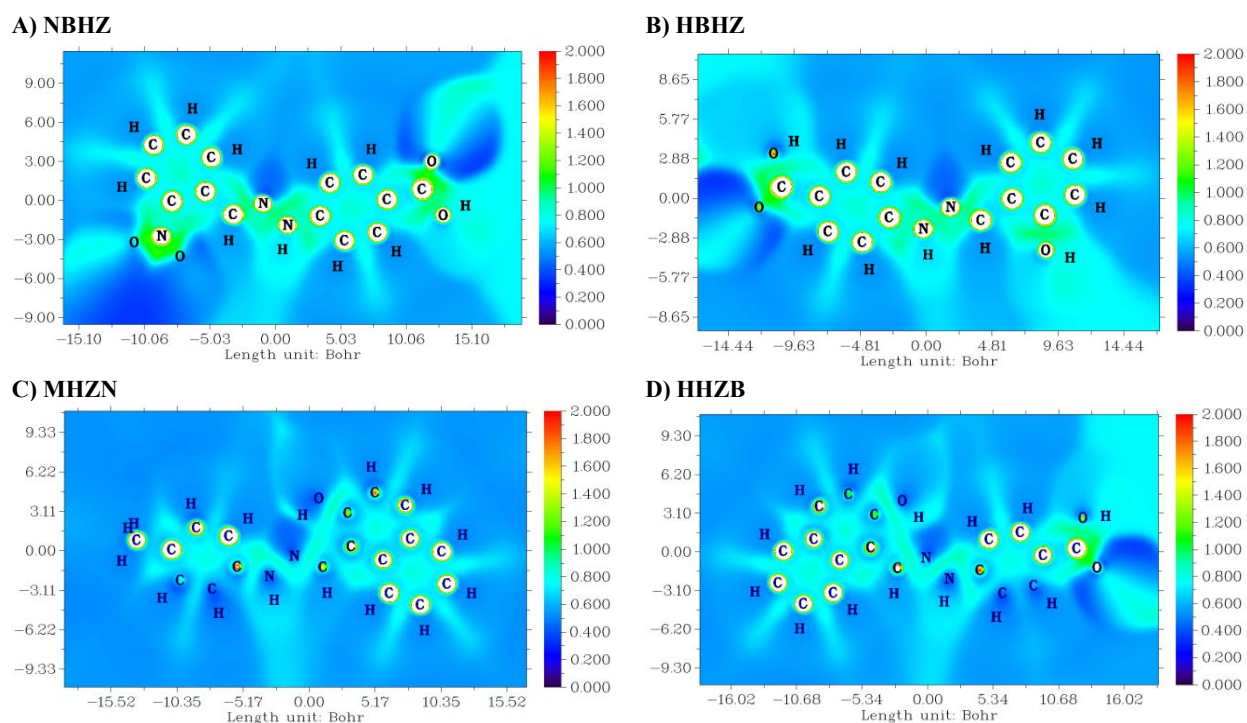


Figure IV. 12: Average localized ionization energy maps of the aromatic hydrazone compounds: A) NBHZ, B) HBHZ, C) MHZN, and D) HHZB.

IV.5.3. Reduced density gradient (RDG) analysis

An innovative theoretical method that is frequently used to investigate intermolecular interactions and define weak forces in molecular systems is the NCI theory. By using visualization indications based on density and relevant metrics, color-coded in accordance with the RDG values at low densities, this advanced approach offers insightful information about the type and strength of these interactions [20]. By evaluating the electron density (ρ) at each point on the isosurface and multiplying it by the sign of the second-highest eigen value of the Hessian

matrix of the electron density, the NCI methodology produces a product, represented as, that provides important insights into the nature of intermolecular forces.

$$s = \frac{1}{2(3\pi^2)^{1/3}} \frac{|\nabla\rho|}{\rho^{4/3}} \quad \text{Eq. (1)}$$

A negative sign denotes interactions that are essentially appealing and are frequently linked to the creation of hydrogen bonds, which are essential for the establishment of molecular associations. Comprehending the stability and characteristics of molecular complexes requires an understanding of these attractive forces. On the other hand, a positive value indicates the existence of non-bonding interactions or steric repulsion. These interactions are of great significance as they influence how molecules interact while maintaining their structural integrity [21]. By applying the NCI theory and its visualization indicators, we can better explore and analyze the intermolecular forces in hydrazone compounds, which will help us learn more about their molecular recognition, reactivity, and potential uses in a variety of scientific fields. The NCI-RDG plots derived from density analysis of the aromatic hydrazone compounds under investigation NHBZ, HBHZ, MHZN, and HHZB are displayed in Figure IV.13. The RDG plots offer an in-depth comprehension of the various intermolecular interactions that exist between the molecules of hydrazone, as seen by the analysis of Figure IV.13. Van der Waals forces, steric repulsive interactions, and hydrogen bonds are represented by the colors blue, green, and red, respectively. The sign of and the RDG isovalue, which range from -0.035 to 0.020 a.u., provide information about the type and severity of these interactions. Notably, these regions' electron clouds exhibit stability when they interact with suitable acceptors. The scatter diagram that shows how all hydrazone chemicals efficiently reduce steric-repellent interactions is especially notable. It is shown in red. The presence of hydrazone groups and electron-rich O and N atoms in the chemical structure of these hydrazone compounds helps to achieve this. The NCI-RDG charts are useful visual aids that clarify the complex intermolecular relationships between the many hydrazone chemicals. The overall stability and behavior of the hydrazone compounds are shaped by hydrogen bonding, van der Waals interactions, and steric repulsion, as demonstrated by these results, which offer significant insights into the spatial organization of intermolecular forces.

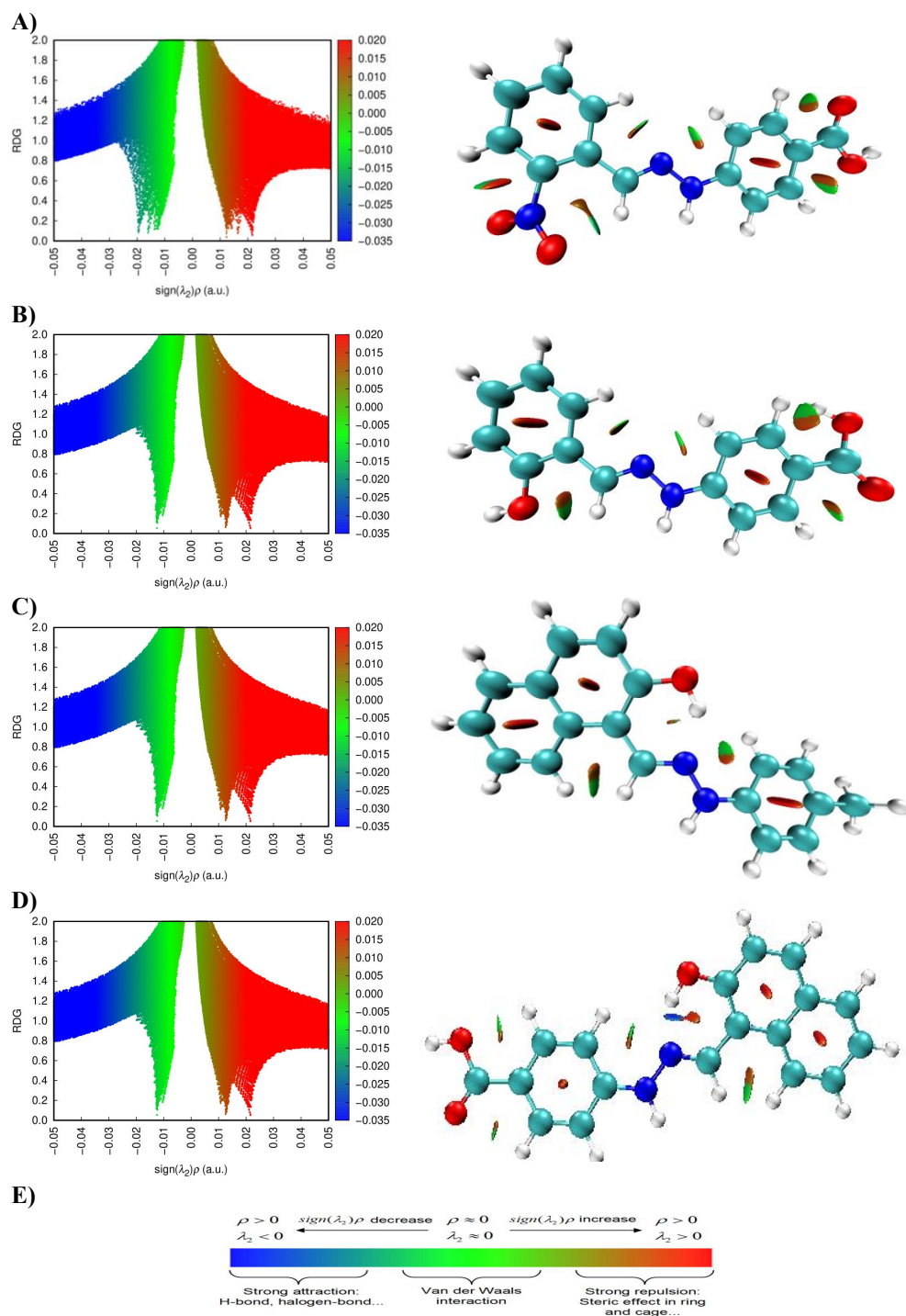


Figure IV. 13: The RDG scatter plots (left) and NCI plots (right) isosurface ($s = 0.5$ a.u.) of the aromatic hydrazones: A) NBHZ, B) HBHZ, C) MHZN, D) HHZB, and E) color map and chemical explanation.

References

- [1] D. Bálint, L. Jäntschi, Comparison of molecular geometry optimization methods based on molecular descriptors, *Mathematics*. 9 (2021) 1–12. <https://doi.org/10.3390/math9222855>.
- [2] M. Bourass, A.T. Benjelloun, M. Benzakour, M. Mcharfi, M. Hamidi, S.M. Bouzzine, M. Bouachrine, DFT and TD-DFT calculation of new thienopyrazine-based small molecules for organic solar cells, *Chem. Cent. J.* 10 (2016) 1–11. <https://doi.org/10.1186/s13065-016-0216-6>.
- [3] Z.M.E. Fahim, S.M. Bouzzine, A.A. Youssef, M. Bouachrine, M. Hamidi, Ground state geometries, UV/vis absorption spectra and charge transfer properties of triphenylamine-thiophenes based dyes for DSSCs: A TD-DFT benchmark study, *Comput. Theor. Chem.* 1125 (2018) 39–48. <https://doi.org/10.1016/j.comptc.2018.01.002>.
- [4] M.H. Jamróz, Vibrational energy distribution analysis (VEDA): Scopes and limitations, *Spectrochim. Acta - Part A Mol. Biomol. Spectrosc.* 114 (2013) 220–230. <https://doi.org/10.1016/j.saa.2013.05.096>.
- [5] N. Rani, Vikas, Computational rotational–vibrational spectroscopic analysis of isomeric species in the interstellar gas-phase stereoinversion of amino acid threonine, *Mol. Astrophys.* 15 (2019) 8–16. <https://doi.org/10.1016/j.molap.2019.04.002>.
- [6] M.C. Scharber, D. Mühlbacher, M. Koppe, P. Denk, C. Waldauf, A.J. Heeger, C.J. Brabec, Design rules for donors in bulk-heterojunction solar cells - Towards 10 % energy-conversion efficiency, *Adv. Mater.* 18 (2006) 789–794. <https://doi.org/10.1002/adma.200501717>.
- [7] A. Kokalj, On the alleged importance of the molecular electron-donating ability and the HOMO–LUMO gap in corrosion inhibition studies, *Corros. Sci.* 180 (2021) 109016. <https://doi.org/10.1016/j.corsci.2020.109016>.
- [8] I. Paster, M. Shacham, N. Brauner, Investigation of the relationships between molecular structure, molecular descriptors, and physical properties, *Ind. Eng. Chem. Res.* 48 (2009) 9723–9734. <https://doi.org/10.1021/ie801318y>.
- [9] A. Choudhury, R.K. Gupta, R. Garai, P.K. Iyer, Tailoring Trap Density of States through

- Impedance Analysis for Flexible Organic Field-Effect Transistors, *Adv. Mater. Interfaces*. 8 (2021) 1–8. <https://doi.org/10.1002/admi.202100574>.
- [10] A. Choudhury, R.K. Gupta, R. Garai, P.K. Iyer, How to analyse a density of states, *Adv. Mater. Interfaces*. 8 (2021) 100002. <https://doi.org/10.1016/j.mtelec.2022.100002>.
- [11] M. Sheikhi, E. Balali, H. Lari, Theoretical investigations on molecular structure, NBO, HOMO-LUMO and MEP analysis of two crystal structures of N-(2-benzoyl-phenyl) oxalyl: A DFT study, *J. Phys. Theor. Chem.* 13 (2016) 155–169.
- [12] M.A. Hermsmeier, T.M. Gund, A graphical representation of the electrostatic potential and electric field on a molecular surface, *J. Mol. Graph.* 7 (1989) 150–152. [https://doi.org/10.1016/0263-7855\(89\)80019-0](https://doi.org/10.1016/0263-7855(89)80019-0).
- [13] A. Oliver, C.A. Hunter, R. Prohens, J.L. Rosselló, An improved methodology to compute surface site interaction points using high density molecular electrostatic potential surfaces, *J. Comput. Chem.* 39 (2018) 2371–2377. <https://doi.org/10.1002/jcc.25574>.
- [14] R. Praveena, K. Sadasivam, V. Deepha, R. Sivakumar, Antioxidant potential of orientin: A combined experimental and DFT approach, *J. Mol. Struct.* 1061 (2014) 114–123. <https://doi.org/10.1016/j.molstruc.2014.01.002>.
- [15] J. Wang, H. Tang, B. Hou, P. Zhang, Q. Wang, B.L. Zhang, Y.W. Huang, Y. Wang, Z.M. Xiang, C.T. Zi, X.J. Wang, J. Sheng, Synthesis, antioxidant activity, and density functional theory study of catechin derivatives, *RSC Adv.* 7 (2017) 54136–54141. <https://doi.org/10.1039/c7ra11496f>.
- [16] T. Lu, F. Chen, Multiwfn: A multifunctional wavefunction analyzer, *J. Comput. Chem.* 33 (2012) 580–592. <https://doi.org/10.1002/jcc.22885>.
- [17] H. Jacobsen, Localized-orbital locator (LOL) profiles of chemical bonding, *Can. J. Chem.* 86 (2008) 695–702. <https://doi.org/10.1139/V08-052>.
- [18] C.A. Reynolds, Theoretical organic chemistry, *Annu. Reports Prog. Chem. - Sect. B.* 90 (1993) 51–70. <https://doi.org/10.1039/OC9939000051>.
- [19] N. Al-Zaqri, T. Pooventhiran, F.A. Alharthi, U. Bhattacharyya, R. Thomas, Structural investigations, quantum mechanical studies on proton and metal affinity and biological activity predictions of selpercatinib, *J. Mol. Liq.* 325 (2021). <https://doi.org/10.1016/j.molliq.2020.114765>.

- [20] J. Priscilla, D. Arul Dhas, I. Hubert Joe, S. Balachandran, Spectroscopic, quantum chemical, hydrogen bonding, reduced density gradient analysis and anti-inflammatory activity study on piper amide alkaloid piperine and wisanine, *J. Mol. Struct.* 1225 (2021) 129146. <https://doi.org/10.1016/j.molstruc.2020.129146>.
- [21] A. Viji, B. Revathi, V. Balachandran, S. Babiyana, B. Narayana, V. V. Saliyan, Analysis of spectroscopic, quantum chemical calculations, molecular docking, RDG, ELF, anticancer and antimicrobial activity studies on bioactive molecule 2-[3-(4-Chlorophenyl)-5-(4-(propane-2-yl) phenyl-4,5-dihydro-1H-pyrazol-1-yl)-4-(4-methoxyphenyl)-1,3-thiazol, *Chem. Data Collect.* 30 (2020) 100585. <https://doi.org/10.1016/j.cdc.2020.100585>.

Chapter V

Evaluation of the anticorrosion activity of the synthesized hydrazones

Chapter V Evaluation of the anticorrosion activity of the synthesized hydrazones

The findings of an experimental investigation of the synthetic product's ability to prevent XC48 carbon steel from corroding in a 1M HCl solution are the main subject of the five chapter. Many approaches were used such as surface characterization methods (atomic force microscopy (AFM)) and electrochemical methods (polarization curves and impedance spectroscopy). By computing quantum chemical indices, these investigations seek to demonstrate a relationship between inhibitory efficiency and molecular structure. In addition, they seek to ascertain the adsorption energy and clarify, depict, and understand the inhibitor molecules' molecular adsorption topologies and behaviors on the metal surface.

V.1. Electrochemical measurements

Given to the effect of inhibitor concentration on the protection efficiency of metals from corrosion we must determine the optimum amount of hydrazone which gives the satisfied results, In our case we had been looking for the optimum concentration which present maximum efficiency of the synthesized inhibitors, for NBHZ, HHBZ and HHZB are insoluble in acidic media and because of this property we could not put them under corrosion study unlike MHZN which was found soluble.

PGZ 301 voltalab 40 was used for the electrochemical measurements, and Volta Master IV software was used to analyze the data. The glass cell used for the measurements had three electrodes: XC48 steel as the working electrode (WE), a carbon plaque as the counter electrode (CE), and saturated calomel electrode (SCE) as a reference, with a surface $S = 0.2 \text{ cm}^2$. For every electrochemical test, the open circuit potential value (OCP) was fixed at 40 minutes at a scan rate of 0.5 mV/s . Different amounts of 1M HCl were utilized as the electrolyte. Using Tafel extrapolation of the polarization curves, the parameters, corrosion potential E_{corr} , and current densities i_{corr} were assessed. The corresponding inhibitory efficiency IE_P was computed using the subsequent formula:

$$IE_P(\%) = [(i_{0\text{corr}} - i_{\text{corr}}) / i_{0\text{corr}}] \times 100 \quad \text{Eq. (1)}$$

where $i_{0\text{corr}}$ and i_{corr} are the corrosion current density in the absence and presence of inhibitors, respectively.

Using alternating current (AC) at open circuit potential, the Electrochemical Impedance Spectroscopy (EIS) tests were carried out over a frequency range of 100 kHz to 10 mHz with an amplitude of 10 mV. Using the equation, the corresponding

Chapter V Evaluation of the anticorrosion activity of the synthesized hydrazones

inhibition efficiency (IE) of inhibitors was determined from the charge transfer resistance data.

$$IE_{EIS}(\%) = [(R_{ct} - R_{ct}^0) / R_{ct}] \times 100 \quad \text{Eq. (2)}$$

where R_{ct}^0 and R_{ct} are the resistance in the absence and presence of the acid respectively in electrochemical test.

V.1.1. EIS measurements

Figure V.1 illustrates how the MHZN concentration affects the Nyquist plot of the carbon steel under study in a 1M HCl solution. Additionally, Table V.1 presents the electrochemical parameters that were found using the Nyquist data, including inhibition efficiency (E_z (%)), solution resistance (R_s), double layer capacitance (C_{dl}), and charge transfer resistance (R_{ct}). The data shown in figure V.1 and table V.1 show that as the inhibitor concentration is increased, the R_{ct} values rise.

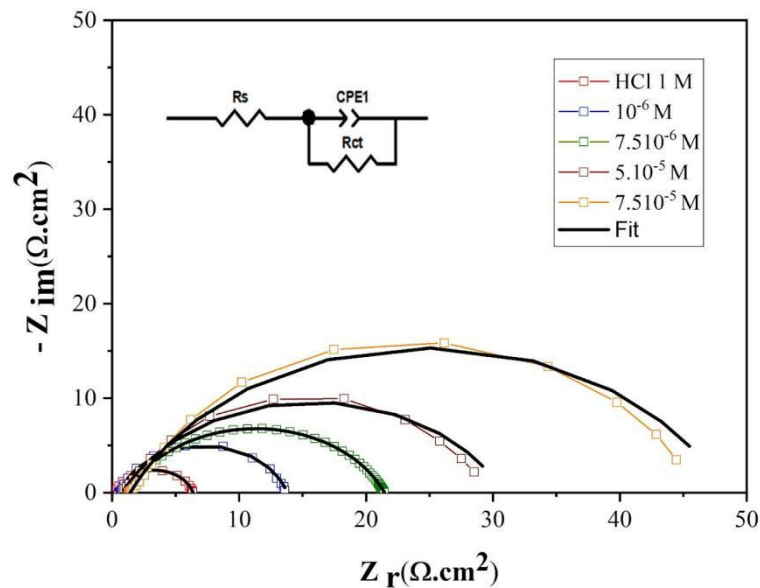


Figure V.1: Nyquist plots for XC48 carbon steel in 1M HCl solution in absence and in presence of various concentrations of MHZN at 25 °C.

The creation of a protective layer on the carbon steel surface is most likely responsible for the increase in R_{ct} . Moreover, the decrease in C_{dl} values is most likely linked to an increase in the electrical double layer's width, revealing that the MHZN shields the carbon steel from corrosion by adsorbing its molecules onto the iron surface.

Chapter V Evaluation of the anticorrosion activity of the synthesized hydrazones

Table V.1. Impedance parameters and inhibition efficiency values for carbon steel XC48 in 1.0 M HCl solution containing different concentrations of MHZN at 298 K.

Inh	C	R _{ct}	R _s	C _{dl uF}	IE _{EIS} (%)
	Blank	6.389	0.21	925	-
	10 ⁻⁶	12.1	0.5982	599	47.19
MHZN	7.5×10 ⁻⁶	20.86	1.262	432.59	69.37
	5×10 ⁻⁵	29.34	0.8129	352.71	78.22
	7.5×10 ⁻⁵	48.8	1.532	269.83	86.90

However, it is evident from figure V.1 that all of the generated Nyquist plots have forms that are almost identical to semi-circles. This suggests that the corrosion mechanism is unaffected by the addition of MHZN. Furthermore, The diameter of the Nyquist plot increased as the MHZN concentration increased, suggesting that the charge transfer mechanism regulates the corrosion of carbon steel in the aggressive medium [1].

The steel/solution interaction is frequently modeled using equivalent circuits, both with and without the inhibitor [1]. Based on the analogous circuit depicted in figure V.1 and ZView 2.3d software was used to match the experimental impedance spectra and yield the values for R_{ct}, R_s, and C_{dl} listed in table V.1. Strong correlation between the simulated and experimental impedance data is shown in figure V.1 which validates the suggested equivalent circuit for precise modeling of the carbon steel/solution interface.

V.1.2. Polarization curves

Table V.2 summarizes the results of the concentration effect of MHZN on the polarization curves, Figure V.2 illustrates how the anodic and cathodic branches of the polarization curves are pushed towards the low currents to the same extent when MHZN is present at varying concentrations. This behavior suggests that the produced hydrozone functions as a mixed-type inhibitor, regulating the anodic and cathodic reactions without altering the metal's anodic degradation or the cathodic release of hydrogen [2].

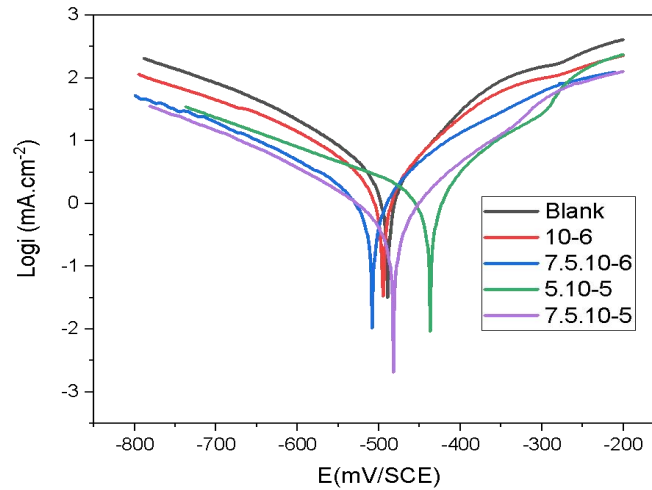


Figure V.2: Potentiodynamic polarization curves obtained for the XC48 carbon steel electrode in 1M HCl solution in presence of various concentrations of MHZN at 25°C.

Table V.2: Polarization parameters and the inhibition efficiency of carbon steel corrosion in 1.0 M HCl medium without and with different concentrations of MHZN at 298 K.

Inh	Concentration	E_{corr} (mV/SCE)	I_{corr} (mA.cm ²)	β_c	β_a	IE _p (%)
MHZN	Blank	-483.1	1.4393	-59.5	49.2	--
	10 ⁻⁶	-494.6	0.7073	-48.1	42.7	50.16
	7.5×10 ⁻⁶	-507.8	0.4357	-58	46.8	69.72
	5×10 ⁻⁵	-437.1	0.3094	-34.5	28.1	78.50
	7.5×10 ⁻⁵	-482.3	0.2308	-64.9	48.4	84.1

Moreover, Table V.2 demonstrates that the measured amounts of i_{corr} decrease as the both hydrazones levels rise. As a result, the inhibition efficiency goes up as the inhibitor concentration is increased and reaches its maximum value at 7.5×10^{-5} M. This suggests that the investigated hydrazone's inhibiting power is likely related to its adsorption on the iron surface, which results in the formation of a barrier film that protects. As a result, there is less space for corrosion on the metal surface, which inhibits the release of cathodic hydrogen and lessens the anodic dissolution of XC48 carbon steel [3].

V.1.3. Adsorption isotherm

For additional insights into the adsorption mechanism of MHZN and HHZB molecules onto the metal surface, alongside the exploration of thermodynamic parameters, various adsorption isotherm models were employed to reconcile the experimental findings. These models included Langmuir, Temkin, and Frumkin, among others. The Langmuir adsorption isotherm model, represented by Eq. (3) [4],

Chapter V Evaluation of the anticorrosion activity of the synthesized hydrazones

exhibited the most favorable agreement, as evidenced by correlation coefficients approaching unity ($R^2=0.999$) across all investigated temperatures. Herein, K_{ads} and θ denote the Langmuir adsorption equilibrium constant and surface coverage, respectively.

$$\frac{C}{\theta} = \left(\frac{1}{K_{ads}} \right) + C \quad \text{Eq. (3)}$$

The K_{ads} , can be obtained from the intercepts in figure V.3 is related to the standard Gibbs free energy of adsorption ΔG^0_{ads} as follow:

$$\Delta G^0_{ads} = -RT \ln (55.5 K_{ads}) \quad \text{Eq. (4)}$$

where R indicates the gas constant ($8.314 \text{ J} \cdot \text{K}^{-1} \cdot \text{mol}^{-1}$), T represents the absolute temperature (K) and the value 55.5 represents the water concentration in the solution (M).

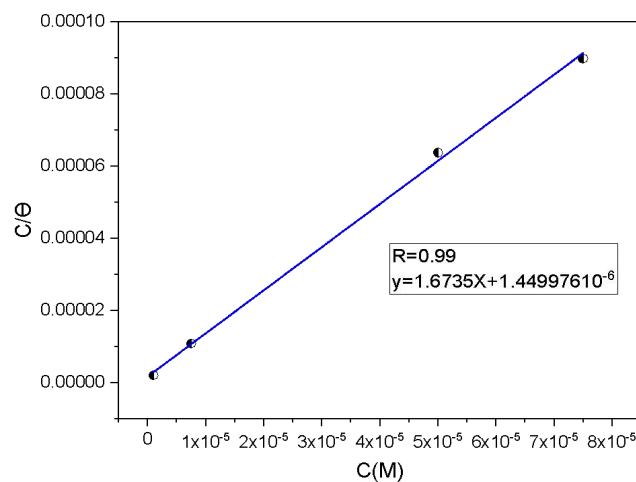


Figure V.3: Langmuir adsorption isotherm of XC48 carbon steel in 1M HCL solution in presence of MHZN inhibitor.

The adsorption of MHZN on the iron surface, the calculated ΔG^0 value is -43.25 kJ/mol. The presence of strong contacts between the inhibitor molecules and the carbon steel surface is generally indicated by the negative sign of ΔG^0 , which also indicates the spontaneous nature adsorption onto the iron surface [5]. Moreover, the calculated ΔG^0 value is less than -40 kJ/mol, indicating that chemical adsorption involving the creation of coordination and covalent bonds is the mechanism by which MHZN is adsorbed on the surface of carbon steel.

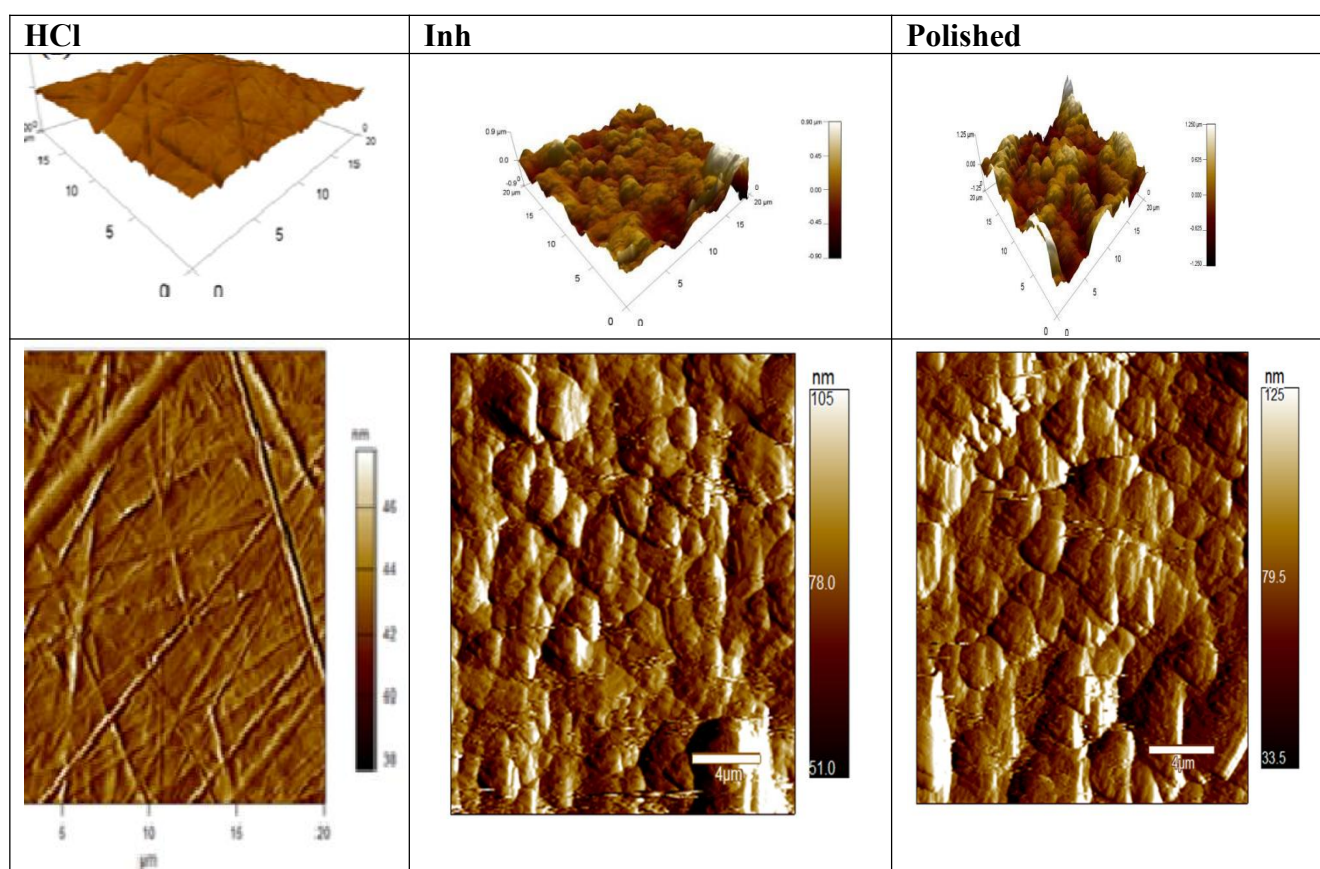
Chapter V Evaluation of the anticorrosion activity of the synthesized hydrazones

Table V.3: Standard thermodynamic parameters of the adsorption of MHZN and HHZB in 1.0 M HCl solution.

Inh	T(k)	K_{ads}	R^2	ΔG^0
MHZN	298	6.89669×10^5	0.99	-43.25 kJ/mol

V.2. Atomic Force Microscopy

AFM equipment was used for (AFM). After being immersed for 24 hours at 25°C in 1M HCl to show how a protective layer forms on the carbon steel surface two- and three-dimensional AFM pictures of a polished mild steel surface were acquired, Both with and without immersion in a 1 M HCl solution and with and without the inhibitor at optimal concentrations. The outcomes are displayed in figure V.4, and table V.4 provides the computed roughness which makes it abundantly evident that acid is causing carbon steel to break on its surface.



Chapter V Evaluation of the anticorrosion activity of the synthesized hydrazones

Figure V.4: 2D (on the Left) and 3D (on the Right) AFM images of carbon steel surface; (a) Polished carbon steel, (b) Carbon steel in 1 M HCl, (c) Carbon steel in 1 M HCl 7.5×10^{-5} M of inhibitor.

Table V.4.: The roughness obtained from AFM of carbon steel surfaces in 1 M HCl solution without and with inhibitor at 298 K.

Mild steel state	Polished	Blank	7.5×10^{-5}
Roughness (nm)	10.54	381.52	201.085

However, Figure V.4 shows that the corrosion on the metal surface decreased and the surface smoothed out when 7.5×10^{-5} M was present. According to table V.5, polished carbon steel had a rougher surface area (10.54 nm) than mild steel (381.52 nm) in 1 M HCl without an inhibitor. This strengthens the surface attack by acid on carbon steel. Nevertheless, the roughness dropped to 201.085 nm when the inhibitor was present at the ideal concentration. These findings suggest that the inhibitor molecules lowered the rate of metal corrosion by being adsorbed on the surface of the carbon steel [6,7].

V.3. Protection mechanism and comparison with other hydrazones

In general terms, The type and charge of the metal as well as the inhibitor molecules' chemical structure should have an impact on the corrosion inhibitor's method of action on metal surfaces in acidic media. The adsorption MHZN on the XC48 surface can be illustrated in figure V.5. The HCl solution used in corrosion inhibition studies causes the metal surface to become positively charged. Furthermore, Protonation is anticipated for the tested inhibitor. This form involves a positively charged metal that will encourage the adsorption of chlorides (Cl^-) on its surface. This will strengthen the attractive interactions between the protonated inhibitor molecules and the charged metallic surface by forming a bridge. At the moment, physisorption is the main mechanism driving corrosion prevention, hindering the mild steel's reaction sites.

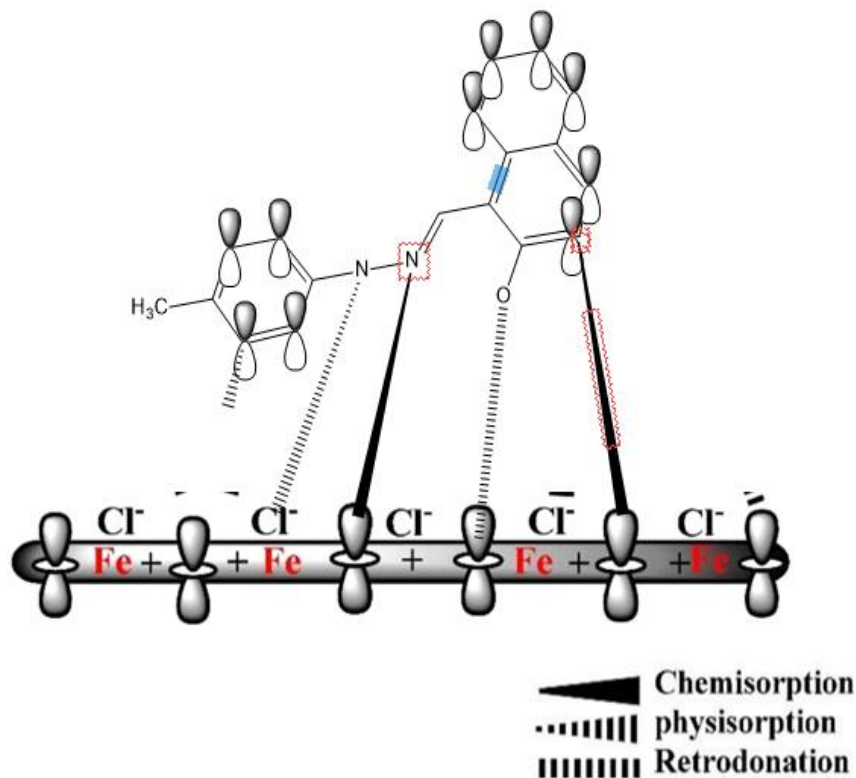


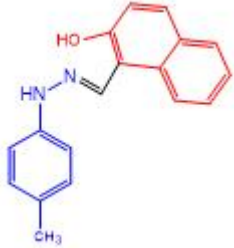
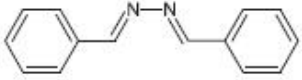
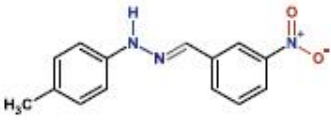
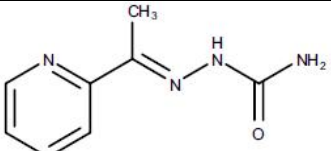
Figure V.5: Illustration of the protection mechanism of MHZN on XC 48 surface.

The transfer of loosely bound electrons from molecules to electron-deficient iron orbitals is predicted to increase in the aromatic rings' rich in electrons. The inhibitor's molecule can contribute π -electrons to unoccupied iron orbitals within this mechanism since it has three aromatic rings.

Several hydrazone derivatives have been evaluated for their ability to control corrosion in various metals and alloys in a number of recent articles. The effectiveness of this inhibitor family to prevent metal corrosion has been shown to be good. Table V.6 provides a comparison of MHZN with various hydrazone derivatives in acid conditions.

Chapter V Evaluation of the anticorrosion activity of the synthesized hydrazones

Table V.5: Comparison of the inhibition efficiency of MHZN with that of some hydrazone derivatives previously published.

Inhibitor Structure	C(M)	Ep	Ez	Reference
	7.5×10^{-5}	84.1	86.90	This work
	10^{-3}	84.00	83.00	[8]
	10^{-3}	87.13	86.41	[9]
	10^{-3}	85.2	87.29	[10]

MHZN demonstrated superior corrosion inhibition behavior and it is almost close to the previous synthesized hydrazones but MHZN can be the best from the economical side as it can be efficient at lower concentrations.

V.4. Molecular dynamic simulations (MDS)

The interactions between the inhibitor molecules and the carbon steel surface have been extensively studied and understood through the application of molecular dynamic simulations (MDS). A model was created for the interaction system with and without solvent molecules (vacuum slab). The equilibrium configurations of inhibitor molecules in aqueous solutions and a vacuum slab on Fe (110) surfaces are shown in figure V.6.

The inhibitor molecule is clearly seen to adsorb onto the Fe (110) surface in the vacuum slab scenario (Figure V.6 (a)), practically parallel to the metal surface and in close alignment with the stiff hydrazone's molecular structures. This finding demonstrates that the inhibitor molecule and iron atoms have a strong connection.

Analyzing the inhibitor's molecular structure reveals that the inhibitor's adsorption on carbon steel surfaces is made possible by the inhibitor's aromatic rings, nitrogen, and oxygen sharing electrons with iron to form coordinate bonds (chemical interaction). Additionally, as the strength of physical interactions typically scales with molecule size, the physical connection between the inhibitor molecules and the metal surface, driven by the Van der Waals dispersion forces, may also contribute to the net molecule surface attraction.

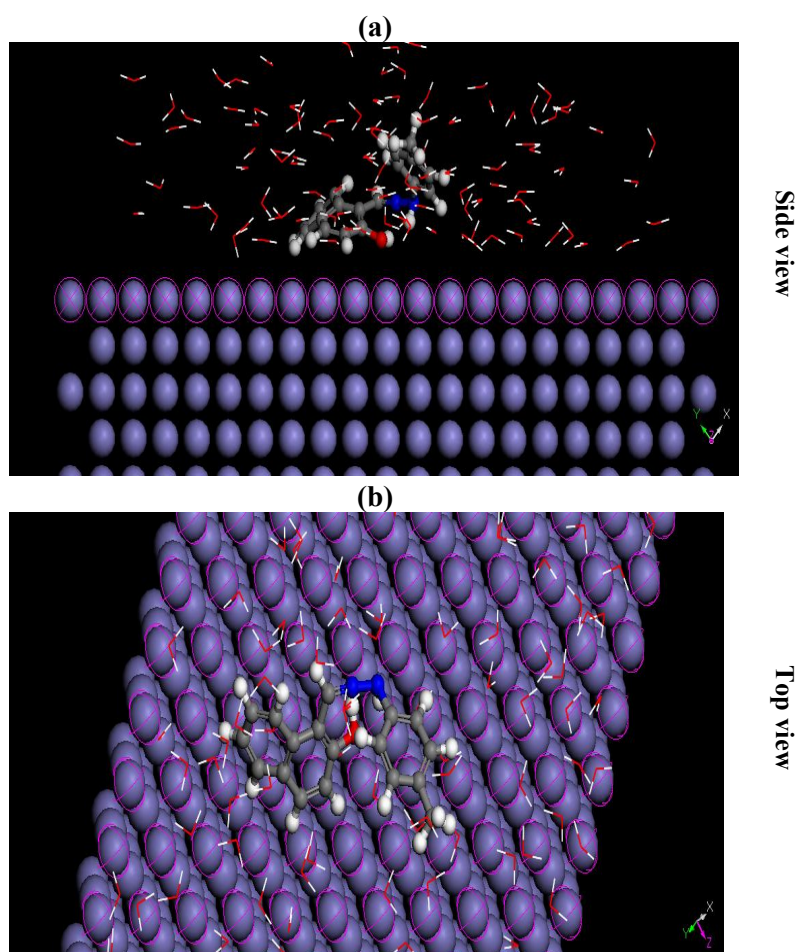


Figure V.6: Equilibrium configurations of the adsorbed inhibitor molecule on Fe (100) surface in (a) Side view and (b) Top view.

Table V.6 presents the computed binding energy and interaction energy. The spontaneity of the adsorption process is indicated by the negative value of the interaction energy ($-663.023 \text{ kJ mol}^{-1}$) between the iron atoms and inhibitor molecules. A more stable inhibitor/surface association results from a negative interaction energy and a higher binding energy between an inhibitor molecule and a metal surface [11,12].

Table V. 6: Interaction and binding energies between the inhibitor molecules and Fe (110) surface.

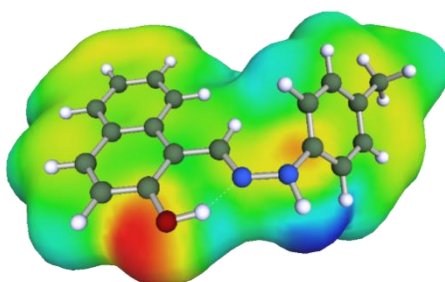
Systems	$E_{\text{Interaction}}$ (kJmol ⁻¹)	E_{binding} (kJmol ⁻¹)
Fe + MHZN	-663.023	663.023
Fe + MHZN + Water	-701.653	701.653

V.5. COSMO-RS implementation

To deeply understand how the MHZN compound and the Fe cluster interact and how their charges are distributed, the COSMO-RS method is very useful. This computational method is great at predicting solvation effects, making it especially helpful for studying corrosion inhibition in complex systems. The COSMO-RS representation uses a specific color scheme: green for non-polar areas, red for regions that can accept hydrogen bonds (HBA), and blue for areas that can donate hydrogen bonds (HBD). Examining the charge surface areas of the studied molecules compared to the Fe cluster shows that they are mostly nonpolar, highlighting their hydrophobic nature. Notably, there are localized hydrogen bond acceptor (HBA) regions, especially around the oxygen atoms in the compounds and some iron atoms in the Fe cluster.

Figure V.7 shows the optimized 3D structures and charge surface areas of the studied compounds interacting with the Fe cluster. The color-coded regions clearly highlight potential interaction sites, providing valuable insights into how the compounds and the Fe cluster interact. The COSMO-RS method is crucial for understanding the solvation and charge distribution of these compounds, which is essential for explaining how they inhibit corrosion. The charge distribution affects how these molecules adsorb onto metal surfaces. Additionally, the COSMO-RS approach helps predict the solubility and stability of the inhibitors in corrosive environments, enhancing our understanding of their effectiveness in preventing corrosion.

(a)



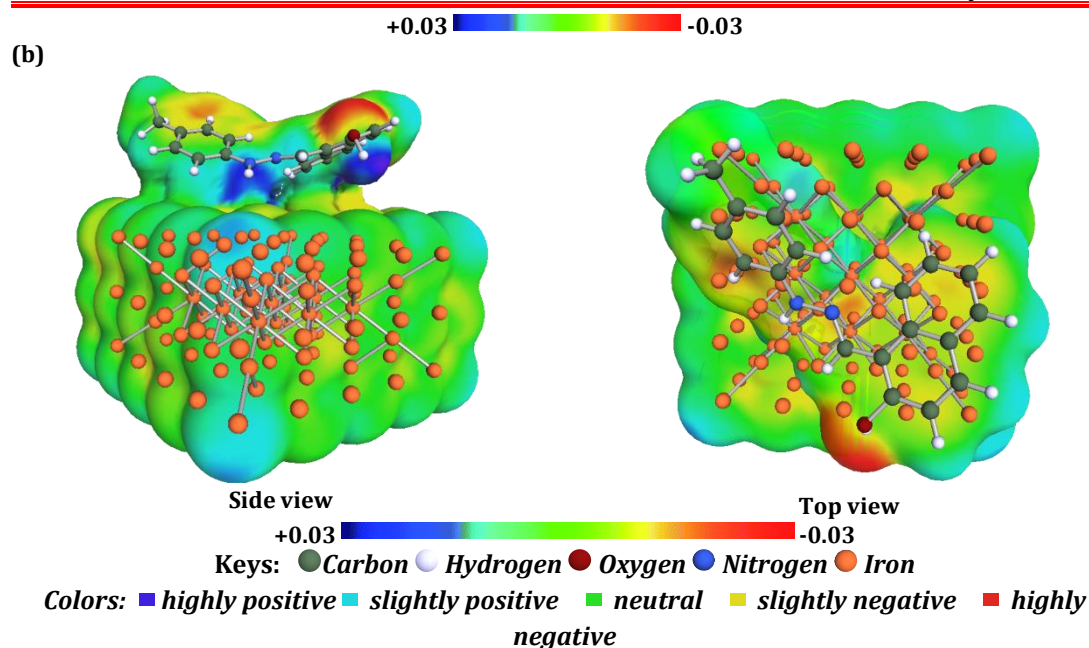
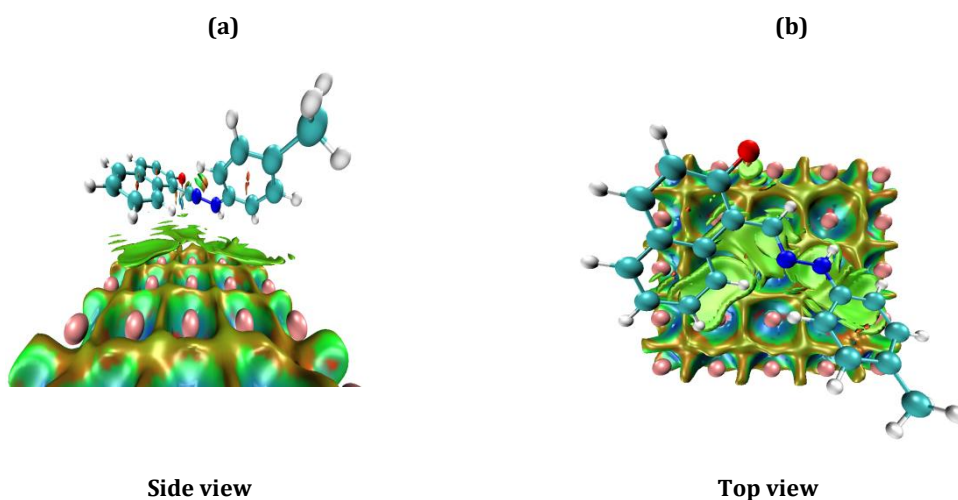


Figure V.7: Optimized COSMO-RS 3D structures and charge surface regions of the investigated compound binary interactions with Fe cluster

V.6 Non-covalent interaction (NCI) analysis

For NCI analyses based on the RDG as well as QTAIM analysis we utilized the computational tool Multiwfn to explore and identify potential weak interactions within the analyzed system. To visualize the results, we generated RDG plots and QTAIM maps by working with the Visual Molecular Dynamics (VMD) interface . Furthermore, color scatter plots of the components were created with the assistance of gnuplot . These advanced computational techniques facilitated an in-depth examination of weak interactions within the system under investigation.



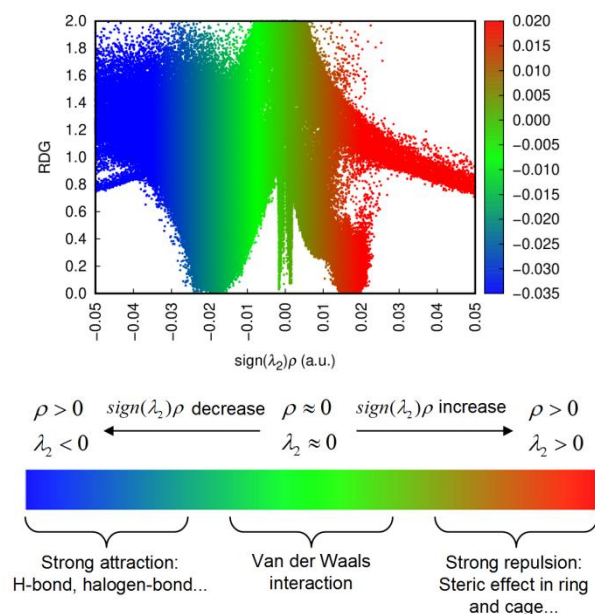
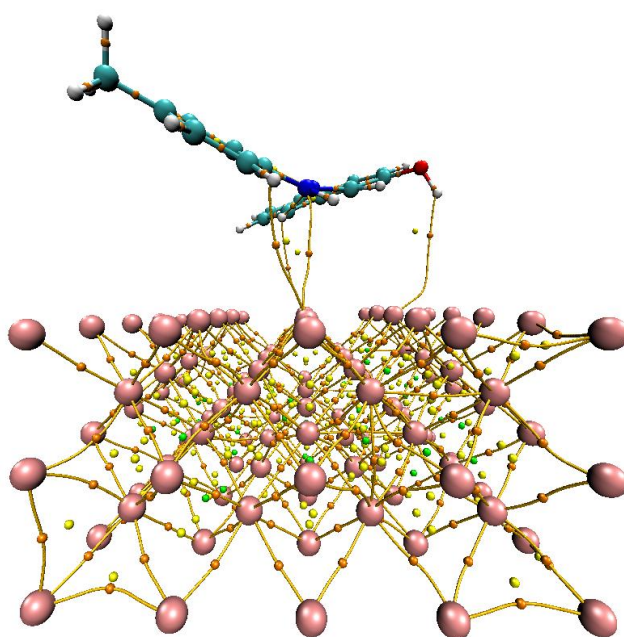


Figure V.8: Optimized COSMO-RS 3D structures and charge surface regions of the investigated compound binary interactions with Fe cluster.

V.7. Quantum theory of atoms in molecules (QTAIM) analysis

The quantum theory of atoms in molecules QTAIM analysis shown in figure V.8 provides a thorough picture of the chemical interactions that were created when MHZN and the XC48 surface interacted. This research, which offers a thorough examination of each component of the MHZN relationship is essential for comprehending the qualities and strengths of these bonds.



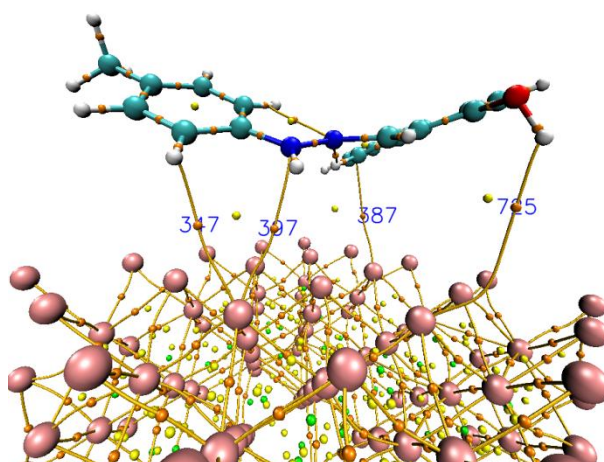


Figure V.9 :Molecular graphical representation using QTAIM for the adsorption of MHZN inhibitor system onto the composite surface XC48.

The QTAIM data demonstrate variations in electron density and Laplacian values, highlighting the varied strengths of the chemical bonds. To understand their behavior, one must grasp the strength of their bonds. The interactions between the MHZN molecules and the XC48 surface such as hydrogen bonding and Van der Waals forces are well captured by this technique.

References

- [1] C. Sci, R. Lett, D. Kesavan, M. Gopiraman, N. Sulochana, N. Sulochana, * D Kesavan, Chemical Science Review and Letters Green Inhibitors for Corrosion of Metals: A Review, Che Sci Rev Lett . 1 (2012) 1–8.
- [2] J. shuo ZHANG, X. xiang ZHONG, L. ZHANG, G. hua WU, W. cai LIU, Effect of heat treatments on microstructure and mechanical properties of sand cast Al–2Li–2Cu–0.5Mg–0.2Sc–0.2Zr alloy, Trans. Nonferrous Met. Soc. China (English Ed. 32 (2022) 411–423. [https://doi.org/10.1016/S1003-6326\(22\)65803-5](https://doi.org/10.1016/S1003-6326(22)65803-5).
- [3] R. Kerkour, S. Chafaa, N. Maouche, O. Moumeni, & N. Chafai, Corrosion inhibition of stainless steel N304 by dihydroxy benzyl phosphonic acid in 0.5 M H₂SO₄: Experimental and theoretical studies, Indian J. Chem. Technol. 26 (2019) 69–75.

Chapter V Evaluation of the anticorrosion activity of the synthesized hydrazones

- [4] O. Moumeni, S. Chafaa, R. Kerkour, K. Benbougerra, N. Chafai, Synthesis, structural and anticorrosion properties of diethyl (phenylamino) methyl phosphonate derivatives: Experimental and theoretical study, *J. Mol. Struct.* 1206 (2020) 127693. <https://doi.org/10.1016/j.molstruc.2020.127693>.
- [5] M. Djenane, S. Chafaa, N. Chafai, R. Kerkour, A. Hellal, Synthesis, spectral properties and corrosion inhibition efficiency of new ethyl hydrogen [(methoxyphenyl) (methylamino) methyl] phosphonate derivatives: Experimental and theoretical investigation, *J. Mol. Struct.* 1175 (2019) 398–413. <https://doi.org/10.1016/j.molstruc.2018.07.087>.
- [6] K. Benbougerra, S. Chafaa, N. Chafai, M. Mehri, O. Moumeni, A. Hellal, Synthesis, spectroscopic characterization and a comparative study of the corrosion inhibitive efficiency of an α -aminophosphonate and Schiff base derivatives: Experimental and theoretical investigations, *J. Mol. Struct.* 1157 (2018) 165–176. <https://doi.org/10.1016/j.molstruc.2017.12.049>.
- [7] G. Bertrand, E. Rocca, C. Savall, C. Rapin, J.C. Labrune, P. Steinmetz, In-situ electrochemical atomic force microscopy studies of aqueous corrosion and inhibition of copper, *J. Electroanal. Chem.* 489 (2000) 38–45. [https://doi.org/10.1016/S0022-0728\(00\)00163-7](https://doi.org/10.1016/S0022-0728(00)00163-7).
- [8] K.F. Khaled, M.M. Al-Qahtani, The inhibitive effect of some tetrazole derivatives towards Al corrosion in acid solution: Chemical, electrochemical and theoretical studies, *Mater. Chem. Phys.* 113 (2009) 150–158.
- [9] N. Chafai, S. Chafaa, K. Benbougerra, A. Hellal, M. Mehri, Synthesis, spectral analysis, anti-corrosive activity and theoretical study of an aromatic hydrazone derivative, *J. Mol. Struct.* 1181 (2019) 83–92. <https://doi.org/10.1016/j.molstruc.2018.12.073>.
- [11] M.P. Binsi, T.K. Joby, K. Ragi, V.C. Sini, J. Reeja, Interaction of two heterocyclic schiff bases derived from 2-acetyl pyridine on mild steel in hydrochloric acid: Physicochemical and corrosion inhibition investigations, *Curr. Chem. Lett.* 9 (2020) 19–30. <https://doi.org/10.5267/j.ccl.2019.006.005>.
- [12] N. Mechbal, M.E. Belghiti, N. Benzbiria, C.H. Lai, Y. Kaddouri, Y. Karzazi, R.

Chapter V Evaluation of the anticorrosion activity of the synthesized hydrazones

Touzani, M. Zertoubi, Correlation between corrosion inhibition efficiency in sulfuric acid medium and the molecular structures of two newly eco-friendly pyrazole derivatives on iron oxide surface, *J. Mol. Liq.* 331 (2021) 115656. <https://doi.org/10.1016/j.molliq.2021.115656>.

Chapter VI
Evaluation of the
biological activities of
the synthesized
hydrazones

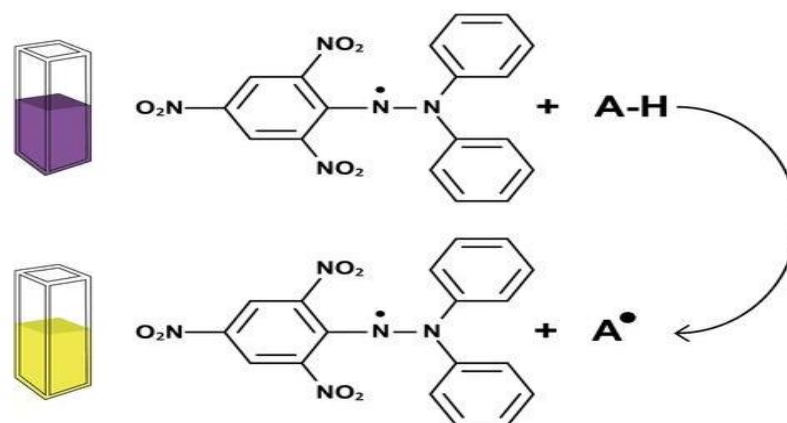
Chapter VI Evaluation of the biological activities of the synthesized hydrazones

An extensive assessment of the antibacterial and antioxidant properties of four different hydrazones is given in this chapter. Through the use of molecular docking to forecast and examine interactions with pertinent biological targets, the study explores the molecular mechanisms underlying their bioactivity. Hydrazones are investigated for their potential to treat bacterial infections and oxidative stress. Hydrazones are well-known for their adaptable chemical characteristics and biological uses. Computational modeling alongside with experimental assays offers a comprehensive understanding of their mechanisms and efficacy, providing important new information about their potential as therapeutic agents. The goal of this comprehensive strategy is to close the gap between chemical characteristics and biological activity.

VI.1. Antioxidant activity.

There are several techniques to assess antioxidant activity. The 2,2-diphenyl-1-picrylhydrazyl (DPPH) method was chosen for this inquiry because of its many benefits, which include cost-effectiveness, speed, convenience of use, and dependability. The DPPH test is a well-known method for determining how effective bioactive chemicals are at preventing radicals and it is well accepted in the scientific community. Interestingly, there is a noticeable change in the color of DPPH, which goes from purple to orange figure VI.1. This change is a good indicator of the antioxidant effectiveness and signifies the occurrence of antioxidant activity *via* the reduction of the (2,2-diphenyl-1-picrylhydrazyl) radical to diphenylpicrylhydrazine.

Chapter VI Evaluation of the biological activities of the synthesized hydrazones



DPPH - 2,2-diphenyl-1-picrylhydrazyl

Figure VI.1 Reduction of the DPPH• radical by A-H, where (AH) is a compound capable of yielding an H to the DPPH radical.

For the production of a radical solution, 4 mg of 2,2-diphenyl-1-picrylhydrazyl (DPPH) was dissolved in a 100 mL methanol solution. Subsequently, various concentrations of NBHZ, HBHZ, MHZN, and HHZB were obtained through dilution from a parent methanolic solution with a concentration of 1 mg/mL. Following this, 1000 μ l of the DPPH solution was introduced into each of the prepared concentrations. The samples were then subjected to a 30-minute incubation period in darkness at 25°C and absorbance was promptly measured at 517 nm. Control and blank solutions, denoted as (DPPH/MeOH) and (product/MeOH), respectively, were prepared. The resulting output was expressed in micrograms per milliliter (μ g/mL) of the sample, and inhibition percentage was quantified using Eq. (1).

$$Inh \% = \left(\frac{Abs_{Controle} - Abs_{Sample}}{Abs_{Controle}} \right) \times 100 \quad \text{Eq. (1)}$$

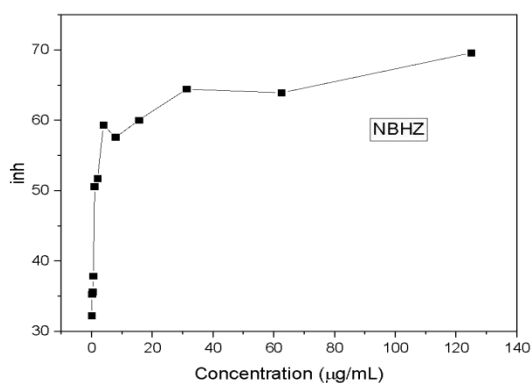
The DPPH assay results are shown in Figure VI.2 and VI.3, where an increasing increase in activity is seen in relation to the increasing amounts that were generated. The effectiveness of the chemicals being studied is gauged by the IC_{50} value, which represents the concentration at which 50% inhibition is achieved. A smaller IC_{50} value implies a concentration that can 50% lower the DPPH concentration. Because of this, our hydrazones show that they can absorb free radicals that are not bound by DPPH. Diminished IC_{50} values suggest that the compounds under test have a greater capacity to neutralize the DPPH radical.

Based on the experimental findings illustrated in figure VI.2 our hydrazone compounds have demonstrated the ability to effectively sequester unbound DPPH free

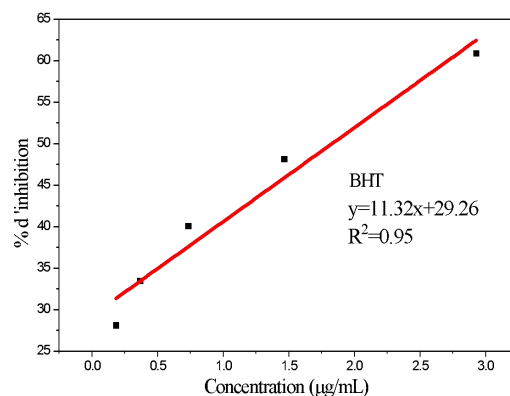
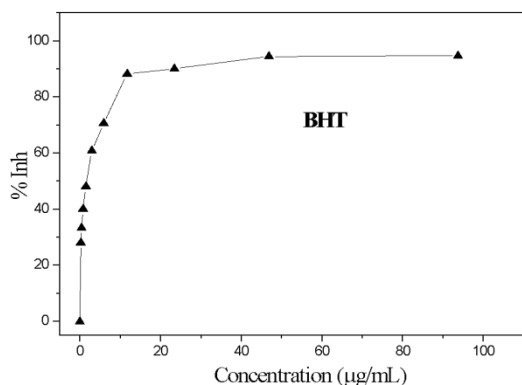
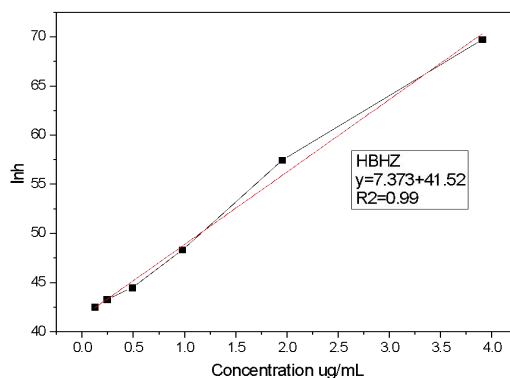
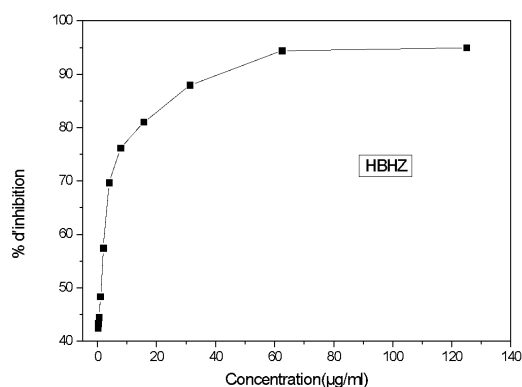
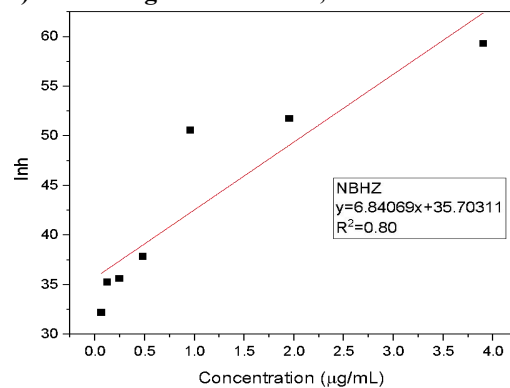
Chapter VI Evaluation of the biological activities of the synthesized hydrazones

radicals. The diminished values of IC_{50} reflect an augmented proficiency in neutralizing the DPPH radical. Notably, among the evaluated compounds, HBHZ emerged as the most efficacious DPPH radical scavenger, boasting an IC_{50} value of $1.15 \mu\text{g/mL}$. This performance compares favorably with the antioxidant BHT, which exhibited an IC_{50} of $1.83 \mu\text{g/mL}$. Conversely, NBHZ, with an IC_{50} of $2.1 \mu\text{g/mL}$, displayed a slightly diminished efficacy in trapping DPPH free radicals in contrast to BHT.

A) IC_{50} of NBHZ, HBHZ and BHT



B) Linear regression NBHZ, HBHZ and BHT



Chapter VI Evaluation of the biological activities of the synthesized hydrazones

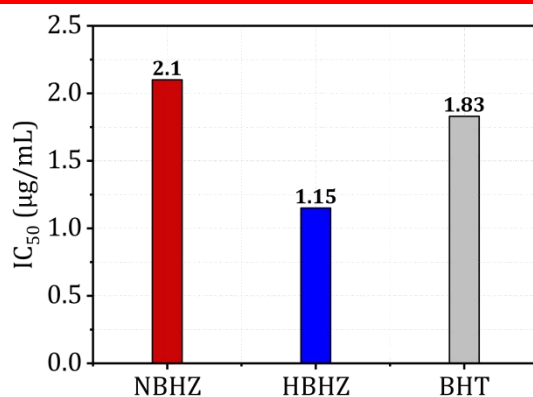
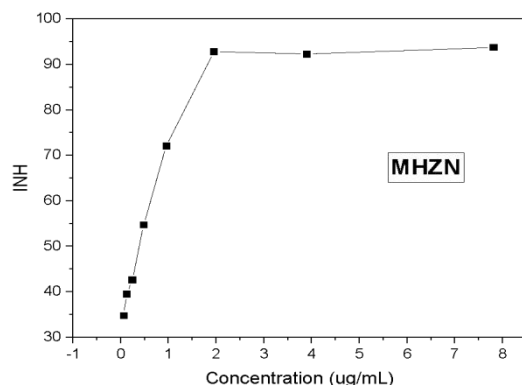


Figure VI. 2. IC₅₀ of NBHZ, HBHZ, and BHT; Linear regression between intern concentration and the inhibition percentage.

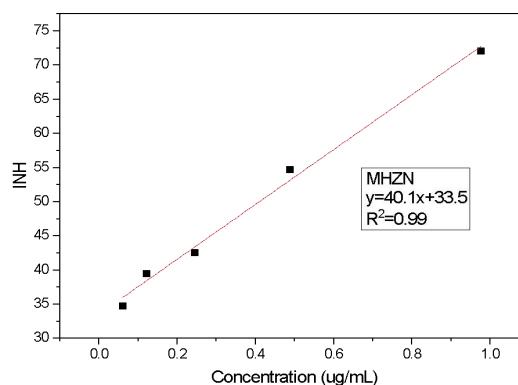
Conversely, as shown in figure VI.3, the investigated compound HHZB showcased the most robust capacity for capturing unbound DPPH free radicals, evident from its exceptionally low IC₅₀ value among all hydrazones, measured at 0.3343 µg/mL. This performance surpasses that of the antioxidant BHT, which registered an IC₅₀ of 1.83 µg/mL. Similarly, MHZN demonstrated notable efficiency against DPPH radicals, yielding an IC₅₀ of 0.4114 µg/mL, comparable to BHT's IC₅₀ of 1.83 µg/mL.

Numerous hydrazone compounds, as documented in literature [1–4], affirm their antioxidant activity. Whether potent, moderate, or comparatively weaker, their efficacy undoubtedly stems from the intricacies of their molecular structures. The presence of hydroxyl (OH) groups and benzene rings, intricately attached to substituents within the molecular framework, plays a pivotal role in this antioxidant activity. These structural elements facilitate the delocalization of π -electrons and ensure a well-dispersed electron distribution. Consequently, the molecule gains the capacity to liberate hydrogen, enabling it to effectively trap radicals.

A) IC₅₀ of MHZN, HHZB and BHT



B) Linear regression MHZN, HHZB and BHT



Chapter VI Evaluation of the biological activities of the synthesized hydrazones

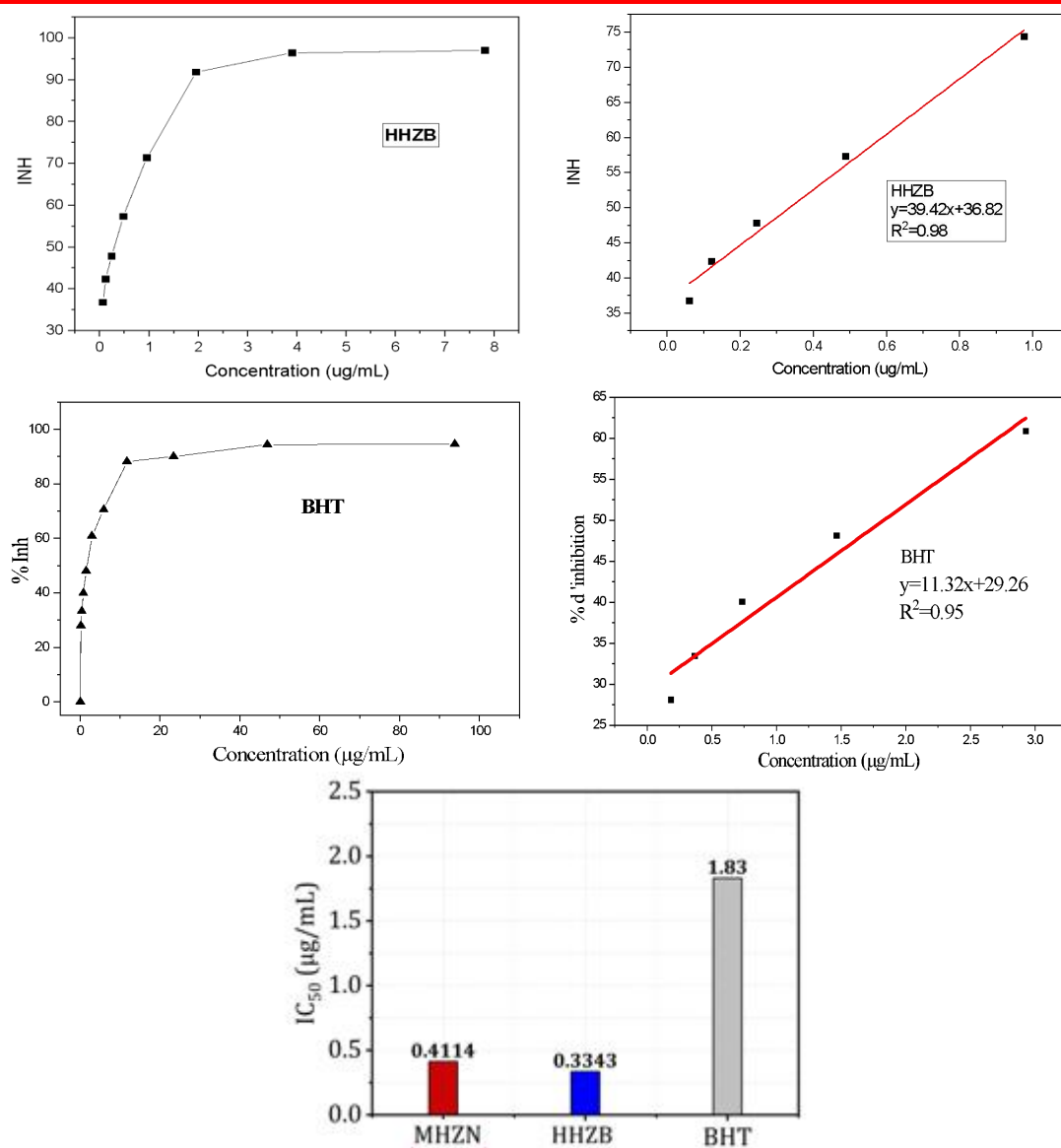


Figure VI.3: IC_{50} of MHZN, HHZB, and BHT; Linear regression between intern concentration and the inhibition percentage.

Through a comprehensive analysis of electronic structure topology, employing LOL and ELF analyses, our investigation indicates the presence of a delocalized electron cloud within the investigated molecules. This distinctive characteristic enhances their potential as antioxidants. Upon scrutinizing the acquired outcomes, it becomes apparent that the presence of a hydroxyl group in HBHZ imparts the molecule with a notable capacity for scavenging free radicals, contingent upon both their quantity and spatial arrangement. This is achieved by serving as a hydrogen donor, thereby neutralizing free radicals. Additionally, the hydroxyl group exhibits the capability to participate in resonance structures, which contribute to the stabilization of free radicals through the delocalization of unpaired electrons.

Chapter VI Evaluation of the biological activities of the synthesized hydrazones

Conversely, the effectiveness of NBHZ appears diminished, potentially attributable to the existence of an electron-withdrawing group (-NO₂). HHZB exhibited a high performance compared to HBHZ after addition of aromatic benzene in its structure which reflects the crucial role of aromatic cycle as mentioned above. Furthermore, MNHZ showed an efficiency slightly lower than HHZB which may refer to replacing CH₃ methyl group rather than carboxylic acid group COOH.

The quantum parameter denoted as HOMO plays a crucial role in anticipating the free radical scavenging potential of a given molecule. A heightened HOMO energy signifies an augmented electron donating capacity. The investigated hydrazone, HHZB, demonstrates the most elevated HOMO energy, recorded at -2.9154 eV as indicated in table VI.2 This observation aligns notably well with experimental findings, underscoring the strong correlation between theoretical predictions and empirical outcomes.

Conversely, the ionization energy parameter is derived from the negative value of the HOMO energy. Molecules characterized by low ionization energy are predisposed to facile electron loss, resulting in cation formation, and vice versa. Evaluating the ionization energy of hydrazones, HHZB, with an energy value of 2.9154 eV, stands notably lower than MHZN (6.4145 eV), HBHZ (6.7162 eV) and NBHZ (7.0496 eV) as depicted in table IV.2. This discrepancy underscores the superior scavenging potential of HHZB hydrazone in comparison to its synthesized counterparts.

VI.2 Antioxidant mechanism exploitation

The three main mechanisms involved in free radical scavenging are Hydrogen Atom Transfer (HAT), Single Proton Loss Electron Transfer (SPL-ET), and Sequential Electron Transfer (SET-ET) are thoroughly examined in this section. Important antioxidant characteristics, such as Bond Dissociation Energy (BDE), Ionization Potential (IP), Proton Dissociation Energy (PDE), Proton Affinity (PA), and Electron Transfer Entropy (ETE) are calculated as part of the study (Table IV.16). To gain a complete grasp of the computational strategy used in this study, refer to the methodology section for detailed descriptions of these factors.

Chapter VI Evaluation of the biological activities of the synthesized hydrazones

Table VI.1. Bond dissociation enthalpy (BDE), Ionization potential (IP), Proton dissociation enthalpy (PDE), proton affinity (PA) and Electron transfer enthalpy (ETE) of NBHZ, HBHZ MHZN and HHZB calculated in Kcal/mol at B3LYP/6-311 G (d, p) level in gas phase.

Inh	OH position	HAT	SPL-ET		SET-PT	
		BDE	PA	ETE	IP	PDE
NBHZ	C7-OH	418.2002	342.4076	76.5095	170.4615	248.4556
HBHZ	C17-OH	658.5589	541.1029	116.456	162.0918	495.4671
	C2-OH	392.4428	331.0849	62.0749	162.0918	231.0680
MHZN	C2-OH	179.2642	296.3651	73.8346	123.5680	243.5297
HHZB	C21-OH	212.8542	305.5624	76.7407	96.7214	285.2161
	C1-OH	153.5861	253.4703	49.0614	96.7214	206.5863

VI.2 .1 HAT mechanism

Table VI.1 displays the BDE values of all suggested antioxidant hydrazones which were calculated in the gas phase. BDE values relate to the enthalpy change that is given at a particular temperature when a chemical bond breaks under standard conditions. BDE values are related to the stability level displayed by the associated OH group; a lower value of this parameter indicates a lower stability level of the corresponding OH bond, making it more likely to break [6]. The following is the order in which the BDE values of NBHZ and HBHZ are found: HHZB (C1-OH) < MHZN (C2-OH) < HHZB (C21-OH) < HBHZ (C2-OH) < HBHZ < (C7-OH) < NBHZ (C17-OH). According to these results, the OH at position C2 of HBHZ differs from HBHZ (C7-OH) and NBHZ (C17-OH) in that it has a lower capacity to release H radicals. This could be the influence of the nearby carbonyl group, which makes it easier to break this OH.

VI.2 .2. Single electron transfer followed by proton transfer (SET-PT)

Table VI.1 compiles the IP and PDE important parameters. Although a lower IP value suggests a better ease of electron transfer, IP characterized the phenomena of electron donation by the antioxidant and reflected the antioxidant's ability to transfer electrons [7]. Although HHZB has the lowest IP value regardless of the position of OH, NBHZ has a greater IP value (170.4615 Kcal/mol) than the other hydrazones, indicating that it will have a harder time donating electrons.

Chapter VI Evaluation of the biological activities of the synthesized hydrazones

Conversely, the PDE values of hydrazones were discovered to be as follows: HHZB (C1-OH) < MHZN (C2-OH) < HHZB (C21-OH) < HBHZ (C2-OH) < HBHZ (C7-OH) < NBHZ (C17-OH). This parameter describes the compound's proton-releasing capacity; a lower PDE value suggests a higher sensitivity for antioxidants to release protons [8]. As a result, the position (C2-OH) of HHZB is the most easily deprotonated.

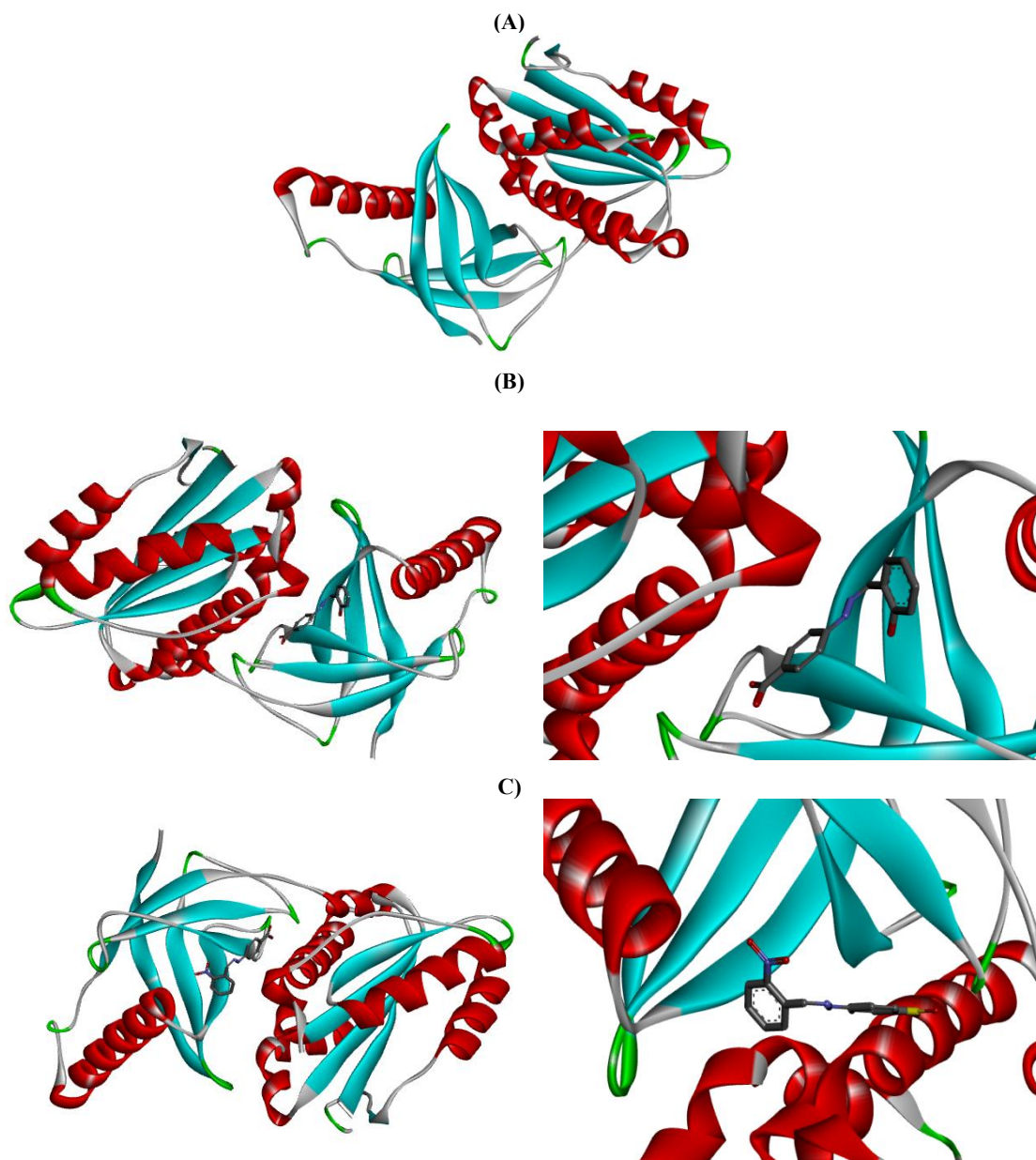
VI.2 .3. Sequential proton loss electron transfer (SPL-ET) mechanism

This mechanism consists of two steps: the first step's proton affinity (PA) and the second step's electron transfer enthalpy (ETE), which are governed by two important parameters. Table IV.16 also shows the proton affinity PA and ETE values of NBHZ and HBHZ. A lower PA score indicates increased antioxidant activity [9]. For every hydrazone, the acquired PA value was discovered in the following order: MHZN (C2-OH) < HHZB (C21-OH) < HBHZ (C2-OH) < HBHZ (C7-OH) < NBHZ (C17-OH). This indicates that HHZB is the most preferred site for deprotonation, which produces a highly stable anion, because it is easier for protons to transfer from C1-OH there than at other locations. Because MHZN (C2-OH) has the lowest ETE value, it is the preferred site to submit electron transfer, according to a comparison of the obtained values of ETE. The comparison of BDE values for HAT mechanism and PA as well as IP which control the first step of SPL-ET and SET-PT mechanisms respectively it was found that the IP has the lower value hence it can be deduced that SET-PT is the most thermodynamically favorable mechanism.

IV.3. Molecular Dockings studies

One important technique for anticipating the complicated binding interactions that result in the creation of a stable complex between a receptor and the ideal conformer of a ligand is molecular docking. Given that it helps the body's defenses against microorganisms by producing reactive oxidant species, antioxidant compounds were chosen with NADPH oxidase (NO) as their target.

Molecular docking studies were carefully carried out to examine the binding interactions between the ligands NBHZ, HBHZ, MHZN, HHZB and the NADPH oxidase receptor. The best-docked states of the NO-HBHZ, NO-NBHZ, NO-HHZB, NO-MHZN and NO-BHT complexes are depicted in Figure VI.26 together with the 3D and 2D binding-interaction diagrams of BHT with NADPH-Oxidase [10–12].



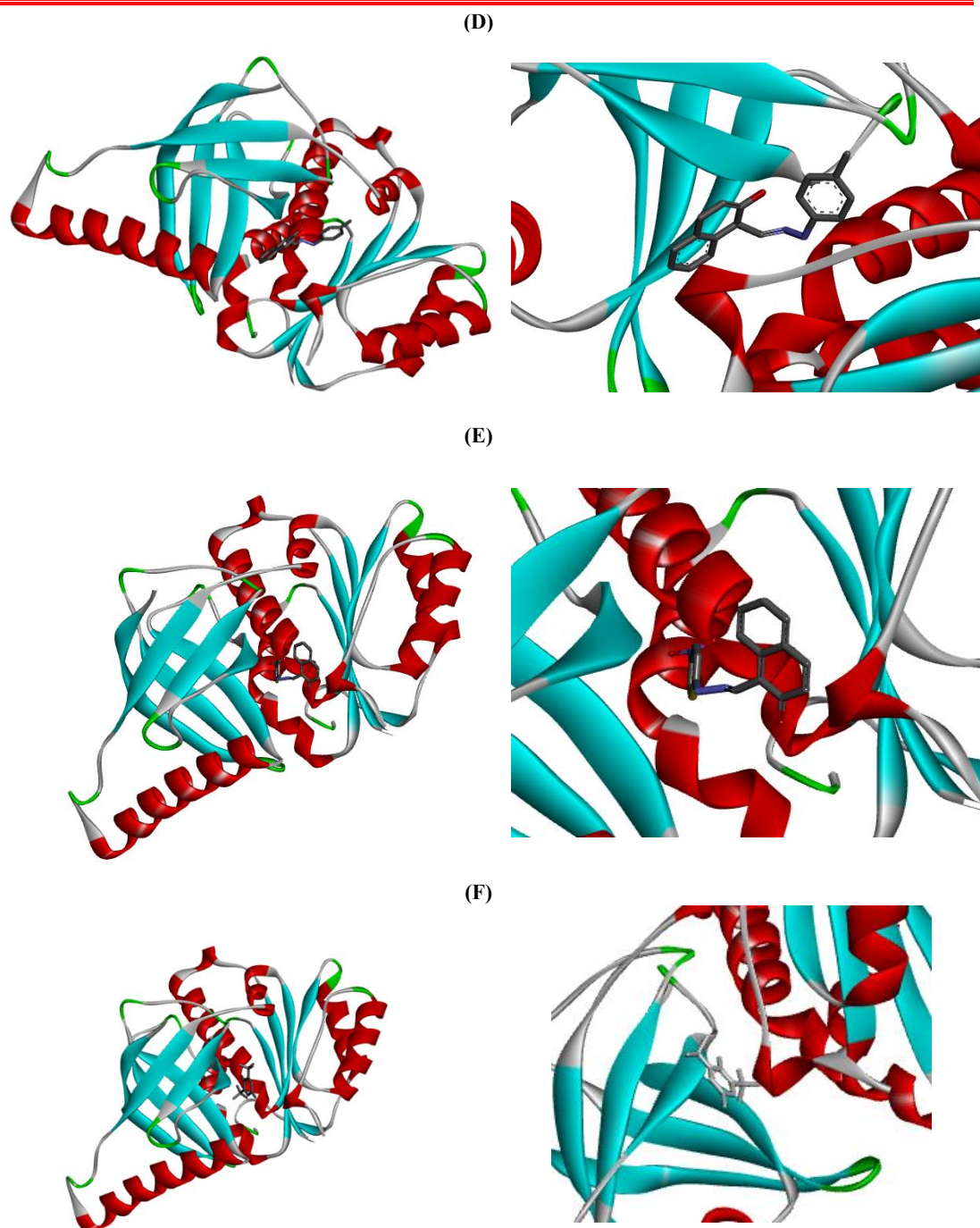


Figure VI.4. A) Crystal Structure of NADPH-Oxidase, B) Best docked pose visualization of HBHZ with NADPH-Oxidase, C) The best docked pose visualization of NBHZ with NADPH-Oxidase, D) The best docked pose visualization of MHZN with NADPH-Oxidase, E) The best docked pose visualization of HHZB with NADPH-Oxidase, and F) The best docked pose visualization of BHT with NADPH-Oxidase.

In table VI.2 it is evident that all ligands prefer to bind to the outer structure of the inner pocket of NADPH oxidase. Remarkably, both hydrazone ligands exhibited

Chapter VI Evaluation of the biological activities of the synthesized hydrazones

promising binding energy values, with -87.44 Kcal/mol for HBHZ, -103.12 Kcal/mol for NBHZ, -110.74 Kcal/mol for MHZN and - 124.32 Kcal/mol for HHZB.

The outcomes underscore the stability of these ligands within the NADPH oxidase pocket, attributed to the formation of diverse bonds with amino acids, including hydrogen and van der Waals bonds.

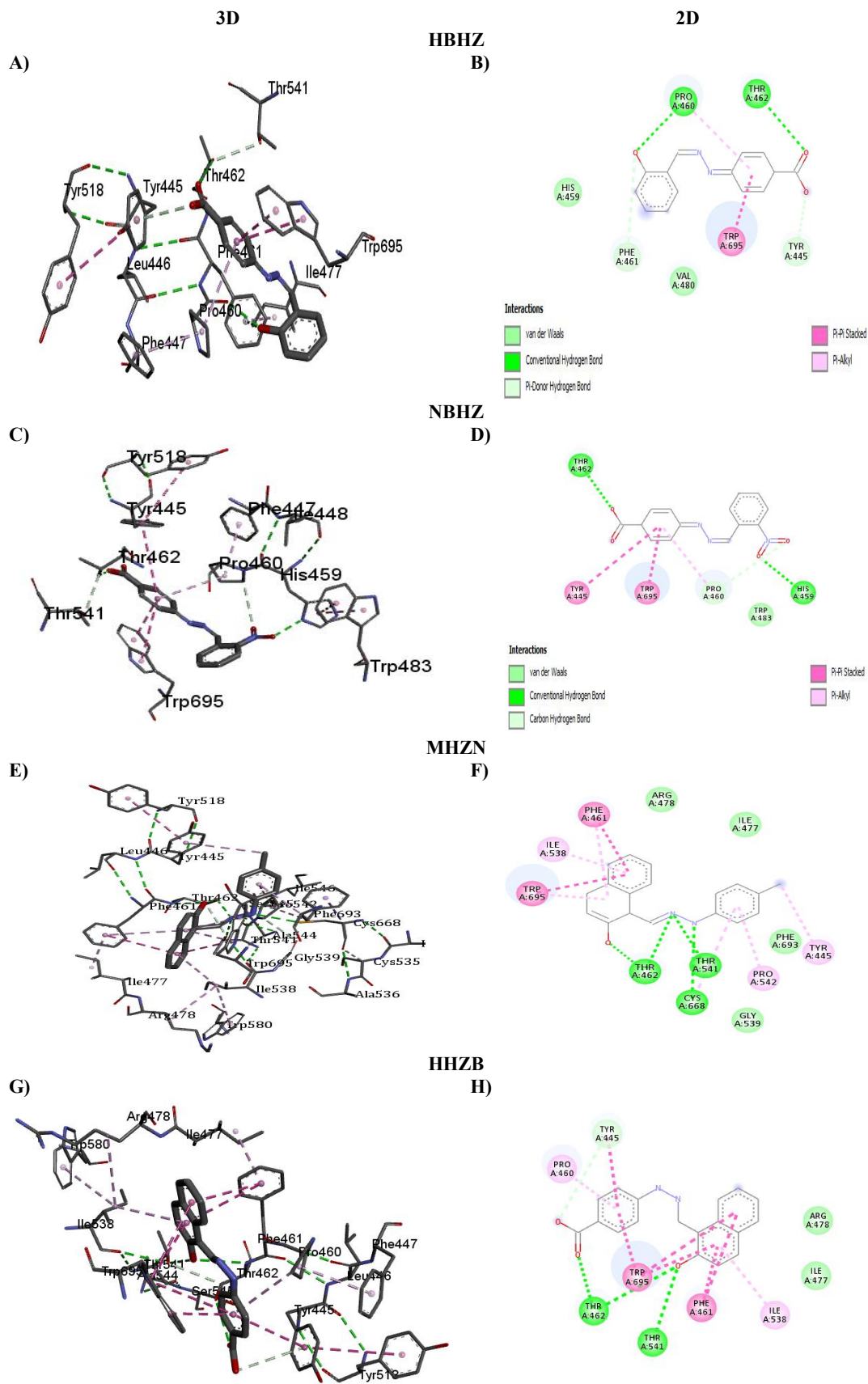
Table VI. 2: Molecular docking results and interactions of the investigated ligands with NADPH-Oxidase.

Ligand	Binding energy in kcal/mol	Amino acids	Interactions
HBHZ	- 87.44	PRO460	H Bonds
		THR462	H Bonds
		TYR445	Pi-Donor Hydrogen Bond
		PRO460	Pi-Alky
		PHE461	Pi-Donor Hydrogen Bond
		TRP695	Pi-Pi
NBHZ	- 103.12	HIS459	H Bonds
		PRO460	H bonds, VdW
		TYR445	Pi-Pi
		PRO460	Pi-Alky
		TRP695	Pi-Pi
HHZB	- 124.32	TRH462	H Bonds
		TRH541	H Bonds
		TYR445	Pi-Pi
		TRP695	Pi-Pi
		PHE461	Pi-Pi
		PRO460	Pi-Alky
		ILE538	Pi-Alky
		MHZN	-110.74
THR541	H Bonds		
CYS668	H Bonds		
PHE461	Pi-Pi		
ILE538	Pi-Alky		
TRP695	Pi-Alky, Pi-Pi		
TYR445	Pi-Alky		
PRO542	Pi-Alky		
BHT	- 84.21	PRO460	Pi-Alky, Pi-Pi
		THR462	H Bonds
		TYR445	Pi-Donor Hydrogen Bond
		PRO460	Pi-Alky
		PHE461	Pi-Donor Hydrogen Bond
		TRP695	Pi-Pi, Pi-Alky

The molecular docking data, as shown in figure VI.5 reveal different binding patterns. particular importance is the use of the nitro group's oxygen to generate a hydrogen bond between the NBHZ ligand and HIS459. Furthermore, a hydrogen bond with the carboxylic acid group's -OH establishes interactions with THR462. Additionally, secondary forces are involved, which enable the benzene group to form

Chapter VI Evaluation of the biological activities of the synthesized hydrazones

bonds with amino acids TRP695, TYR445, and PRO460 via Pi-Pi and Pi-Alkyl interactions, respectively.



Chapter VI Evaluation of the biological activities of the synthesized hydrazones

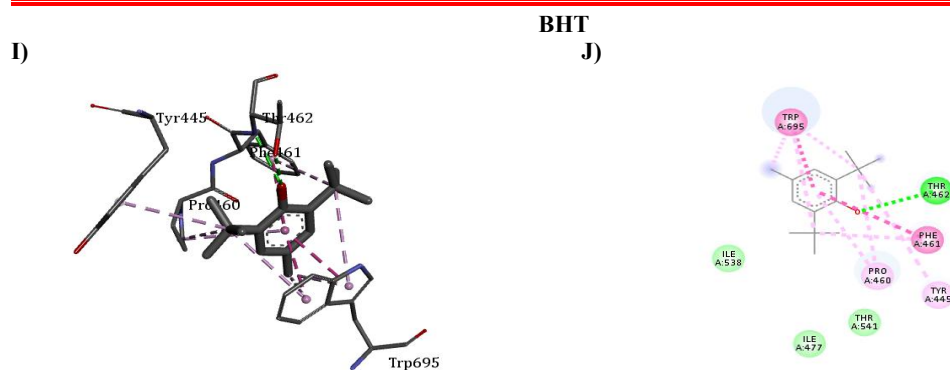


Figure VI. 5: 3D and 2D Binding-interaction diagrams of HBHZ (A and B), NBHZ (C and D), HHZB (E and F), MHZN (G and H) and BHT (I and J) with NADPH-Oxidase.

It is clear from looking more carefully at the 2D interaction diagram that HBHZ interacts with PRO460 and THR462 *via* a hydrogen bond. The stability of the complex is further aided by a number of secondary factors, such as Pi-Pi with TRP695, Pi-Alkyl with PRO460, and Pi-Pi with TYR445 amino acid. Lower binding energies are generally associated with stronger binds and higher stability, which are signs of greater potential for inhibition.

A deeper look at the 2D interaction diagram in figure VI.5 reveals that MHZN forms hydrogen bond interactions with THR462, THR541, and CYS668. A number of secondary variables, such as Pi-Pi interactions with PHE461 and Pi-Alkyl interactions with ILE538, TYR445, and PRO542 amino acids, contribute to the resilience of this complex. Lower binding energies typically indicate stronger bonds and greater stability, which suggests a greater chance of efficient inhibition.

IV.4. Antibacterial activity evaluation.

The minimum inhibitory concentration (MIC) of all compounds was ascertained by evaluating their *in vitro* antibacterial activity using a serial dilution method. *B. subtilis* and *S. aureus*, two gram-positive bacteria, were the subjects of the assessment. Furthermore, incorporated into the investigation were Gram-negative bacteria, specifically *S. enterica* and *E. coli*.

According to the outcomes displays in table VI.3 NBHZ shows an MIC values of 250 $\mu\text{g/mL}$ for all the strains while HBHZ exhibits 250 $\mu\text{g/mL}$ with just *B. subtilis* whereas 125 $\mu\text{g/mL}$ for the rest of strains. On the other hand, With an MIC value of 125 $\mu\text{g/mL}$, the MHZN compound exhibited equivalent antibacterial efficacy against

Chapter VI Evaluation of the biological activities of the synthesized hydrazones

Salmonella enterica, *E. coli*, and *B. subtilis*. On the other hand, it showed a MIC of 62.5 $\mu\text{g/mL}$ with *S. aureus*. At concentrations lower than this, the MHZN compound did not exhibit any antibacterial activity against any of the strains. The HHZB compound exhibited antibacterial activity against *S. enterica* (MIC of 31.25 $\mu\text{g/mL}$), *E. coli* (MIC of 125 $\mu\text{g/mL}$), *B. subtilis* (MIC of 62.5 $\mu\text{g/mL}$). and with MIC value of 15.62 $\mu\text{g/mL}$ against *S. aureus*, it was observed to have the maximum antibacterial activity against *S. aureus*. At levels below this value nevertheless, it exhibited no effect against any of the strains.

Table VI.3: MIC values ($\mu\text{g/mL}$) of hydrazone derivatives against gram-negative and gram-positive bacterial strains.

Compounds	Gram-positive		Gram-negative	
	<i>B. subtilis</i>	<i>S. aureus</i>	<i>E. coli</i>	<i>S. enterica</i>
NBHZ	250	250	250	250
HBHZ	250	125	125	125
HHZB	62.5	15.62	125	31.25
MHZN	125	62.5	125	125

Hydrazones have been investigated for a range of biological activities, such as their antibacterial capabilities. It has been discovered that certain hydrazones show moderate to strong antibacterial action against a variety of bacterial species. Depending on the particular hydrazone chemical and the bacterial strain under investigation, the activity may differ [13–17]. The carboxylic acid group (-COOH) may contribute to increased antibacterial action. It is well known that carboxylic acid groups make substances more hydrophilic and more soluble which may increase antibacterial activity may result from the carboxylic acid group's facilitation of interactions with particular bacterial targets, such as enzymes or receptors. If there is a methyl group (-CH₃) present in (MHZN) rather than a carboxylic acid group in HHZB the antibacterial activity can be reduced. On the other hand, by the examination of the investigated electronic properties of the tested compounds However, the dipolar moment values for NBHZ, HBHZ, MHZN and HHZB were found to be 0.8089, 0.8726, 2.5185 and 3.7422 debye, respectively, indicating their polarity. A molecule's polarity, which influences its solubility in various solvents, is influenced by its dipole

Chapter VI Evaluation of the biological activities of the synthesized hydrazones

moment. A compound's solubility can affect its bioavailability and dispersion. In comparison to a less polar chemical, a more polar compound with a larger dipole moment may show distinct solubility characteristics.

VI.4.1 Molecular docking

The Protein Data Bank (PDB) (www.rcsb.org) provided the first three-dimensional (3D) structures of *Salmonella enterica* serovar Typhimurium DsbA (PDB ID: 3L9S) [18], *Bacillus subtilis* YABJ (PDB ID: 1QD9) [19], *Staphylococcus aureus* OpuCA (PDB ID: 5IIP) [20], and *Escherichia coli* DNA Polymerase II (PDB ID: 1Q8I) [21]. Figure 2 displays their crystal structures. The optimized structures of HHZB and MHZN were then obtained by DFT calculations using the standard basis sets 6-311G (d,p) and the B3LYP functional. The iGEMDOCK software version 2.1 was used to perform docking simulations between the ligands and protein structures. To further aid in the viewing and study of the resultant complexes and their interactions, Accelrys' Discovery Studio Visualizer was used.

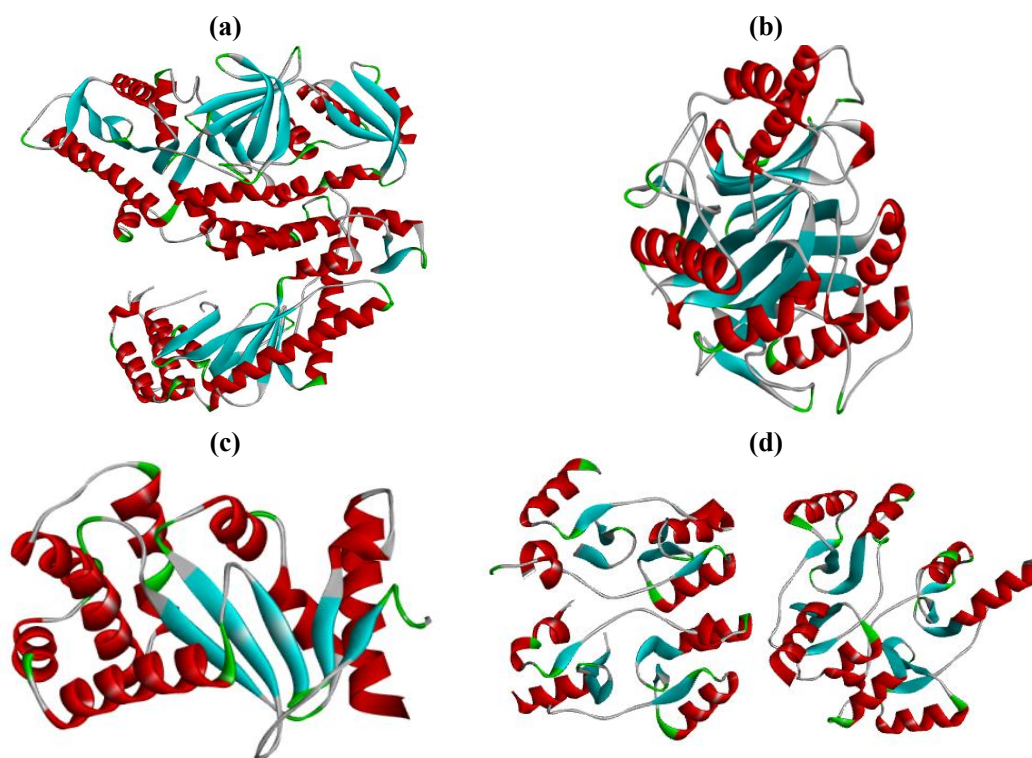
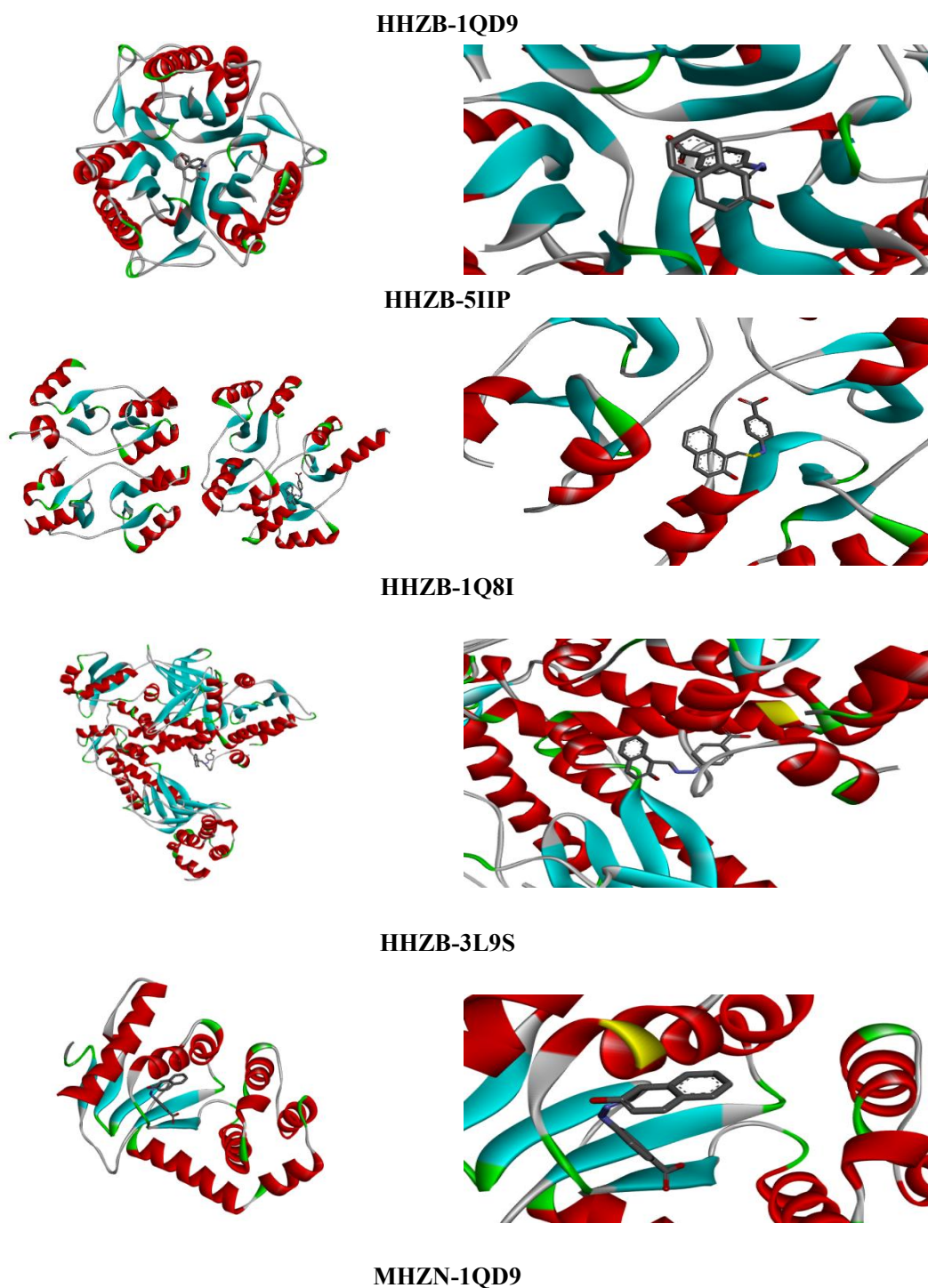


Figure VI. 6: Crystal structure of selected proteins (a) 1Q8I, (b) 1QD9, (c) 3L9S, and (d) 5IIP.

Employing molecular modeling methods to forecast how the hydrazones will bind to possible bacterial targets. In this context, Molecular docking simulations can be used to determine the binding poses that are most energetically favorable and can reveal important interactions that are responsible for the antibacterial activity.

Chapter VI Evaluation of the biological activities of the synthesized hydrazones

Molecular docking is used to forecast which way a ligand (or preferred orientation) would bind to a receptor to form a stable complex. Molecular docking can be utilized to examine the relationship between putative antibacterial drugs (ligands) and particular bacterial targets (receptors), like proteins or enzymes necessary for bacterial survival or replication, in the context of antibacterial activity . Figure VI 7 represents the crystal structures of the best-docked modes of MHZN and HHZB with 1QD9, 5IIP, 1Q81 and 3L9S.



Chapter VI Evaluation of the biological activities of the synthesized hydrazones

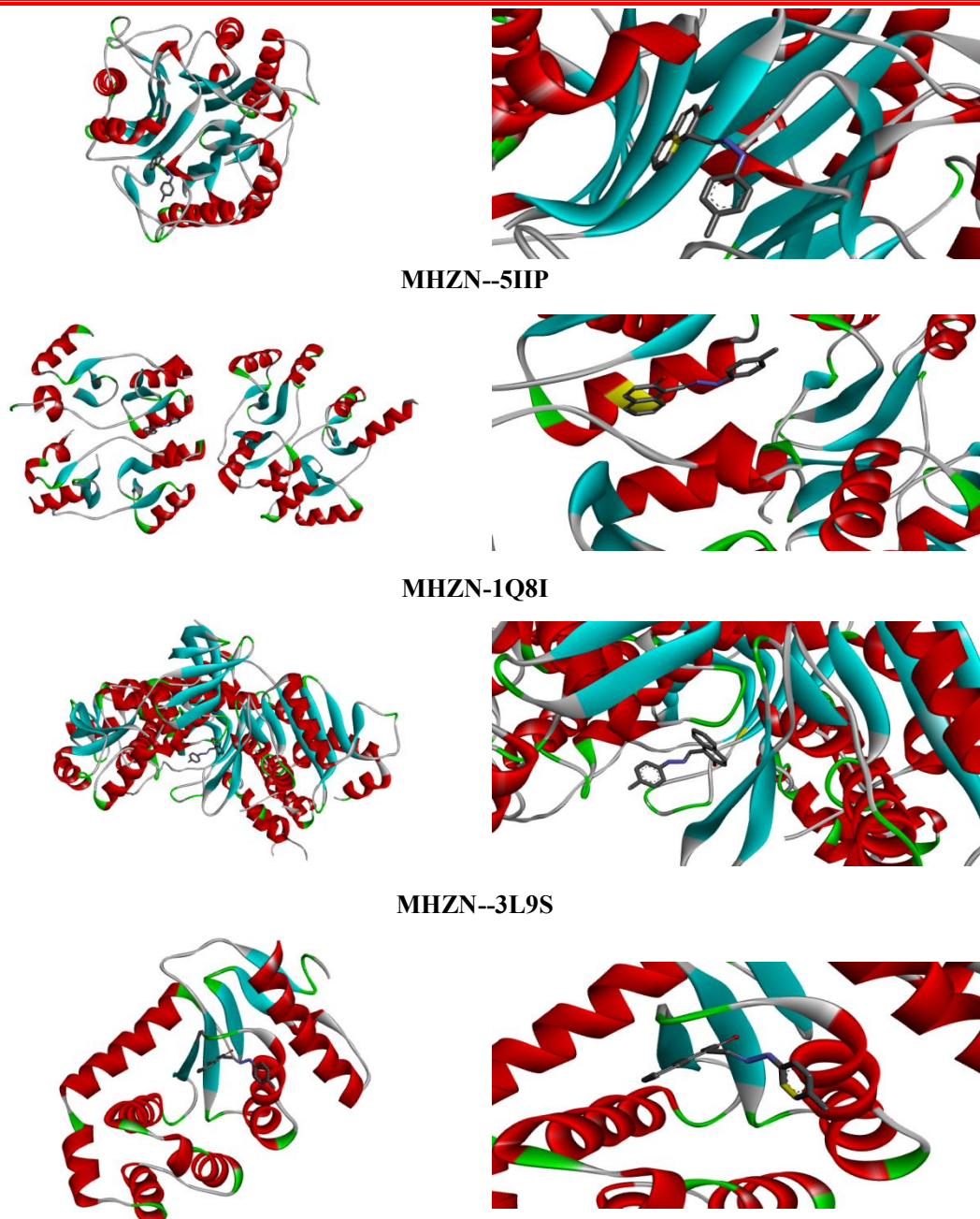


Figure VI. 7:. Best docked pose visualization of MHZN and HHZB with 1QD9, 5IIP, 1Q81 and 3L9S.

Chapter VI Evaluation of the biological activities of the synthesized hydrazones

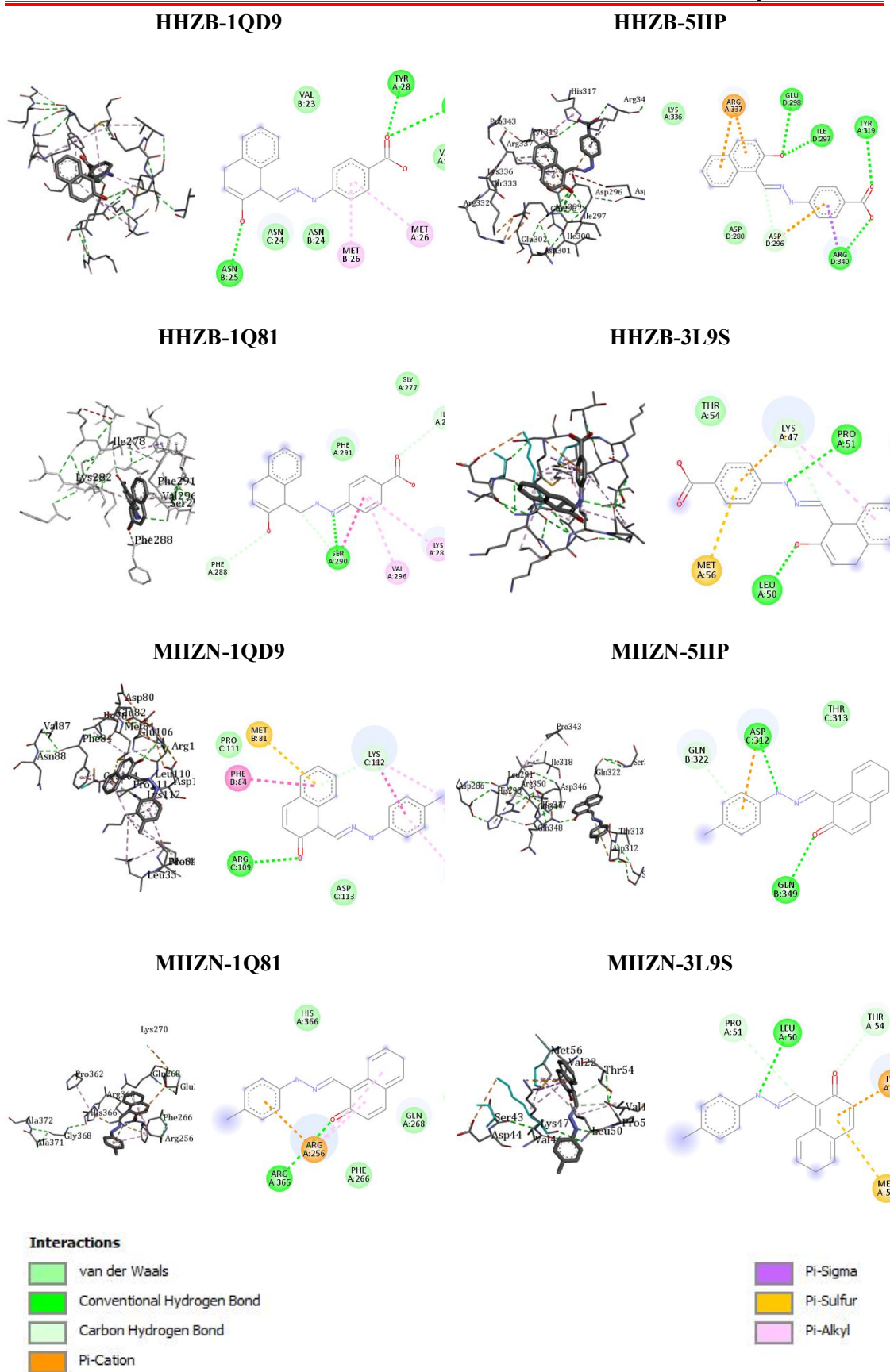


Figure VI. 8: 3D and 2D Binding-interaction diagrams of MHZN and HHZB with 1QD9, 5IIP, 1Q81 and 3L9S.

Chapter VI Evaluation of the biological activities of the synthesized hydrazones

Table VI.4: Molecular docking results and interactions of the investigated ligands.

Ligand	Complex	Binding energy in kcal/mol	Amino acids	Interactions
HHZB	HHZB-3L9S	- 104.13	LYS A47	Pi-Sulfur,VDW
			MET A56	Pi-Sulfur
			PRO A51	H Bond
			LEU A50	H Bond
	HHZB-1QD9	- 93.79	TYR A28	H Bond
			TYR C28	H Bond
			MET A26	Pi-Alky
			MET B26	Pi-Alky
			ASN B25	H Bond
	HHZB-5IIP	-117.37	ARG A377	Pi-Sulfur
			GLU D298	H Bond
			ILE D297	H Bond
TYR A313			H Bond	
ARG D340			H Bond,Pi-Sigma	
ASP D296			Pi-Sulfur,VDW	
HHZB-1Q8I	-92.62	PHE A288	VDW	
		SER A290	H Bond,Pi-Sigma	
		VAL A296	Pi-Alky	
		LYS A282	Pi-Alky	
		ILE A258	VDW	
MHZN	MHZN-3L9S	- 87.67	LYS A47	Pi-cation
			MET A56	Pi-sulfur
			LEU A50	H Bond
			THR A54	H Bond
			PRO A51	H Bond
	MHZN-1QD9	- 84.93	MET B81	Pi-cation
			PHE B84	Pi-Sigma
			ARG C109	H Bond
			LYS C112	Pi-Sigma, Pi-Alky
	MHZN-5IIP	-99.53	MET C41	Pi-Alky
			ASP C312	H Bond, Pi-Sulfur
	MHZN-1Q8I	-89.29	GLN B349	H Bond
ARG A256			Pi-Cation	
ARG A365			H Bond	
			ARG A256	Pi-Alkyl

The 1QD9, 5IIP, 1Q8I, and 3L9S crystal structures of the most favorable docking conformations of the resultant complexes are shown in figure VI.8 collectively with the 3D and 2D binding interaction diagrams of MHZN and HHZB. Both MHZN and HHZB ligands have a tendency for binding to the outer surface of the inner pocket within the chosen targets, according to an analysis of figure IV. 7.

Significant binding affinity was shown by both hydrazone ligands, with the following binding energy values for HHZB noted: HHZB-3L9S: -104.13 kcal/mol; HHZB-5IIP: -117.37 kcal/mol; HHZB-1QD9: -93.79 kcal/mol; and HHZB-1Q8I: -

Chapter VI Evaluation of the biological activities of the synthesized hydrazones

92.62 kcal/mol. Conversely, for MHZN, the binding energies were as follows: -87.67 kcal/mol for (MHZN-3L9S), -99.53 kcal/mol for (MHZN-5IIP), -84.93 kcal/mol for (MHZN-1QD9), and -89.29 kcal/mol for (MHZN-1Q8I).

By the comparison of the above binding energy values, we can observe that all the complexes formed by HHZB are lower than those formed by MHZN. Furthermore, we can see that the lowest energy value was with 5IIP in both complexes. These values signify higher stability and stronger binding affinity, indicative of superior potential for inhibition. These results indicate that the presence of carboxylic acid group instead of methyl group has led to noticeable increase in antibacterial activity of the studied hydrazone.

Furthermore, it can be seen from an in-depth examination of the 2D interaction diagram in figure IV. 8 that HHZB interacts via hydrogen bonding with GLU D298, ILE D297, TYR A313, and ARG D340. The total stability of the complex may also be influenced by a number of secondary forces, including those involving amino acids listed in table 4 and Pi-Sulfur and Van der Waals interactions with ASP D296.

References

- [1] Y.N. Azizah, I. Mulyani, D. Wahyuningrum, D.N. Bima, Synthesis, Characterization and Antioxidant Activity of Kobalt (II)-Hydrazone Complex, *EduChemia (Jurnal Kim. Dan Pendidikan)*. 5 (2020) 119. <https://doi.org/10.30870/educhemia.v5i2.7987>.
- [2] H.A. Abuelizz, H.A.A. Taie, A.H. Bakheit, G.A.E. Mostafa, M. Marzouk, H. Rashid, R. Al-Salahi, Investigation of 4-hydrazinobenzoic acid derivatives for their antioxidant activity: In vitro screening and DFT study, *ACS Omega*. 6 (2021) 31993–32004.
- [3] I. Amine Khodja, H. Boulebd, C. Bensouici, A. Belfaitah, Design, synthesis, biological evaluation, molecular docking, DFT calculations and in silico ADME analysis of (benz)imidazole-hydrazone derivatives as promising antioxidant, antifungal, and anti-acetylcholinesterase agents, *J. Mol. Struct.* 1218 (2020) 128527. <https://doi.org/10.1016/j.molstruc.2020.128527>.
- [4] Y. Toledano-Magaña, J.C. García-Ramos, M. Navarro-Olivarria, M. Flores-Alamo, M. Manzanera-Estrada, L. Ortiz-Frade, R. Galindo-Murillo, L. Ruiz-

Chapter VI Evaluation of the biological activities of the synthesized hydrazones

- Azuara, R.M. Meléndrez-Luevano, B.M. Cabrera-Vivas, Potential amoebicidal activity of hydrazone derivatives: Synthesis, characterization, electrochemical behavior, theoretical study and evaluation of the biological activity, *Molecules*. 20 (2015) 9929–9948. <https://doi.org/10.3390/molecules20069929>.
- [5] A. Baj, J. Cedrowski, E. Olchowik-Grabarek, A. Ratkiewicz, S. Witkowski, Synthesis, DFT calculations, and in vitro antioxidant study on novel carba-analogs of vitamin E, *Antioxidants*. 8 (2019) 1–17. <https://doi.org/10.3390/antiox8120589>
- [6] J. Lengyel, J. Rimarčík, A. Vagánek, E. Klein, On the radical scavenging activity of isoflavones: Thermodynamics of O-H bond cleavage, *Phys. Chem. Chem. Phys.* 15 (2013) 10895–10903. <https://doi.org/10.1039/c3cp00095h>.
- [7] S. Baliyan, R. Mukherjee, A. Priyadarshini, A. Vibhuti, A. Gupta, R.P. Pandey, C.-M. Chang, Determination of antioxidants by DPPH radical scavenging activity and quantitative phytochemical analysis of *Ficus religiosa*, *Molecules*. 27 (2022) 1326.
- [8] H.Y. Zhang, Y.M. Sun, X.L. Wang, Substituent effects on O-H bond dissociation enthalpies and ionization potentials of catechols: A DFT study and its implications in the rational design of phenolic antioxidants and elucidation of structure - Activity relationships for flavonoid antioxidant, *Chem. - A Eur. J.* 9 (2003) 502–508. <https://doi.org/10.1002/chem.200390052>.
- [9] L. Messaadia, Y. Bekkar, M. Benamira, H. Lahmar, Predicting the antioxidant activity of some flavonoids of *Arbutus* plant: A theoretical approach, *Chem. Phys. Impact*. 1 (2020) 100007. <https://doi.org/10.1016/j.chphi.2020.100007>.
- [10] G.T. Lountos, R. Jiang, W.B. Wellborn, T.L. Thaler, A.S. Bommarius, A.M. Orville, The crystal structure of NAD (P) H oxidase from *Lactobacillus sanfranciscensis*: insights into the conversion of O₂ into two water molecules by the flavoenzyme, *Biochemistry*. 45 (2006) 9648–9659.
- [11] S. Aitha, V. Thumma, R. Matta, S. Ambala, K. Jyothi, S. Manda, J. Pochampally, Antioxidant Activity of Novel 4H-Chromene Tethered 1, 2, 3-Triazole Analogues: Synthesis and Molecular Docking Studies, *Results Chem.* (2023) 100987.
- [12] B.M. Babior, NADPH oxidase: an update, *Blood*, *J. Am. Soc. Hematol.* 93 (1999) 1464–1476.
- [13] T. Moreira, F. Delle, L. Domeneghini, A. Mascarello, T. Regina, C. Roberto, D. Bardini, C. Regina, M. Barardi, E. De Fatima, A. Smânia, A. Viancelli, L. Ariel,

Chapter VI Evaluation of the biological activities of the synthesized hydrazones

- T. Garcia, R. Augusto, R. José, A. Smânia, *Bioorganic & Medicinal Chemistry Letters* Antibacterial activity of chalcones , hydrazones and oxadiazoles against methicillin-resistant *Staphylococcus aureus*, 22 (2012) 225–230. <https://doi.org/10.1016/j.bmcl.2011.11.059>.
- [14] X. Yao, H. Hu, S. Wang, W. Zhao, M. Song, *Synthesis , Antimicrobial Activity , and Molecular Docking Studies of Aminoguanidine Derivatives Containing an Acylhydrazone Moiety*, 20 (2021) 536–545. <https://doi.org/10.22037/ijpr.2020.113711.14446>.
- [15] Ł. Popiołek, A. Biernasiuk, *Synthesis and investigation of antimicrobial activities of nitrofurazone analogues containing hydrazide-hydrazone moiety*, (2017). <https://doi.org/10.1016/j.jsps.2017.05.006>.
- [16] M.A. Salem, A. Ragab, A. El-khalafawy, A.H. Makhlof, A.A. Askar, Y.A. Ammar, *Bioorganic Chemistry Design , synthesis , in vitro antimicrobial evaluation and molecular docking studies of indol-2-one tagged with morpholinosulfonyl moiety as DNA gyrase inhibitors*, *Bioorg. Chem.* 96 (2020) 103619. <https://doi.org/10.1016/j.bioorg.2020.103619>.
- [17] M.C. Mandewale, B. Thorat, Y. Nivid, R. Jadhav, A. Nagarsekar, R. Yamgar, *Synthesis , structural studies and antituberculosis evaluation of new hydrazone derivatives of quinoline and their Zn (II) complexes*, *J. SAUDI Chem. Soc.* (2016). <https://doi.org/10.1016/j.jscs.2016.04.003>.
- [18] M. Totsika, R. Jarrott, S.R. Shouldice, G. Gunc, M.E.S. Achard, T.J. Wells, M.P. Argente, A.G. Mcewan, M.A. Schembri, *Structural and Functional Characterization of Three DsbA Paralogues from Salmonella enterica Serovar Typhimurium * □*, 285 (2010) 18423–18432. <https://doi.org/10.1074/jbc.M110.101360>.
- [19] H. Zalkin, J.L. Smith, S. Sinha, P. Rappu, S.C. Lange, P. Ma, *Crystal structure of Bacillus subtilis YabJ , a purine regulatory protein and member of the highly conserved YjgF family*, 96 (1999) 13074–13079.
- [20] C.F. Schuster, L.E. Bellows, T. Tosi, I. Campeotto, R.M. Corrigan, P. Freemont, A. Gründling, *The second messenger c-di-AMP inhibits the osmolyte uptake system OpuC in Staphylococcus aureus*, *Sci. Signal.* 9 (2016) 1–14. <https://doi.org/10.1126/scisignal.aaf7279>.

Chapter VI Evaluation of the biological activities of the synthesized hydrazones

[21] F. Wang, W. Yang, Structural Insight into Translesion Synthesis by DNA Pol II, *Cell*. 139 (2009) 1279–1289. <https://doi.org/10.1016/j.cell.2009.11.043>.

General conclusions

This study focused on the synthesis and characterization of four hydrazone derivatives namely: (a) 4-[(2E)-2-(2-nitrobenzylidene) hydrazinyl] benzoic acid (NBHZ), (b) 4-[(2E)-2-(2-hydroxybenzylidene) hydrazinyl] benzoic acid HBHZ, (c) {(2E)-2-[(2-hydroxynaphthalen-1-yl) methylidene] hydrazinyl} benzoic acid HHZB, (d) 1{(E)-[2-(4methylphenyl) hydrazinylidene] methyl} naphthalen-2-ol (MHZN), which were produced by combining various aldehydes with 4-methylphenylhydrazine benzoic acid and 4p-tolyhydrazine achieving yields of 70%, 58% ,71% and 74% respectively.

The synthesis route, which was based on a previously documented method discovered in the literature, made it possible to produce these hydrazone compounds, each of which has a distinct chemical structure.

Sophisticated spectroscopic techniques were employed to characterize the produced hydrazones UV-Vis FTIR and NMR of ^1H and ^{13}C yielding a comprehensive comprehension of their chemical composition and structural attributes. UV-Vis confirms the presence of aromatic rings , chromophore groups and conjuguated double bands in obtained hydrazones. FTIR revealed the presence of azomethine group vibrations such as C=N , N-N, C-N and N-H , Using the VEDA program, a potential energy distribution (PED) analysis was conducted to provide a more accurate interpretation of vibrational modes. The experimental spectrums are supported by the simulated ones.

A comprehensive evaluation of the chemical and physical characteristics of the produced hydrazones was carried out such as melting points (NBHZ MP=267.1 °C , HBHZ MP=280°C ,HHZB MP=275 °C , MHZN MP=190°C) ,Solubility test in cold and hot states and polarity of the compounds by using thin layer chromatography (TLC) which showed that HHZB is the most polar one with retention factor $R_f=0.52$. Determining the melting temperatures of hydrazone derivatives contributes to our understanding of their solid-state properties by providing information about their purity and crystalline structure. Furthermore, by revealing the hydrazones' interactions with solvents, the solubility investigations provided crucial details regarding their dissolving characteristics and possible uses in solution-based processes.

Using the B3LYP/6-311G(d,p) basis set and the Gaussian09 program, a DFT investigation was conducted to theoretically investigate the chemical reactivity of the hydrazone derivatives that were produced. Quantum parameters were utilized to assess the compounds'

electronic structure and reactivity namely the Lowest Unoccupied Molecular Orbital (LUMO) , the Highest Occupied Molecular Orbital (HOMO) and gap energy. Ionization Potential (I), Electron Affinity (A), Hardness (η), Softness (σ), Chemical Potential (μ), Electronegativity (χ), and Global Electrophilicity (ω). in addition to dipolar moment and atomic charges provided valuable insights into the active sites and electronic properties

The Multiwfn program was used for a topological analysis was included in an attempt to thoroughly investigate the electrical structure and bonding characteristics of the produced hydrazone derivatives. Comprehensive studies into the electron density distribution, bonding properties, and other electronic features are made possible by this sophisticated computational tool. LOL (Localized Orbital Locator), ELF (Electron Localization Function), RDG (Reduced Density Gradient), DOS (Density of States), and AILP (Average ionization Localization Potential) were the topological analyses that were selected.

✓ Corrosion inhibition evaluation

The hydrazone derivative MHZN was particularly selected for corrosion experiments in the larger context of this work because of its distinct solubility profile in acidic environments (1M HCl) which distinguished it from the other substances. It is critical to comprehend how MHZN functions in these conditions in order to assess its possible suitability as a corrosion inhibitor for XC 48.

Electrochemical tests including Tafel, Electrochemical Impedance Spectroscopy (EIS), Weight loss and adsorption isotherm investigations were used methodically to evaluate MHZN's anti-corrosion properties. These electrochemical techniques offer a thorough examination of factors like polarization behavior, adsorption properties, and impedance,

-According to EIS the corrosion inhibition efficacy of MHZN is reached to $IE_{EIS}=86.9\%$.

-The shapes of all the generated Nyquist plots are nearly identical to those of semicircles. This implies that the addition of MHZN has no effect on the corrosion mechanism.

-Strong agreement between the experimental and simulated impedance data, supporting the recommended equivalent circuit for accurate carbon steel/solution interface modeling.

-The Nyquist plot's diameter increase as the concentration of MHZN increased, indicating that the charge transfer mechanism controls carbon steel corrosion in the aggressive medium.

- The generated hydrozone acts as a mixed-type inhibitor, as demonstrated by polarization curves, and its inhibition efficiency increases with increasing inhibitor concentration, peaking at 7.5×10^{-5} M.

-The Langmuir adsorption isotherm model and the negative sign of ΔG^0 , which also show the spontaneous nature of adsorption onto the carbon steel surface, indicate that the adsorption mechanism of MNHZ on XC 48 surface involved the formation of covalent bonds and coordination.

-By significantly lowering metal corrosion and surface roughness, the inhibitor demonstrated good adsorption on carbon steel in acidic conditions, as demonstrated by atomic force microscopy.

-Molecular dynamic simulations (MDS) show that inhibitor molecules interact with the carbon steel surface both in aqueous solutions and in a vacuum. Conversely, the high binding energy and negative interaction energy ($-663.023 \text{ kJ mol}^{-1}$) indicate the stable and spontaneous adsorption of the inhibitor molecules on the surface of the carbon steel.

-The COSMO-RS method reveals that MHZN compounds and Fe clusters are primarily nonpolar and hydrophobic, with localized hydrogen bond acceptor (HBA) regions. This information facilitates a better understanding of the interaction and charge distribution of these materials for the purpose of corrosion inhibition.

✓ **Anti-antioxidant activity**

The 2,2-diphenyl-1-picrylhydrazyl (DPPH) method, a frequently used assay for assessing antioxidant potential, was employed in this investigation. When evaluating the ability to scavenge free radicals, the DPPH experimental method is essential. The results showed:

- IC₅₀ values for HBHZ, NBHZ, HHZB, and MHZN are 1.15 $\mu\text{g/mL}$, 2.1 $\mu\text{g/mL}$, 0.3343 $\mu\text{g/mL}$, and 0.4114 $\mu\text{g/mL}$, respectively. A comparative study using the benchmark antioxidant BHT (IC₅₀ = 1.83 $\mu\text{g/mL}$) highlighted the influence of functional groups on the hydrazones' capacity for scavenging.

-The three major radical pathways Hydrogen Atom Transfer (HAT), Single Electron Transfer-Proton Transfer (SET-PT), and Single Electron Transfer-Electron Transfer (SET-ET) were the focus of the obtained hydrazones' mechanism of action against radicals. Calculations are made as part of the study using thermodynamic parameters like Bond Dissociation Energy (BDE), Ionization Potential (IP), Proton Dissociation Energy (PDE), Proton Affinity (PA), and Electron Transfer Entropy (ETE). According to the findings, the most thermodynamically advantageous mechanism was identified as (SET-ET)

-The NADPH oxidase receptor binding affinity and interactions between ligands and the receptor were carefully investigated and analyzed by the molecular docking experiments. In

order to identify important amino acid residues involved in the ligand-receptor interactions and to forecast the energetically advantageous binding postures, docking simulations were used. The binding interactions of the chosen ligands NHBZ, HBHZ, MHZN, and HHZB with the NADPH oxidase (NO) receptor were assessed. A key player in the production of reactive oxygen species (ROS), NADPH oxidase is a focus of great interest in research on antioxidant mechanisms and oxidative stress.

✓ **Anti-bacterial activity**

-Through serial dilution, the antibacterial activity of all hydrazones against Gram-positive (*B. subtilis*, *S. aureus*) and Gram-negative (*S. enterica*, *E. coli*) bacteria was assessed in order to determine their minimum inhibitory concentration (MIC).

-the results indicating that HBHZ has a MIC of 125 µg/mL for *B. subtilis* and 250 µg/mL for all other strains, while NBHZ has a MIC value of 250 µg/mL for all strains. MHZN demonstrated a minimum inhibitory concentration (MIC) of 125 µg/mL against *S. aureus* and 62.5 µg/mL against *S. enterica*, *E. coli*, and *B. subtilis*. HHZB exhibited minimum inhibitory concentrations (MIC) of 31.25 µg/mL for *S. enterica*, 125 µg/mL for *E. coli*, 62.5 µg/mL for *B. subtilis*, and 15.62 µg/mL for *S. aureus*. Neither compound showed any antibacterial activity below these concentrations.

-The 3D structures of *Salmonella enterica* serovar Typhimurium DsbA (PDB ID: 3L9S), *Bacillus subtilis* YABJ (PDB ID: 1QD9), *Staphylococcus aureus* OpuCA (PDB ID: 5IIP), and *Escherichia coli* DNA Polymerase II (PDB ID: 1Q8I) were provided by the Protein Data Bank (PDB) (www.rcsb.org) and were selected for molecular docking studies.

-Hydrazone ligands Both HHZB and MHZN exhibited noteworthy binding energies and significant binding affinities, with HHZB beating MHZN for all targets. Superior inhibitory potential is suggested by these values' higher stability and stronger binding affinity. The presence of a carboxylic acid group, as opposed to a methyl group, greatly increases the investigated hydrazone's antibacterial activity.

Perspectives

- ✓ Synthesis of other hydrazones with different functional groups to increase their potential .
- ✓ Overcoming the insolubility in water of hydrazones can be achieved through structural modification or addition of surfactant agent.
- ✓ Continue to highlight the biological and pharmaceutical activities of the synthesized molecules,
- ✓ Conduct in vitro toxicity tests and to explore their therapeutic properties.
- ✓ Studying the relationship between the antioxidant antibacteria activities and corrosion

ملخص:

يستكشف هذا التحقيق الشامل التركيب والتوصيف والتحليل التفصيلي لأربعة مشتقات مختلفة من الهيدرازون. تم الحصول على المركبات ذات الهياكل الكيميائية المتميزة من التركيب باتباع البروتوكولات المقدمة من المراجع المكتبية المنشورة. من أجل معرفة المزيد عن الخصائص والاستخدامات المحتملة لمشتقات الهيدرازون هذه، قدمت التحقيقات النظرية من برنامج Gaussian 09 تفسيرات كمية حول مشتقات الهيدرازون، بما في ذلك الخصائص الإلكترونية. تم استخدام برنامج VEDA لدراسة السلوك الاهتزازي وتوزيع الطاقة الكامنة (PED). علاوة على ذلك، تم الكشف عن ميزات التفاعل وطبيعة الروابط من خلال التحليلات الطوبولوجية باستخدام برنامج Multiwfn، وتم اختيار MHZN لأبحاث التآكل نظراً لطبيعته المميزة القابلة للذوبان في الأحماض. وقد تم إثبات نموذجها المثبط من نوع لانجميور من خلال دراسات تساوي درجة حرارة الامتزاز والاختبارات الكهروكيميائية مثل تحليل Tafel و EIS. تم تقييم نشاط مضادات الأكسدة للهيدرايونات الأربعة باستخدام طريقة DPPH وتم تحديد آلية العمل من خلال المعاملات الديناميكية الحرارية. بالإضافة إلى ذلك، قامت دراسات الالتحام الجزيئي عبر iGEMDOCK بتقييم إمكانات مشتقات الهيدرازون كمضادات للأكسدة من خلال التفاعلات مع مستقبل أكسيداز NADPH، كما تم دراسة الفعالية ضد أربعة أنواع من البكتيريا بالإضافة إلى الالتحام الجزيئي وهذه الاستراتيجية الشاملة تجمع بين التركيب. عمل التقييمات والتحليلات العملية على تحسين فهمنا لمشتقات الهيدرازون وتضع الأساس لمجموعة متنوعة من التطبيقات في علوم المواد والوقاية من التآكل.

الكلمات المفتاحية: تركيب , تشخيص , هيدرازون, DFT , تثبيط التآكل , لانشطة البيولوجية.

Abstract :

This thorough investigation explores the synthesis, characterisation , and detailed analysis of four different hydrazone derivatives. Compounds with distinct chemical structures were obtained from the synthesis by following published protocols from the literature. In order to learn more about the characteristics and possible uses of these hydrazone derivatives, theoretical investigations with Gaussian09 offered quantum insights into the hydrazone derivatives, including electronic characteristics. VEDA program was utilized to investigate vibrational behavior and potential energy distribution (PED). Moreover, reactivity and bond nature features were revealed by topological analyses utilizing the Multiwfn program, MHZN was selected for corrosion research due to its distinct acid-soluble nature. Its Langmuir-type inhibitory model was demonstrated by adsorption isotherm studies and electrochemical testing such as Tafel analysis and EIS. The antioxidant activity of the four hydrazones was evaluated using DPPH method .the mechanism of action was determined via thermodynamic parameters Additionally Molecular docking studies via iGEMDOCK assessed the hydrazone derivatives' potential as antioxidants through interactions with the NADPH oxidase receptor, The effectiveness against four types of bacteria was assessed in addition to molecular docking. This comprehensive strategy combines synthesis, practical assessments, and analysis improves our understanding of hydrazone derivatives and lays the groundwork for a variety of applications in materials science and corrosion prevention.

Keywords: Synthesis, Characterization, hydrazone, DFT, Corrosion inhibition , Biological activities

Résumé :

Cette étude approfondie explore la synthèse, la caractérisation et l'analyse détaillée de quatre dérivés différents de l'hydrazone. Des composés ayant des structures chimiques distinctes ont été obtenus à partir de la synthèse en suivant les protocoles publiés dans la littérature. Afin d'en savoir plus sur les caractéristiques et les utilisations possibles de ces dérivés de l'hydrazone, des recherches théoriques avec Gaussian09 ont offert des informations quantiques sur les dérivés de l'hydrazone, y compris leurs caractéristiques électroniques. Le programme VEDA a été utilisé pour étudier le comportement vibratoire et la distribution d'énergie potentielle (PED). De plus, les caractéristiques de réactivité et de nature de liaison ont été révélées par des analyses topologiques utilisant le programme Multiwfn. MHZN a été sélectionné pour la recherche sur la corrosion en raison de sa nature distincte soluble dans l'acide. Son modèle inhibiteur de type Langmuir a été démontré par des études isothermes d'adsorption et des tests électrochimiques tels que l'analyse Tafel et l'EIS. L'activité antioxydante des quatre hydrazones a été évaluée à l'aide de la méthode DPPH. Le mécanisme d'action a été déterminé via des paramètres thermodynamiques. De plus, des études d'amarrage moléculaire via iGEMDOCK ont évalué le potentiel des dérivés de l'hydrazone en tant qu'antioxydants grâce à des interactions avec le récepteur de la NADPH oxydase. L'efficacité contre quatre types de bactéries a également été étudiée en plus docking moléculaire . Cette stratégie globale combine la synthèse , Les évaluations pratiques et des analyses améliorent notre compréhension des dérivés de l'hydrazone et jettent les bases d'une variété d'applications dans la science des matériaux et la prévention de la corrosion.

Mots clés : Synthèse, Caractérisation, Hydrazone, DFT, Inhibition de la corrosion, Activités biologiques.